On the detection of dark matter: New prospects for a multi-component dark sector and global fits of Pseudo-Nambu Goldstone dark matter

Andre Scaffidi

Center of Excellence for Particle Physics at the Terascale
School of Physical Sciences, Adelaide University.
University of Adelaide

This dissertation is submitted for the degree of
Doctor of Philosophy

July 2020

Declaration

I certify that this work contains no material which has been accepted for the award of any other degree or diploma in my name, in any university or other tertiary institution and, to the best of my knowledge and belief, contains no material previously published or written by another person, except where due reference has been made in the text. In addition, I certify that no part of this work will, in the future, be used in a submission in my name, for any other degree or diploma in any university or other tertiary institution without the prior approval of the University of Adelaide and where applicable, any partner institution responsible for the joint-award of this degree. I acknowledge that copyright of published works contained within this thesis resides with the copyright holder(s) of those works. I also give permission for the digital version of my thesis to be made available on the web, via the University's digital research repository, the Library Search and also through web search engines, unless permission has been granted by the University to restrict access for a period of time. I acknowledge the support I have received for my research through the provision of an Australian Government Research Training Program Scholarship.

Andre Scaffidi
July 2020

*

Acknowledgements

I would like to offer my sincerest thanks to the people who have helped or encouraged me in my PhD journey. First and foremost, I would like to thank my supervisors Prof. Anthony Williams, Dr. Martin White and Dr. Juan Hererro-Garcia, between them providing an endless supply of knowledge, advice and providing me with some fantastic projects that I thoroughly enjoyed every bit of. I am very glad that I found supervisors that complemented my study style so well, giving me the opportunity to produce results to the best of my potential, while not feeling overwhelmed. I would like to thank the department of physics here at the University of Adelaide for always promptly being happy to help with any inquiry or paperwork. Next, I'd like to thank the Center of Excellence for Particle Physics at the Terascale (CoEPP), for all of the opportunities to conduct work overseas or participate in workshops that have enabled me to gain skills and knowledge that have benefited me greatly and that I will continue to utilize in the future. Furthermore, thank you to the CoEPP admin staff here in Adelaide for always being friendly and welcoming as well as extremely helpful with any and all matters. I would like to offer special thanks to Dr. Ankit Beniwal, Dr. Chiara Arina as well as the CP3 (UCLouvain) staff for the hospitality offered during my visit where part of this work was completed. Special thanks to Ankit for facilitating my inclusion in the groups work and generally being a great source of discussion and a good friend. Next, I would like to thank my friends and bands for just accepting that I can't make a gig/gathering/event because of something uni related. I'm really gratefully for the support and understanding, as well as your company. Special thanks to all occupants of the physics building at the University of Adelaide colleges. I especially treasure lunch time and coffee break chats, where no topics were left out of discussion. Lastly and most importantly, I want to thank my family and loving partner. From showing me my first physics documentary, to making sure that my health is the best it can possibly be, I can't overstate the appreciation I have for the constant and unconditional source of love and support. Most of all I am thankful for what you've had to give up on my account.

Abstract

The so called ‘dark matter’ is one of the most well researched enigmas in modern physics. There currently exist a multitude of experimental observations that would infer the existence of some gravitationally heavy, weakly interacting matter that has baffled physicists since the early 1900’s. In this thesis, I will present four publications that constituted the main body of work of my PhD work. These papers explored new avenues in WIMP research: the introduction of more than one dark matter species, as well as a new type of DM model that can evade current direct detection constraints.

Table of contents

Chapter 1

Introduction

Evidence for a large amount of non-baryonic “dark matter” (DM) in the universe has been accumulating for decades [1, 2]. Recent observations of the cosmic microwave background have provided a precise measurement of the DM relic density, and also strongly support the idea of “cold” DM in the form of weakly interacting massive particles (WIMPs) [3–5][1]. The failure of the Standard Model (SM) of particle physics to adequately explain a variety of astrophysical observations has prompted the development of a large number of particle theories beyond the SM [7], commonly known as BSM theories. Concurrently with these theoretical developments, a large number of experiments have been conducted to search for DM annihilation in distant astrophysical objects, produce and observe DM particles in high energy particle collisions, or observe the direct interaction of particles of DM with Earth bound detectors. Although there are tantalizing hints of DM signatures in one or more of these experiments, there is as yet no uncontroversial detection of (non-gravitational) WIMP interactions with ordinary matter [8].

Some of the most popular candidates are Weakly-Interacting-Massive-Particles (WIMPs), in particular those that have (additionally to gravitational) non-vanishing interactions with the standard model (SM) and therefore can be tested. In fact, they are actively being searched for in direct detection (DD) experiments, which look for their nuclear scatterings in underground detectors [9], as missing transverse energy at colliders, and indirectly via possible annihilation products from astrophysical sources. As the years go by however, more and more of the WIMP parameter space is being constrained by progressively more sensitive detectors and larger detector exposure.

In this publication format thesis , I’ll detail what I think is the newest avenue in WIMP research: the introduction of more than one dark matter species, as well as a new type of DM model that can evade current direct detection constraints. This

---

[1] A variety of other candidate models have also been proposed, see REf.[6] for an overview.

thesis is structured as follows: Each publication is presented with a background and supplementary information chapter which will provide a motivation for the publication as well as detailed descriptions of concepts that are not general knowledge and/or not well presented in the literature. The background and supplementary information chapters will also present any results of the studies that were not published due to journal word limits or otherwise. Each publication will contain the required authorship statement signed by all authors. In chapter 2, a brief overview of the field of WIMPs is presented, summarizing the current landscape of observational evidence that indicates the existence of a non-baryonic particle DM.

Chapter 2

Particle dark matter - a brief history

The earliest identification of dark matter came from the velocity dispersions of galaxies within clusters. Zwicky noticed that the outer members of the Coma galaxy cluster were moving far too quickly to be merely tracing the gravitational potential of the visible cluster mass [1]. The only way the observed velocities of the cluster members could be reconciled with the virial theorem was to postulate that the cluster also contained another large, but unseen, mass component: dark matter (DM).

Nowadays, the existence of DM is a paradigm within physics and it is well established that its gravitational interactions dominate on scales from tiny dwarf galaxies, to large spirals such as the Milky Way, to clusters of galaxies, to the largest scales yet observed. There exist countless studies verifying its existence and basic properties, as well as numerous particle physics models that include a DM candidate [10][1]. In this chapter we explore the most commonly cited evidence and constraints that provide such a strong argument for the existence of a dark matter particle. We begin with a discussion of the rotation curves of spiral galaxies, which have been observed by countless analyses to be rotating much faster than expected from simply accounting for the regular luminous matter (stars galaxies etc). We then discuss the bullet cluster, a smoking-gun for the existence of a non-luminous matter component, followed by a discussion of the Cosmic Microwave Background (CMB) and how precise measurements of primordial density fluctuations obtained from its observation have led to one of the most rigid pieces of evidence for a stable, cold dark matter particle. Next, we discuss the physical properties the DM must exhibit in order to comply with observations, finally explaining why a cold, particle candidate

---

[1] Although there exist alternate theories of gravity or modified gravitational dynamics to explain the phenomena that DM does, these are strongly disfavored [11], and will not be discussed further.

is the best suited explanation. We conclude the chapter with a very brief overview of the efforts geared at detecting the DM particle. We then narrow down to the methods of particular interest to the publications presented later in this thesis, namely, these methods are direct, indirect and collider searches, discussing the motivations and methods behind each as well as a list of current and past experiments. We do not go into a high level of detail in this introduction of the experiments relevant to this work, instead saving such a discussion for later chapters.

2.1 Rotation curves of spiral galaxies

One of the most staple sources of evidence for the existence of DM is the non-canonical nature of the circular velocities of SM matter in spiral galaxies. Newton's law can be used to show that an orbiting body's orbital velocity falls off with r^{-1}:

$$v(r) = \sqrt{\frac{GM(r)}{r}} \, , \tag{2.1}$$

where $M(r)$ denotes the mass contained within the orbital radius r and is given by

$$M(r) = 4\pi \int_0^r dr \, \rho(r) \, r^2 \, , \tag{2.2}$$

where $\rho(r)$ is the *density profile* of the galaxy. However, the 21-cm hydrogen line emission can be used to measure the circular velocities of the galactic gas and deduce that, contrary to Newtonian dynamics, the orbital velocity profile in fact flattens at large r. A timeless result of this measurement comes from the spiral galaxy NGC 6503 and was presented by [12] as shown in figure 2.1. In NGC 6503, the luminous galactic disk extends no further than about 5 kpc from the center of the galaxy. If the luminous matter was all there was, the rotation curve would drop at larger radii. By analyzing the discrepancy between the true measured rotation curve and that expected by just luminous (baryonic) matter[2], one can infer the existence of an dark extended dark halo which has a symmetric or possibly tri-axial ([13]) density profile that falls off with $r^{-\gamma}$, where γ is some profile index. Many have, and still do, debate the exact form of the dark halo density profile, as certain profiles fit different contexts better (e.g. spiral galaxies vs. dwarf galaxies vs. galaxy clusters).

Of course, flattened rotation curves have been observed in many other spiral galaxies using several different tracers. For external spiral galaxies, Ref. [14] provides

---

[2] When one says baryonic matter in the context of cosmology, they really mean 'standard model' content. The reason that baryons are referred to explicitly is that protons and neutrons make up most of the astrophysical matter that we know of.

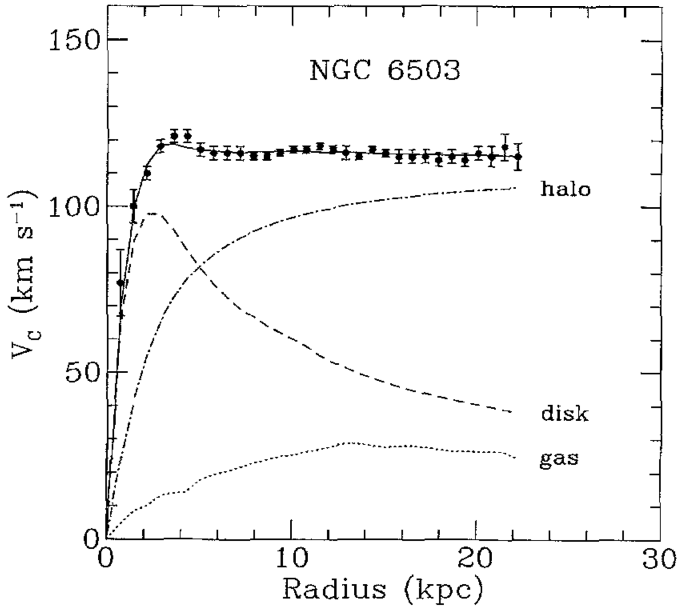

Fig. 2.1 Figure from Ref. [12]. Rotation curve of the spiral galaxy NG 6503. The points are the measured circular rotation velocities as a function of distance from the center of the galaxy. The dashed and dotted curves are the contribution to the total (solid line) rotational velocity due to the observed disk and surrounding gas, respectively, and the dot-dash curve is the contribution from the dark halo.

a comprehensive review. For a more recent study of the rotation curve and dark component of the Milky Way, see Ref. [15].

2.2 Evidence from galaxy clusters

Since one can roughly infer that the presence of a dark, gravitationally-interacting component will become increasingly prevalent in more massive systems, looking at large clusters of galaxies would then be a good idea. Indeed, the observation of stellar velocity dispersions in the Coma cluster was how Zwicky first proposed the existence of dark matter. Modern methods involve the observation of gravitational lensing, which refers to the bending of light from a background source around massive bodies as per Einstein's theory. From the severity of the distortion of this light one can measure the mass of the massive body. A variety of studies of several galaxy clusters over the years have unanimously observed far more lensing that can be accounted for by the luminous matter in the foreground cluster. For a summary of such studies as well as benchmark measurements, see [16] and [17].

Perhaps the most famous galaxy cluster to yield evidence of DM is the bullet cluster [18] shown in figure 2.2. The bullet cluster is a collision between two galaxy clusters perpendicular to the line of sight. One can use X-rays to trace the

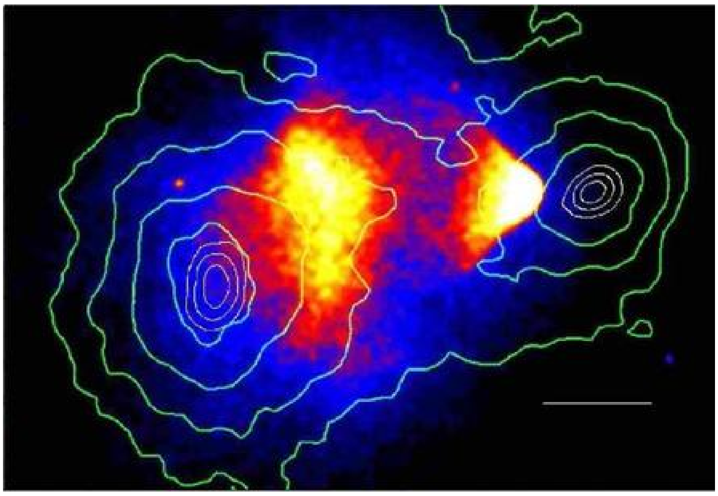

Fig. 2.2 Figure from [18]. Composite image of the bullet cluster showing just the X-ray emission overlayed on top of gravitational lensing contours. The contours represent the strength of the lensing and hence map the morphology of the mass density of the cluster merger. The fact that the mass content of each cluster has effectively passed through the collision indicates that there is another essentially collisionless invisible mass component.

electromagnetically coupled gas content of the merger event. Clearly shown in figure 2.2 is the bow shock feature of the baryonic content that results from conventional electromagnetic frictional loss in the standard model matter. What makes the bullet cluster interesting is that gravitational lensing measurements show that most of the mass content of the merger does not trace the luminous matter. In fact, it is as if most of the mass content passed straight through the merger event unaffected. This shows that dark matter does not necessarily have to track luminous matter in any way, and that it does not interact strongly with either gas or itself; this means that it is effectively collisionless.

2.3 Dark Matter in Large Scale Structure, Cosmology and the cosmic microwave background

The cosmic microwave background (CMB) is a very nearly uniform background of photons in all directions on the sky. Its spectral distribution follows a black body spectrum of a body at 2.73 K. In the hot early universe, temperatures were high enough such that matter was ionized, and thus photons could not propagate freely. As the universe expanded and cooled, photons decoupled from matter and were allowed to freely propagate. Over time as the universe expanded, the free photons have red-shifted to microwave wavelengths, which is what was first discovered by

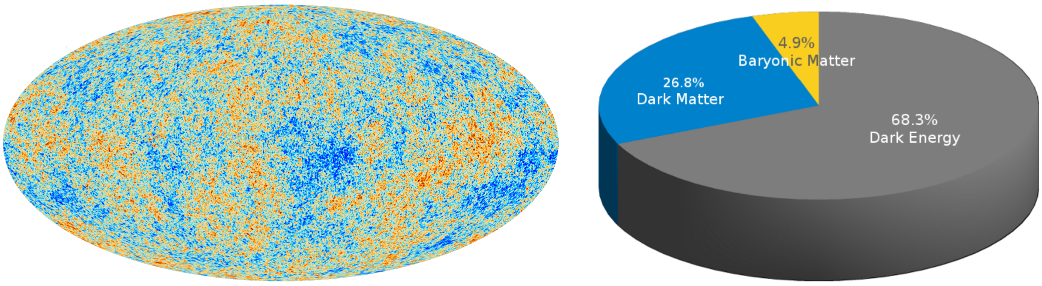

Fig. 2.3 Figures from [20]. Left: The CMB temperature perturbation spectrum as viewed by the Planck telescope (2013). Colors represent the relative change of temperature with respect to 2.7 K (red color indicates warmer regions, blue color colder areas). Right: The relative contributions of dark matter, dark energy and baryonic matter to the universe's total energy density as deduced by the Planck collaboration.

Wilson and Penzias in 1964 [19]. From the power spectrum of the CMB photons, the size of the energy density fluctuations can be derived, thus yielding a map of the mass distribution in the early universe which is shown in figure 2.3 (left) as temperature perturbations taken from the most recent CMB analysis by the Planck satellite [20].

2.3.1 The ΛCDM model

Often called the "standard model" of cosmology, the ΛCDM predetermination is a framework that incorporates a cosmological constant Λ associated with the dark energy (DE), regular baryonic matter and a cold DM particle (CDM) in a flat (Freidmann, Walker metric with $k = 0$, [11]) space-time. 'Cold' dark matter means that the DM moves non-relativistically, and so has a short free-streaming length (less than the size of a gas cloud undergoing gravitational collapse, for example). The ΛCDM cosmology will give a theoretical prediction for the angular power spectrum of the CMB as shown in figure 2.4 by the green line. More specifically, the height of the third peak in this spectrum depends primarily on the relative contribution of dark energy and matter (dark + SM).

Define the density parameter, or *relic density* Ω as the total energy density of the universe divided by the critical energy density $\rho_{\text{crit}} = 3H_0^2/8\pi G$. With such a definition, the requirement of a flat space-time is simply given by $\Omega = 1$ [21]. The total relic density is the sum of all contributions of the ΛCDM model:

$$\Omega = \Omega_{\text{DE}} + \Omega_{\text{DM}} + \Omega_{\text{SM}} \ . \tag{2.3}$$

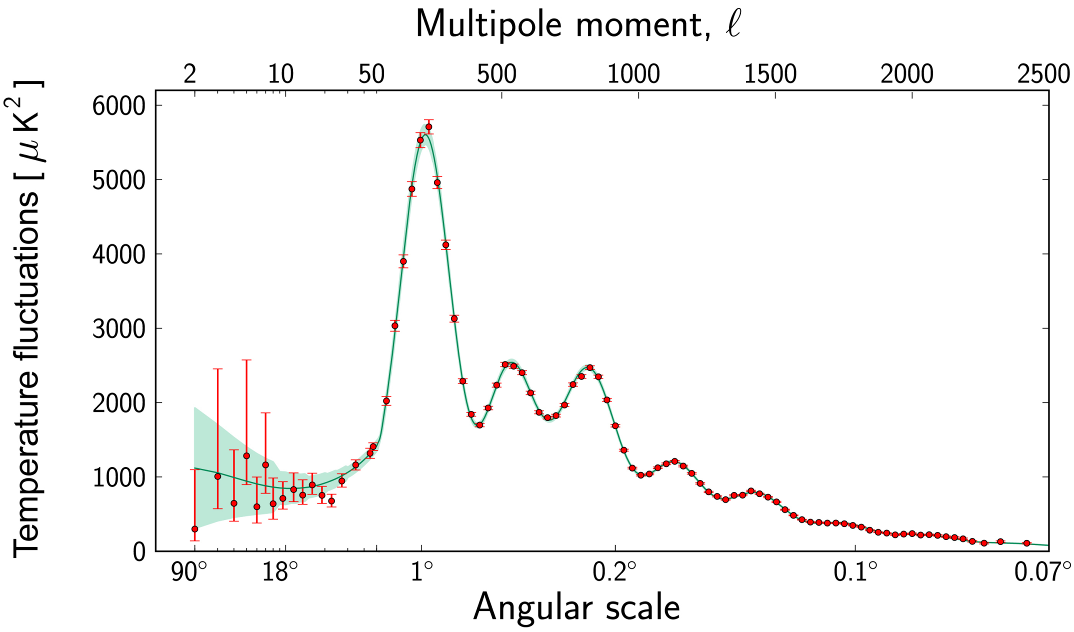

Fig. 2.4 Figure from [22]. The map of the anisotropies in the Cosmic Microwave Background temperature spectrum as observed by the Planck satellite. In green is the best fit ΛCDM configuration, yielding $\Omega_{\rm DE} \sim 0.68$, $\Omega_{\rm DM} \sim 0.27$ and $\Omega_{\rm SM} \sim 0.05$.

Using their renewed analysis of the CMB, the Planck collaboration have found the current best measurement of the total relic abundance. The relic density of DM was found to be

$$\Omega_{\rm DM} \equiv \rho_{\rm DM}/\rho_{\rm crit} \simeq 0.27 \; . \tag{2.4}$$

The Planck results are summarized in a nice pie chart shown in figure 2.3 (right).

2.3.2 Dark matter in large scale structure

The Millennium simulation is an N-body simulation that uses the ΛCDM cosmology to visualize the large scale distribution of structure throughout the universe at progressive red-shifts [23]. Figure 2.5 (left) shows a snapshot of this colossal simulation at a red-shift of $z = 1.4$ corresponding to the universe at age 4.6 Gyr. The gravitational amplification of small density fluctuations in the Cosmic Microwave Background (CMB) leads to structures resembling the observed large scale structure distributions. The resulting mass density distribution resembles a “cosmic web” made of different structures: low density ‘voids’, surrounded by thin ‘sheets’ of matter. A network of

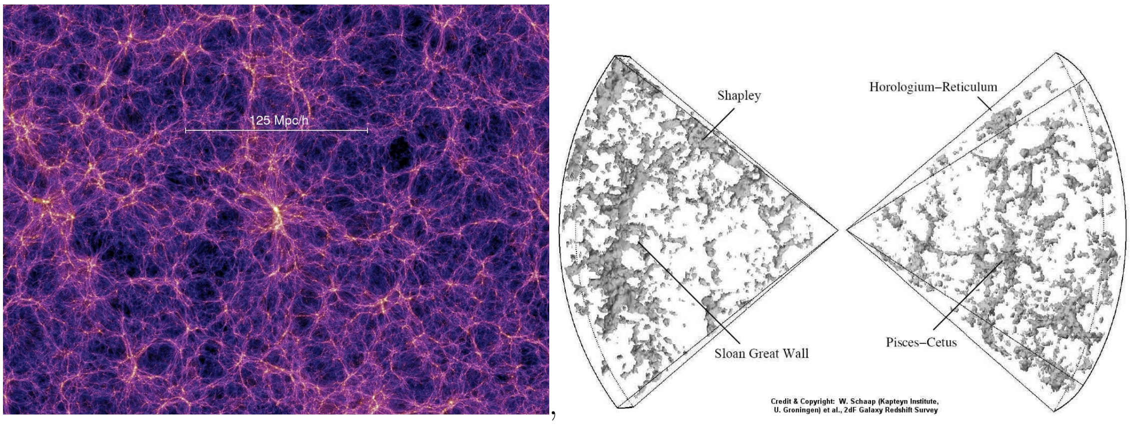

Credit & Copyright: W. Schaap (Kapteyn Institute, U. Groningen) et al., 2dF Galaxy Redshift Survey

Fig. 2.5 Left: Image from the work of [23]. A snapshot of the Millennium simulation at $z = 1.4$ (4.6 Gyr). The filaments and voids are easily seen through the image. At the junctions of these filaments, clusters of galaxies and such structures congregate and form within large DM halos. Right: The Sloan great wall as presented by the 2df Galaxy Redshift Survey.

'filaments' of different sizes and density contrast depart from the sheets and visually dominate the mass distribution. Dense clumps of matter lie at the intersections of these filaments. Matter tends to flow out of the voids, transit through the sheets and finally accrete onto the largest clumps through filaments. The positions of CDM haloes trace the large scale structure. Galaxies then form within these haloes.

The first observational evidence for the large scale structure was discovered by observing a filament that was illuminated by a background quasar [24]. Before this evidence was discovered, the 2df Galaxy red-shift survey [25] has mapped distant galaxies and clusters and has seen structures that resemble sheets, namely the 'Sloan Great Wall' (figure 2.5 right). With this picture in mind, one can then deviate away from the paradigm that it is localized DM halos that encompass singular structures, clusters and galaxies, and now view the universe as a large web of intertwining structures. These structures comprising mostly of DM, arising from primoridal fluctuations in the CMB, then house small scale structures, leading to the non-linear dynamics we observe today.

2.4 Properties of dark matter

In the previous sections of this chapter, we discussed the leading evidence for a gravitationally interacting dark component to the total relic abundance Ω. However, despite this abundance of evidence for the *existence* of dark matter, the *nature* of dark matter remains to be understood precisely. From the previously discussed evidence, one can create a list of properties any dark matter candidate must adhere to [26].

Electromagnetic neutrality

Dark matter was named as such solely due to the fact that its existence can not be directly inferred by astronomical observations of photons - at least given current experimental sensitivity. Hence, any DM candidate must couple significantly weaker via QED than conventional astrophysical SM matter. The strongest constraint comes from the requirement that the dark matter not couple too strongly to photons during the recombination epoch, avoiding disruption of the CMB perturbations [27].

Stability

For the dark matter to exert the gravitational influence it does as well as conform with Large Scale Simulations (LSS) and CMB observation, it must be stable on cosmological timescales [28]. Particle models of DM that subsequently decay into daughter DM have been proposed, but they are highly constrained by the fact that the observed and simulated DM halo structures do not indicate such dynamics [29, 30].

Non-baryonic, particle nature

In section 2.3 we discussed how the assumption of a ΛCDM cosmology provides an overwhelmingly good fit to the observed power spectrum of the CMB. In general, any new theory of cosmology incorporating a dark matter component must necessarily reproduce a power spectrum consistent with that observed in the latest measurements of the CMB. The extreme precision of the CMB measurement renders such a criterion arguably the most important. More fundamentally, the CMB measurement heavily favors a dark matter *particle*, and further still, that the particle is non-baryonic. With this said, baryonic solutions to the DM problem have indeed been proposed. To this end, massive halo compact objects (MACHOs), which are dark baryonic objects including faint neutron stars, brown dwarfs, white dwarfs, planets, etc. were proposed as such baryonic DM candidates. Strong limits on the MACHO interpretation have been set by observation of the incorrect chemical abundance to that which is expected from a population of MACHOs, as well as gravitational lensing searches [31–33]. Such limits on stellar scale DM further favor the particle interpretation.

Interaction strength

The interaction strength of the DM with itself as well as regular matter must be consistent with astronomical observations. The foremost constraint comes from the bullet cluster discussed in section 2.2, which puts an upper bound of the DM self-interaction of $\sigma/m \leq 1$ cm^2 g^{-1}, where σ is the DM-DM interaction cross-section which parameterizes the physics of the scattering process.

Temperature

The LSS of DM would indicate that the DM must be able to collapse under gravity to form small-scale structure in the form of cluster/galaxy halos after it has decoupled from the thermal bath just after the big bang. The immediate conclusion from this logic would demand that the dark matter have a small or non-relativistic velocity at that time so as to not free stream out of such density perturbations observed in the CMB. It is thus said the DM must be 'cold'. At most, it must be 'lukewarm', with free-streaming lengths on the order of galactic scales, if the correct matter power spectrum is to be realized [34].

2.4.1 The zoo of candidates, and the WIMP

Even after the seemingly long list of prerequisites, there is no shortage of well-motivated particle theory candidates. A non exhaustive diagram of theoretical models is pictorially represented in figure 2.6. Arguably the most famous (or infamous) class of DM candidates is the Weakly Interacting Massive Particle, or WIMP [11, 35, 36]. In the early universe, equilibrium is maintained by $\bar{\chi}\chi$ annihilation processes to standard-model particles and antiparticles[3]. As discussed in section 3.3.1, any particle with a weak-scale interaction will fall out of equilibrium with the hot plasma of the early universe and produce approximately the correct observed relic abundance $\Omega_{\text{DM}} \simeq 0.27$. This fact is appropriately dubbed, the '*WIMP miracle*'. Furthermore, any such particle adhering to the WIMP miracle is expected to interact with SM matter via interactions of approximately the same order in strength as the weak force, and hence in principal, should be detectable at the current experimental sensitivities.

Since the WIMP miracle is such an enticing coincidence, the focal point of nearly all direct and indirect searches for DM is the WIMP. Indeed, both main parts of this work were conducted with a WIMP DM particle in mind. Hence, using the label

---

[3] Note here the fact that we have assumed the DM has an anti-particle, or more plainly, is a fermion. This is not generally true for all WIMP models. All that is required here is that there exists a finite DM-DM annihilation channel into SM particles

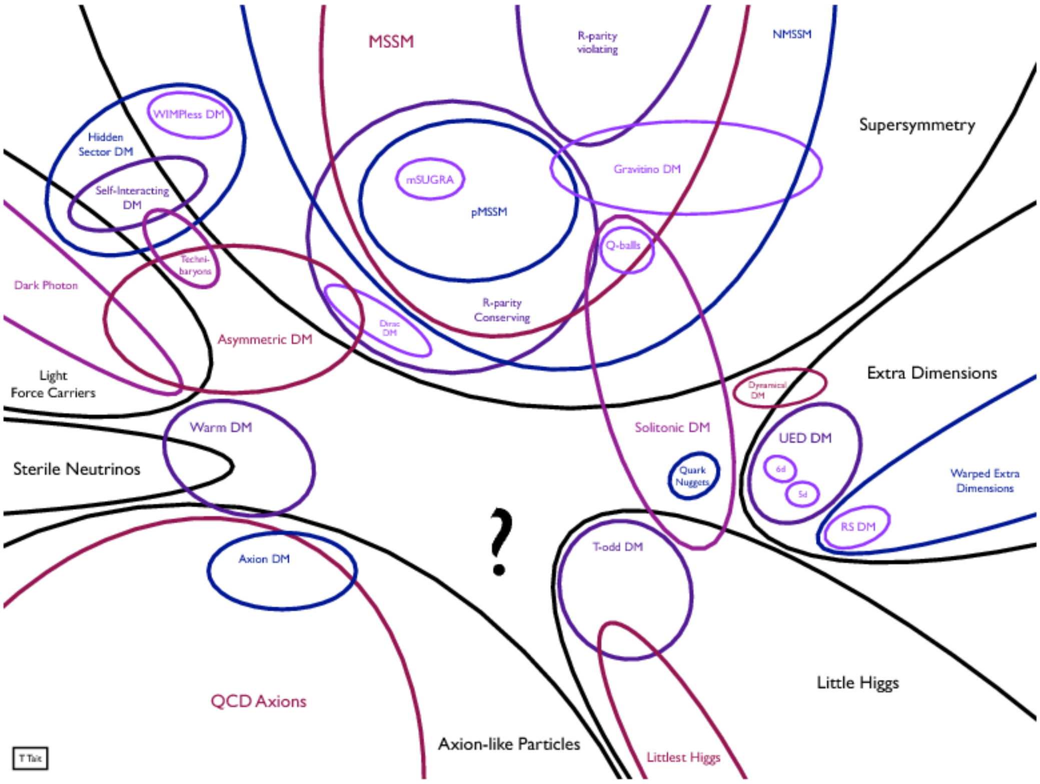

Fig. 2.6 Diagram from [26]. Diagrammatic representation of the (incomplete) landscape of DM candidates.

‘DM’ and ‘WIMP’ should be taken as synonymous from here on in, unless otherwise stated.

For all the glory of the WIMP, there are many who have shown a lack of enthusiasm toward the WIMP miracle, providing frameworks in which dark matter particles with a wide range of masses naturally have the correct thermal relic density. For a summary, see [37, 38]. With this said, the WIMP parameter space is far from completely excluded, and the general paradigm remains that the WIMP is still one of the most well motivated candidate class.

2.5 Detecting particle dark matter: A brief overview

The exciting possibility that dark matter has stronger-than-gravitational interactions with everyday particles of the standard model, potentially allowing for detectable signals, remains well motivated. From looking at the necessary properties DM must have to conform with the observational constraints described in the previous sections, experimentalists can design experiments targeted at detecting either products of DM annihilation, recoil energy of SM nuclei after a DM-SM interaction or missing energy in SM-SM particle collisions such as at the Large Hadron Collider (LHC). The overall aim of these procedures is to measure or at least constrain properties of DM such as cross sections and/or mass and/or self/SM-interactions. Once measured these properties can then be used to determine/constrain/exclude or constrain any particular particle physics model of the DM. A neat representation of the physical interactions that each method of detection aims to probe is given in figure 2.7.

The jargon is rather misleading in that all methods are technically indirect searches. Thus the labels should not be confused with how each method goes about detecting (or rather inferring) the properties of the DM particle. Each method has benefits and shortcomings that another method may either compliment or supplement accordingly, but as of now these three methods have had the greatest support partially due to the model independent nature of the experimental methods required for each, and their predicted accuracy (as opposed to say, seaching for DM with galaxy cluster mergers, see [39]). This is not to say, however, that searching for DM is easy.

2.5.1 Direct detection

Direct detection experiments aim to observe the recoil of a standard model nucleus after an elastic collision with a DM particle as the Earth moves through the ambient (assumed static) DM halo as depicted in Fig. 2.8. Direct detection provides the current strongest limits on WIMP-SM interactions. The experiments, which are

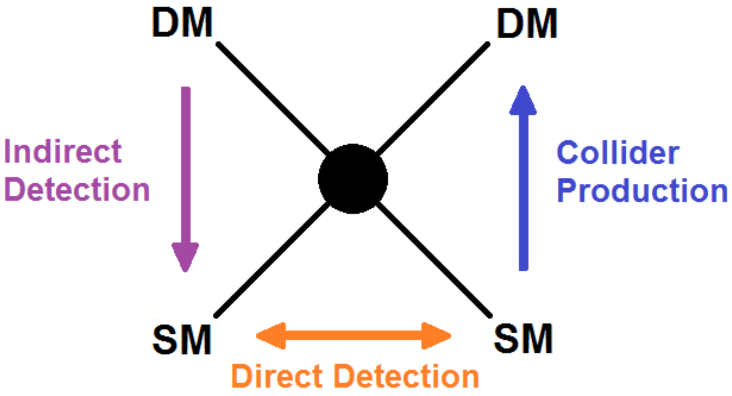

Fig. 2.7 The direction in which the diagram is read determines the physical process that can be probed by one of the three detection methods. If the diagram is read from top to bottom, this involves the DM-DM self interaction which then proceeds to SM particles. The detection of these SM particles is the focus of *indirect detection*. From bottom to top: This process represents the creating of DM particles from SM collisions such as in *particle colliders*. Left to right: Measuring the recoil energy from DM-SM elastic scattering is the subject of *direct detection*.

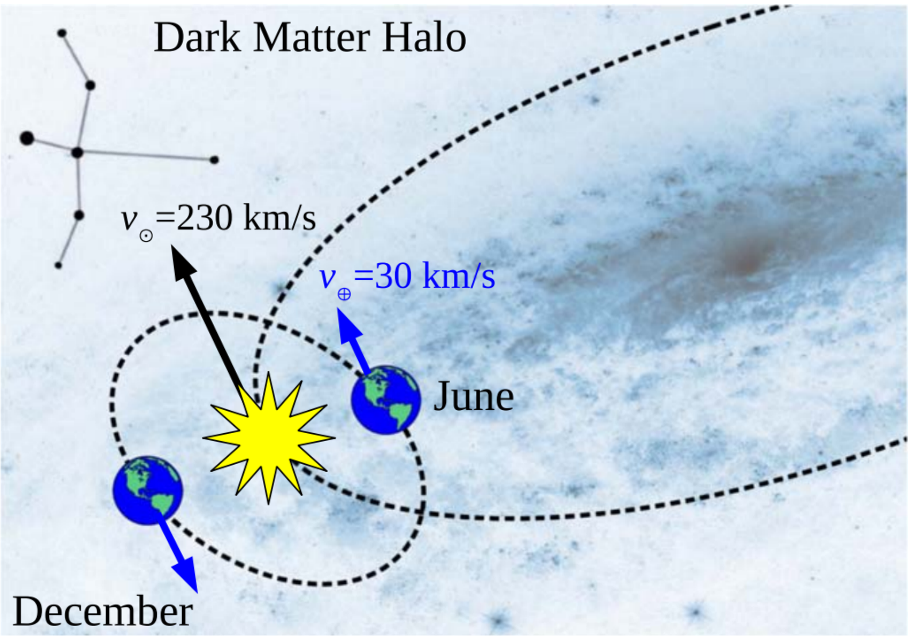

Fig. 2.8 Illustration from Ref. [40]. Illustration of the Sun–Earth system moving around the galactic center and through the dark matter halo in the direction of the constellation Cygnus.

typically located far underground to reduce background contamination, are sensitive to WIMPs that stream through the Earth and interact with nuclei in the detector target. This is primarily due to the expected mass and interaction strength of WIMPs. The recoiling nucleus can deposit energy in the form of ionization, heat, and/or light that is subsequently detected [41]. The expected energy of nuclear recoils induced by WIMP interactions is in the range from several keV to several hundreds of keV depending on m_χ and type of nuclei in the detector. A wide variety of experiments have been designed to detect and if not, place constraints on the physical properties of the WIMP using direct methods, including ANAIS [42], ArDM [43], CDEX/TEXONO [44], CDMS [45–48], CoGeNT [49–51], COUPP [52], CRESST [53], DAMA/NaI [54], DAMA/LIBRA [55, 56], DEAP/CLEAN [57], DM-Ice [58], DRIFT [59, 60], EDELWEISS [61–63], EURECA [64], LUX [65], NAIAD [66], PandaX [67], PICASSO [68, 69], ROSEBUD [70], SIMPLE [71], TEXONO [72], WArP [73], XENON10 [74–76], XENON100 [77, 78], XENON1T [79], XMASS [80], ZEPLIN [81, 82] and many others. The current limits on the vanilla WIMP-SM cross-section set by the most stringent direct searches are shown in Fig. 2.9. Future efforts in the field of direct detection effectively surmount to detectors with larger fiduciary masses and exposures, as well as enhanced background veto and target sensitivity. Publications 1&2 will focus heavily on forecasting experimental sensitivity in such detectors. One cannot do this forever though, since there will come a point where

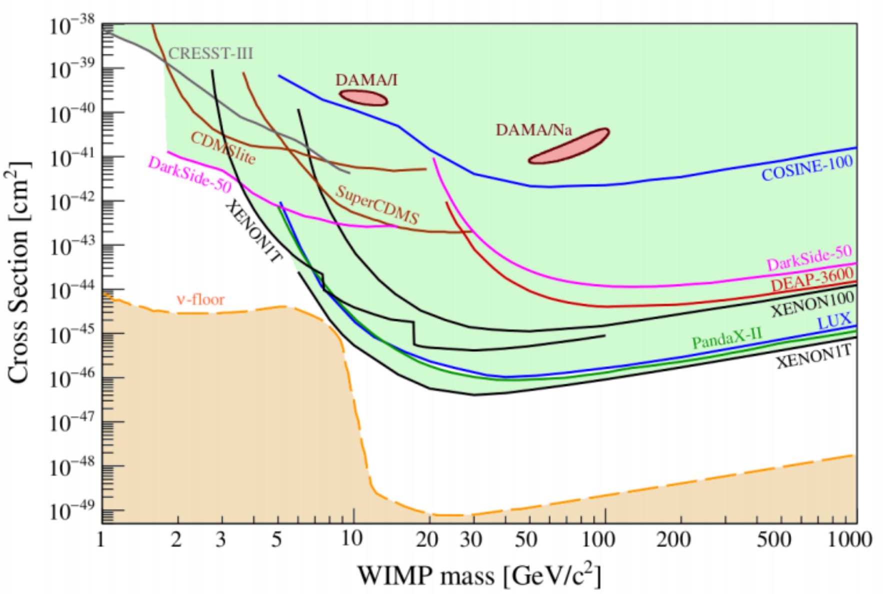

Fig. 2.9 Current experimental limits on spin-independent dark matter-nucleon cross section. Parameter combinations above the lines (i.e., the green shaded area) are disfavoured at 90% confidence level. The dashed line represents the neutrino floor. The regions labeled "DAMA" mark the preferred parameter space if the annual modulation seen by DAMA/LIBRA [85] would be interpreted as originating from dark matter interactions. Figure from Ref. [40].

there is an irreducible background due to coherent neutrino scattering. This lower bound is known as the neutrino floor and is shown in Fig. 2.9. One way around this is to have a detector become sensitive to the incoming WIMP direction, since neutrinos will scatter isotropically but the DM wind is directional [83].

As first proposed by Freese et al. [84], an alternative way to eliminate a majority of the systematic uncertainties associated with observing very low energy WIMP recoils is to look for an annual modulation in the total signal. Because the relative velocity of the detector with respect to the WIMPs depends on the time of year, the count rate exhibits (in most cases) a sinusoidal dependence with time. This concept is discussed more in the supplementary material for publication 3.

2.5.2 Indirect Detection

Indirect detection of dark matter involves searching for products, or the derivative thereof of DM-DM self-annihilation (or decay, if stability constraints are obeyed). Of course, if a signal from such an approach is to be detected then the DM must necessarily have some finite self-interaction. The conventional way to indirectly search for DM is to first simulate the observed signal that one would expect from background only processes. Then, generate the signal from background + DM annihilation and compare these to the data observed from an experiment. If one does not find a significant signature of WIMP annihilation, then constraints are placed on the WIMP parameters. In indirect searches, the physical DM property that is constrained is the self-annihilation cross-section denoted $\langle \sigma v \rangle$. We will see what this means as well as go through an explicit derivation in chapter 8.1, but for now this parameter should just be thought of as (along with the DM mass) completely characterizing the DM self scattering process. The DM self annihilation rate is related to the interaction cross-section via

$$\Gamma \propto \langle \sigma v \rangle \times n^2 \tag{2.5}$$

where n is the number density of DM. Depending on the mass of the DM, as well as the underlying gauge theory governing its dynamics, the DM can annihilate to a variety of SM leptons, quark pairs or gauge bosons. As a result of subsequent decays of the primal annihilation products, many kinds of particles will be created. This is illustrated in figure 2.10. The primary products of the annihilation subsequently decay and will eventually produce photons, electrons/positrons and in some models protons/anti-protons. It is these products that propagate through the interstellar medium and can be detected by experiments. Hence, there are two main particle avenues that indirect searches aim to observe:

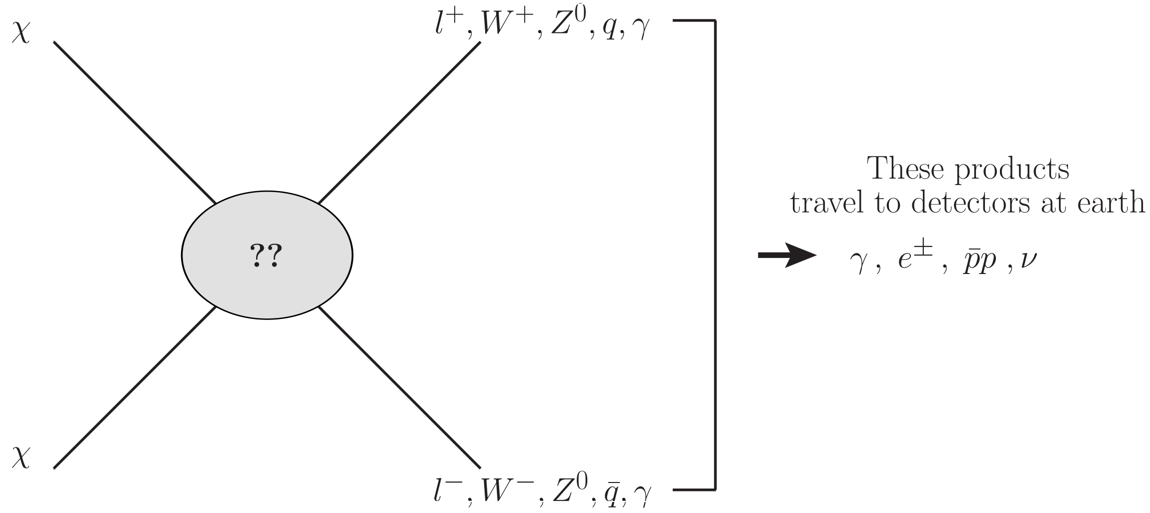

Fig. 2.10 Diagrammatic representation of the DM annihilation process.

Antimatter

Due to the relative abundance of matter compared to antimatter in the universe, it would be difficult to measure a significant excess of electrons or protons due to

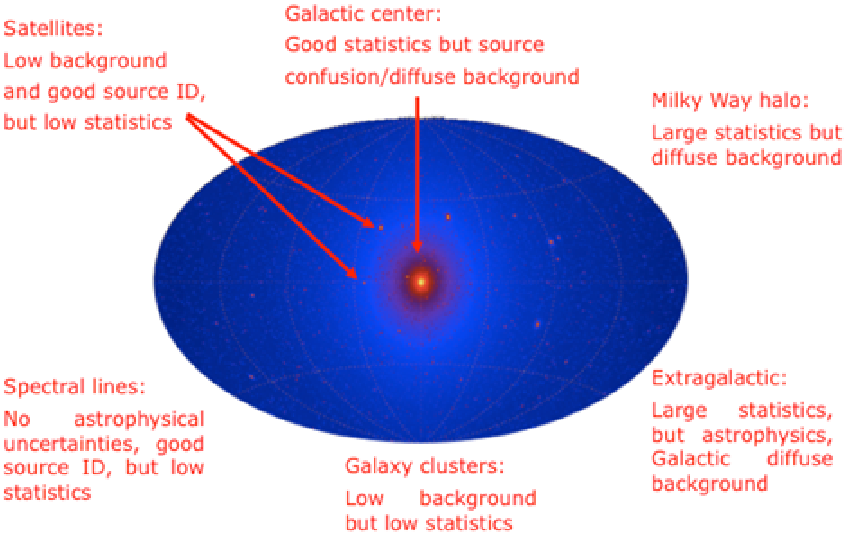

Fig. 2.11 Picture from [93]. Cartoon illustration of the Milky Way. Shown are the range of astrophysical targets for indirect detection along with a brief summary of the pros and cons of using them.

DM annihilation above the already high astrophysical background. Hence, indirect searches look for antimatter instead. In fact, experiments usually quote the antimatter/matter ratio as the main observable. The front running experiments are currently satellite based, namely AMS-02 [86], Fermi-LAT [87] and PAMELA [88, 89], with earlier studies being carried out by HEAT [90–92]. The main limitation of using antimatter as a probe for DM annihilation is the fact that the propagation of charged particles is affected by the interstellar medium magnetic field and other energy loss processes which change their energy distribution, and hence the results we can deduce about the DM.

Photons

Unlike charged final states, photons propagate in the galaxy without any appreciable deflection due to the magnetic field. They are also only weakly attenuated over the large galactic distance scales. As a result the morphology and energy distribution of the photons give a very accurate interpretation of the DM annihilation that created them. Also, unlike neutrinos, they are easy to detect. WIMP dark matter annihilation will in most models produce photons in the GeV-TeV energy range (gamma rays) depending of course on the WIMP mass and how far down the decay chain the photons are produced. If photons are promptly produced as primary products of the DM-annihilation, then one will observe a line feature in the energy spectrum with a kinematic cut-off at the DM mass. Such gamma-ray lines if observed would

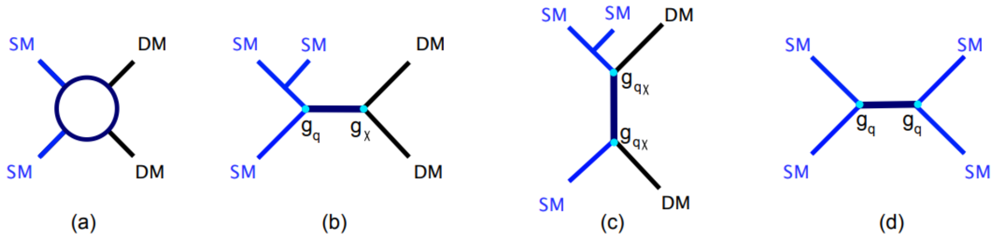

Fig. 2.12 Figure from Ref. [102]. Time from left to right. (a) The interaction between DM and Standard Model particles via an unspecified interaction (e.g., an EFT). (b) and (c) Examples of simplified model processes where the interaction is mediated by an intermediate particle (with additional radiation off one of the initial-state quarks). (d) The same model, in which the mediator decays back into Standard Model particles, with coupling constant g_q for the mediator–quark–quark vertex and constant g_χ for the mediator–DM vertex.

be the 'smoking-gun' for DM annihilation, due to the low astrophysical background able to replicate such a signal [94, 95]. If the photons are produced further down the decay tree, then one will observe an extended diffuse energy spectrum [96, 97]. Most models of WIMPS predict this sort of spectral feature mainly due to the fact that DM coupling directly to photons (to produce line features) at tree level is not favoured. The current forerunners for DM searches in gamma-ray final states are Fermi-LAT [98] in the GeV range and H.E.S.S [99] in the high TeV range. Previous experiments include EGRET [100] and MAGIC [101]. So far, there has been no definitive detection of WIMP annihilation to photonic final states, but increasingly strong constraints have been placed on the WIMP parameters. Experiments will typically conduct many analyses directed at different DM rich areas. Figure 2.11 shows a diagram of the various astrophysical targets for indirect detection along with descriptions of the experimental benefits and shortcomings of each.

2.6 Collider detection

Colliders, among the most successful tools in particle physics, have revealed much about ordinary matter. If DM can be produced at colliders, they will likely remain one of our preferred tools for learning more about it, regardless of where DM particles are first discovered. Driving the collider searches for DM in the modern era are the Large Hadron Collider (LHC) experiments ATLAS [103] and CMS [104]. As with direct and indirect experiments, collider DM production relies upon the existence of interactions between the colliding Standard Model particles and the DM particles. Most DM particle candidates produced in particle collisions are effectively invisible to traditional collider experiments. However, any remaining products of the collision event are not. Invisible particles can be accompanied by one or more visible particles, leading to missing energy in the transverse plane, whose magnitude is termed missing E_T or 'MET'. This is one of the main signatures of DM in colliders, although many models with a variety of final states are able to be probed. Fig. 2.12 shows a variety of diagrams that are representative of some the interactions explored at the LHC's experiments.

Chapter 3

Background and supplementary information for Publications one & two

The next three chapters of this thesis detail the first major block of work conducted during my PhD. This chapter aims to primarily lay the groundwork for concepts covered in publications 1 and 2, however the direct detection preliminaries will be relevant for the rest of the thesis. Here we will motivate the introduction of a multi-component dark sector as well as provide a foundational background for the methods and theory involved in modern direct searches for WIMP dark matter.

3.1 Motivation

With the SM being so rich in particle content, it would seem prudent, from a naturalness perspective, that one should somewhat disfavour a dark sector comprising only of a single dark matter species. The first test bed for a multi-component dark sector was within Supersymmetric theories [105], with the first formal data driven investigation being initially introduced to resolve the discrepancy between the observed positron excess and anti-proton non-excesses in the PAMELA cosmic ray experiment [106]. A more general conclusion of this work was that such hidden sectors with GeV mass dark matter particles and dark forces with GeV mass mediators arise naturally in a framework where the hidden sector communicates to the SM through kinetic mixing - a common property in many BSM theories. For the last decade since, there have been quite a few studies introducing new models which include one or more dark matter particle candidates with a variety of phenomenological features. Our work takes a more model independent approach by observing that two WIMP-like particles will generally yield a unique smoking gun signal in fixed target direct detection experiments. As introduced in section 2.5.1 the current parameter space of the WIMP is progressively becoming heavily constrained. As a result, we must forecast how a two-component DM signal will look in future planned detectors. While we do this completely model independently, we found that it would be interesting to see how the results change given some very generalized assumptions about the DM genesis scheme. Namely, we explore a two-component WIMP scenario that originates via canonical freeze-out or via some asymmetry in the dark sector.

3.2 Direct detection preliminaries.

The aim of all direct detection experiments is to identify nuclear recoils produced by the collisions between WIMPs and a detector's target nuclei, and by either observing or not observing a positive signal, constrain the WIMP properties which are generally the WIMP-nucleon cross-section σ and WIMP mass m_χ. To unambiguously identify such low-energy interactions, a detailed knowledge of the signal signatures, the particle physics, astrophysics and nuclear physics modelling is mandatory. The basic picture is illustrated in figure 3.1. A galactic halo WIMP elastically scatters off a nucleus within the detector. The principal experimental observable is the differential recoil rate dR/dE (usually measured in events/keV/kg/day) which depends primarily on the astrophysical WIMP velocity distribution as well as the particle physics scattering cross-section:

$$\frac{dR}{dE} = \frac{dR}{dE}\left(f(v), \sigma\right) . \tag{3.1}$$

In this section, we will introduce and then derive an expression for the differential recoil rate dR/dE from first principles. We will also introduce the vanilla velocity distribution $f(v)$ that is often assumed as well as introduce a general form for the WIMP-nucleon interaction, finally moving onto how one formulates the expected number of DM-nucleus scattering events at detector level.

3.2.1 The differential recoil rate

WIMP-Nucleus scattering kinematics

As previously mentioned, direct detection experiments aim to measure nuclear recoils that arise from a rare WIMP-nucleus collision. Consider a WIMP of mass m_χ scattering off a nucleus of mass M. Analysis of galactic rotation curve data suggests

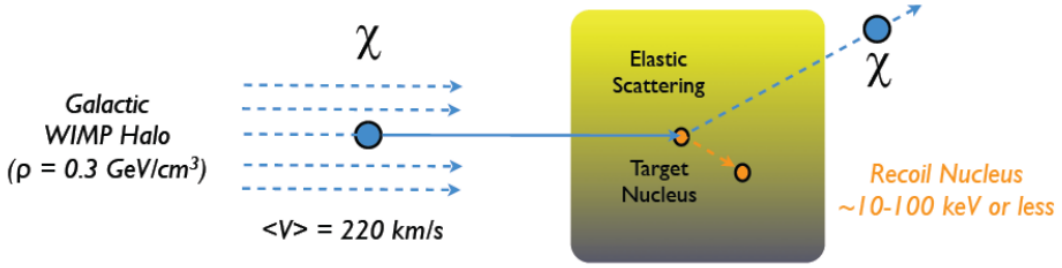

Fig. 3.1 Cartoon schematic of WIMP-nucleus elastic scattering: A WIMP in the galactic DM halo collides with a nucleus inside of a detector. The quantifying observable of a direct detection experiment is the differential recoil rate dR/dE, which is a measure of the frequency of WIMP-nucleus collisions in a given energy bin. The WIMP-nucleus scattering is characterized by the particle physics scattering cross-section σ.

a local WIMP velocity of ~ 200 km/s and thus, the kinematics of direct DM detection can be treated non relativistically. Define the lab frame as the frame where the nucleon momentum is zero. In the center of mass momentum frame, let $\mathbf{k}$ and $\mathbf{p}$ denote the initial incoming nucleon and WIMP momenta respectively, while setting $\mathbf{k'}_{\text{cm}}$ and $\mathbf{p'}_{\text{cm}}$ as the final outgoing momenta. Then in this frame we have

$$\mathbf{p} = -\mathbf{k} \quad \text{Incoming} \; , \tag{3.2}$$

$$\mathbf{p'}_{\text{cm}} = -\mathbf{k'}_{\text{cm}} \quad \text{Outgoing} \; . \tag{3.3}$$

Since we are considering non-relativistic kinematics, consider the following Galilean transformation:

$$\mathbf{v}_{\text{cm}} = \mathbf{v}_{\text{lab}} - \mathbf{v}_{\text{rel}} \; , \tag{3.4}$$

where $\mathbf{v}_{\text{cm}}$ is the COM velocity of the WIMP, $\mathbf{v}_{\text{lab}}$ is it's velocity in the lab frame and $\mathbf{v}_{\text{rel}}$ is the relative velocity between the lab and the COM frame, which is simply negative the velocity of the nucleus in the COM frame. Then multiplying through by m_χ we obtain

$$\mathbf{p} = m_\chi \mathbf{v}_{\text{lab}} - m_\chi \mathbf{v}_{\text{rel}} \; , \tag{3.5}$$

however,

$$-m_\chi \mathbf{v}_{\text{rel}} = m_\chi \left(\frac{\mathbf{k}}{M} \right)$$

$$\Rightarrow \mathbf{p}\left(\frac{m_\chi}{M}+1\right) = m_\chi \mathbf{v}_{\mathrm{lab}} \;, \tag{3.6}$$

which then leads to the common parameterisation

$$\mathbf{p} = \left(\frac{m_\chi M}{m_\chi + M}\right)\mathbf{v}_{\mathrm{lab}} = \mu \mathbf{v}_{\mathrm{lab}} \;, \tag{3.7}$$

where μ is defined as the reduced mass of the WIMP nucleon system. The momentum transfer of the interaction is defined as

$$\mathbf{q} \equiv \mathbf{p'}_{\mathrm{cm}} - \mathbf{p} \;, \tag{3.8}$$

with corresponding recoil energy

$$\begin{aligned} E_R &= \frac{\mathbf{q}^2}{2M} \qquad\qquad (3.9) \\ &= \frac{1}{2M}\left(\mathbf{p}^2 + \mathbf{p'}^2_{\mathrm{cm}} - 2|\mathbf{p}||\mathbf{p'}_{\mathrm{cm}}|\cos\theta_{\mathrm{cm}}\right) \;, \end{aligned}$$

where θ_{cm} is the scattering angle in the COM frame. In the COM frame, $|\mathbf{p}| = |\mathbf{p'}_{\mathrm{cm}}|$. Hence

$$\begin{aligned} E_R &= \frac{1}{2M}\left(\mathbf{p}^2 + \mathbf{p}^2 - 2\mathbf{p}^2\cos\theta_{\mathrm{cm}}\right) \\ &= \frac{2\mathbf{p}^2}{2M}\left(1 - \cos\theta_{\mathrm{cm}}\right) \;. \end{aligned}$$

Then substituting in the expression for $\mathbf{p}$ obtained in equation 3.7 we obtain

$$E_R = \frac{\mu^2 \mathbf{v}^2_{\mathrm{lab}}}{M}\left(1 - \cos\theta_{\mathrm{cm}}\right) \tag{3.10}$$

Note from equation 3.10 that for a given E_R, the minimum velocity $\mathbf{v}_{\mathrm{min}}$ (and hence velocity magnitude v_{min}) required to achieve this recoil energy occurs when $\cos\theta_{\mathrm{cm}}$ is maximised (i.e. $\cos\theta_{\mathrm{cm}} = -1$). Then

$$\begin{aligned} E_R &= 2\frac{\mu^2 v^2_{\mathrm{min}}}{M} \;, \\ \Rightarrow v_{\mathrm{min}} &= \sqrt{\frac{M E_R}{2\mu^2}} \;. \qquad\qquad (3.11) \end{aligned}$$

This minimum velocity has a corresponding maximum momentum transfer $q_{\rm max}$:

$$\begin{aligned} \mathbf{q}_{\rm max} &= \mathbf{p}'_{\rm cm} - \mathbf{p} \\ &= \mathbf{p}'_{\rm cm} - \mu \mathbf{v}_{\rm min} \ . \end{aligned} \tag{3.12}$$

So when v is minimised, q is maximised. An expression for $|\mathbf{q}_{\rm max}|$ can easily be found. From 3.10 we have

$$E_R = \frac{q^2}{2M} = \frac{\mu^2 v^2}{M}\left(1 - \cos\theta_{\rm cm}\right) \ , \tag{3.13}$$

then for a given v^2, the minimum and maximum values of E_R ($E_R^{\rm min}/E_R^{\rm max}$) correspond to $\cos(\theta_{\rm cm}) = \pm 1$ respectively. Hence

$$q^2_{\rm max} = 2ME_R^{\rm max} = 2M\left(2\frac{\mu^2 v^2}{M}\right) = 4\mu^2 v^2 \tag{3.14}$$

and

$$q^2_{\rm min} = 2ME_R^{\rm min} = 2M\left(0\right) = 0 \ . \tag{3.15}$$

The scattering rate

The rate of scattering in a process consisting of a beam of particles with number density n_χ and average velocity $\langle v\rangle$ scattering of a target consisting of N particles is

$$R = n_\chi \langle v\rangle N\sigma \ . \tag{3.16}$$

where σ is the total scattering cross-section. This can be reduced to differential form:

$$\begin{aligned} dR &= n_\chi \langle v\rangle N d\sigma \\ &= n_\chi \langle v\rangle N \left(\frac{d\sigma}{d\Omega}\right) d\Omega \ . \end{aligned} \tag{3.17}$$

In the context of the direct detection experiments considered in this thesis, scattering is isotropic and uniform in $\theta_{\rm cm}$ (i.e the detectors do not have directional sensitivity). The solid angle differential can be related to the recoil energy differential using equation 3.13:

$$dE_R = \frac{\mu^2 v^2}{M} d(\cos\theta) = \frac{\mu^2 v^2}{M} d\Omega \ ; , \tag{3.18}$$

where $\mu = Mm_\chi/\left(M + m_\chi\right)$ is the reduced mass of the WIMP nucleus system. Note θ is not equivalent to $\theta_{\rm cm}$. Since dE_R is a scalar quantity, it must be the same in all frames. That is, it does not care what axes we choose to define the scattering angle in the COM frame. Hence, above we have chosen a θ such that mathematically, the differentials have the same sign. Note: This is only possible because the scattering is assumed to be *isotropic* and uniform in $\theta_{\rm cm}$. Using Eqn. 3.18 in Eqn. 3.17 we obtain

$$\begin{aligned} dR &= n_\chi \langle v \rangle N \left(\frac{d\sigma}{dE_R}\right) dE_R \ , \\ \Rightarrow \frac{dR}{dE_R} &= n_\chi \langle v \rangle N \left(\frac{d\sigma}{dE_R}\right) . \end{aligned} \tag{3.19}$$

Since in the context of DM direct detection, $\frac{d\sigma}{dE_R}$ is generally velocity dependent, then it must also be velocity averaged:

$$\frac{dR}{dE_R} = n_\chi N \left\langle v \frac{d\sigma}{dE_R}(q^2, v) \right\rangle . \tag{3.20}$$

This is the differential recoil rate of a WIMP nucleon interaction; N is the number of target nucleons and n_χ is the local number density of WIMPS. Per unit detector mass this becomes equation 2 of [41]:

$$\frac{dR}{dE_R} = \frac{n_\chi}{M} \left\langle v \frac{d\sigma}{dE_R}(q^2, v) \right\rangle , \tag{3.21}$$

(since the unit detector mass here is just $N \times M$). One can show that

$$\begin{aligned} \frac{dE_R}{dq^2} &= \frac{1}{2M} \ , \\ \Rightarrow dE_R &= \frac{1}{2M} dq^2 \ , \\ \Rightarrow \frac{d\sigma}{dE_R}(q^2, v) &= 2M \frac{d\sigma}{dq^2}(q^2, v) \ . \end{aligned} \tag{3.22}$$

Then, substituting in this for $\frac{d\sigma}{dE_R}$ in equation 3.21 yields

$$\frac{dR}{dE_R} = 2n_\chi \left\langle v \frac{d\sigma}{dq^2}(q^2, v) \right\rangle . \tag{3.23}$$

Assuming that the DM in our galaxy has some local distribution of velocities $f(v,t)$, equation 3.23 becomes

$$\frac{dR}{dE_R} = 2\frac{\rho_\chi}{m_\chi}\int d^3v\, v f(v,t)\frac{d\sigma}{dq^2}(q^2,v)\ , \tag{3.24}$$

where we have made the substitution for the local DM density $\rho_\chi \equiv n_\chi/m_\chi$, an important empirical parameter discussed later in section 3.2.4.

3.2.2 The differential scattering cross-section

The particle physics interactions in direct detection phenomenology are encoded within the differential scattering cross section $\frac{d\sigma}{dq^2}(q^2,v)$. For this purpose, one needs to map the effective interactions between relativistic DM particles and quarks to some effective interactions between non-relativistic DM particles and nuclei. Such an effective field theory (EFT) for non-relativistic interactions can be written as

$$\mathcal{L}_{\rm int} = \sum_{i,N} c_i^N\left(q^2\right)\mathcal{O}_i^N\ , \tag{3.25}$$

where the operators $\mathcal{O}_i^N$ will in general depend only on the DM spin $\mathbf{S}_\chi$, the nucleon spin $\mathbf{S}_N$, the momentum transfer q and the DM-nucleon relative velocity v [107, 108]. For the work covered in publications 1 and 2, we only consider the canonical non-momentum suppressed spin-independent and spin-dependent operators:[1]

$$O_{SI}^N = \mathbf{1}, \quad O_{SD}^N = \vec{S}_\chi\cdot\vec{S}_N\ . \tag{3.26}$$

For scattering off larger nuclei, the momentum-transfer dependence which comes from evaluating matrix elements of quark currents like $\langle N'|\bar{q}\Gamma^\mu q|N\rangle$ of the cross section can be parameterized into a form factor $F^2(q)$. Define

$$\sigma_0 \equiv \int_0^{q_{\rm max}}\frac{d\sigma(q=0)}{dq^2}dq^2\ . \tag{3.27}$$

where $q_{\rm max} = 2\mu v$ is the maximum momentum transfer in a collision given by Eqn. 3.14 and $\frac{d\sigma(q=0)}{dq^2}$ is the differential cross-section evaluated at zero momentum

---

[1] For a more exhaustive list of all non-relativistic operators, see Ref. [109]

transfer. The actual cross section can then be written in terms of σ_0,

$$\begin{aligned}\sigma &= \int_0^{q_{\max}} dq^2\, \frac{d\sigma}{dq^2} \\ &= \int_0^{q_{\max}} dq^2\, F^2(q)\, \frac{d\sigma(q=0)}{dq^2} \\ &= \frac{\sigma_0}{4\mu^2\, v^2} \int_0^{q_{\max}} dq^2 \left[F^2(q)\right] \, . \end{aligned} \tag{3.28}$$

An important note to make here is that σ_0 is a very important quantity, in that it is σ_0 and **not** the total momentum dependent cross section σ that is used in constraints from direct detection experiments[2]. Notice from Eqn. 3.28 that the range of momentum values always ranges from 0 to $q_{\max}$. We can then introduce a step function into the differential cross-section:

$$\frac{d\sigma}{dq^2}(q^2, v) = \frac{\sigma_0}{4\mu^2\, v^2}\, F^2(q)\Theta(q_{\max} - q) \, . \tag{3.29}$$

Substituting Eqn. 3.29 into equation 3.24 for the differential recoil rate we obtain

$$\begin{aligned}\frac{dR}{dE_R} &= 2\frac{\rho_\chi}{m_\chi} \int d^3v\, v f(v,t) \frac{\sigma_0}{4\mu^2 v^2}\, F(q^2)\, \Theta(q_{\max} - q) \\ &= 2\frac{\rho_\chi}{m_\chi} \int_{v_{\min}} d^3v\, v f(v,t) \frac{\sigma_0}{4\mu^2 v^2}\, F(q^2) \, , \end{aligned} \tag{3.30}$$

since the step function enforces an upper limit of $q_{\max} \Leftrightarrow$ a lower limit of $v_{\min}$. Leaving the integral with an explicit velocity dependence we are finally left with the familiar expression

$$\boxed{\frac{dR}{dE_R} = \frac{\sigma_0 \rho_\chi}{2\mu^2 m_\chi}\, F(q^2)\, \eta(v_{\min}, t)} \, , \tag{3.31}$$

where

$$\eta(v_{\min}, t) \equiv \int_{v_{\min}} d^3v\, \frac{1}{v} f(v,t) \tag{3.32}$$

is the called the *mean inverse speed.* The functional form of $f(v,t)$ will be discussed in the next section.

---

[2] More specifically it is the WIMP-*nucleon* cross-section at zero momentum transfer that is constrained in direct detection searches.

3.2.3 The Standard Halo Model (SHM)

The local DM density and velocity distribution are not very well known and introduce sizable uncertainties in the prediction of experimental signals. However, it is often assumed that the DM halo in the local neighbourhood is most likely dominated by a smooth and well-mixed (virialized) component with an average density ρ_0. The simplest and most overwhelmingly used model for this smooth component is often taken to be the Standard Halo Model (SHM) [110, 111], a non-rotating isothermal sphere with an isotropic, Maxwellian velocity distribution and most probable speed v_0, where for the SHM, v_0 is equal to the disk rotation speed v_{rot}. In the literature, the DM velocity distribution is usually denoted

$$f(\mathbf{v}, t) \equiv \text{distribution of DM particles with velocity } \mathbf{v} \text{ at time t,} \tag{3.33}$$

with units $[f(\mathbf{v}, t)] = \text{km}^{-1}\,\text{s}$. The vector $\mathbf{v}$ is defined such that $\hat{\mathbf{x}}$ is the direction to the Galactic Center, $\hat{\mathbf{y}}$ the direction of disk rotation, and $\hat{\mathbf{z}}$ the direction of the North Galactic Pole. The time dependence of the velocity distribution is obtained via the Galilean boost from the halo rest frame to the lab frame:

$$f_{\text{lab}}(\mathbf{v}, t) \equiv \tilde{f}_{\text{halo}}(\mathbf{v} + \mathbf{v}_{\text{obs}}(t)) \ , \tag{3.34}$$

where $\mathbf{v}_{\text{obs}}$ is the velocity of the Earth in the dark matter halo rest frame. We will explicitly derive this time dependence in section 6.2 for the results of publication 3, but for now we deal with experiments that are only sensitive to the average rate over the year.

Definition in halo rest frame

Let $\tilde{f}(\mathbf{v})$ represent the velocity distribution in the dark matter halo *rest* frame where

$$\mathbf{v} = (v_x, v_y, v_z) \tag{3.35}$$

is the WIMP velocity relative in this dark matter rest frame. The SHM models the dark matter halo as a simple isothermal sphere with a Maxwellian velocity distribution:

$$\tilde{f}(\mathbf{v}) = \left(\frac{m_\chi}{2\pi kT}\right)^{\frac{3}{2}} e^{-\frac{m_\chi(v_x^2+v_y^2+v_z^2)}{2kT}} \ . \tag{3.36}$$

Since this has the form of a multivariate Gaussian with independent normally distributed variables v_x, v_y and v_z, we can assert that the variances of the components of **v** take the form

$$\sigma_i^2 = \frac{kT}{m_\chi} \; . \tag{3.37}$$

Hence, the variance of the multivariate vector distribution of velocities **v** has variance $3\sigma_i^2$ or

$$\sigma_{\mathbf{v}}^2 = \frac{3kT}{m_\chi} \; . \tag{3.38}$$

The standard deviation of this distribution is physically interpreted as the velocity dispersion of the dark matter halo. Re-writing the velocity distribution in Eqn.(3.36) with this new parameter definition we obtain the form most commonly found in the literature

$$\tilde{f}(\mathbf{v}) = \left(\frac{3}{2\pi\sigma_{\mathbf{v}}^2}\right)^{\frac{3}{2}} e^{-\frac{3v^2}{2\sigma_{\mathbf{v}}^2}} \; , \tag{3.39}$$

where $v \equiv |\mathbf{v}|$. It is common to impose an upper limit on v set by the escape velocity of the galaxy v_{esc}

$$v < v_{\text{esc}} \; . \tag{3.40}$$

One must therefore normalize the function in Eqn.(3.39) appropriately to ensure $\int_0^{v_{\text{esc}}} dv \, \tilde{f}(\mathbf{v}) = 1$

$$\tilde{f}(\mathbf{v}) = \begin{cases} \frac{1}{N_{\text{esc}}} \left(\frac{3}{2\pi\sigma_{\mathbf{v}}^2}\right)^{\frac{3}{2}} e^{-\frac{3v^2}{2\sigma_{\mathbf{v}}^2}} & , v < v_{\text{esc}} \\ 0 & , \text{otherwise} \; . \end{cases} \tag{3.41}$$

Here,

$$N_{\text{esc}} \equiv \text{erf}(z) - \frac{2}{\sqrt{\pi}} \, z \, e^{-z^2} \; , \tag{3.42}$$

where $z \equiv \sqrt{\frac{3}{2}} \frac{v_{\text{esc}}}{\sigma_{\mathbf{v}}}$. Note the sharp cut-off at v_{esc} in the velocity distribution shown in Eqn.(3.41) is not physical and is expected to fall off more smoothly [112]. The probability to find a WIMP with velocity $\mathbf{v} + d\mathbf{v}$ is

$$\tilde{f}(\mathbf{v}) \, d^3\mathbf{v} = \tilde{f}(\mathbf{v}) \, v^2 \sin\theta \, d\theta \, d\phi \, dv \; , \tag{3.43}$$

where the angles θ and ϕ are the "path" and "course" angle in velocity space. Since the SHM (Eqn.(3.39)) is by construction a well virilized Maxwellian, and thus has no dependence on θ or ϕ, one may marginalize over these degrees of freedom ending up with a function that is only dependent on the magnitude of the velocity

$$\tilde{f}(v)\, dv \propto 4\pi \left(\frac{3}{2\pi\sigma_{\mathbf{v}}^2} \right)^{\frac{3}{2}} v^2\, e^{-\frac{3v^2}{2\sigma_{\mathbf{v}}^2}} \; . \tag{3.44}$$

Eqn.(3.44) is exactly equation 9 of [113].

The mean inverse speed

The DM velocity distribution enters Eqn. 3.31 via the mean inverse speed given by the integral

$$\eta(v_{\min}, t) \equiv \int_{v>v_{\min}} d^3v\, \frac{f(\mathbf{v}, t)}{v} \; , \tag{3.45}$$

where $v_{\min} = v_{\min}(E_R)$ is the minimum WIMP velocity in the lab frame required to produce recoil energy E_R in a detector as introduced in Eqn. 3.11. The mean inverse speed can be analytically calculated for simple velocity distributions such as the SHM.

We have already denoted $\tilde{f}(\mathbf{v}, t)$ as the velocity distribution in the rest frame of the dark matter population, that is

$$\int d^3v\, \mathbf{v}\, \tilde{f}(\mathbf{v}, t) = 0 \; . \tag{3.46}$$

We have also seen that the velocity distribution in the lab frame is determined via the Galilean transformation $f(v, t) = \tilde{f}(\mathbf{v} + \mathbf{v}_{\mathrm{obs}}(t))$, where $\mathbf{v}_{\mathrm{obs}}(t)$ is the (time-dependent) motion of the lab (observer) relative to the rest frame of the dark matter population. Below we show the mean inverse speed for a regular Maxwellian velocity distribution as well as the truncated Maxwellian that is the SHM.

Simple Maxwellian

A simple Maxwellian velocity distribution has the form

$$\tilde{f}(\mathbf{v}) = \left(\frac{1}{\pi v_0^2} \right)^{3/2} e^{-\frac{1}{v_0}\mathbf{v}^2} \; , \tag{3.47}$$

with mean inverse speed [112, 114]

$$\eta(v_{\rm min}, t) = \frac{1}{2v_{\rm obs}}\left[{\rm erf}(x+y) - {\rm erf}(x-y)\right] \ , \tag{3.48}$$

where $x = \frac{v_{\rm min}}{v_0}$ and $y = \frac{v_{\rm obs}}{v_0}$.

Truncated Maxwellian

For the case where the Maxwellian distribution is truncated at the escape velocity, the mean inverse speed is evaluated analytically by first defining $z \equiv v_{\rm esc}/v_0$ and is given by [114, 115]

$$\eta(v_{\rm min}, t) = \begin{cases} \frac{1}{v_{\rm obs}} & \text{for } z < y,\ x < |y-z|, \\ \frac{1}{2N_{\rm esc}v_{\rm obs}}\left[{\rm erf}(x+y) = {\rm erf}(x-y) - \frac{4}{\sqrt{\pi}}\right] & \text{for } z > y, x < |y-z|, \\ \frac{1}{2N_{\rm esc}v_{\rm obs}}\left[{\rm erf}(z) = {\rm erf}(x-y) - \frac{2}{\sqrt{\pi}}(y+z-x)e^{-z^2}\right] & \text{for } \ |y-z| < x < y+x, \\ 0 & \text{for } \ y+x < z \end{cases} \tag{3.49}$$

where $N_{\rm esc}$ is defined as on Eqn. 3.42.

3.2.4 The local dark matter density

It is crucial for the interpretation of results from direct (and indirect) detection searches to have a good estimate of the local dark matter density ρ_χ. This parameter was originally estimated empirically from measurements of the rotation curve of the Milky Way (assuming spherical symmetry) or from the vertical kinematics and position of stars in the solar neighbourhood. These methods yielded a value which was unanimously adopted for the interpretation of direct detection experiments of $\rho_\chi = 0.3\,{\rm GeV/cm^3}$. However, this number has a rather large uncertainty of ∼50% as individual measurements show considerable variations [116]. A recent measurement (2017) using Sloan Digital Sky Survey data yields $\rho_\chi = 0.46^{+0.07}_{-0.09}\,{\rm GeV/cm^3}$ [117]. In the absence of a signal, the direct detection community have typically adopted $\rho_\chi = 0.4$ GeV/cm^3 as a canonical value in order compare the different experiments rather than adopting a perpetually updated result. More common practice even involves including ρ_χ as a statistical nuisance parameter. For the work undergone in this thesis, and more specifically in the context of a two-component dark sector, we usually adopt $\rho_\chi = 0.4$ GeV/cm^3 for the *total* local density, unless stated otherwise.

3.2.5 The quenching factor

The quenching factor describes by how much the ionization signal from a nuclear recoil energy deposition in the nuclear target is reduced compared to a nuclear recoil of the same energy. In case of low-energy nuclear recoils, significantly more energy is lost to atomic motion (heat), which is often not detected. This leads to considerably smaller scintillation and ionization signals and makes their detection even more challenging. Signal quenching is typically energy dependent and has to be measured accurately in order to establish an energy scale for the detector. It is an intrinsic feature of the detection material and independent from the actually used detector (if detector-specific effects such as signal collection efficiency and thresholds are properly accounted for); this allows for quenching factor measurements in detectors specifically designed for this purpose. The events are measured in electron equivalent energy (keVee), which is related to the true recoil energy E_R through the target and recoil energy-dependent quenching factors Q [40]:

$$E_{\rm ee}\left[{\rm keV_{ee}}\right] = Q\left(E_R\right) \times E_R\left[{\rm keV}\right] \ .$$

3.2.6 What we observe in a detector: The expected number of events

In a realistic experiment, one must fold detector effects into the differential recoil rate in a way which is independent of the type of WIMP interaction or spectrum. This is done by taking into account the finite energy resolution of the detector as well as the detector efficiency. For a given WIMP spectrum, the average expected number of signal events in some energy bin $E_R \in [E_1, E_2]$ centered at $E_{\rm ee}^{\rm Bin\ center}$ is

$$\begin{aligned} N(E_{\rm ee}^{\rm Bin\ center}) &\equiv MT \int_{E_1}^{E_2} dE_{\rm ee} \ \left[\frac{dR}{dE_{\rm ee}}\left(E_{\rm ee}, t\right)\right] \\ &= MT \int_{E_1}^{E_2} dE_{\rm ee} \ \left[\int_0^{\infty} dE_R \ \ \varepsilon\left(QE_R\right) \phi\left(E_R, E_{\rm ee}\right) \frac{dR}{dE_R}\left(E_R, t\right)\right] \ , \end{aligned} \tag{3.50}$$

where, $\phi\left(E_R, E_{\rm ee}\right)$ is the differential response function or *energy resolution* defined such that $\phi\left(E_R, E_{\rm ee}\right)\, dE_{\rm ee}$ is the probability that a nuclear recoil of energy E_R will produce a scintillation signal measured between $E_{\rm ee}$ and $E_{\rm ee} + dE_{\rm ee}$. ϵ is the detector efficiency and MT is the total target detector mass × exposure time and is called the *exposure* and serves as an overall normalization. Figure 3.2 shows a Monte Carlo realizations a variety of energy spectra for the case of two WIMP particles interacting

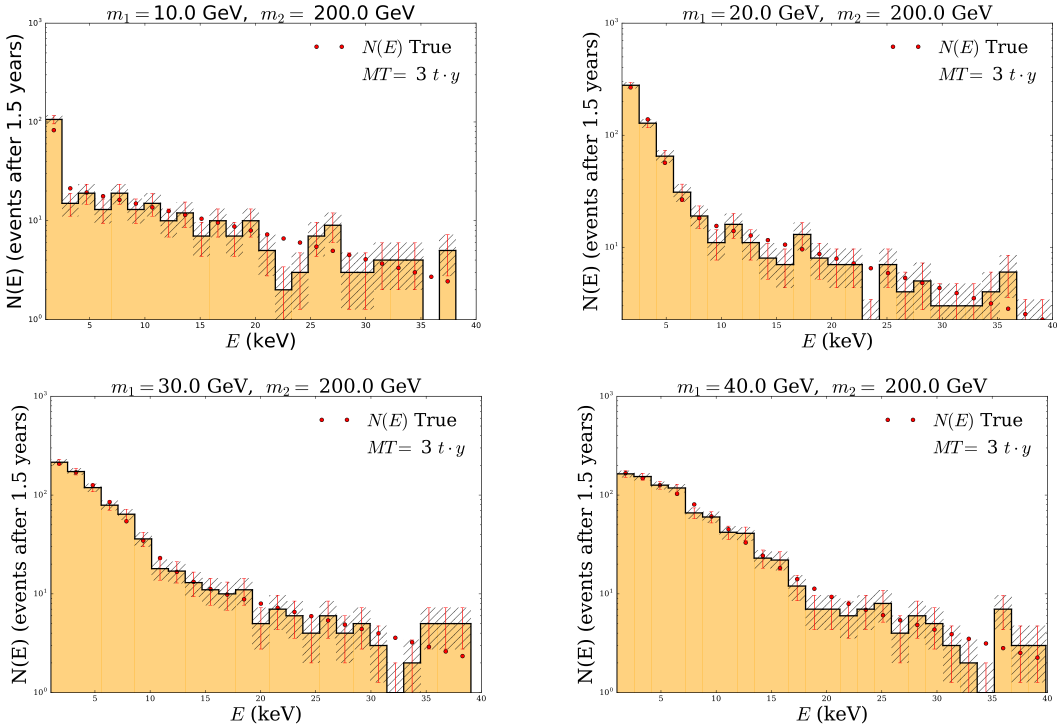

Fig. 3.2 Binned spectrum from 10,000 Monte Carlo realisations of a two-component dark matter scenario in a Xenon-type direct detection experiment (yellow) with Poissonian uncertainties. Red points are the expected bin-by-bin numbers of events as given by Eqn. 3.50.

.

with a Xenon type detector. These energy spectra simulate the detector response to a two-component WIMP spectrum for a variety of mass splittings. Indeed these are the spectra derived from the rates shown in Fig. 4.2 that were used to generate some of the analyses seen in publication 1 in chapter 4.

3.3 DM Genesis scenarios

We consider two DM genesis schema in our studies of multi-component DM: Freeze out, and asymmetric DM.

3.3.1 Freeze out

Qualitatively, the process of freeze-out can be thought of as follows: very shortly after the big bang, the DM was in equilibrium with the rest of the cosmic plasma. Equilibrium in the dark sector was kept via DM-DM self annihilations through a finite (but small) self interaction cross-section. As the universe expanded, the equilibrium maintained by DM annihilation was skewed. That is, the rate of DM annihilations decreased significantly as a function of scale factor. Hence, the DM population was "frozen out" or equivalently the rate of DM annihilations were suppressed. It's important to note that the freeze out condition is an assumption about the DM in order to explain the relative abundance we see today; if the DM where allowed to be kept in thermal equilibrium, it's number density would be suppressed by $e^{-m/T}$ as the temperature of the universe of course decreases [118]. There would therefore be no such particles today. But how do we model the number density of such a "thermal relic" in a quantitative manner? Introduce the *Boltzmann equation.* The Boltzmann equation formalises the statement that the rate of change in the abundance of a given particle is the difference between the rates for producing and eliminating that species. In other words, freeze out occurs when the expansion rate overtakes the DM annihilation rate. Formally this is written as a temporal differential equation involving the current DM number density n, scale factor a and equilibrium number density

$$n_{\mathrm{EQ}} = g \int \frac{d^3p}{(2\pi)^3} \, e^{-E/T} \, , \tag{3.51}$$

where g is the number of degrees of freedom of the DM (for example spin polarisations of the DM field etc), T is the temperature and E is the energy. In the generic WIMP framework, two massive (possibly identical) particles χ can annihilate to produce two infinitesimally massive particles l. These light particles are assumed to then remain in thermal equilibrium with the cosmic plasma with $n^l_{\mathrm{EQ}} = n^l$. There is then only one unknown parameter - the DM number density n. One can then write the Boltzmann equation to describe its evolution:

$$a^{-3} \frac{d(na^3)}{dt} = \langle \sigma v \rangle \left[(n_{\mathrm{EQ}})^2 - n^2 \right] , \tag{3.52}$$

where

$$\langle \sigma v \rangle \equiv \frac{1}{n^2_{\mathrm{EQ}}} \left(\prod_{i=1}^{4} \frac{d^3p_i}{(2\pi)^3 \, 2E_i} \right) e^{-(E_1+E_2)/T} \times (2\pi)^4 \delta^4(p_1 + p_2 - p_3 - p_4) |\mathcal{M}|^2 \tag{3.53}$$

is defined as the velocity averaged annihilation cross section for a $\chi_1 + \chi_2 \to l_3 + l_4$ process. This is the primary quantity used for constraining DM from indirect detection as is discussed in chapter 8.1. It is essentially $\sigma \cdot v$ integrated over a Maxwellian velocity distribution and was primarily introduced in this form as a definition rather than an empirically derived expression. It is easy to re-write equation 3.52 in a more convenient manner, convenient in that the following form is how a majority of the literature expresses it. From a typical thermodynamic treatment of cosmology, the temperature $T \propto a^{-1}$. Hence, one can treat the quantity aT as a temporal invariant, thus factoring it out of the derivative in equation 3.52. Write na^3 as $n(aT)^3/T^3$ and define the new variable $Y \equiv n/T^3$. Then

$$\begin{aligned} a^{-3}\frac{d(na^3)}{dt} &= T^3\frac{dY}{dt} \\ \Rightarrow \frac{dY}{dt} &= T^3\langle\sigma v\rangle\left[Y_{\mathrm{EQ}}^2 - Y^2\right] , \end{aligned} \tag{3.54}$$

where the definition $Y_{\mathrm{EQ}} \equiv n_{\mathrm{EQ}}/T^3$ has been made.

The WIMP relic density

Section 3.3.1 introduced a means of describing the time evolution of the DM number density over cosmic history. The aim of this sub-section is to approximately solve the Boltzmann equation for the well-measured DM relic density $\Omega_{\mathrm{DM}} \equiv \rho_{\mathrm{DM}}/\rho_{\mathrm{crit}} \simeq 0.27$ [20] which subtly implies the assumption that the DM is made up of a single species. Hence, we only need the simplest version of the Boltzmann equation introduced earlier. Start with defining a new variable, $x \equiv m/T$, where m is the mass of the DM. This new variable has an implicit time dependence given by the Jacobian

$$\frac{dx}{dt} = Hx , \tag{3.55}$$

where H is the familiar Hubble rate parameter. Again using Dodelson [118], eventually this leads to the following expression for the Boltzmann equation:

$$\frac{dY}{dx} = -\frac{\lambda}{x^2}\left[Y^2 - Y_{\mathrm{EQ}}^2\right] , \tag{3.56}$$

where

$$\lambda \equiv \frac{m^3\langle\sigma v\rangle}{H(m)} , \tag{3.57}$$

where $H(m)$ is the value of the Hubble parameter at $T = m$. This is taken to be during the radiation era i.e when energy density scales as T^4. The first step for determining the DM relic density is to determine the final freeze out abundance $Y_\infty \equiv Y(x = \infty)$. It can be shown that $Y_\infty =\simeq x_f/\lambda$ where $x_f \equiv x$(at freeze out) (see Dodelson for explicit derivation). Note that this approximation is dependent on the freeze out temperature (x_f). A common order of magnitude estimate is $x_f \sim 10$. Thus, λ and more importantly from a particle physics view $\langle\sigma v\rangle$ is purely responsible for the DM abundance. Figure 3.3 shows numerical solutions of the Boltzmann equation for differing values of $\langle\sigma v\rangle$. Once a particle has frozen out, its number density falls off according to the scale factor, a^{-3} (volume goes as a^3). Thus the mass density today is $m(a_1/a_0)^3 n$, where a_1 is assumed to be at a sufficiently late time that $Y \sim Y_\infty$. Given the estimate for Y_∞ shown earlier, the present number density is then $n = Y_\infty T_1^3$. Hence, the mass density today is

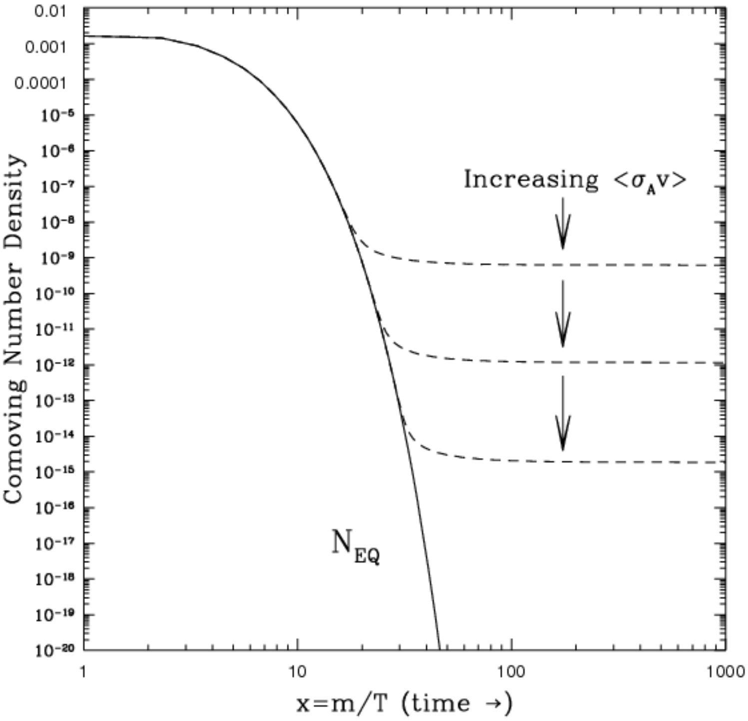

Fig. 3.3 Plot from [119]. Numerical solutions of the Boltzmann equation for varying values of $\langle\sigma v\rangle$.

$$\rho = m(a_1/a_0)^3 n = mY_\infty T_0^3 \left(\frac{a_1 T_1}{a_0 T_0}\right)^3 \sim \frac{mY_\infty T_0^3}{30}\,. \tag{3.58}$$

The last term comes from the fact that the ratio $(a_1T_1/a_0T_0)^3$ is approximately 1/30. The reason for this is basically due to the fact that aT is not constant over cosmic time due to the reheating of photons from the annihilation of particles between 1 MeV and 100 GeV. Hence, writing the relic density using $\rho_{\text{crit}} = 3H_0^2/8\pi G$ and the

Boltzmann solution $Y_\infty = x_f \lambda$:

$$\begin{aligned} \Omega_{\text{DM}} &= \frac{\rho}{\rho_{\text{crit}}} && (3.59) \\ &= \frac{x_f}{\lambda} \frac{m T_0^3}{30 \rho_{\text{crit}}} && (3.60) \\ &= \frac{H(m) x_f T_0^3}{30 m^2 \langle \sigma v \rangle \rho_{\text{crit}}} \; . && (3.61) \end{aligned}$$

The Hubble rate during the radiation era $H(m)$ is given as

$$H(T = m) = T^2 \sqrt{\frac{4\pi^3 G g_*(T)}{45}} \; , \tag{3.62}$$

where $g_* = \frac{\pi^2}{30} T^4$ is the effective number of relativistic degrees of freedom as a function of temperature. Hence putting this all together one obtains

$$\Omega_{\text{WIMP}} = \sqrt{\frac{4\pi^3 G g_*(T)}{45}} \frac{x_f T_0^3}{30 \langle \sigma v \rangle \rho_{\text{crit}}} \; . \tag{3.63}$$

A very interesting fact to take out of this is that, besides its implicit dependence through x_f and g_*, the DM mass m does not enter the expression for the relic density. Hence the primary model dependent quantity that influences Ω_{DM} is the velocity averaged cross section $\langle \sigma v \rangle$. For $T_0 \sim 100$ GeV, $g_*(T_0)$ includes contributions from all of the particles of the SM except for the top or Higgs, and so is of order 100. Putting in all the numbers one sees that in order to obtain $\Omega_{\text{DM}} = 0.27$ requires $\langle \sigma v \rangle \sim 10^{-26} \text{cm}^3 \text{s}^{-1}$. The fact that this cross section is that of a weak main reason for the popularity of this class of DM candidate.

3.3.2 Asymmetric DM

The visible matter (VM) abundance in the universe today is made from a small number of SM fields: protons and bound neutrons (formed mainly from valence up and down quarks, and gluons), and electrons (with neutrinos and photons comprising the current radiation content of the VM). These are the stable relics of a much larger SM particle content. Since asymmetric dark matter (ADM) models seek to draw a connection between DM and VM, it is natural to suppose that the DM may also be the stable member(s) of some relatively complicated gauge theory constituting a hidden sector. In general, ADM models have gauge groups that contain the product structure

$$G_V \times G_D \; ,$$

where the first factor is the SM gauge group or some extension thereof, and the second factor is a dark gauge group. Some models have a gauge force that couples to both sectors, with an extended U(1) being a common example. The dark sector in general may have various fermion and scalar multiplets in representations of G_D, and spontaneous gauge-symmetry breaking may occur. Many models have the dark sector as simply just fermions or scalars or a mixture of the two. Taking our cue once again from the visible world, it could well be that the DM is multi-component and that there is dark radiation (bosonic and/or fermionic) as well as dark matter. A relatively complicated dark sector is not mandatory, but it is perfectly consistent with the ADM philosophy. There are two features that are not optional: a conserved or approximately-conserved dark global quantum number so that a dark asymmetry can be defined in the first place, and an interaction that annihilates away the symmetric part of the dark plasma, just as strong and electroweak interactions annihilate the symmetric component of the SM plasma into radiation. If DM also carries a particle-antiparticle asymmetry, then gauge invariance implies that there must be at least two dark species with compensating asymmetries, such that the total gauge charge of the universe vanishes [120]. Discussing a mechanism that specifies the dynamics of the asymmetry generation was beyond the scope of this work. However, a (non-exhaustive) list includes: out-of-equilibrium decays of heavy particles [121], Affleck-Dine dynamics [122], bubble nucleation during a first-order phase transition [123], asymmetric freeze-out [124], asymmetric freeze-in [125], and spontaneous genesis [126].

Asymmetric two-component dark matter

For the work detailed in chapter 5, we considered a dark QED-like model that consists of two Dirac fermions that couple to a dark $U(1)_D$ such that the total gauge theory becomes $SU(3) \times SU(2) \times U(1)_Y \times U(1)_D$. We now consider the case that the two species are produced in some asymmetric scenario but are coupled to a light vector mediator with mass $m_{A'}$. We consider an extra $U(1)_D$ gauge symmetry with dark coupling g_D, such that the gauge theory becomes $SU(3)_C \times SU(2)_L \times U(1)_Y \times U(1)_D$. As the dark symmetry is Abelian, a Stueckelberg mass for the dark photon is gauge invariant, but it can also be generated by a new scalar higgs that takes a VEV. Just considering the $U(1)_Y$ and $U(1)_D$ parts and a two-component dark sector, the

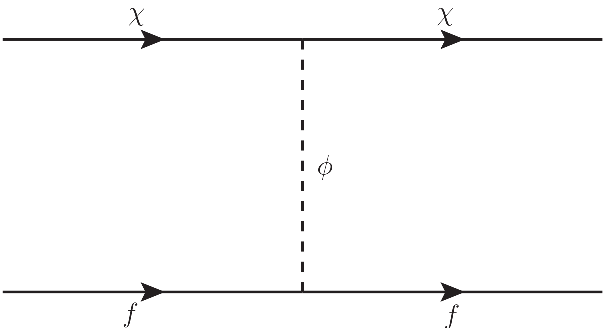

Fig. 3.4 Diagram relevant for direct detection through the mediation of a light mediator.

Lagrangian at this stage has the following relevant terms:

$$\begin{aligned}\mathcal{L} \supset & -\frac{\epsilon_Y}{2} B_{\mu\nu} F'_{\mu\nu} - \frac{1}{4} B_{\mu\nu} B_{\mu\nu} - \frac{1}{4} F'_{\mu\nu} F'_{\mu\nu} + \frac{m_{A'}^2}{2} A'^{\mu} A'_{\mu} \\ & + \sum_{i=1}^{2} Q_{\chi_i} \bar{\chi}_i (i \not{D}_D - m_{\chi_i}) \chi_i + \sum_f Q_f \bar{f} i \not{D}_Y f \end{aligned} \tag{3.64}$$

where ϵ_Y is an effective coupling that absorbs the effects of heavy messengers in the UV complete theory and the covariant derivative $D_\mu^D = \partial_\mu + i g_D A'_\mu$ involves the dark photon. After the standard model Higgs acquires a VEV and breaks the electroweak symmetry $SU(2) \times U(1)_Y \to U(1)_{\text{EM}}$, we can re-write the hyper charge gauge field in the mass basis in the usual way $B_\mu = \cos\theta_w A_\mu - \sin\theta_w Z_\mu$. Transforming the field in this way will give terms in the Lagrangian that looks like[3]:

$$\begin{aligned}\mathcal{L} \supset & -\frac{\epsilon}{2} F_{\mu\nu} F'_{\mu\nu} - \frac{1}{4} F_{\mu\nu} F_{\mu\nu} - \frac{1}{4} F'_{\mu\nu} F'_{\mu\nu} + \sum_{i=1}^{2} Q_{\chi_i} \bar{\chi}_i (i \not{D}_D - m_{\chi_i}) \chi_i + \sum_f Q_f \bar{f} (i \not{D} - m_f) f \\ = & -\frac{1}{4} \mathcal{F}_{\mu\nu}^T K \mathcal{F}_{\mu\nu} + \sum_{i=1}^{2} Q_{\chi_i} \bar{\chi}_i (i \not{D}_D \ - m_{\chi_i}) \chi_i + \sum_f Q_f \bar{f} (i \not{D} - m_f) f \end{aligned} \tag{3.65}$$

where $\epsilon = \cos\theta_w \, \epsilon_Y$ and $F_{\mu\nu} = \partial_\mu A_\nu - \partial_\nu A_\mu$ is the electromagnetic field strength tensor and $D_\mu = \partial_\mu + ie \, A_\mu$. In the second line we have written the kinetic terms in a canonical matrix form with

$$\mathcal{F}_{\mu\nu}^T = (F_{\mu\nu}, F'_{\mu\nu}) \ \text{ and } \ K = \begin{pmatrix} 1 & \epsilon \\ \epsilon & 1 \end{pmatrix} . \tag{3.66}$$

---

[3] Noting that we have neglected terms that involve Z mixing since these will eventually lead to suppressed couplings, and therefore we do not include them in our study.

At $\mathcal{O}(\epsilon)$, the transformation that simultaneously diagonalises the kinetic terms as well as the dark photon mass terms is $\mathcal{F}_{\mu\nu} \to T\mathcal{F}_{\mu\nu}$, where

$$K \to TKT^{-1} \ : \ T = \begin{pmatrix} 1 & \epsilon \\ 0 & 1 \end{pmatrix} . \tag{3.67}$$

This implies the photon field is transformed, whilst the dark photon field is left invariant:

$$\Rightarrow A_\mu \to A_\mu + \epsilon A'_\mu \ \ , \ \ A'_\mu \to A'_\mu \ . \tag{3.68}$$

In the resulting mass basis the $U(1)_{\rm EM}$ covariant derivative will pick up a term that involves the dark photon: $D_\mu = \partial_\mu + ieA_\mu + i\epsilon\, g_D A'_\mu$. Substituting this into Lagrangian in Eqn. 3.65 gives us currents that couple the dark photon A' to the SM fermions in the mass basis:

$$\mathcal{L}_{\rm int} \supset \epsilon\, e J^\mu_{EM} \phi_\mu + g_D\, J^\mu_{DM} \phi_\mu \ , \tag{3.69}$$

where J^{EM}_μ is the electromagnetic current $J^{EM}_\mu = \sum_f Q_f \bar{f} \gamma^\mu f$ and J^{DM}_μ is the dark fermion current $\sum\limits_{i=1}^{2} Q_{\chi_i} \bar{\chi_i} \gamma^\mu \chi_i$. These are the interaction terms that are relevant for tree level direct detection as shown in Fig. 3.4. Note that the vector A' is equivalent to the ϕ represented in Fig. 3.4.

Statement of Authorship

Title of Paper	On the direct detection of multi-component dark matter: sensitivity studies and parameter estimation
Publication Status	Published
Publication Details	J. Herrero-Garcia, A. Scaffidi, M. White, and A. G. Williams. On the direct detection of multi-component dark matter: sensitivity studies and parameter estimation. JCAP, 1711(11):021, 2017.

Principal Author

Name of Principal Author (Candidate)	Andre Scaffidi		
Contribution to the Paper	Writing of manuscript Numerical results Theoretical results		
Overall percentage (%)	75%		
Certification:	This paper reports on original research I conducted during the period of my Higher Degree by Research candidature and is not subject to any obligations or contractual agreements with a third party that would constrain its inclusion in this thesis. I am the primary author of this paper.		
Signature		Date	

Co-Author Contributions

By signing the Statement of Authorship, each author certifies that:

i. the candidate's stated contribution to the publication is accurate (as detailed above);

ii. permission is granted for the candidate in include the publication in the thesis; and

iii. the sum of all co-author contributions is equal to 100% less the candidate's stated contribution.

Name of Co-Author	Juan Herrero-Garcia		
Contribution to the Paper	Writing of manuscript Numerical results Theoretical results		
Signature		Date	17/02/2020

Name of Co-Author	Anthony G. Williams
Contribution to the Paper	Writing of manuscript Theoretical results

Signature		Date	17/1/2020

Name of Co-Author	Martin White		
Contribution to the Paper	Writing of manuscript Theoretical results		
Signature		Date	21/1/20

Chapter 4

Publication one: On the direct detection of multi-component dark matter: sensitivity studies and parameter estimation

Abstract

We study the case of multi-component dark matter, in particular how direct detection signals are modified in the presence of several stable weakly-interacting-massive particles. Assuming a positive signal in a future direct detection experiment, stemming from two dark matter components, we study the region in parameter space where it is possible to distinguish a one from a two-component dark matter spectrum. First, we leave as free parameters the two dark matter masses and show that the two hypotheses can be significantly discriminated for a range of dark matter masses with their splitting being the critical factor. We then investigate how including the effects of different interaction strengths, local densities or velocity dispersions for the two components modifies these conclusions. We also consider the case of isospin-violating couplings. In all scenarios, we show results for various types of nuclei both for elastic spin-independent and spin-dependent interactions. Finally, assuming that the two-component hypothesis is confirmed, we quantify the accuracy with which the parameters can be extracted and discuss the different degeneracies that occur. This includes studying the case in which only a single experiment observes a signal, and also the scenario of having two signals from two different experiments, in which case the ratios of the couplings to neutrons and protons may also be extracted.

4.1 Introduction

We know from gravitational effects that dark matter (DM) constitutes a significant fraction of the energy density in the universe, but no confirmed detection in the laboratory has been made so far. Some of the most popular candidates are Weakly-Interacting-Massive-Particles (WIMPs), in particular those that have non-vanishing interactions with the standard model (SM) and therefore can be tested. In fact, they are actively being searched for in direct detection (DD) experiments, which look for their nuclear scatterings in underground detectors [9]. Interestingly, current and planned next-generation experiments are probing a very large portion of the parameter space of well-motivated theories of WIMPs.

A plausible scenario is that DM is not made up of a single species, but that it has a multi-component nature. In this work we study direct detection signals in the presence of multi-component WIMP-like DM, i.e., several types of WIMPs (labelled by Greek sub indices $\alpha = 1, 2 ..., N$) with individual global energy density Ω_α such that they constitute the observed total DM energy density of the Universe, $\Omega_{\rm DM} = \sum_\alpha^N \Omega_\alpha$. Purely on theoretical grounds, having the individual energy densities (the global Ω_α, or the local ρ_α) exactly equal would seem to be a highly unnatural scenario, requiring a fine-tuning between masses and number densities (unless there is some underlying mechanism to equalise the densities). On the other hand, that the densities are similar up to order one factors seems rather plausible, that is to say, that there are several species contributing in a non-negligible way to the global and local energy densities. For instance, in the SM there are baryons forming different stable nuclei with a non-negligible density: H, He, Li..., and also electrons, photons and neutrinos. Therefore, it is not difficult to imagine that a similar situation could occur in the dark sector, which has an energy density five times larger than the visible one.

There have been only a few works in the past regarding the direct detection of multi-component DM [127–133]. Let us discuss the main points studied there and the most relevant differences with our analysis. In Ref. [128] the authors considered very small mass splittings ($<$ 200 keV) for the particles, such as arise in inelastic scenarios [134–136]. In Ref. [129] a continuum spectrum of closely spaced DM particles was considered. In this work we will focus mainly on the case of two DM states and consider splittings comparable to the DM masses. In Refs. [129, 130] the possibility of testing multi-component DM using collider, indirect and direct searches was studied. In Ref. [130] the authors related the WIMP-nucleon scattering cross-section to the annihilation one, motivated by thermal freeze-out and supersymmetric scenarios. Therefore they were able to express the scattering cross-section as a function of the global (and local) density and the DM mass. In our study we will keep the analysis as phenomenological and model-independent as possible. In particular, we will not make any assumptions in the numerical analysis regarding the production mechanisms for the DM, i.e., we will keep the abundance and the scattering cross-sections as independent parameters. Furthermore, we will adopt a different statistical approach to that in Ref. [130] and we will study the effects of all relevant parameters entering the scattering rate. As pointed out in this last reference, indirect detection of one DM particle could mimic the effects of two components, as it may annihilate/decay not only to two gamma rays but also to Higgs/Z plus a photon. In addition these interactions are loop-suppressed. Regarding colliders, the authors studied the case of models with charged partners decaying into DM. In Ref. [137] the authors also considered the possibility of discriminating the number of DM particles generating missing energy distributions. In this work we will focus on how multi-component DM can be studied using only information stemming from direct detection signals.

We will first discuss some general expectations of multi-component DM. In particular, the relevant quantity that enters in DD is the local DM number density, $n_{\rm loc} = \rho_{\rm loc}/m_{\rm DM}$, and we will discuss this in some detail. Afterwards, in order to draw quantitative conclusions, we will focus on the case of having a two-component DM signal in a direct detection experiment. The questions we would like to answer are two-fold: first, how significantly can we distinguish the one-component and the two-component hypotheses? Second, assuming that the two components can indeed be distinguished, with what accuracy can we extract the DM properties? In order to answer these questions, we will simulate a signal generated by two DM components in different target nuclei, assuming either spin-independent (SI) or spin-dependent (SD) interactions. We will adopt a frequentist framework in order to compare the one- and two-component hypotheses and to extract the preferred regions for the free parameters. We will also discuss the case of having two experimental signals, and how accurately one can extract the DM properties in this case, including the couplings to neutrons and protons.

This paper is structured as follows. In sec. 4.2 we give some general remarks on multi-component DM. This section may be skipped for readers interested more in the main results of this work. In sec. 4.3 we present the framework relevant for direct detection of multi-component DM. In sec. 4.4 we analyse in detail the case of a two-component DM event rate and how, from a given signal, the one- and two-DM hypothesis can be discriminated. Assuming that the 2DM hypothesis has been confirmed, in sec. 4.5 we study the extraction of the DM parameters. We conclude in sec. 7.4. Finally we elaborate on some statistical methods used in App. 4.7, and show the results of the parameter estimation using Bayesian methods in App. 4.8.

4.2 General remarks on multi-component dark matter densities

The relevant quantity for DD is the DM local energy density in the solar neighbourhood, which should obey $\rho_{\rm loc} = \sum_{\alpha}^{N} \rho_\alpha$. More precisely, it is the local *number* density that is important in determining the total event rate in a DD experiment. Given arbitrary local energy densities for two DM components, it is not entirely straightforward to determine which one dominates the event rate. For example, even though the heavier DM mass has a smaller number density, it probes a larger part of the velocity distribution, and therefore it is not straightforward which particle dominates the rate, the lighter or the heavier.

One feature to keep in mind is that the proportionality of the global and local densities is expected in the case of cold DM, such as WIMPs [138] (see also its effects in Ref. [139]). We will assume such a proportionality in the following discussion. Furthermore, for simplicity, we will focus on the case of two DM components, taken to have masses $m_2 > m_1$ without loss of generality.

The production mechanism of DM is unknown. Up to now, we have defined multi-component DM as the scenario in which several particles have similar energy densities. Another option is that they have similar number densities. The first one is relevant in the context of thermal freeze-out, while the second one could in principle be more natural in asymmetric scenarios (see Ref. [140] for a review on the topic). In the latter case, however, the masses are typically of $\mathcal{O}$(GeV), and therefore DD is quite challenging, although detectors with low thresholds exist (typically with Germanium). Focusing on two components, in the case of similar local energy densities, we have that

$$\rho_1 \approx \rho_2 \approx \frac{\rho_{\rm loc}}{2}\,, \tag{4.1}$$

i.e., both species have a significant contribution to the energy density. Instead, for similar number densities $n_1 \approx n_2 \approx n_{\rm loc}$, we have

$$\rho_{\rm loc} = n_{\rm loc}(m_1 + m_2) \approx n_{\rm loc}\, m_2\,, \tag{4.2}$$

where in the last step we assumed $m_2 \gg m_1$. Therefore,

$$n_{\rm loc} \approx \frac{\rho_{\rm loc}}{m_2}\,.$$

Of course, in the case of equal masses, i.e., $m_1 = m_2$ (as roughly expected for asymmetric DM), both expressions in eqs. (4.1) and (4.2) are equivalent. This means that, in this case, direct detection signals for multi-component DM models are suppressed by the heaviest DM mass (really the total sum of the masses), and similarly with indirect detection signals.

The number densities n_1, n_2 are plotted in Fig. 4.1 versus $r_\rho = \rho_2/\rho_1$ for $m_1 = 9$ GeV and $m_2 = 10$ GeV in the left figure, and for $m_1 = 9$ GeV and $m_2 = 45$ GeV in the right one. We show the exact values in solid, and the different approximations $n_1 = n_2$ in dashed black, $\rho_1 = \rho_{\rm loc}/2$ in dotted blue and $\rho_2 = \rho_{\rm loc}/2$ in dotted red. In

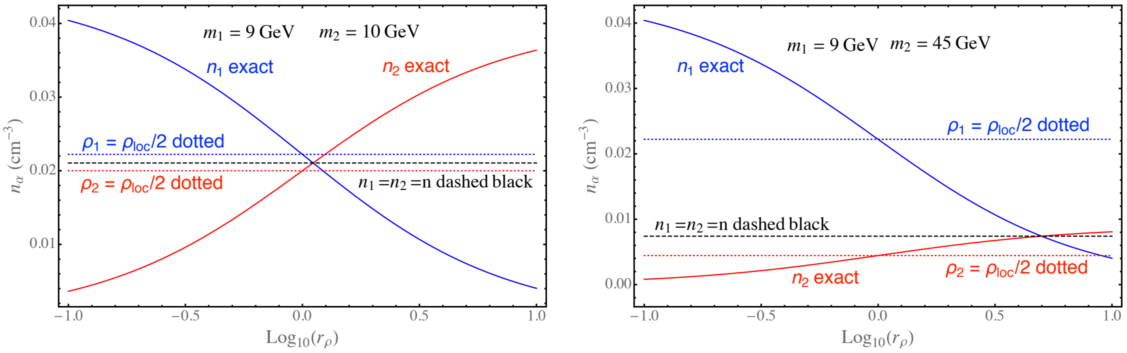

Fig. 4.1 Number densities n_α with $\alpha = 1, 2$ versus $\log_{10}(r_\rho)$, where $r_\rho = \rho_2/\rho_1$. In the left panel we plot $m_1 = 9$ GeV and $m_2 = 10$ GeV. In the right panel, we plot $m_1 = 9$ GeV and $m_2 = 45$ GeV. We show the exact values of n_α in solid. Also shown are the different approximations: $n_1 = n_2 = n$ (dashed black), $\rho_1 = \rho_{\rm loc}/2$ (dotted blue) and $\rho_2 = \rho_{\rm loc}/2$ (dotted red). For $m_1 = m_2$ all three approximations collapse into a single horizontal line. A plot for $m_1 = 45$ GeV, $m_2 = 9$ is the mirror image of the right plot with respect to a vertical axis passing through $\log_{10}(r_\rho) = 0$.

the case of $\rho_1 = \rho_2 = \rho_{\rm loc}/2$, for $r_\rho = 1$ it is of course exact. One can also see that taking $n_1 = n_2$ gives the average of the exact number densities. In the regime where the local energy density of particle 1 (2) is large, i.e. $r_\rho \ll 1 (\gg 1)$, the respective approximations are a (roughly constant) factor of two weaker, while in the opposite regime they are more discrepant.

When the masses are similar (left panel), both approximations are roughly the same. In fact all the approximations collapse for $m_1 = m_2$. On the other hand, when the masses are very different (right panel), the approximations are quite different. In the case of $n_1 = n_2$, it is an exact solution for $r_\rho = m_2/m_1 = 1.1\,(5)$ in the left (right panel). This qualitative behaviour is similar for other DM masses: the assumption of equal number densities is an average of the real number densities for any true value of the local energy densities, while that of equal energy densities is a worse approximation at least for one of the two candidates whenever $r_\rho \neq 1$.

In the rest of the paper, we will not make any approximation regarding energy densities, which we will treat as free parameters, just subject to the constraint that their sum gives the observed local energy density.

4.3 Direct detection of multi-component DM

4.3.1 The differential event rate

We present in the following the general notation for multi-component DM in detectors with different types of nuclei. For the time-being, we assume elastic spin-independent

(SI) scattering of DM particles χ_α ($\alpha = 1, 2 ..., N$) with masses m_α off nuclei with atomic and mass numbers (Z_j, A_j) ($j = 1, 2 .. M$), depositing the nuclear recoil energy E_R. The total differential rate (usually measured in events/keV/kg/day) observed by a detector is given by the sum of the event rates of the individual DM particles on each of the nuclear elements:

$$R(E_R, t) = \sum_{j=1}^{M} \sum_{\alpha=1}^{N} R_j^\alpha(E_R, t)\,, \tag{4.3}$$

where

$$R_j^\alpha(E_R, t) = x_j \frac{\rho_\alpha \sigma_\alpha^p}{2 m_\alpha \mu_{\alpha p}^2} (A_{\alpha,j}^{\text{eff}})^2 F_j^2(E_R)\, \eta_{\alpha,j}(v_{m,j}^{(\alpha)}, t)\,, \tag{4.4}$$

with ρ_α the individual local DM energy density (with the restriction $\rho_{\text{loc}} = \sum_{\alpha=1}^{N} \rho_\alpha$), σ_α^p the individual DM–proton scattering cross-section at zero momentum transfer, $\mu_{\alpha p}$ the χ_α particle–proton reduced mass and $F_j(E_R)$ the nuclear form factor of element j. We also denoted the effective mass-number of the nucleus j with DM α by

$$A_{\alpha,j}^{\text{eff}} = Z_j + (A_j - Z_j)\kappa_\alpha\,, \tag{4.5}$$

with

$$\kappa_\alpha \equiv f_\alpha^n / f_\alpha^p\,, \tag{4.6}$$

where $f_\alpha^{n,p}$ are the SI individual couplings of the DM particle α to neutrons and protons. x_j is the mass fraction of element j in the detector, i.e., $x_j = m_j / (\sum_j^M m_j)$.

We will discuss spin-independent (SI) and spin-dependent (SD) interactions in this paper; in the case of SD interactions, Eq. (4.4) can be used by substituting $A_{\alpha j}^{\text{eff}} \to 1$ and the form factor $F_j^2(E_R) \to F_{\alpha,j}^{\text{SD}}(E_R, \kappa_\alpha)$ now has a κ_α dependence. In the numerical analysis, for the SI form factors we will use the Helm parametrisation [141, 142], while for SD in xenon (and fluorine) we will use the results of Ref. [143].

In addition to ρ_α, the astrophysics enters in Eq. (4.4) through the halo integral

$$\eta_{\alpha,j}(v_{m,j}^{(\alpha)}, t) \equiv \eta(f_{\text{det}}^{(\alpha)}, v_{m,j}^{(\alpha)}, t) = \int_{v > v_{m,j}^{(\alpha)}} d^3 v \frac{f_{\text{det}}^{(\alpha)}(\mathbf{v}, t)}{v}\,, \tag{4.7}$$

with

$$v_{m,j}^{(\alpha)} \equiv v_m(m_\alpha, m_j) = \sqrt{\frac{m_j E_R}{2 \mu_{\alpha j}^2}}, \tag{4.8}$$

where $v_{m,j}^{(\alpha)}$ is the minimal velocity of the particle α required to produce a recoil of energy E_R in element j, and $f_{\text{det}}^{(\alpha)}(\mathbf{v}, t)$ describes the distribution of DM particle velocities in the detector rest frame, with $f_{\text{det}}^{(\alpha)}(\mathbf{v}, t) \geq 0$ and $\int d^3v f_{\text{det}}^{(\alpha)}(\mathbf{v}, t) = 1$. The velocity distributions in the rest frames of the detector and the galaxy are related by a Galilean transformation, $f_{\text{det}}^{(\alpha)}(\mathbf{v}, t) = f_{\text{gal}}^{(\alpha)}(\mathbf{v}+\mathbf{v}_e(t))$, where $\mathbf{v}_e(t)$ is the velocity vector of the Earth in the galaxy rest-frame. Notice that $\eta_{\alpha j}(v_{m,j}^{(\alpha)})$ is a decreasing function of $v_{m,j}^{(\alpha)}$, which for large DM masses does not depend on m_α. Throughout this paper, we will use the so-called Standard Halo Model (SHM), with $\rho_{\text{loc}}^{\text{exp}} \simeq 0.4\,\text{GeV/cm}^3$, a Maxwellian velocity distribution $f_{\text{gal}}(v) = \frac{1}{(2\pi\sigma_{H_\alpha}^2)^{3/2}} \exp\left(-\frac{3v^2}{2\sigma_{H_\alpha}^2}\right)$, and a cut-off at the escape velocity $v_{\text{esc}} = 550\,\text{km}\,\text{s}^{-1}$.

In principle, $\eta_{\alpha j}(v_{m,j}^{(\alpha)}, t)$ depends on the DM particle α in two different ways: directly, via its velocity distribution $f^{(\alpha)}(\mathbf{v}, t)$ (which, in addition may depend in a non-trivial way on the micro-physics of the DM, like its mass and interactions) and indirectly, through its mass m_α that enters into $v_{m,j}^{(\alpha)}$ (unless $m_\alpha \gg m_j$, in which case the dependence on the DM mass drops, $v_{m,j}^{(\alpha)} \to v_{m,j}$). In the following, we will assume that the functional form of the velocity distributions of the different DM components is equal, i.e., $f^{(\alpha)}(\mathbf{v}, t) \equiv f(\mathbf{v}, t)$. We will however consider the case of different velocity dispersions later on. Also, we will focus on constant rates, i.e., averaged over the year, so that

$$\bar{R}(E_R) = \frac{R(E_R, t_{\text{max}}) + R(E_R, t_{\text{min}})}{2}\,, \tag{4.9}$$

where $t_{\text{max}}\,(t_{\text{min}})$ are the times of the year at which the rate reaches a maximum (minimum). [1]

4.3.2 The rate for two DM particles

We now fix the notation for the DD signals expected from 2 DM particles $\alpha = 1, 2$ with masses $m_1 < m_2$, cross-sections with protons σ_1^p, σ_2^p, and densities ρ_1, ρ_2, such that $\rho_1 + \rho_2 = \rho_{\text{loc}}$. We will also study their signals in two different detectors $j = A_1$, A_2, with mass and atomic numbers $(A_1, Z_1) \neq (A_2, Z_2)$, and taken to have mass fractions $x_1 = x_2 = 1$ for simplicity (in the case of xenon, we will consider the different mass fractions of its isotopes). We define

$$r_\rho \equiv \frac{\rho_2}{\rho_1}\,, \qquad \text{such that} \qquad \rho_2 = r_\rho\, \rho_1 = r_\rho\, \frac{\rho_{\text{loc}}}{1 + r_\rho}\,. \tag{4.10}$$

---

[1] We will not discuss annual modulation signals, the reader is referred to refs. [112, 114, 144–149] for studies on the topic.

From eqs. (4.3), (4.4) and (4.9) (dropping the bar from the notation of $R(E_R)$), and using $\mu_{1p} = \mu_{2p} = m_p$, we can write the total rate as:

$$\begin{aligned} R_1(E_R) &= R_1^1(E_R) + R_1^2(E_R) \\ &= C(r_\rho, \sigma_1^p)\, F_{A_1}^2(E_R) \left(\frac{(A_{1,1}^{\rm eff})^2}{m_1}\, \eta(v_{m,A1}^{(1)}) + \frac{(A_{2,1}^{\rm eff})^2}{m_2}\, r_\rho\, r_\sigma\, \eta(v_{m,A1}^{(2)}) \right) , \end{aligned} \tag{4.11}$$

where we defined

$$C(r_\rho, \sigma_1^p) \equiv \frac{\rho_{\rm loc}\, \sigma_1^p}{2\,(1 + r_\rho)\, m_p^2} , \qquad \text{and} \qquad r_\sigma \equiv \frac{\sigma_2^p}{\sigma_1^p} . \tag{4.12}$$

$R_{A_2}(E_R)$ is similar, after making the following substitutions: $A_1 \to A_2$, $A_{1,1}^{\rm eff} \to A_{1,2}^{\rm eff}$ and $A_{2,1}^{\rm eff} \to A_{2,2}^{\rm eff}$. In the case of a DM signal generated from two components, it is clear that the particle masses will determine the slope of their individual rates, while r_ρ, r_σ and $\kappa_{1,2}$ will determine their relative normalisation. Therefore, a first conclusion is that using just information from a given direct detection signal, we can only distinguish if there are one or two components if the particles have different masses.

In the following numerical analysis, we will use different targets: fluorine, sodium, germanium and xenon. The strongest limits for the SI cross-section come from XENON1T [150], and are $10^{-45}\,\text{cm}^2$ for a 10 GeV DM particle and $10^{-46}\,\text{cm}^2$ for $m_{\rm DM} = 30$ GeV at 90% C.L. For SD couplings with protons, PICO-2L [151] (and PICO-60 [152] for heavier masses) set the strongest bounds, at the level of $10^{-40}\,\text{cm}^2$ for a 10 GeV DM particle. The values of the energy threshold ($E_{\rm th}$), mass, time and exposures for the different nuclei based on future expected experimental sensitivities are given in table 4.1. Notice that there are many different proposed experiments, and very large uncertainties are present in the literature regarding these values. For Ge, although smaller thresholds are possible ($\lesssim$ keV), we take a conservative value similar to the other detector ones. Therefore our analysis can be understood as a proof of concept, with more sophisticated experimental simulations needed once there is a signal. We provide some examples of illustrative proposed experiments in the last column of the table. [2] We also provide in the third column the minimum DM mass that can be detected for each element assuming perfect energy resolution.

---

[2] This is by no means an exhaustive list, and other elements and experiments are also very promising, for instance those using argon [153, 154], which however typically have higher energy thresholds ($\sim \mathcal{O}(20)$ keV). Moreover, in addition to XENONnt [155], other very promising xenon experiments are DARWIN [156] and LZ [157]. For further details of the current status of DD experiments, the interested reader is referred to Refs. [158, 159].

Element	$E_{\rm th}$ (keV)	$m_{\rm DM}^{\rm min}$ (GeV)	M (t)	T (y)	MT $(t \cdot y)$	Experiments
F	3	2	0.5	2	1	PICO-500 [152]
Na	3	2.5	0.25	10	2.5	PICO-LON [160]
Ge	2	3.5	0.4	10	4	SuperCDMS [161]
Xe	1	3	2	1.5	3	XENONnT [155]

Table 4.1 Experimental values used in the numerical analysis for future direct detection experiments. Columns 2 to 6 show respectively the recoil energy threshold $E_{\rm th}$ (keV), the minimum DM mass that can be detected in GeV, the mass of the detector M in tonnes, the data collection time T in years and the total exposure MT $(t \cdot y)$. The last column shows an illustrative experimental reference for the type of experiment considered. For xenon we consider both isotopes Xe^{129} and Xe^{131} with mass fractions x_j equal to 0.264 and 0.212, respectively.

In Fig. 4.2 we show the differential spectrum of two component DM for a variety of DM mass splittings. One can see the different slopes of the two components and the presence of a *kink* in the total rate, which rapidly vanishes for smaller mass splittings. This is the smoking gun of multi-component DM. We have checked that sensible energy resolutions do not significantly affect the spectra, and in the following we assume perfect energy resolution and efficiency.

Something important to keep in mind in the case of multi-component DM is that, the heavier DM particle may contribute to the rates in different experiments. On the other hand, the lightest particle may only scatter in the lightest detector, as in the heaviest detector the recoils may be below its energy threshold.

We plot in Fig. 4.3 the lightest DM mass m_1 (GeV) versus the recoil energy E_R (keV) where the spectrum of the DM component 1 intercepts that of DM component 2, for both SI (left) and SD (right) interactions. The SI targets include xenon, germanium and sodium, whilst for SD interactions we only consider xenon and fluorine nuclei. We fix $m_2 = 200$ GeV and $r_\rho = r_\sigma = 1$. The cut-off for the curves indicates the values of m_1 for which the spectra for the constituent components are parallel. One can see that this cut-off is highly dependent on the mass number of the nuclear target (i.e, the lower the mass number, the lower the cut-off). Notice that the maximum recoil energy that can be detected sets a conservative upper limit to the maximum m_1 that can be discriminated, i.e., such that the energy of the intersection is below its value. Similarly, the maximum m_1 sets the maximum energy of the intersection above which the rates cannot be discriminated. This means that there are both lower and upper bounds on the splitting between the DM masses m_2-m_1 for a discrimination between a two-component and one-component signal to be possible. This is due to the fact that, for fixed m_2, m_1 cannot be arbitrarily light, as it would not give recoils below threshold. Similarly, for a fixed m_1, m_2 cannot be

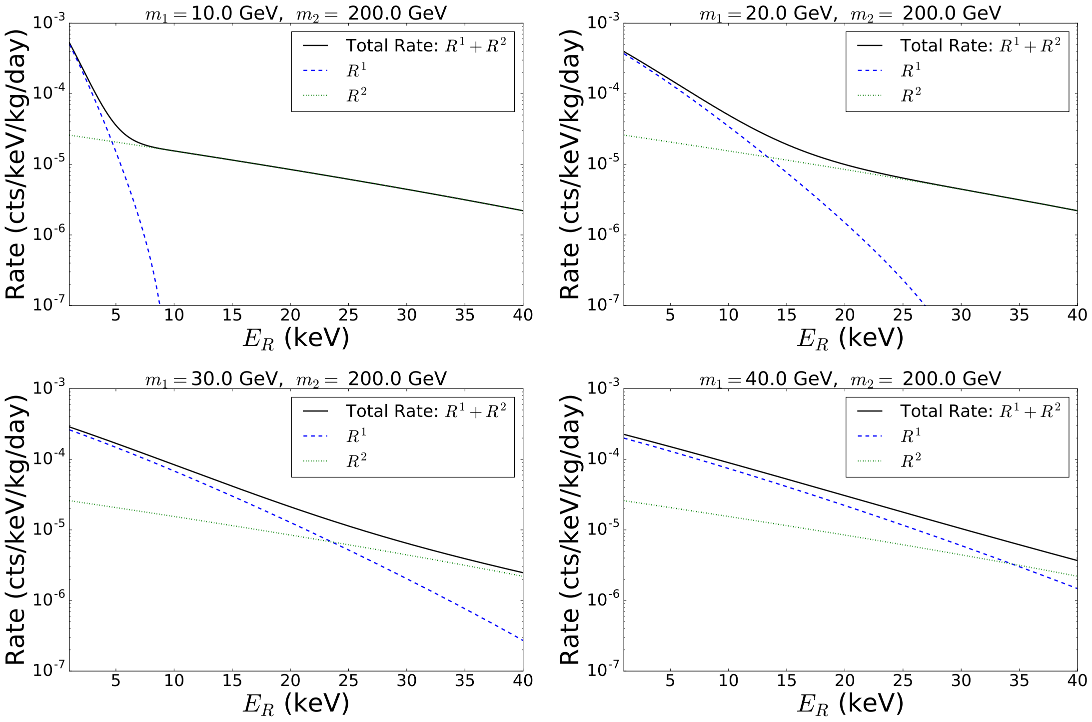

Fig. 4.2 Total differential event rate for 2 DM particles (solid black), as well as their individual contributions (1 dashed blue, 2 dotted green) for a variety of DM mass splittings on the energy range $[2, 30]$ keV. One should notice that the *kink* feature in the combined spectrum rapidly vanishes with smaller mass splittings.

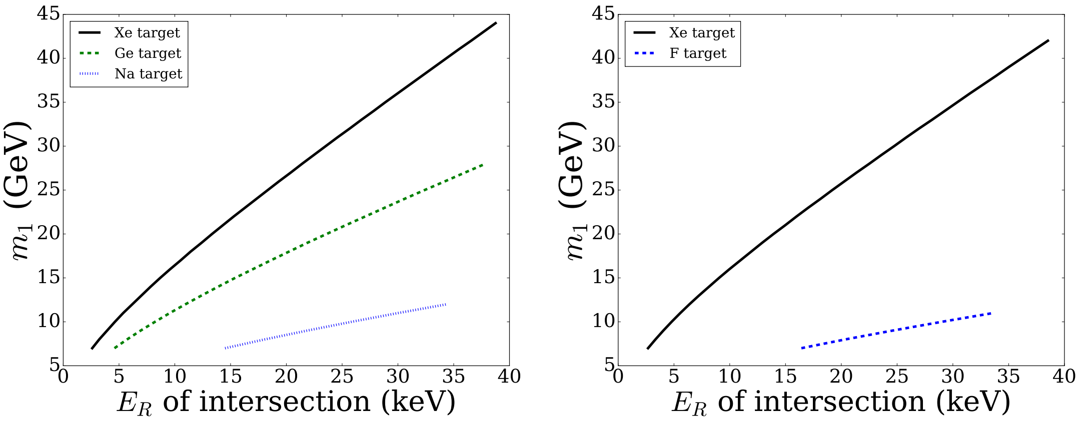

Fig. 4.3 The lightest DM mass m_1 (GeV) versus the recoil energy E_R (keV) where the spectrum of the DM component 1 intercepts the spectrum of the DM component 2. We show different targets for both SI (left) and SD (right) interactions. For SI interactions we consider Xe, Ge and Na nuclei whereas for the SD case we only take Xe and F nuclei. We fix $m_2 = 200$ GeV and $r_\rho = r_\sigma = 1$. Notice that the maximum recoil energy of the interception sets an upper limit on the maximum m_1 that can be discriminated.

arbitrarily large, as its number density (and therefore its rate) would be extremely suppressed.

We can try to see which particle dominates the rate, the heaviest or the lightest. As we have seen, this depends on the recoil energy considered. For a fixed E_R, as $m_2 > m_1$ (by definition), we have that $\eta(v^1_{m,A1}) < \eta(v^2_{m,A1})$. However, it could well be that the lightest particle (number 1) dominates if $r_\rho \ll 1$ or $r_\sigma \ll 1$. Therefore which particle gives the largest contribution to the rate depends also on the product $r_\rho r_\sigma$. We plot in Fig. 4.4 the regions in the plane $\log(m_1)$–$\log(m_2)$ where DM particle 2 (1) dominates as shaded light blue (shaded light brown) areas for $E_R = 2$ keV (upper panel) and for $E_R = 30$ keV (lower row). We show results for two different values of $r_\rho r_\sigma = 1$, (0.2) in the left (right) panel. Of course, the areas are symmetric under interchange of particles 1 and 2 for $r_\rho = r_\sigma = 1$. In this case, one can see that lightest DM species always dominates: DM 1 to the upper-left region of the diagonal, and DM2 to the lower-right, except in a small region where the lightest DM is so light that we are probing the tail of the velocity distribution, which is exponentially suppressed. For $r_\rho r_\sigma = 0.2$, the regions where DM 1 dominates are somewhat larger than for $r_\rho r_\sigma = 1$. A similar plot for $r_\rho r_\sigma = 5$ can be obtained by the reflection of the $r_\rho r_\sigma = 0.2$ plot by interchanging $m_1 \leftrightarrow m_2$ everywhere, and therefore, in this case, the regions where DM 2 dominates are larger than for $r_\rho r_\sigma = 1$. The regions to the left (bottom) of the vertical (horizontal) dashed lines imply $v_m^{(1)}(E_R) > v_{\text{esc},\text{det}}$ ($v_m^{(2)}(E_R) > v_{\text{esc},\text{det}}$) and therefore there is no DM 1 (2) that can give recoils at that recoil energy. They set the lowest DM mass that can be detected. For $E_R = 30$ keV, the regions where the scattering is allowed shrink, as the minimum DM mass that can produce a recoil is larger than for $E_R = 2$ keV.

We therefore conclude that in the general case, which particle dominates the rate is a rather model-dependent statement. If we take equal energy densities and cross-sections, i.e. $r_\rho r_\sigma = 1$, again, which one dominates depends on the DM masses and cross-sections, see Eq. (7.1) and Fig. 4.4. On the other hand, if we assume $n_1 = n_2 \equiv n$, then $\rho_{\text{loc}} = n\, m_{\text{tot}}$, where $m_{\text{tot}} = m_1 + m_2$, and $r_\rho = m_2/m_1$. Therefore, in this scenario the total rate can also be computed using Eq. (7.1) for $r_\rho = m_2/m_1$, and it simplifies to:

$$R_{A_1}(E_R) = \frac{C_n(\sigma_1^p)}{m_{\text{tot}}}\; F^2_{A_1}(E_R)\; \Big((A^{\text{eff}}_{1,1})^2\, \eta(v^{(1)}_{m,A1}) + (A^{\text{eff}}_{2,1})^2\, r_\sigma\, \eta(v^{(2)}_{m,A1}) \Big)\,, \tag{4.13}$$

where we defined

$$C_n(\sigma_1^p) \equiv \frac{\rho_{\text{loc}}\, \sigma_1^p}{2m_p^2}\,. \tag{4.14}$$

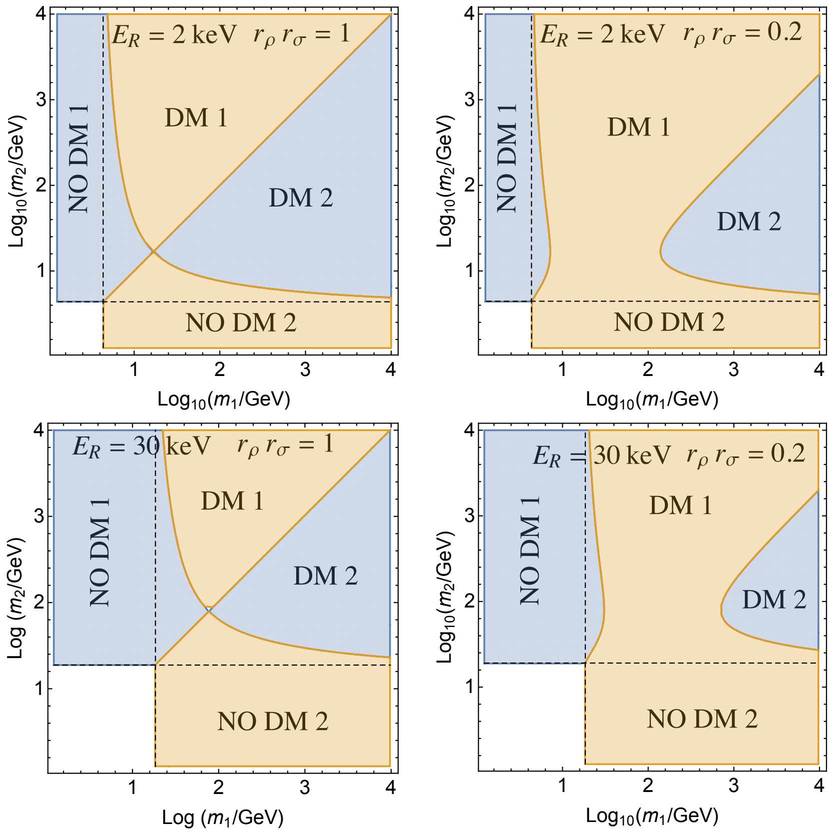

Fig. 4.4 Regions in the plane $\log(m_1)$–$\log(m_2)$ where DM particle 2 (1) dominates as shaded light blue (shaded light brown) areas. The upper row is for $E_R = 2$ keV and the lower row for $E_R = 30$ keV. Left (right) column is for $r_\rho r_\sigma = 1\,(0.2)$. The regions to the left (bottom) of the vertical (horizontal) dashed lines imply $v_m^{(1)}(E_R) > v_{\mathrm{esc\,,det}}$ ($v_m^{(2)}(E_R) > v_{\mathrm{esc\,,det}}$) and therefore there is no DM 1 (2) that can give recoils at that recoil energy.

Interestingly, in this case the DM masses m_1, m_2 only enter in the rate through the dependence on $\eta(v_m)$. This means that the lower the DM mass, the larger the minimum velocity, and therefore the smaller the rate. Therefore, in this case, for $r_\sigma = 1$ and $\kappa_1 = \kappa_2$, the largest DM mass clearly dominates the rate. The implications of this will be further discussed below in sec. 4.3.2.

Suppression of the rate for equal number densities

In the case of equal number densities, if we assume that the DM particles have roughly the same kind of interactions with the SM ($r_\sigma = 1$, $\kappa_1 = \kappa_2$), calling $\sigma_1^p \approx \sigma_2^p \equiv \sigma_p$, with SI isospin-conserving interactions, the total rate for a particular nucleus can be written using Eq. (4.13) as:

$$R(E_R) \simeq \frac{\sigma_p}{2m_p^2} \frac{\rho_{\rm loc}}{m_2} A^2 F^2(E_R)\, \eta(v_m^{(2)})\,, \tag{4.15}$$

where we used that $\eta(v_m^{(2)}) \gg \eta(v_m^{(1)})$ and $m_{\rm tot} \approx m_2$, which are valid when there is a significant hierarchy in masses, $m_1 \ll m_2$. Notice also that in the limit $m_2 \gg m_A$, $v_m^{(2)}$ becomes independent of the DM mass m_2, and so does $\eta(v_m^{(2)})$, so we could drop its superscript (we assume this in the following). From this expression, we can derive an upper bound on the heaviest DM mass to have a signal in a direct detection experiment for a given cross-section. For an experimental sensitivity of $R_{\rm exp}(E_R)$ at a given recoil energy E_R, we get:

$$\frac{\rho_{\rm loc}\, \sigma_p}{m_2} \simeq \frac{2\, m_p^2\, R_{\rm exp}(E_R)}{A^2 F^2(E_R)\, \eta[v_m(E_R)]}\,, \tag{4.16}$$

or similarly, for a fixed DM cross-section:

$$m_2 \simeq \frac{1}{2\, m_p^2} \frac{\rho_{\rm loc}}{R_{\rm exp}(E_R)} \sigma_p A^2 F^2(E_R)\, \eta[v_m(E_R)]\,. \tag{4.17}$$

Notice that one can use the inequality $\eta(v_m) < 1/v_m$ that is independent of the velocity distribution [139, 162–164], and therefore derive an upper limit on the DM mass (or a lower limit on $\rho_{\rm loc}\, \sigma_p/m_2$) that is $f(v)$-independent as a function of the recoil energy:

$$m_2 < \frac{1}{2\, m_p^2\, v_m(E_R)} \frac{\rho_{\rm loc}}{R_{\rm exp}(E_R)} \sigma_p A^2 F^2(E_R)\,. \tag{4.18}$$

Therefore one can check the E_R at which the upper bound is weakest. As an example, using $\sigma_p = 10^{-45}\,\mathrm{cm}^2$, and taking the the form factor equal to one, in Germanium, for an expected sensitivity of $R_{\rm exp} \geq 10^{-5}$ cts/kg/day at a typical recoil energy $E_{\rm R} = 2$ KeV, we get that $m_2 \lesssim 200$ GeV, i.e., unless the heaviest mass is lighter than 200

GeV, the rate will be too low to be detected. For the same conditions in Iodine (DAMA) and Xenon, we obtain upper bounds of ~ 600 and ~ 700 GeV respectively. Similarly, if the DM properties were known from other probes (colliders, indirect detection), eq. (4.18) could be used to derive an upper limit on the event rate as a function of recoil energy. The bottom line is that, for equal number densities, if the DM components have similar interaction strength, the heaviest mass of the DM group dictates the sensitivity of DD.

4.4 Hypothesis testing: one versus two DM components

In the following (sec. 4.4.1) we detail the statistical methods used to calculate the sensitivity of future experiments to discriminate a two-component DM scenario from the one-component one. We formulate this analysis as a frequentist hypothesis test, with the null-hypothesis being one-component, and the alternative hypothesis being two-component. The test should be able to select the two-component interpretation when the energy recoil spectrum has a significant *kink* feature, as shown in Fig. 4.2, since this feature cannot be explained with only one DM particle. The statistical techniques used in this study have been previously applied and thoroughly detailed in the context of neutrino mass ordering analyses [165–167]. We then show in subsequent subsections that the best model discriminator is the mass splitting between the two DM components. We first show in sec. 4.4.2 results taking as free parameters m_1, m_2 and the overall normalisation σ_p^1, keeping $\kappa_{1,2} = r_\rho = r_\sigma = 1$ and assuming the SHM for both DM particles with $\sigma_{\mathrm{H1}} = \sigma_{\mathrm{H2}} = 270$ km/s. Afterwards, in sec. 4.4.3 we proceed to see how the discrimination is worsened by allowing $r_\rho \neq r_\sigma \neq 1$, the dispersion velocities $\sigma_{\mathrm{H1}} \neq \sigma_{\mathrm{H2}} \neq \sigma_{\mathrm{SHM}}$, or the ratios of couplings $\kappa_1 \neq \kappa_2 \neq 1$.

4.4.1 Test statistic for hypothesis testing

We construct the hypothesis test in a frequentist framework, defining the null hypothesis to be the one-component scenario which we denote H_{1DM}. Similarly we denote the two-component alternative hypothesis H_{2DM}. Notice that the one DM hypothesis is a subset of the two DM hypothesis, as can be seen easily by taking $r_\rho = 0$ in Eq. (7.1). H_{1DM} is said to be a *nested* hypothesis of H_{2DM}. We will see later that this has important ramifications.

Suppose that we have a detector that has observed a set of binned count measurements $\mathbf{x} = x_1, x_2 ..., x_N$ over N bins with uncertainties $\sigma_i = \sqrt{x_i}$. We parameterise the likelihood of observing this data given a hypotheses $H_{\rm 1DM}/H_{\rm 2DM}$ with a binned Gaussian distribution:

$$\mathcal{L}(\mathbf{x}\,|\,H_\alpha) = \prod_i^N \frac{1}{\sqrt{2\pi}\sigma_i} e^{-\frac{[x_i-\mu_i(\theta_\alpha)]^2}{2\sigma_i^2}} \qquad \alpha = [H_{\rm 1DM}, H_{\rm 2DM}], \tag{4.19}$$

where $\mu_i(\theta_\alpha)$ is the expected number of counts in bin i as a function of the model parameters $\theta_{H_{\rm 1DM}}/\theta_{H_{\rm 2DM}}$ under the hypothesis $H_{\rm 1DM}/H_{\rm 2DM}$. Maximising the likelihood in Eq. (4.19) with respect to the hypothesis parameters θ_α is equivalent to minimising -2 times the log-likelihood as follows:

$$\min_{\theta_\alpha}\Big(-2\ln\mathcal{L}\Big) = \min_{\theta_\alpha}\sum_i^N \frac{[x_i-\mu_i(\theta_\alpha)]^2}{\sigma_i^2} \equiv \min_{\theta_\alpha}\chi^2(\theta_\alpha)\ . \tag{4.20}$$

This is the familiar ‘chi-square’ statistic which, as showed by Pearson [168] in the limit of large x_i follows a χ^2 distribution with $N - n(\theta_\alpha)$ degrees of freedom, where $n(\theta_\alpha)$ is the number of parameters θ_α.

One should immediately notice that Eq. (4.20) only provides a ‘goodness of fit’ for the hypothesis α, and does not explicitly reject one in favour of the other. For this task, we require a test-statistic $\mathcal{T}$ that explicitly discriminates between $H_{\rm 1DM}$ and $H_{\rm 2DM}$. A commonly used test statistic is:

$$\mathcal{T} = \min_{\theta_{H_{\rm 1DM}}}\chi^2(\theta_{H_{\rm 1DM}}) - \min_{\theta_{H_{\rm 2DM}}}\chi^2(\theta_{H_{\rm 2DM}})\,. \tag{4.21}$$

Notice that the definition of $\mathcal{T}$ is such that the larger its value, the larger the preference for $H_{\rm 2DM}$, and the smaller its value, the more $H_{\rm 1DM}$ is preferred.

In order to quantify how much the data supports either hypothesis, we require the limiting probability distribution of the $\mathcal{T}$ statistic in the case either $H_{\rm 1DM}$ and $H_{\rm 2DM}$ is true. Under some general assumptions, the theorem from Wilk [169] states that in the case of nested hypotheses (i.e when $H_{\rm 1DM}$ is true), $\mathcal{T}$ will follow a χ^2 distribution with $k \equiv n(\theta_{H_{\rm 2DM}}) - n(\theta_{H_{\rm 1DM}})$ degrees of freedom, where n is the number of parameters that parameterise a given hypothesis. We denote this by $\mathcal{T}^{\rm 1DM}$.

However, in the case that $H_{\rm 2DM}$ is true, we show in Appendix 4.7 that the $\mathcal{T}$ statistic, which we denote $\mathcal{T}^{\rm 2DM}$, will follow a Gaussian distribution that is solely dependent on the true parameter values $\mu(\theta^{\rm true}_{H_{\rm 2DM}})$ with mean given by $\mathcal{T}_0^{\rm 2DM}$ and standard deviation $2\sqrt{\mathcal{T}_0^{\rm 2DM}}$, where

$$\mathcal{T}_0^{\rm 2DM} \equiv \mathcal{T}(x_i = \mu_i(\theta^{\rm true}_{H_{\rm 2DM}})) = \min_{\theta_{H_{\rm 1DM}}}\sum_i^n \left(\frac{\mu_i(\theta^{\rm true}_{H_{\rm 2DM}}) - \mu_i(\theta_{H_{\rm 1DM}})}{\sqrt{\mu_i(\theta^{\rm true}_{H_{\rm 2DM}})}}\right)^2\ . \tag{4.22}$$

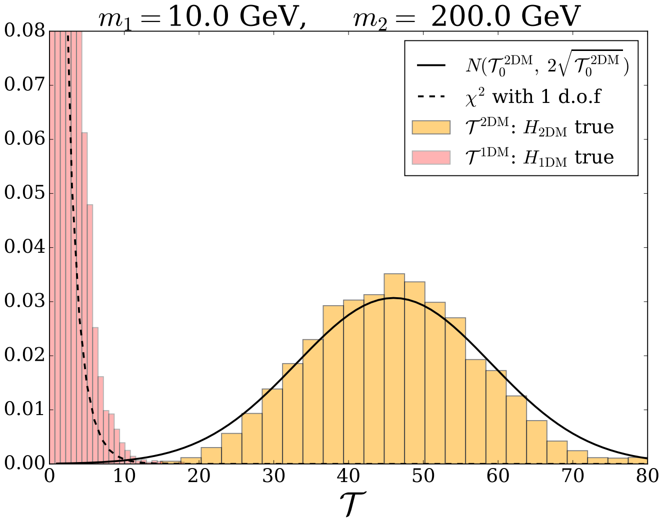

Fig. 4.5 Normalised probability distribution of the test statistic $\mathcal{T}$ in a Xe target for true one-component $\mathcal{T}^{\rm 1DM}$ (light red) and two-component $\mathcal{T}^{\rm 2DM}$ (light yellow) DM hypothesis. We fixed $m_1 = 10$ GeV and $m_2 = 200$ GeV. We used 8500 samples. We see that the one-component DM follows a χ^2 distribution with one degree of freedom, while the two-component DM hypothesis is well-approximated by a Gaussian centered at $\mathcal{T}_0^{\rm 2DM}$, with standard deviation $2\sqrt{\mathcal{T}_0^{\rm 2DM}}$.

That is, $\mathcal{T}_0^{\rm 2DM}$ has no statistical fluctuations from the data and is often called the *'Asimov likelihood'*. The Asimov likelihood can be qualitatively thought of as an approximation of the median value of a test statistic. See Ref. [170] for details. Note that large values of $\mathcal{T}_0^{\rm 2DM}$ disfavour the null hypothesis $H_{\rm 1DM}$.

In Fig. 4.5 we show the probability distribution of $\mathcal{T}$ for the two hypotheses in a Xe target: $H_{\rm 1DM}$ in light red and $H_{\rm 2DM}$ in light yellow. We fix $m_1 = 10$ GeV and $m_2 = 200$ GeV and use 8500 Monte Carlo samples. Since the only free parameters we are considering are the two DM masses, the difference in degrees of freedom of the two hypotheses is $k = 2 - 1 = 1$ degrees of freedom. Hence, from Wilk's theorem, we expect that under $H_{\rm 1DM}$, $\mathcal{T}$ will follow a $\chi^2_{\rm 1d.o.f}$ distribution. One can see that $\mathcal{T}^{\rm 2DM}$ is approximately Gaussian distributed with median $\mathcal{T}_0^{\rm 2DM}$ and standard deviation $2\sqrt{\mathcal{T}_0^{\rm 2DM}}$, while $\mathcal{T}^{\rm 1DM}$ is approximately estimated by a χ^2-distribution with one degree of freedom as expected.[3]

---

[3] One will also notice that the width of the Gaussian approximation in Fig. 4.5 slightly overestimates $\mathcal{T}^{\rm 2DM}$. This of course could be primarily because we have assumed Monte Carlo realisations of the recoil spectrum are Gaussian distributed instead of Poisson. We have exploited the assumption that for large number of events the bin by bin distribution starts looking Gaussian. In practice, however, we are only interested in the median of the $H_{\rm 2DM}$ distribution, since its variance does not enter in the calculation of the median sensitivity, as will be discussed in sec. 4.4.1.

Median sensitivity

The aim of this analysis is to quantify how sensitive an "average experiment" operating at future benchmarks is to rejecting $H_{\rm 1DM}$ in favour of $H_{\rm 2DM}$. The quantity that allows us to do this is called the *median sensitivity* and can be easily visualised as follows: Under $H_{\rm 2DM}$ an experiment will generate a $\mathcal{T}^{2DM}$ statistic that is approximately Gaussian as shown in Fig. 4.5. In this vein, the median (mean) of this Gaussian $\mathcal{T}_0^{\rm 2DM}$ quantifies the experiments' 'average' capability.

Since we know that the distribution of $\mathcal{T}$ under $H_{\rm 1DM}$ is a χ^2 with k degrees of freedom, we can then calculate the probability of having a $\mathcal{T}_0^{\rm 2DM}$ at least as extreme as the one we observed. This is called the *p-value* and is given by

$$p = \int_{\mathcal{T}_0^{\rm 2DM}}^{\infty} f(\mathcal{T}|H_{\rm 1DM})\, d\mathcal{T} = 1 - {\rm CDF}^{\chi^2}_{\rm k\ d.o.f}(\mathcal{T}_0^{\rm 2DM})\ , \tag{4.23}$$

where ${\rm CDF}^{\chi^2}_{\rm k\ d.o.f}$ is the cumulative density function for the $\chi^2_{k\ \rm d.o.f}$. As a result, a larger $\mathcal{T}_0^{\rm 2DM}$ which favours $H_{\rm 2DM}$ will produce a smaller p-value, and vice-versa. We define α to be the probability of making an error of the 1st kind, i.e, rejecting $H_{\rm 1DM}$ if its true. If $p < \alpha$, then the data supports $H_{\rm 2DM}$ over $H_{\rm 1DM}$. In more conventional words, we have defined our critical region to be where there is a low probability to observe $\mathcal{T}$ if $H_{\rm 1DM}$ is true but a high probabi1ity if the alternative hypothesis $H_{\rm 2DM}$ is true. The p-value in Eq. (5.27) can be converted to a two-sided number of unit Gaussian standard deviations, which we will denote throughout the rest of this paper as Z, and call it the *median sensitivity* using [4]

$$Z(p) = \sqrt{2}\,{\rm erfc}^{-1}({\rm p})\ , \tag{4.24}$$

where ${\rm erfc}({\rm p}) \equiv 1 - {\rm erf}({\rm p})$ is the complimentary error function. If $Z \geq Z(\alpha) \equiv 5$ then the median experiment can reject $H_{\rm 1DM}$ in favour of $H_{\rm 2DM}$ at the 5-sigma confidence level (CL). In the special case that the difference in number of degrees of freedom is $k = 1$, the sensitivity is just given by [170]

$$Z|_{k=1} = \sqrt{\mathcal{T}_0^{\rm 2DM}}\ . \tag{4.25}$$

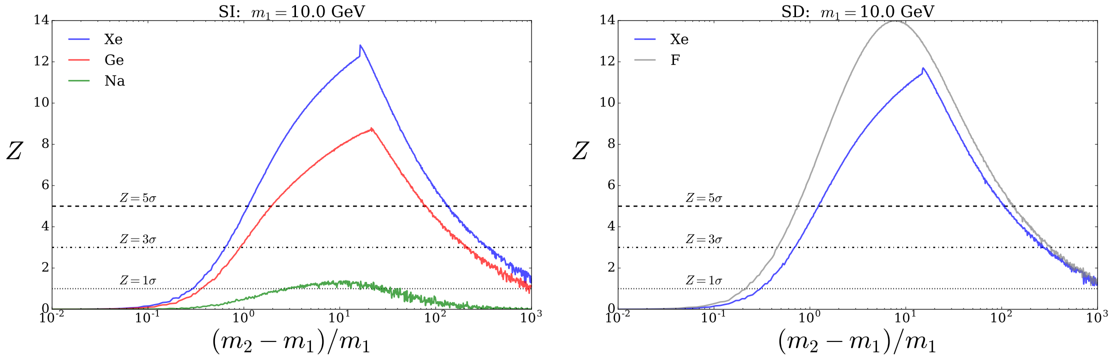

Fig. 4.6 Significance Z with which the median experiment can reject the one-DM hypothesis in favour of the two-DM hypothesis as a function of the mass splitting $(m_2 - m_1)/m_1$, for fixed m_1 equal to 10 GeV. We show as dotted, dash-dotted and dashed (black) horizontal lines the 1, 3 and 5 σ C.L. The left panel shows the SI targets xenon (in blue), germanium (in red) and sodium (in green). The right panel shows the SD targets fluorine (in grey) and xenon (in blue).

4.4.2 Fixed parameters except for the DM masses

We perform the analysis discussed in sec. 4.4.1 firstly for the case that all hypothesis parameters are fixed except for m_1 and m_2. As a result, the difference in number of degrees of freedom between $H_{\rm 1DM}$ and $H_{\rm 2DM}$ is $k = 1$. Thus, Eq. (4.25) is used in this case to calculate the median sensitivity. Later on in sec. 4.4.3, we will study how our results are changed in more general cases by relaxing the restrictions on other parameters. We do the following analysis both for SI and SD WIMP-nucleon couplings.

For SI interactions we will consider future sodium, germanium and xenon experiments, with a true SI cross-section with protons of $\sigma^{p}_{1({\rm SI})} = 10^{-45}\,{\rm cm}^2$. For SD interactions we will consider future fluorine and xenon experiments with true SD cross-section with protons of $\sigma^{p}_{1({\rm SD})} = 10^{-40}\,{\rm cm}^2$. We adopt the experimental configurations shown in tab. 4.1. The choice of the nuclei for our assumed SI interaction experiments is such that there is a large range in masses, while for SD interactions there is an additional feature: fluorine (xenon) is most sensitive to DM couplings to protons (neutrons). We also assume a true (known) r_ρ, $r_\sigma = 1$, i.e., equal energy densities and cross-sections for the two DM particles, as well as equal couplings to protons and neutrons ($\kappa_{1,2} = 1$).

In order to illustrate how the mass splitting controls the hypothesis discrimination, we show in Fig. 4.6 the median significance Z as defined in Eq. (4.25) versus the

---

[4] An alternate definition of the median sensitivity as seen in Ref. [165] is given by the CL at which an experiment will reject the wrong hypothesis with a probability of 50%, that is, with a rate for an error of the second kind of 0.5. We will use the definition in Eq. (5.26) for this study.

normalised mass splitting $(m_2 - m_1)/m_1$, for a fixed lightest DM mass m_1 equal to 10 GeV. The left panel shows SI targets: xenon (in blue), germanium (in red) and sodium (in green). The right panel shows the SD targets fluorine (in grey) and xenon (in blue). We also show for reference the 1, 3, and 5 sigma contours as horizontal dotted, dash-dotted and dashed (black) lines. In the case of sodium, the significance is always very poor. This is due to two reasons. Firstly, the rate goes for spin-independent interactions as A^2. As a result, one obtains suppressed statistics in a Na based experiment as opposed to Xe and Ge when similar exposures are used. This dominates the height of the curve in figure 6, left panel (c.f. figure 6 right panel for SD). Secondly, in general one is always more sensitive to recoils when roughly $m_{\rm DM} \sim m_{\rm Nucleus}$. Hence since one will only ever observe a significant 'kink' in the recoil spectrum for large enough mass splittings, a Na experiment will have trouble significantly rejecting the one-component hypotheses because it won't see the heavier particle. This effect is reflected by the relative shift of the peaks of the three curves (red, green and blue) in the left panel of figure 6. In all other cases, one should notice that the median significance is globally maximised at a mass splitting that is approximately equal to ~ 10 and drops to zero for very small $\lesssim 0.1$ or very large $\gtrsim 10^3$ mass splittings. This illustrates that there exists only a finite window in masses, roughly $m_2 \sim \mathcal{O}(1 - 100)\, m_1$, where there can be a significant ($\gtrsim 5\,\sigma$) discrimination.

In Fig. 4.7 we show the median sensitivity in the full mass plane $m_2 - m_1$. The top panel is for SI and the bottom panel for SD. One can see that the DM mass regions of large significance increase with the mass of the nucleus. Indeed, as discussed above, the significance for sodium is always negligible. Notice also that the regions shrink for very large masses of the heaviest DM, where its number density is so suppressed that it gives no signal in the detector. The exposure for such heavy masses is a critical factor to obtain a signal and achieve discrimination. For xenon, the largest sensitivity occurs when the lightest DM mass is around 10-20 GeV, and the heavy mass is in the range 50-400 GeV. For germanium, the largest significance occurs when the heaviest DM is lighter than roughly 300 GeV. For the SD case the main features are preserved for xenon, however the maximum significance that can be achieved is slightly lower. Fluorine however achieves maximum significance for m_2 in the range 50-200 GeV. Another feature of the SD fluorine result is that the median significance also drops above $m_1 \gtrsim 15$ GeV.

An important note to make is that the median (statistical) sensitivity scales as usual with the square root of the exposure

$$Z \propto \sqrt{MT}\ . \tag{4.26}$$

This is true for all detector types for both SI and SD interactions. This is important, since the results we show in this section can always be scaled accordingly for different experimental exposures to those given in tab. 4.1.

4.4.3 General scenarios

In the following we drop some of our simplifying assumptions to see how our results are affected. We use values of m_1-m_2 that yield high median significance: we fix m_2 to have a mass of 150 (200) GeV for SD (SI) respectively. We then consider three different generalised scenarios (we do not show the results for sodium since in all cases the maximum median significance achieved is negligible):

1. In the first general scenario we consider we include the velocity dispersions of the two components' velocity distributions into the parameter space of $H_{\rm 1DM}$ and $H_{\rm 2DM}$: $H_{\rm 1DM} = [\sigma_1^p, m_1, \sigma_{H_1}]$ and $H_{\rm 2DM} = [\sigma_1^p, m_2, m_2, \sigma_{H_1}, \sigma_{H_2}]$. In Fig. 4.8 we show the median sensitivity in the plane of m_1 versus σ_{H_1} for the SI targets (top panel) and SD targets (bottom panel). We fix the velocity dispersion of the heavier particle to $\sigma_{H_2} = 270$ km/s, while the lightest (DM one) has a free velocity dispersion in the range $50 < \sigma_{H_1} < 400\,$km/s. The low velocity dispersion case corresponds to a stream. The median sensitivity is calculated realising that $H_{\rm 2DM}$ has two more degrees of freedom than $H_{\rm 1DM}$. Hence, $k = 2$ and the median sensitivity is calculated using Eq. (5.26). In the case of SI xenon (and similarly for germanium), one can see that there is a correlation between the lightest DM mass and its velocity dispersion, which is expected. This is because the median significance is large, whether for very low DM masses with large dispersions such that events are above threshold, or for medium-range masses with small dispersions. With respect to the SHM case, for m_1 in the region of $\sim$ 15 GeV, the hypotheses can be somewhat better resolved by a smaller velocity dispersion. Sodium (not shown) can only discriminate between $H_{\rm 1DM}/H_{\rm 2DM}$ at the level of 1.6-sigma.

   In Fig. 4.9 we show m_1 versus σ_{H_2} for the SI targets (top panel) and SD targets (bottom panel). In a similar way to Fig. 4.8, here we fix $\sigma_{H_1} = 270$ km/s and let σ_{H_2} run over $50 < \sigma_{H_2} < 400\,$km/s. We see that the median significance is almost insensitive to σ_{H_2} (at $m_1 \sim 12$ GeV) for all targets except for fluorine in the SD case, where Z starts to decrease for smaller σ_{H_2} ($\lesssim 100$ km/s). The lack of dependence on σ_{H_2} is due to the fact that for heavy WIMPs the whole velocity distribution is probed.

2. In the second scenario we drop the assumption of equal energy densities and cross-sections, i.e, we take $r_\rho \neq r_\sigma$. We now allow r_ρ and r_σ to enter the parameter space of $H_{\rm 2DM}$ in the range $0.01 < r_\rho < 2.5$ and $0.01 < r_\sigma < 10$: $H_{\rm 1DM} = [\sigma_1^p, m_1]$ and $H_{\rm 2DM} = [\sigma_1^p, m_2, m_2, r_\rho, r_\sigma]$. Since r_ρ and r_σ only exist within the parameter space of $H_{\rm 2DM}$ then in this case we have $k = 3$ and hence in order to calculate the median significance we need to resort to Eq. (5.26).

   In Fig. 4.10 we show the r_ρ–m_1 plane for SI (top panel) and SD (bottom panel) interactions, whilst keeping $r_\sigma = 1$. One can see that, for any fixed DM mass, Z drops once we move away from the $r_\rho = 1$ case. Conversely, for the SD case in a fluorine target the significance is approximately constant in the range $0.25 < r_\rho < 2.5$. These results are similar to that of Fig. 4.11 which shows the r_σ–m_1 plane for SI (top panel) and SD (bottom panel) interactions for fixed $r_\rho = 1$. However, the region of high significance is slightly more elongated along the r_σ axis for both the SI and SD cases. The SD fluorine target significance now drops lower at $r_\sigma < 0.1$. We can conclude that if r_ρ $[r_\sigma]$ are different from one, but not more than a factor $\mathcal{O}(1\,[10])$ from it, the sensitivity is not significantly worsened.

3. The final scenario we consider involves isospin-violating DM (see also [171, 172]). We perform a scan over the WIMP-nucleon coupling ratios κ_1 and κ_2. We let the coupling ratios enter the hypotheses' parameter space in the ranges $\kappa_1, \kappa_2 \in [-5, 5]$, keeping in mind that these parameters enter the rate differently for SI and SD interactions: $H_{\rm 1DM} = [\sigma_1^p, m_1, \kappa_1]$ and $H_{\rm 2DM} = [\sigma_1^p, m_2, m_2, \kappa_1, \kappa_2]$. The total difference in number of degrees of freedom is $k = 2$ and hence the median sensitivity is again calculated using Eq. (5.26).

   In figure 4.12 we show the κ_2–κ_1 plane for SI (top panel) and SD (bottom panel) interactions. In the SI case, one can easily see from inspection of Eq. (4.5) that $A^{\rm eff} \to 0$ as $\kappa \to -0.7$ for Xe and -0.8 for Ge. Hence if either one of κ_1 or κ_2 are close to zero, the rate due to this component will be vanishing and hence there will be no good hypothesis discrimination. One will also notice that the median sensitivity grows for larger $\kappa_{1,2}$, where $A^2_{\rm eff} \propto |\kappa_{1,2}|^2$, becoming independent of the signs of the κ_i. In the SD case, since Xe targets are more sensitive to WIMP-neutron couplings, we see that the rate diminishes for $\kappa \to 0$. In the case of a fluorine target however, since the nuclear mass is much lower than Xe, for a given E_R, the SD form factor is approximately 1, and hence varying κ does not significantly effect the median sensitivity. For this reason we do not show the result for the fluorine target. [5]

4.5 Parameter estimation: extracting the DM properties from 2DM signals

Previous studies have conducted parameter estimation analyses for ensembles of WIMP parameters in current generation detectors under the assumption of only one component DM [173, 174]. In the following we want to study the case where the 2 DM hypothesis has been confirmed, so that one would try to extract the DM parameters. We again adopt a frequentist framework to conduct our parameter estimation by making use of the method of maximum likelihood. We use the `MultiNest` [175] package which obtains likelihood samples within a user-specified prior boundary via an importance nested sampling algorithm. We also do the analysis under a Bayesian framework for completion, however we present these results in appendix 4.8. We choose this prior range to span over parameter values that give good discrimination between $H_{\rm 1DM}$ and $H_{\rm 2DM}$ as observed from the results of sec. 4.4. In the following sections we briefly discuss the statistical methods and then present our results.

4.5.1 Statistical methods

Method of maximum likelihood

The method of maximum likelihood (ML) allows us to make estimations about model parameters by finding the parameter configuration $\hat{\boldsymbol{\theta}}$ that maximises the likelihood function $\mathcal{L}(\mathbf{x}|\boldsymbol{\theta})$. The values $\hat{\boldsymbol{\theta}}$ are called the ML estimators of the model. For this study we wish to examine the parameter space of only two of the 8 model parameters at a time. One may explicitly 'profile out' all other parameters by writing the likelihood function in terms of the ML estimators of these parameters. The result is called the profile likelihood

$$\mathcal{L}(\mathbf{x}\,|\,\theta_1,\theta_2) = \mathcal{L}(\mathbf{x}\,|\,\theta_1,\theta_2,\hat{\hat{\theta}}_3 ... \hat{\hat{\theta}}_n) \ , \tag{4.27}$$

---

[5] The median sensitivity is $Z > 15 \ \ \forall \ \kappa_{1,2} \in [-5,5]$ and hence not much is gained from inspection of this result.

Benchmark	m_1	m_2	κ_1	κ_2	r_ρ	r_σ	σ_{H_1}	σ_{H_2}	Targets
SI	15	200	2	2.5	0.7	1.1	220	230	Xe, Ge, Xe+Ge
SD	7	150	2.5	1.5	0.9	0.9	220	230	Xe, F, Xe+F

Table 4.2 Parameter benchmarks used to generate the Asimov data in Eq. (5.30). These benchmarks are chosen taken into account the results of sec. 4.4, i.e., choosing illustrative regions of parameter space that give a large discrimination between the one and two-component hypotheses. DM masses $m_{1,2}$ are measured in GeV.

where the double hat notation denotes the ML estimators of $\theta_3 ... \theta_n$ for the given values of θ_1 and θ_2. Maximising the likelihood in Eq. (4.27) with respect to $\theta_{1,2}$ is equivalent to maximising the profile likelihood ratio (PLR)

$$\lambda(\theta_1, \theta_2) = \frac{\mathcal{L}(\mathbf{x} \,|\, \theta_1, \theta_2, \hat{\hat{\theta}}_3 ... \hat{\hat{\theta}}_n)}{\mathcal{L}(\mathbf{x} \,|\, \hat{\boldsymbol{\theta}})} \equiv \frac{\mathcal{L}(\mathbf{x} \,|\, \theta_1, \theta_2, \hat{\hat{\theta}}_3 ... \hat{\hat{\theta}}_n)}{\mathcal{L}_{\max}} \, . \tag{4.28}$$

In our analysis we will call the point in the θ_1-θ_2 plane that maximises the profile likelihood ratio the 'best-fit' point. In the limit of large statistics, the distribution of $-2 \ln \lambda(\theta_1, \theta_2)$ will tend towards a χ^2 with $k = 2$ degrees of freedom as given by Wilk's theorem. As a result, this leads to a critical region that is defined by a cut on λ that we will choose to represent contours of the standard 2σ (95.45%) frequentist confidence level (C.L).

4.5.2 Results

The likelihood function we use for our analysis is a Gaussian as defined in Eq. (4.19) but we now require that the likelihood is a function of all eight model parameters shown in tab. 5.1:

$$\mathcal{L}(\mathbf{x} \,|\, \boldsymbol{\theta}) = \prod_i^N \frac{1}{\sqrt{2\pi}\sigma_i} e^{-\frac{[x_i - \mu_i(\boldsymbol{\theta})]^2}{2\sigma_i^2}} \qquad \boldsymbol{\theta} = [m_1, m_2, \kappa_1, \kappa_2, r_\rho, r_\sigma, \sigma_{H1}, \sigma_{H2}] \, , \tag{4.29}$$

where again, x_i, σ_i and $\mu_i(\boldsymbol{\theta})$ are the data, error and predicted number of counts in the ith energy bin. In a similar way to the approach in sec. 4.4.1, we use the Asimov likelihood in our parameter estimation in order to obtain a measure of the median experiments ability to determine the model parameters. The likelihood that enters the profile likelihood ratio is then

$$\mathcal{L}(\mathbf{x} = \mu(\boldsymbol{\theta}^{\text{true}}) \,|\, \boldsymbol{\theta}) = \prod_i^N \frac{1}{\sqrt{2\pi \mu_i(\boldsymbol{\theta}^{\text{true}})}} e^{-\frac{\left[\mu_i(\boldsymbol{\theta}^{\text{true}}) - \mu_i(\boldsymbol{\theta})\right]^2}{2\mu_i(\boldsymbol{\theta}^{\text{true}})}} \, . \tag{4.30}$$

Parameter	Range	Type
$m_{1,2}$ (GeV)	$[10, 1000]$	Flat
σ_{H_1,H_2} (km/s)	$[20, 400]$	Flat
σ_p (cm^2)	$[10^{-48}, 10^{-38}]$	Log
r_ρ	$[10^{-2}, 10^{2}]$	Log
$\kappa_{1,2}$	[-5,5]	Flat

Table 4.3 Ranges for the parameter estimation.

As for generating the Asimov data $\boldsymbol{\theta}^{\text{true}}$, we use a few benchmark scenarios as given in tab. 5.1 that contain parameter values that ensure a good discrimination between the one and two-component hypotheses, as deduced from the results of sec. 4.4. We provide benchmarks for SI and SD, that generate data for both one signal and two signals in detectors with different nuclei. We exclude sodium since the results from sec. 4.4 show that no significant discrimination between $H_{1\text{DM}}$ and $H_{2\text{DM}}$ is possible. Another thing to note is that we don't assume that the DM particles have equal couplings to protons and neutrons, i.e., $\kappa_1 \neq \kappa_2 \neq 1$, or equivalently $A_{\text{eff},1} \neq A_{\text{eff},2}$. For the case of just one experimental signal from one detector, this could be absorbed into σ_1^p and r_σ. That is, from one signal one cannot extract information about couplings to neutrons and protons, while one can do this using two signals (also using information on the coupling to protons from neutrinos from the sun, see Refs. [134, 176–179]). However, in the case of two experimental signals in two different types of nuclei (we use Ge and Xe for SI, and Xe and F for SD) information about the interactions with protons and neutrons can in principal be obtained. Our chosen ranges for the scan are shown in table 4.3.

In Figs. 4.13 and 4.14 we show parameter estimates using the PLR method for the combination of two signals Xe+Ge (SI) and Xe+F (SD) respectively. Visualisation is done with the `Pippi` plotting package [180]. We show the 2σ C.L contours (solid line), as well as the best-fit point and normalised profile likelihood density $\mathcal{L}/\mathcal{L}_{\text{max}}$ on the colour scale. For comparison, we show the best-fit points and 2σ C.L contours (dashed/dotted lines) for the one-signal cases (Xe/Ge for SI and Xe/F for SD) in order to display any improvement in parameter realisation. We show results in the same planes that were used for the previous section, as well as parameter combinations that showed an interesting degree of uncertainty/degeneracy. We notice in general that the PLR distribution of the SD results are in general more non-localised and uniform, as opposed to the SI cases where definitive regions of high PLR display a good degree of resolution for certain parameters. We also notice that the combined signal in the SD case generally produces regions that are more extended than the F-only case. This may initially seem counter-intuitive. The reason is that we have an eight-parameter scan with a likelihood which is highly multi-modal and non-trivial. As a result, one should not expect parameter estimates from the combined and one signal cases to give the same best-fit point, but rather significantly different regions of PLR. In fact, in general, we will see that for SD interactions the xenon form factor makes the parameter estimation much harder in the combined case than in the case of just a signal in fluorine, where the form factor suppression is absent. This makes the combined signal somewhat worse than the individual one.

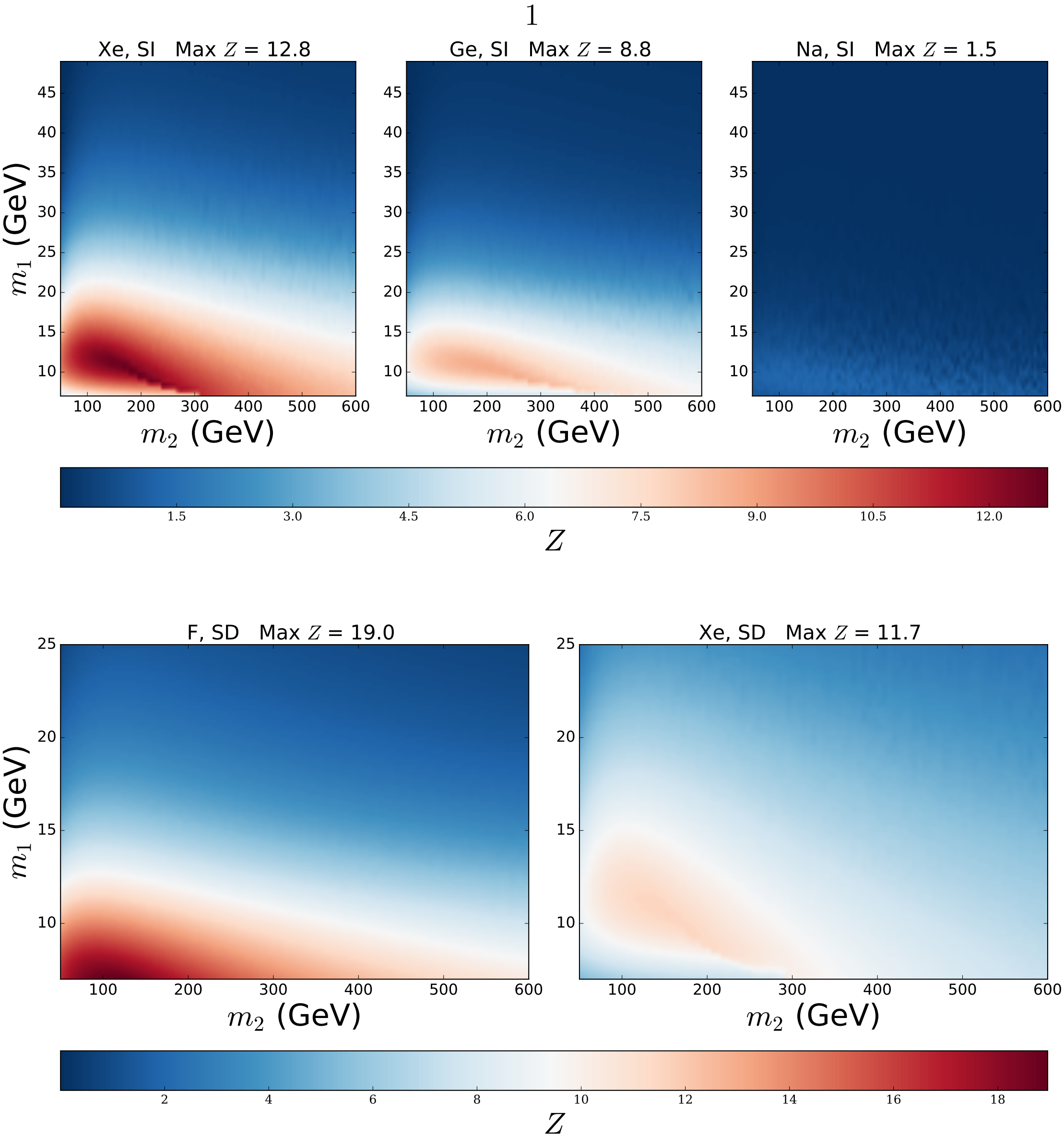

Fig. 4.7 Significance Z with which the median experiment can reject the one-DM hypothesis in favour of the two-DM hypothesis in the $m_2 - m_1$ plane for different target nuclei. All other model parameters are fixed when generating the Asimov data: $r_\rho = r_\sigma = 1$, $\kappa_{1,2} = 1$ and $\sigma_{H_{1,2}} = 270$ km/s. We do not plot the symmetric region around the axis $m_1 = m_2$ for clarity. The top panel is for SI interactions for Xe, Ge and Na, while the bottom panel is for SD interactions for F and Xe.

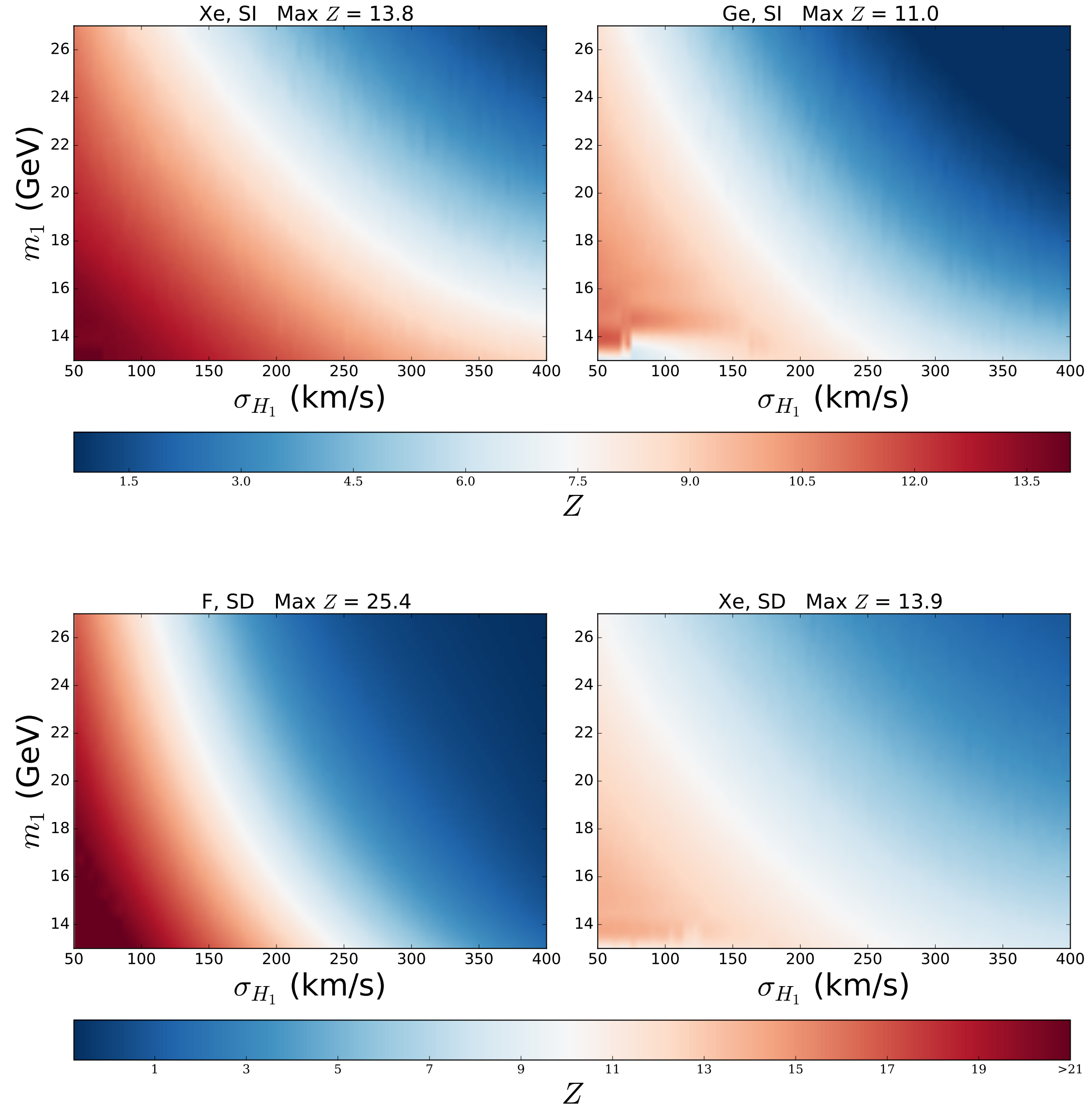

Fig. 4.8 Significance Z with which the median experiment can reject the one-DM hypothesis in favour of the two-DM hypothesis in the σ_{H_1}–m_1 plane. The fixed parameters are $m_2 = 150\,(200)$ GeV for SD (SI), $r_\rho = r_\sigma = 1$, $\kappa_{1,2} = 1$ and $\sigma_{H_2} = 270$ km/s. The top panel shows SI targets: Xe, Ge and the bottom is for SD targets: F and Xe.

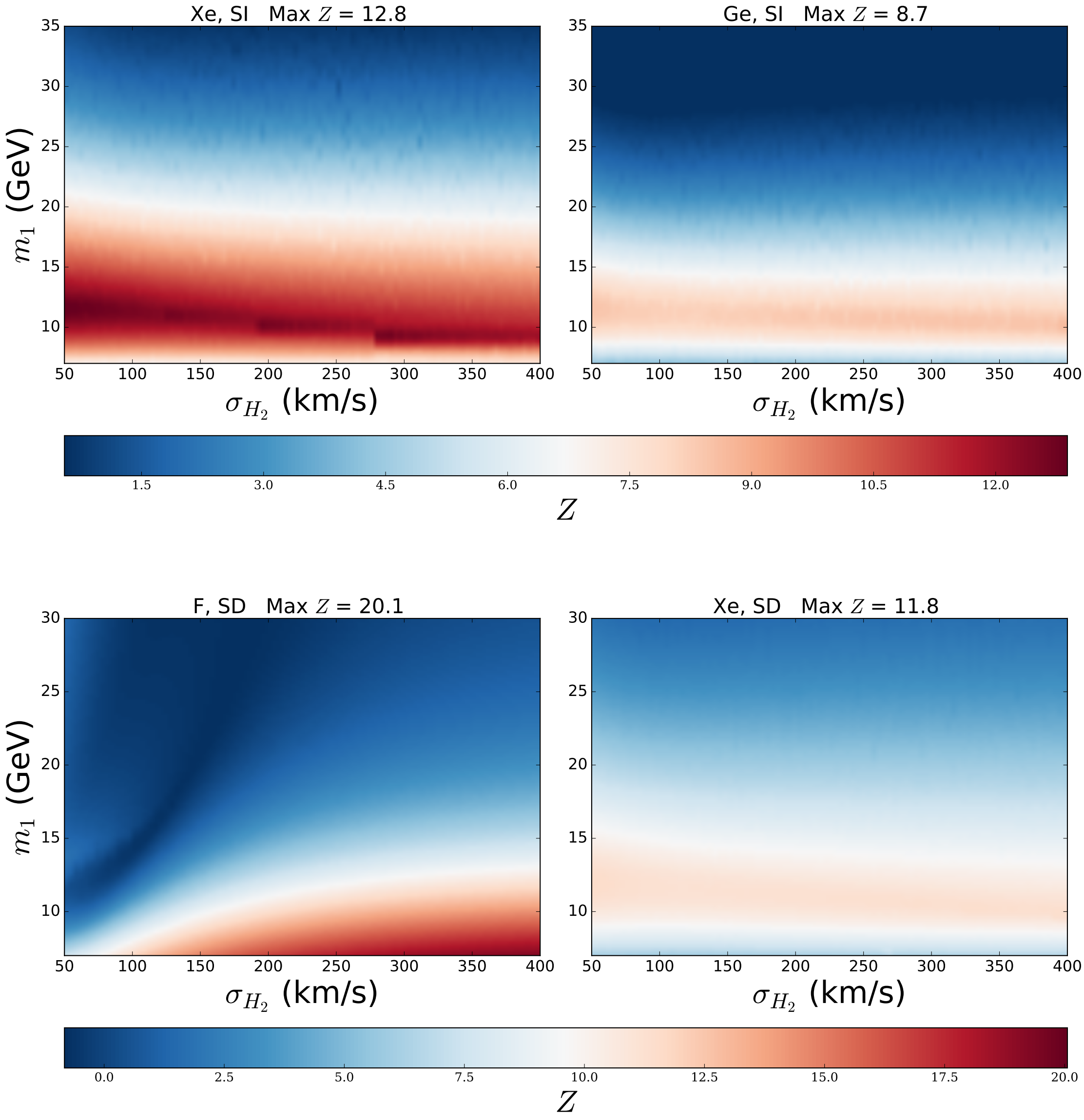

Fig. 4.9 The same as Fig. 4.8 but in the σ_{H_2}–m_1 plane, where at each point σ_{H_1} is fixed to 270 km/s.

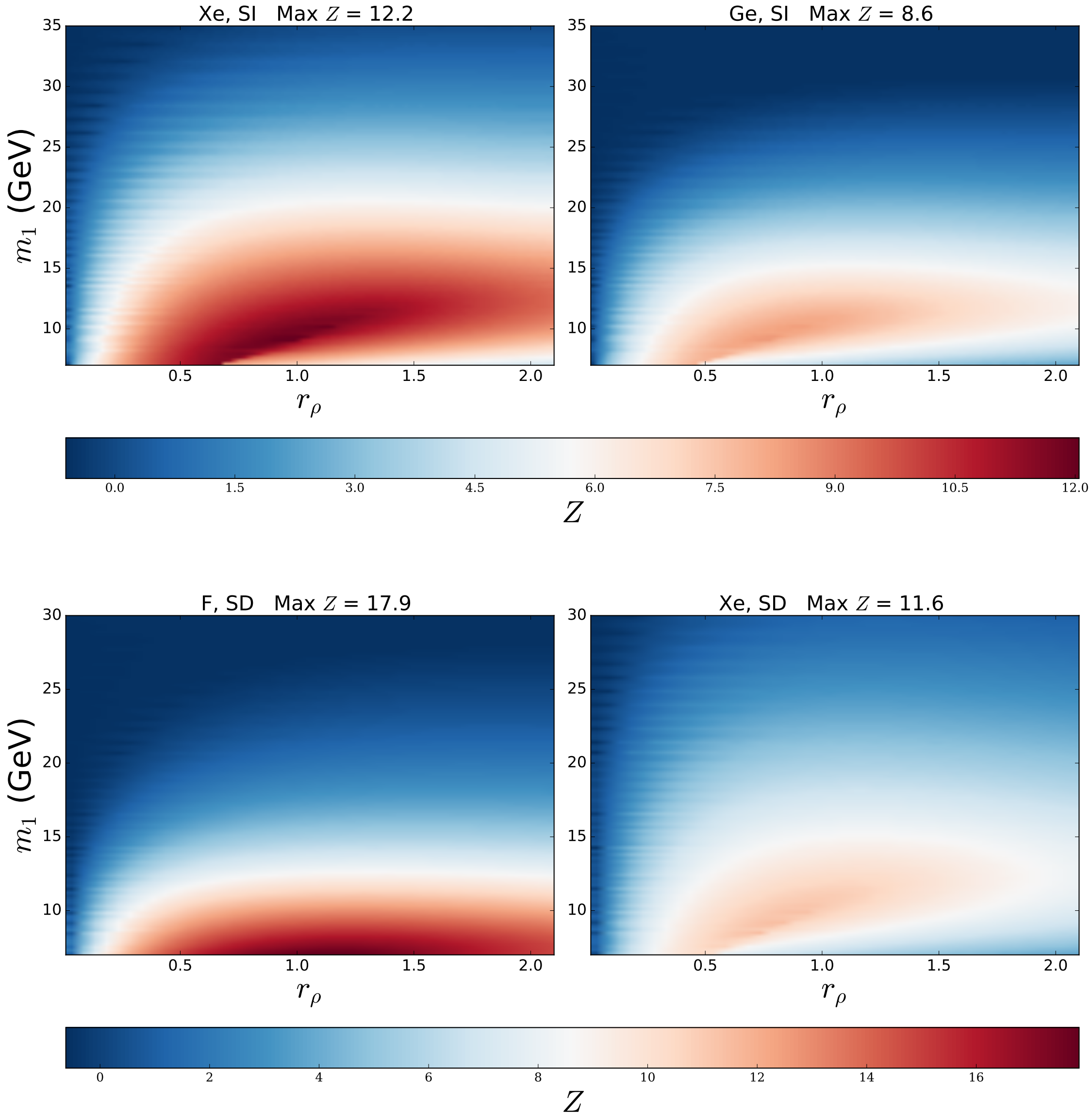

Fig. 4.10 Significance Z with which the median experiment can reject the one-DM hypothesis in favour of the two-DM hypothesis in the r_ρ–m_1 plane. The fixed parameters are $m_2 = 150\,(200)$ GeV for SD (SI), $\kappa_{1,\,2} = 1$ and $\sigma_{H_{1,\,2}} = 270$ km/s. The top panel shows SI targets: Xe and Ge, while the bottom is for SD targets: F and Xe.

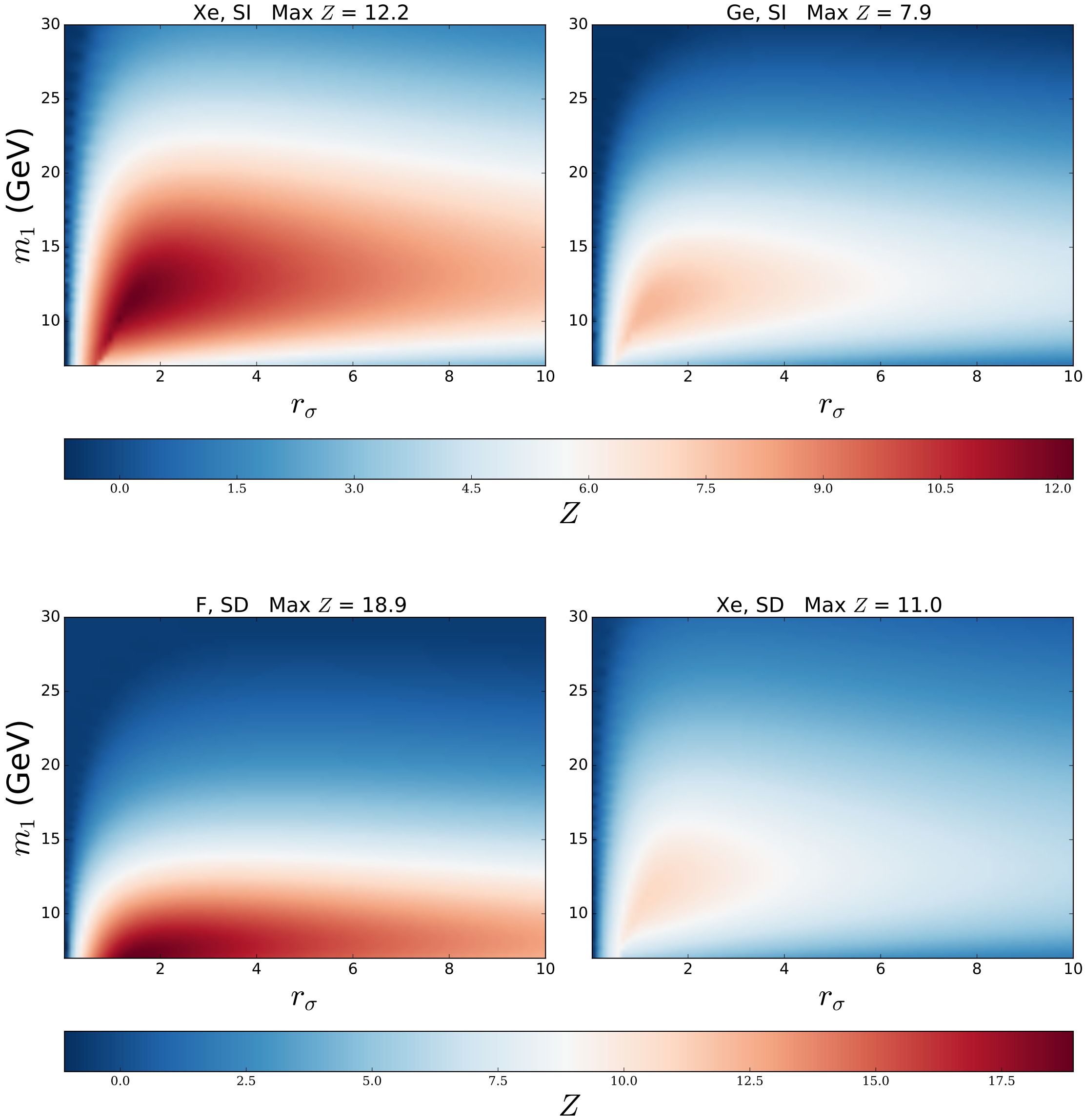

Fig. 4.11 The same as Fig. 4.8 but in the r_σ–m_1 plane.

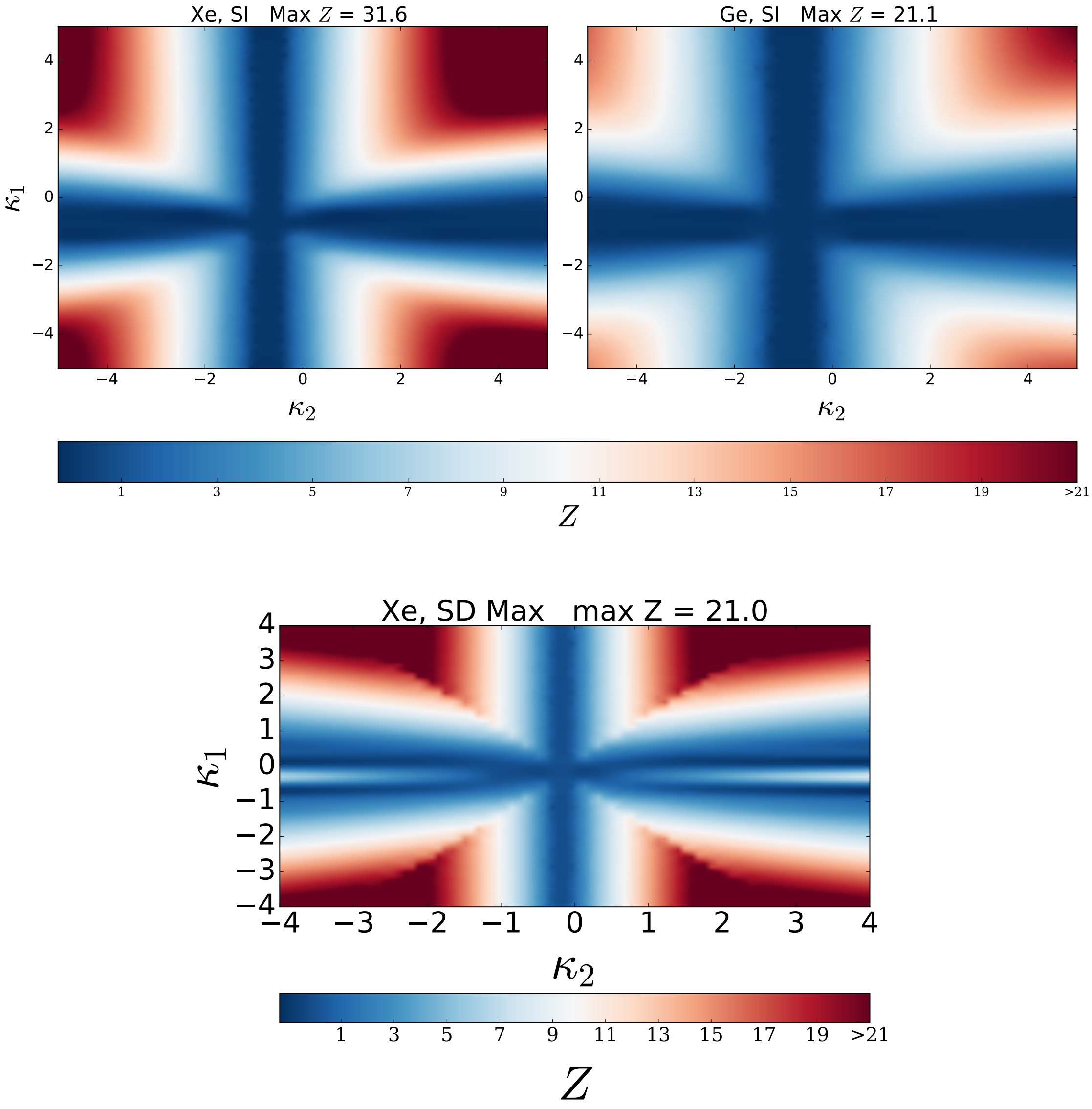

Fig. 4.12 Significance Z with which the median experiment can reject the one-DM hypothesis in favour of the two-DM hypothesis in the κ_2–κ_1 plane. The fixed parameters are $m_2 = 150\,(200)$ GeV for SD (SI), $r_\rho = 1$ and $\sigma_{H_{1,2}} = 270$ km/s. The top panel is for SI targets: Xe and Ge. The bottom is for a SD Xe target. We do not show the results for F since the median significance does not change with varying κ, and hence is not illustrative.

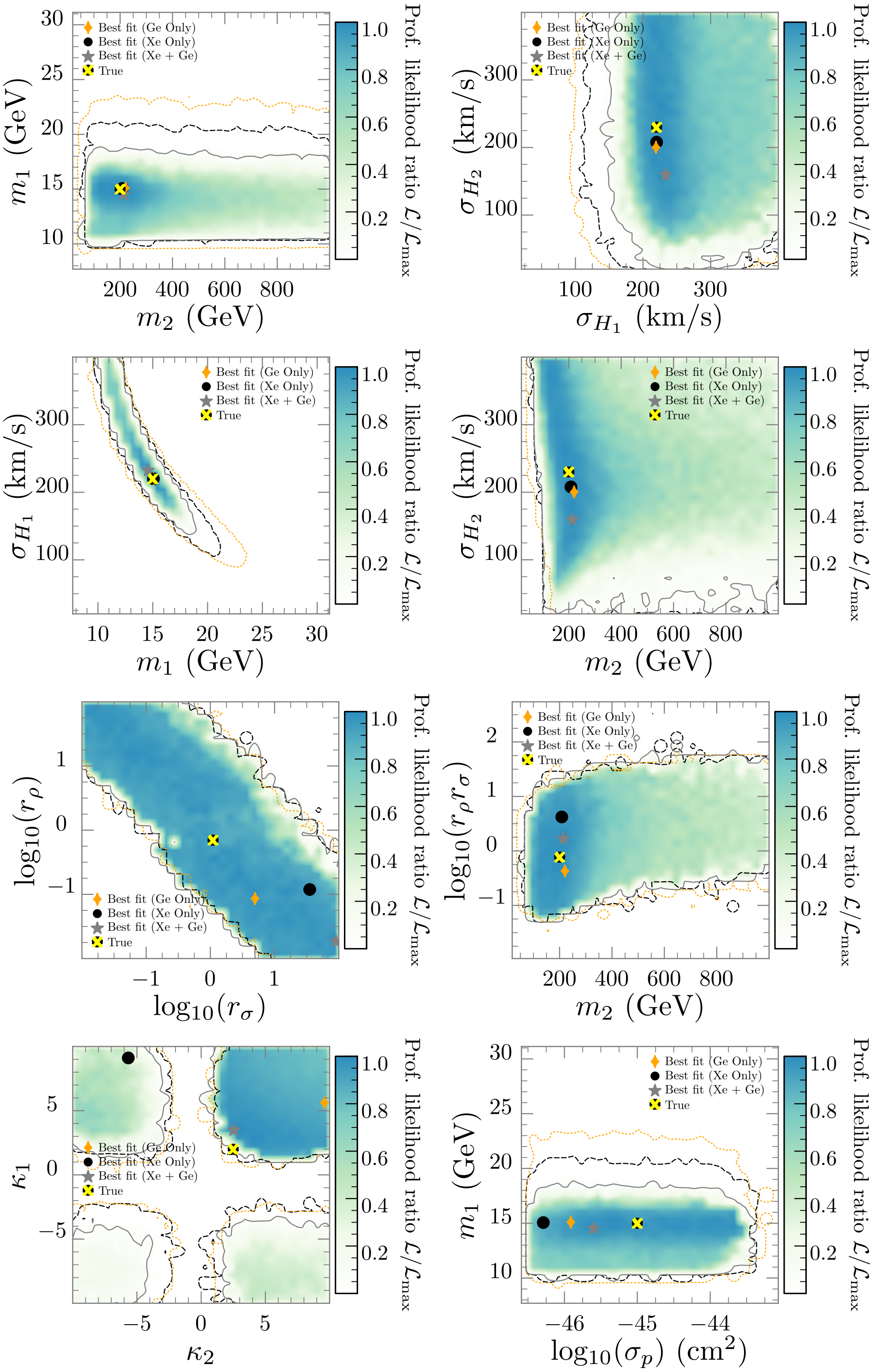

Fig. 4.13 SI results of the parameter estimation for one and two signals in Xe and Ge. The colour scale shows PLR while the solid (grey), dashed (black) and dotted (orange) lines show 2σ C.L contours for the combined Xe+Ge, Xe-only and Ge-only signals respectively. The best-fit PLR point for the Ge/Xe/combined Xe+Ge signal is shown with a diamond/dot/star. The true parameter values (see tab. 5.1) are depicted by the yellow cross.

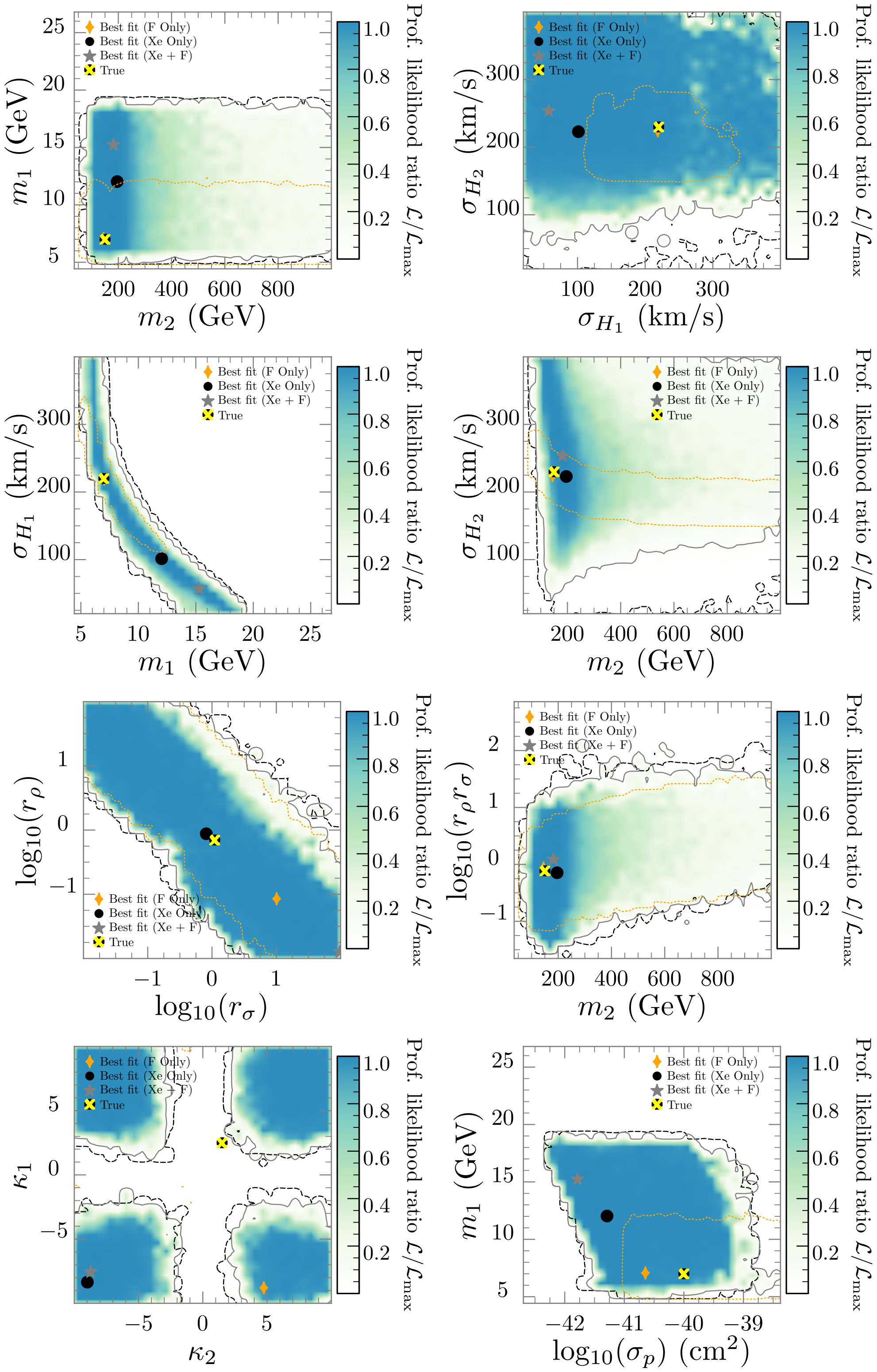

Fig. 4.14 SD results of the parameter estimation from the fit to one signal in Xe/F, and two signals in Xe + F. Figure properties are the same as for Fig. 4.13. The solid (grey), dashed (black) and dotted (orange) lines show 2σ C.L contours for the combined Xe+F signal, Xe-only signal and F-only signal respectively.

Looking first at the top-left panel of Fig. 4.13, one can see excellent realisation of the two DM masses with the best-fit PLR, however the uncertainty in m_2 extends over a large region of the m_2 parameter space (although it is peaked around the true value). This is because for large m_2, v_{min} and therefore $\eta(E_R)$ become independent of m_2. Therefore the same signal can be fitted with increasing $r_\rho r_\sigma \propto m_2$ as can be seen from Eq. 7.1. In the SD case in Fig. 4.14, the uncertainty in m_1 is increased and the true point is covered by an extended region of high PLR, however the best-fit point for the combined case does not resolve m_1 and m_2 accurately. The best-fit point for a signal with only fluorine however does resolve the benchmark point. There is no distinct difference between the Xe+Ge and Xe/Ge-only cases for SI other than a slight improvement in the m_1 precision, however the F-only region shows less uncertainty in m_1 for the SD case. Notice that the light m_1 chosen for SD (equal to 7 GeV) implies that lighter nuclei (like F) are much more sensitive to it.

The top-right panels of Figs. 4.13 and 4.14 show the SI/SD results in the plane of σ_{H_1}–σ_{H_2}. We notice that in the SI case we are less sensitive to σ_{H_2}, whilst the best-fit PLR is able to resolve the true σ_{H_1}. This is because for the heavier particle an experiment is able to probe the entire velocity distribution, whereas for the lighter particle we are more sensitive to fact that we need velocities to provide recoil energies above threshold. This is not the case for the SD result however, which shows that whilst the true point lies well within 2σ contour, the uncertainty has increased in both σ_{H_1} and σ_{H_2}. Interestingly, the F-only 2σ contour is much more resolved than the combined Xe+F result, with the best-fit PLR lying on top of the benchmark point.

Next we show results in the m_1–σ_{H_1} plane. For the SI case, we see that the extended degeneracy decreases in length from the Xe/Ge-only to the combined signal case. Moreover, the true point is well estimated by all best-fit points. For the SD case, the benchmark point is only resolved by the best-fit PLR for the F-only case. The degenerate region for the combined signal and Xe-only is significantly more extended than the SI case. Of all results shown in Fig. 4.14, the SD case seems to have the most dramatic increase in the 2σ region going from the F-only signal case to the combined signal and Xe-only case.

Next, we consider the m_2–σ_{H_2} plane where we can see the true point lies well within 2σ for the combined signals in the SI and SD case, and is well resolved by the best-fit PLR. The PLR density in both the SI and SD cases is high for the true m_2, however it is not localised in the σ_{H_2} direction. The F-only signal in the SD case interestingly still covers the true point, and has a larger degree of precision in σ_{H_2}.

The next figure shows an extended degeneracy in the $\log_{10}(r_\sigma)$–$\log_{10}(r_\rho)$ plane for both SI and SD cases, i..e, we have that $r_\rho \propto 1/r_\sigma$. Notice that we do not observe an exactly symmetric plot in r_ρ and r_σ since r_ρ also enters the rate in the pre-factor $\propto 1/(1 + r_\rho)$. The best-fit points for the combined and one signal cases are not able to resolve true values for both the SI and SD scenarios, except for the Xe-only SD case. Given such a large degeneracy of high PLR density however, one can safely ignore the significance of the best fit points on this plot. The true point does however fall within the 2σ C.L region for all combined and single signal cases. The results of this figure show that in general, the median experiment will have trouble resolving the individual $r_{\rho,\sigma}$.

We next show the result for the combination $\log_{10}(r_\rho r_\sigma)$ vs. m_2 in order to explicitly explore the degeneracy that was previously mentioned. In both the SI and SD results we observe similar extended 2σ regions for the combined signal, as well as very good accuracy for the best-fit PLR in the product $r_\rho r_\sigma$, much better than for the individual $r_{\rho,\sigma}$ (c.f. previous figure and discussion). In both cases, the PLR density is peaked (> 0.9) at roughly the correct m_2.

The next panel in each figure shows a fourfold degeneracy in the κ_2–κ_1 plane. This is because, as we saw in hypothesis testing section, we are insensitive to the sign of κ for large values, as then $A^2_{\text{eff}} \propto |\kappa|^2$. In the SI case, the degeneracy is resolved by the best-fit PLR for the combined signal (also the PLR density is peaked in the correct quadrant) as well as the Ge-only signal. The Xe and Ge-only cases produce 2σ contours that are all equally large indicating equal preference for all degenerate regions. This is not the case for the combined signal, where the PLR density favours the correct quadrant. In the SD case, the F-only signal has no sensitivity, and thus its contour covers the whole region ($\kappa_{1,2} \in [-10, 10]$). In addition the fourfold degeneracy is not broken by either Xe-only or combined signal best-fit PLR. Furthermore, each quadrant of the degeneracy contains an equally high ($\gtrsim 0.9$) PLR. Therefore we can conclude that the couplings to neutrons and protons are difficult to resolve in the case of SD interactions.

Lastly, we show results in the $\log(\sigma_p^1)$–m_1 plane. The combined signal for the SI case contains the true point in a region of high PLR and well within the 2σ contour. The combined signal also offers a slightly more constrained region than the Xe-only and Ge-only cases. This is not true in the SD case, where the combined signal produces a large region of high PLR density, and the F-only case provides a best-fit that is closer to the benchmark, as well as a more tightly constrained region.

4.6 Conclusions

We have studied the implications of multi-component DM in DD signals. On general grounds, in the case of similar energy densities, we have argued that it is not possible to know which type of particle dominates the direct detection rate, the heavier or the lighter. For the cases in which one expects similar number densities, and assuming that the interactions of the dark sector are roughly the same, the total rate is suppressed by the heaviest DM particle, which also dominates the (suppressed) rate. Therefore, if this is the case, there is an upper bound on the heaviest DM expected to be able to be detected, and we have estimated it for several nuclei. For this case, indirect detection rates are also suppressed by the heaviest DM particles. In the case of similar masses, the approximations of equal number/energy densities are of course equivalent.

Focusing on two-component DM, we showed that the discerning feature of the two component scenario is a *kink* in the (somewhat low energy) recoil spectrum. Such a feature cannot be present in the one-component scenario, and can thus be used to discriminate between the one/two component hypotheses. We then simulated the sensitivity of an 'average' experiment to the one or two-component hypothesis. We adopted several experimental configurations (energy threshold, exposure) for a variety of different nuclear targets to roughly simulate the next generation of direct detection experiments for both SI and SD interactions. Our first results assumed equal cross-sections, energy densities, couplings to neutrons and protons and velocity dispersions. We showed that the mass splitting between the two WIMP components provides the best means for the median experiment to reject the one-component hypothesis in favour of the two-component hypothesis, and there are both lower and upper bounds on it for discrimination to be possible. In general, that the heaviest DM mass should be smaller than a hundred times the lightest one. The mass configurations that maximise the median significance are roughly $m_1 = 15$, $m_2 = 200$ (SI) and $m_1 = 7$, $m_2 = 150$ (SD). After fixing the mass of the heavier WIMP at $m_2 = 200\,(150)$ GeV for SI (SD), we then incrementally included more parameters into the hypotheses parameter space, starting with the velocity dispersion of the WIMPS $\sigma_{H_{1,2}}$ then moving onto the ratios of the local energy density and WIMP-proton cross-section r_ρ/r_σ. In general, small variations in these parameters around ~ 1 do not affect significantly the results. We finished by scanning over the WIMP-neutron/proton coupling ratios $\kappa_{1,2}$. In each of these three generalised scenarios we observed that the median significance can increase in localised regions of the parameter space.

For the regions of parameter space in which there is especially strong hypothesis discrimination, we have estimated the precision and accuracy with which the model parameters can be extracted. We conducted parameter estimates for both SI and SD scenarios, and we considered the case of a combined signal from two experiments and compared the results to the one signal case. We observed that parameter estimation is worsened for SD scenarios, where regions of high PLR density were less localised than in the SI case. The parameters that show the greatest degree of uncertainty are the mass of the heavier WIMP and the individual ratios of energy densities and cross-sections ($r_{\rho,\sigma}$), as well as the velocity dispersion of the heavier WIMP, σ_{H_2}. However, the product $r_\rho \, r_\sigma$ was much better resolved. We observed degeneracies in the parameter space of r_ρ-r_σ as well as κ_1-κ_2. In the SI case, the κ_1-κ_2 degeneracies were broken by the combined-signal best-fit PLR. No degeneracies in any parameter space were observed to be broken in the SD case by going from single to dual experimental signals.

We would also like to emphasize that our analysis assumes a simplified idealised scenario, with known background and perfect energy resolution and efficiency. Hence, more sophisticated experimental simulations are needed once a signal is observed. We note that the median sensitivity scales with $\sim \sqrt{\text{exposure}}$ (before systematics dominate) and hence our results serve as a guide for more detailed studies of future experimental designs.

Although we focused on elastic SI and SD interactions, further studies can be performed with more complicated DM interactions, like inelastic endothermic/exothermic DM [135, 136, 181–184], or with interactions with nuclei mediated by different operators, which can have non-standard velocity/momentum dependencies [185–192]. An interesting avenue to pursue would be to study to what extent non-trivial interactions can be degenerate with multi-component DM, i.e., can show a *kink*-like feature.

To finish we would like to mention that multi-component DM could give rise to specific signals also in indirect detection and at colliders. The smoking gun signal would seem to observe two gamma ray lines at different DM masses. However this could also be produced by a single DM annihilating into a boson (Z or Higgs) and a photon [130], and therefore other information is necessary to break such degeneracy. However, even the continuum gamma ray spectrum could in principle show features pointing to multi-component DM, like the presence of a *kink*, in a similar way as in DD. For similar densities and interactions, depending on whether the DM particles decay or annihilate, the heaviest or the lightest DM particle would give the strongest signal, as the dependence of the decay width with the mass is very strong ($\propto m^5$ for decaying DM with four-fermion interactions, for example). Therefore the preferred energy ranges and strategies to search for indirect DM signals are model-dependent.

Regarding collider searches, if the masses of the particles in the dark sector are $\lesssim \mathcal{O}(1)$ TeV, they could be produced at the LHC. In this case, disentangling whether there is one type of DM produced or more is not an easy task [137], as different DM masses or operators (models) could generate similar missing energy distributions.

Optimistically, one can imagine a situation in which DM is first observed being multi-component in direct detection, the underlying interaction is extracted (say SD), and that is used to predict halo-independently a signal at colliders [139, 164] and from annihilation into neutrinos in the Sun [134, 177].

Acknowledgements: JH-G would like to thank Thomas Schwetz for useful discussions regarding multi-component dark matter. AS would like to thank Ankit Beniwal for useful discussions regarding technical aspects. The work of JH-G, AS and AGW is supported by the Australian Research Council through the Centre of Excellence for Particle Physics at the Terascale CE110001004. MW is supported by the Australian Research Council Future Fellowship FT140100244.

4.7 Distribution of the $\mathcal{T}$ statistic when $H_{2\mathrm{DM}}$ is true

In sec. 4.4.1 we claim that one can easily show that for Gaussian distributed data, the $\mathcal{T}$ statistic under $H_{2\mathrm{DM}}$ is Gaussian with mean given by $\mathcal{T}_0^{2\mathrm{DM}}$ as defined in Eq. (5.28), and standard deviation given by $2\sqrt{\mathcal{T}_0^{2\mathrm{DM}}}$. In this appendix we show why this is true, following the method of Ref. [167]. We start by writing the data x_i as a Gaussian distributed variable

$$x_i = \mu_i(\theta_{H_{2\mathrm{DM}}}^{\mathrm{true}}) + g\sigma_i \, , \tag{4.31}$$

where $\mu_i(\theta_{H_{2\mathrm{DM}}}^{\mathrm{true}})$ is the true data under the two-DM hypothesis $H_{2\mathrm{DM}}$, $\sigma_i = \sqrt{\mu_i(\theta_{H_{2\mathrm{DM}}}^{\mathrm{true}})}$ and g is a unit Gaussian variable. Then, from the definition of $\mathcal{T}$ from Eq. (5.25), one finds that

$$
\begin{aligned}
\mathcal{T}^{\rm 2DM} &= \min_{\theta_{H_{\rm 1DM}}} \chi^2(\theta_{H_{\rm 1DM}}) - \min_{\theta_{H_{\rm 2DM}}} \chi^2(\theta_{H_{\rm 2DM}}) && (4.32)\\
&= \sum_i^N \left(\min_{\theta_{H_{\rm 1DM}}} \frac{[x_i - \mu_i(\theta_{H_{\rm 1DM}})]^2}{\sigma_i^2} - \min_{\theta_{H_{\rm 2DM}}} \frac{[x_i - \mu_i(\theta_{H_{\rm 2DM}})]^2}{\sigma_i^2} \right) && (4.33)\\
&= \sum_i^N \left(\min_{\theta_{H_{\rm 1DM}}} \frac{\left[\mu_i(\theta^{\rm true}_{H_{\rm 2DM}}) + g\sigma_i - \mu_i(\theta_{H_{\rm 1DM}})\right]^2}{\sigma_i^2} - \min_{\theta_{H_{\rm 2DM}}} \frac{\left[\mu_i(\theta^{\rm true}_{H_{\rm 2DM}}) + g\sigma_i - \mu_i(\theta_{H_{\rm 2DM}})\right]^2}{\sigma_i^2} \right) && (4.34)\\
&= \min_{\theta_{H_{\rm 1DM}}} \sum_i^N \frac{\left[\mu_i(\theta^{\rm true}_{H_{\rm 2DM}}) - \mu_i(\theta_{H_{\rm 1DM}})\right]^2}{\sigma_i^2} + \frac{2\left[\mu_i(\theta^{\rm true}_{H_{\rm 2DM}}) - \mu_i(\theta_{H_{\rm 1DM}})\right]}{\sigma_i} g \, . && (4.35)
\end{aligned}
$$

The last line here explicitly shows that $\mathcal{T}^{\rm 2DM}$ is a Gaussian random variable with mean given by the first term

$$\min_{\theta_{H_{\rm 1DM}}} \sum_i^N \frac{\left[\mu_i(\theta^{\rm true}_{H_{\rm 2DM}}) - \mu_i(\theta_{H_{\rm 1DM}})\right]^2}{\sigma_i^2} \equiv \mathcal{T}_0^{\rm 2DM} \, , \qquad (4.36)$$

and standard deviation given by the second term

$$\min_{\theta_{H_{\rm 1DM}}} \sum_i^N \frac{2\left[\mu_i(\theta^{\rm true}_{H_{\rm 2DM}}) - \mu_i(\theta_{H_{\rm 1DM}})\right]}{\sigma_i} g = 2\sqrt{\mathcal{T}_0^{\rm 2DM}} \, . \qquad (4.37)$$

4.8 Bayesian parameter estimation

In this appendix we conduct the same parameter estimation study as in sec. 4.5 but in a Bayesian framework. We first give an overview of the methods used followed by the results.

Bayes' theorem

$$P(\boldsymbol{\theta}\,|\mathbf{x}) = \frac{\mathcal{L}(\mathbf{x}|\boldsymbol{\theta}) \cdot \pi(\boldsymbol{\theta})}{\int d\boldsymbol{\theta}\, \mathcal{L}(\mathbf{x}|\boldsymbol{\theta}) \cdot \pi(\boldsymbol{\theta})} \, , \qquad (4.38)$$

allows one to explicitly solve for the probability of a given set model parameters $\boldsymbol{\theta}$ having observed some data $\mathbf{x}$. This probability function $P(\boldsymbol{\theta}\,|\mathbf{x})$ is called the 'posterior' probability, and is a function of the likelihood $\mathcal{L}(\mathbf{x}|\boldsymbol{\theta})$ that the data is observed given the model parameters as well as the 'prior probability' function $\pi(\boldsymbol{\theta})$, which parameterises one's prior degree of belief in $\boldsymbol{\theta}$ as well as sets the allowed size of the parameter space. The integral in the denominator of Bayes' theorem is called the 'Bayesian evidence' and ensures that the posterior is normalized to 1 with respect to the model parameters. In order to constrain a slice of the full parameter space, one can integrate over unwanted nuisance parameters to give the ‘marginalised posterior’

$$P(\theta_1, \theta_2 \,|\mathbf{x}) = \int d\theta_3 ... d\theta_n \, P(\boldsymbol{\theta} \,|\mathbf{x}) \; . \tag{4.39}$$

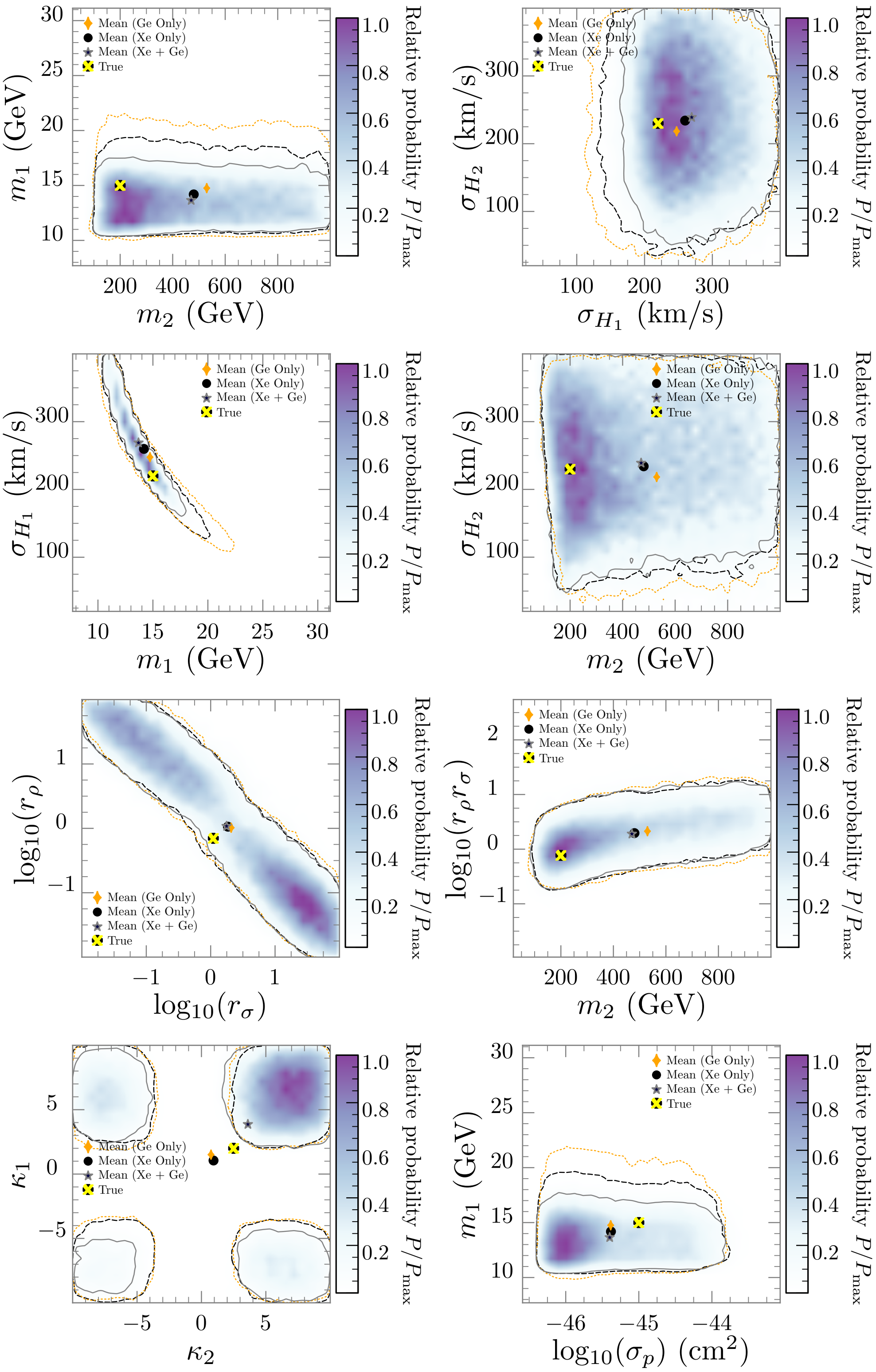

Fig. 4.15 Normalised posterior probability from the fit to one and two SI signals in Xe and Ge. Shown are the 2D regions of parameter space as given in Fig. 4.13.

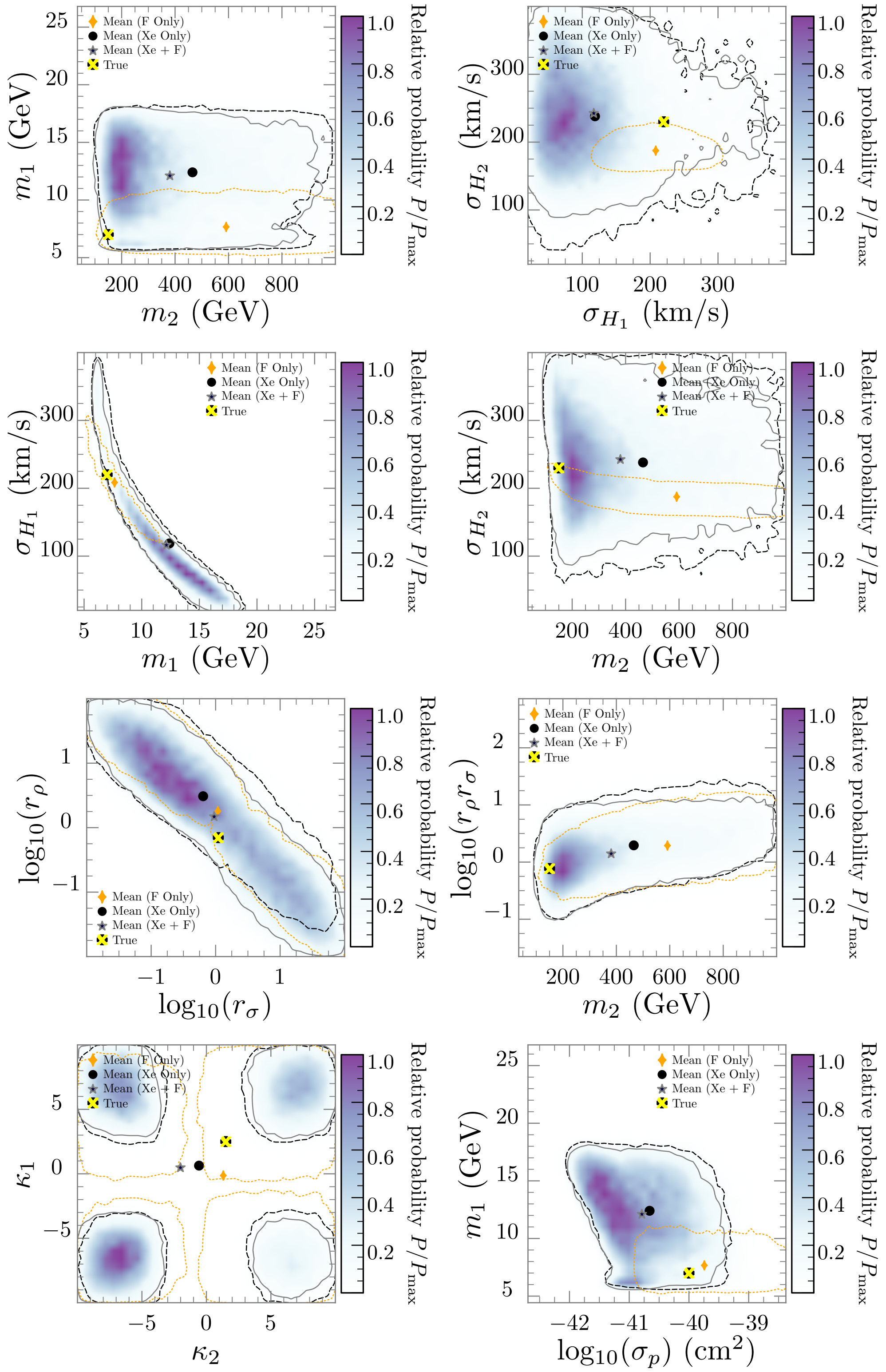

Fig. 4.16 Normalised posterior probability from the fit to one and two SD signals in Xe and F. Shown are the 2D regions of parameter space as given in Fig. 4.14.

The example given in Eq. (4.39) would be an example of a 2D posterior. A Bayesian 'credible region' (CR) is the interval on the parameter θ_1 such that

$$1 - \alpha = \int d\theta_1 \, P(\theta_1, \theta_2 \,|\mathbf{x}) \; , \tag{4.40}$$

where we choose $1 - \alpha = 0.9545$ to define a 2σ CR.

Our results are shown in figs. 4.15 and 4.16, where the likelihood that enters Bayes' theorem is the Asimov likelihood defined in Eq. 5.30. We chose a combination of flat and log-flat priors so as to not give any preference to any region of parameter space. Our chosen priors are shown in table 4.3 and the results are not expected to change significantly under translation of the prior intervals. The results shown are of the normalised posterior probability $P/P_{\rm max}$ with 2σ CR (solid line) for data obtained from the combined signal Xe + F as well as for comparison the 2σ CR (dashed line) for the F-only signal.

The posteriors shown in figs. 4.14 and 4.16 for the most part spatially resemble the PLR results shown in sec. 4.5 (keeping in mind that strictly speaking one can not qualitatively compare the two), however, there are some distinct differences. In general, for both SI and SD results, the posterior probability seems to be able to resolve degeneracies quite well, contrary to the PLR for the SD case. The Bayesian method also seems to resolve certain parameters with less uncertainty, although we caution that the definition of the uncertainty is different in this case. The most notable differences are present in the $\log_{10}(r_\sigma)$–$\log_{10}(r_\rho)$ and κ_2–κ_1 planes. In this first case, the extended degenerate region $r_\rho r_\sigma = \text{cte}$ is distinctly separated into two regions of high posterior probability. The true point still does not fall within the 2σ CR however. In the κ_1-κ_2 plane, we observe that in the SI case, the four-fold degeneracy has regions that do not contain the true point, but are smaller than the regions of high PLR. The posterior does however favour the correct quadrant. In the SD case, the benchmark point is contained by the 2σ CR for the F-only signal, however the combined signal produces smaller regions with the incorrect quadrant favoured by the posterior density.

Statement of Authorship

Title of Paper	On the direct detection of multi-component dark matter: implications of the relic abundance
Publication Status	
Publication Details	J. Herrero-Garcia, A. Scaffidi, M. White, and A. G. Williams. On the direct detection of multi-component dark matter: implications of the relic abundance. JCAP, 1901(01):008, 2019.

Principal Author

Name of Principal Author (Candidate)	Andre Scaffidi		
Contribution to the Paper	Writing of manuscript Numerical results Theoretical results		
Overall percentage (%)	75%		
Certification:	This paper reports on original research I conducted during the period of my Higher Degree by Research candidature and is not subject to any obligations or contractual agreements with a third party that would constrain its inclusion in this thesis. I am the primary author of this paper.		
Signature		Date	

Co-Author Contributions

By signing the Statement of Authorship, each author certifies that:

i. the candidate's stated contribution to the publication is accurate (as detailed above);

ii. permission is granted for the candidate in include the publication in the thesis; and

iii. the sum of all co-author contributions is equal to 100% less the candidate's stated contribution.

Name of Co-Author	Juan Herrero-Garcia		
Contribution to the Paper	Writing of manuscript Numerical results Theoretical results		
Signature		Date	17/02/2020

Name of Co-Author	Anthony G. Williams
Contribution to the Paper	Writing of manuscript Theoretical results

Signature		Date	31/01/2020

Name of Co-Author	Martin White		
Contribution to the Paper	Writing of manuscript Theoretical results		
Signature		Date	21/1/20

Chapter 5

Publication two: On the direct detection of multi-component dark matter: implications of the relic abundance

Abstract

Recently we studied the direct detection of multi-component dark matter with arbitrary local energy densities. Although the generation of the dark matter relic abundance is model-dependent, and in principle could be only indirectly related to direct detection, it is interesting to consider the implications of the former on the latter. In this work we conduct an extended analysis to include constraints from two natural scenarios of dark matter genesis: asymmetric dark matter and thermal freeze-out. In the first (second) case, the dark matter number (energy) densities of the different components are expected to be similar. In the case of thermal freeze-out, we assume that the global energy density scales with the local one. In our numerical analysis we analyse the median sensitivity of direct detection experiments to discriminate a two-component scenario from a one-component one, and also the precision with which dark matter parameters can be extracted. We analyse these generic scenarios for both light and heavy mediators. We find that most scenarios have a relatively suppressed maximum median sensitivity compared to the previously studied general cases. We also find that the asymmetric scenario is more promising than the thermal freeze-out one.

5.1 Introduction

Some form of non-visible matter, termed dark matter (DM), constitutes a significant fraction of the universe. Several different particle physics scenarios have been proposed as an origin of this DM (see for instance Ref. [2] for a review). Among them, some of the best motivated ones are Weakly-Interacting-Massive-Particles (WIMPs), with their energy density originated from thermal freeze-out, and Asymmetric DM models (ADM) [193], where the abundance stems from an asymmetry in a similar fashion to the case of the observed baryon and lepton energy densities (see also Refs. [140, 194] for reviews on the topic). However, it is by no means guaranteed that just a single state or particle (1DM) constitutes the whole dark sector, which may have a multi-component nature as occurs in the visible sector.

In this work we focus on the direct detection (DD) of DM in underground detectors [9]. We extend our previous study of the DD of two-component (2DM) averaged rates [195], in which we considered arbitrary local energy densities (see also Refs. [127–133, 196], and Ref. [197] for the study of annual modulations), by taking into account the implications that reproducing the DM abundance has on DD. Under a given particle physics model, both the scattering and the annihilation cross section can be obtained, and as is well known, the global DM relic abundance can be obtained from the latter [198]. This approach was taken in Ref. [130], where the authors related the WIMP-nucleon scattering cross-section to the annihilation one, motivated by supersymmetric models. By further assuming that the local energy density relevant for DD is proportional to the global one, one further reduces the allowed parameter space [138, 139] (see also Ref. [199] for the validity of this assumption).

In this work we do not consider specific models, but concentrate on two generic particle physics scenarios: thermal freeze-out and ADM. In the asymmetric scenario the number densities of the two species are expected to be similar, whereas in the thermal case we assume that the local energy densities, which are of similar size for both components, scale as the global ones. For each scenario considered we study both heavy and light mediators. We test how well an average experiment can discriminate between the 1DM and the 2DM hypothesis as well as how accurately and precisely the DM parameters can be obtained from a positive signal.

The paper is structured as follows. In Sec. 5.2 we review the relevant notation for the DD of 2DM. In Sec. 5.3 we study the case of ADM, while in Sec. 5.4 we consider the case of thermal WIMPs. Finally we give our main conclusions in Sec. 7.4. We provide some details of the analysis methods used for hypothesis testing and parameter estimation in App. 5.6. We give some expressions for thermal freeze-out scenarios with light mediators in App. 5.7.

5.2 Direct detection of two-component dark matter

We present in the following the relevant expressions for the DD of 2DM scenarios. See Ref. [195] for more details and expressions for the general case of multiple components.

5.2.1 The *general* scenario

We take the DM components to have masses $m_1 < m_2$, spin-independent (SI) and isospin-conserving cross-sections with protons σ_1^p, σ_2^p, and local energy densities ρ_1, ρ_2, such that $\rho_1 + \rho_2 = \rho_{\rm loc}$, which we fix to be $0.4\,{\rm GeV/cm}^3$. We define

$$r_\rho \equiv \frac{\rho_2}{\rho_1}\,, \qquad r_\sigma \equiv \frac{\sigma_2^p}{\sigma_1^p}\,, \tag{5.1}$$

such that $\rho_2 = r_\rho\,\rho_{\rm loc}/(1+r_\rho)$. We can write the averaged rate over the year, typically measured in events/(kg keV day), for a detector with target nucleus labelled by (A, Z) (with mass m_A), as

$$\begin{aligned} R_A(E_R) &= R_A^{(1)}(E_R) + R_A^{(2)}(E_R) \\ &= \frac{\rho_{\rm loc}\,\sigma_1^p}{2\,(1+r_\rho)\,\mu_{p1}^2\,m_1}\,A^2\,F_A^2(E_R)\left[\eta(v_{m,A}^{(1)}) + r_\rho\,r_\sigma\,\frac{\mu_{p1}^2\,m_1}{\mu_{p2}^2\,m_2}\,\eta(v_{m,A}^{(2)})\right]. \end{aligned} \tag{5.2}$$

Here $F_A(E_R)$ is the SI nuclear form factor of element with mass number A, for which we use the Helm parametrisation [141, 142], and μ_p^2 is the DM-proton reduced mass. In addition to ρ_β ($\beta = 1, 2$ for the two DM particles), the astrophysics enters in Eq. (5.6) through the halo integral

$$\eta(v_{m,A}^{(\beta)}) = \int_{v>v_{m,A}^{(\beta)}} d^3v\,\frac{f_{\rm det}^{(\beta)}(\mathbf{v})}{v}, \qquad \text{with} \qquad v_{m,A}^{(\beta)}(E_R) = \sqrt{\frac{m_A E_R}{2\mu_{\beta A}^2}}\,, \tag{5.3}$$

where $v_{m,A}^{(\beta)}(E_R)$ is the minimum velocity of the DM particle $\beta = 1, 2$ required to produce a nuclear recoil of energy E_R, and $\mu_{\beta A}$ is the DM-nucleus reduced mass. $f_{\rm det}(\mathbf{v}, t)$ describes the distribution of DM particle velocities in the detector rest-frame, which we take to have the same functional form for both species. It can be written in terms of the galactic velocity distributions by doing a Galilean boost, $f_{\rm det}(\mathbf{v}, t) = f_{\rm gal}(\mathbf{v}+\mathbf{v}_e)$, where $\mathbf{v}_e$ is the velocity vector of the Earth in the galactic rest-frame.[1] As we are considering only averaged rates, we use a constant $|\mathbf{v_e}| = 230\,{\rm km\,s^{-1}}$. We use a Maxwellian velocity distribution $f_{\rm gal}(v) = \frac{1}{(2\pi\sigma_{H_\beta}^2)^{3/2}}\exp\left(-\frac{3v^2}{2\sigma_{H_\beta}^2}\right)$, with velocity dispersion σ_{H_β} and a cut-off at the escape velocity $v_{\rm esc} = 550\,{\rm km\,s^{-1}}$. Notice that the velocity dispersions of both components can be different, as we discuss in the following section. We refer to Eq. (5.6) as the *general* scenario.[2]

---

[1] We do not include the effects of the gravitational focusing (GF) by the Sun (see Refs. [147, 148, 200]) since it only affects the phases of the annual modulation and hence has no bearing on the average rates considered in this work. We include the effects of GF in Ref. [197] in the context of annual modulations, where it is a relevant effect.

[2] In the following whenever the *general* scenario is plotted we fix $r_\rho = r_\sigma = 1$.

Scenario	Mediator	r_R	m_1 (GeV)	m_2 (GeV)	r_ρ	r_σ	$m_{A'}$ (MeV)
Asymmetric	Heavy	$r_\sigma\,\mu_{p1}^2/\mu_{p2}^2$	10	50	-	1	-
Asymmetric	Light	1	10	50	-	-	30
Freeze-out	Heavy	m_1^3/m_2^3	10	40	10^{-3}	-	-
Freeze-out	Light	m_2/m_1	8	20	1	-	1

Table 5.1 Benchmark points used to generate the Asimov data for parameter estimation. Cases where certain parameters have been absorbed into other degrees of freedom or are not applicable are shown with a dash. All coupling strengths are fixed to either $\sigma_p^1 = 10^{-45}$ cm^2 or $\epsilon_{\rm eff} = \alpha\,\epsilon^2 = 10^{-22}$. Also shown in the third column is the factor r_R that determines the position of the kink in the rate of 2DM scenarios.

Apart from an overall normalisation, the slopes of the energy spectra of the different DM components are governed primarily by the term in squared brackets (and to a lesser extent the form factor). As discussed in Ref. [195], the smoking gun signature of 2DM is the presence of a *kink* in the total rate. This is because (in the *general* model at least) the light component generates a spectrum that falls off more rapidly at low E_R than the heavy component. This distinctive feature rapidly vanishes for smaller mass splittings, when both components have the same slope, and also for very large values of the heavy DM mass, for which the number density of the heavy component is very suppressed. Notice in Eq. (5.6) that the DM masses (and the form factor) control the slopes of the spectra, while the ratio of the rates of the heavy and light components at a certain energy, $R_A^{(2)}(E_R)/R_A^{(1)}(E_R)$, specifies the position of the *kink*. We define r_R to be the factor in front of the $\eta(v_{m,A}^{(2)})$ term, i.e., $R_A^{(2)}/R_A^{(1)} \equiv r_R\,\eta^{(2)}/\eta^{(1)}$, which hence summarizes the different underlying particle physics of the scenarios considered. In the third column of Tab. 5.1 we present r_R for each scenario considered in this study.

As before we have checked that sensible energy resolutions do not significantly affect the detection rates, and in the following analysis we assume perfect energy resolution and efficiency. Hence, our results are intended to understand the underlying physics and more sophisticated experimental studies are needed once a signal is observed. In the numerical analysis we consider xenon and germanium targets, as they have quite different masses. For xenon (germanium) we use an exposure of $3\,(4)\ t\cdot y$ with an energy threshold of $1\,(2)$ keV. We note that the median sensitivity scales with $\sim\sqrt{\text{exposure}}$ (before systematics dominate) and hence our results can be rescaled for other exposures.

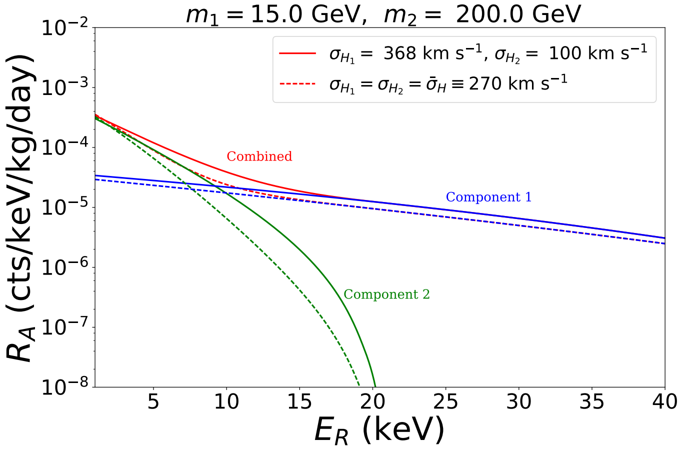

Fig. 5.1 Differential event rates in xenon for mass-dependent velocity dispersions according to Eq. (5.4) (solid), and for constant ones equal to $\bar{\sigma}_H = 270$ kms^{-1} (dashed), for $m_1 = 15$ GeV (green), $m_2 = 200$ GeV (blue) and the combined rates (red).

5.2.2 Velocity dispersions

The effective temperature for an isometric Maxwellian thermal distribution is given by $T_\beta \simeq \frac{1}{2}\, m_\beta\, \bar{\sigma}_H^2$, where we take a canonical value for the velocity dispersion, $\bar{\sigma}_H \sim 270$ kms^{-1}. This is valid for the single species case, and for multiple species N (labelled by $\beta = 1, 2..., N$) that interact with each other. For multiple species which are self-interacting on time scales much shorter than those relevant for the halo formation, the dark plasma attains hydrostatic equilibrium at a temperature $T_{\rm eq}$ on galactic scales. The result is that the Maxwellian velocity dispersion of each component of the dark sector, σ_{H_β}, becomes mass dependent [201],

$$\sigma_{H_\beta} = \bar{\sigma}_H \sqrt{\frac{\bar{m}}{m_\beta}}\,, \tag{5.4}$$

where $\bar{m} = \sum_\beta n_\beta m_\beta / \sum_\beta n_\beta$, with $n_\beta = \rho_\beta / m_\beta$ the number density of the DM particle β. As can be seen, the heavier DM particle has a narrower velocity distribution than the lighter one.

In Fig. 5.1 we show how the event rate changes between equal velocity dispersions (dashed curves) equal to $\bar{\sigma}_H$, and the mass-dependent case (solid curves). We use $m_1 = 15$ GeV (red), $m_2 = 200$ GeV (blue), and fixed $r_\rho = 1$. In this case, $\sigma_{H_1} = 368 > \bar{\sigma}_H$ and $\sigma_{H_2} = 100 < \bar{\sigma}_H$. We observe that there are no large differences between both cases, although the rates slightly increase in the case of mass-dependent velocity dispersions. However, in this case the *kink* of the 2DM spectrum is more smooth than for constant velocity dispersions, and therefore will be harder to observe.

In the following we consider 2DM scenarios that have either heavy or light mediators. For the case of a light mediator DM self-interactions are not suppressed, and therefore it seems more natural that the DM components have mass-dependent velocity dispersions. However, as the difference with the case of constant velocity dispersion is not very large, in order to more readily investigate the differences between the different cases, in the following we take constant velocity dispersions equal to $\bar{\sigma}_H$ for each DM component.

5.3 Asymmetric dark matter

The production mechanism of DM is unknown. One of the most natural ways to obtain the correct dark matter relic abundance is via an asymmetry, in the same spirit as is expected to happen in the baryon and lepton sectors [140, 201]. ADM scenarios also naturally feature multi-component DM for models with a light or massless force carrier which follows from the requirement of gauge symmetry and the possible formation of bound states [120].

5.3.1 Heavy mediator

In this first case, we assume that any heavy physics is point-like. We also assume that the two DM particles have similar number densities, $n_1 = n_2$, so that

$$r_\rho = \frac{m_2}{m_1}\,, \tag{5.5}$$

and the event rate in Eq. (5.6) becomes

$$R_A(E_R) = \frac{\rho_{\rm loc}\,\sigma_1^p}{2\,(m_1+m_2)\,\mu_{p1}^2}\,A^2\,F_A^2(E_R)\,\left[\eta(v_{m,A}^{(1)}) + r_\sigma\,\frac{\mu_{p1}^2}{\mu_{p2}^2}\,\eta(v_{m,A}^{(2)})\right]\,. \tag{5.6}$$

The simplification in this expression is due to the fact that the individual rates are proportional to the (equal) DM number densities. In most asymmetric models the number densities of DM and baryons are related by order one factors, and therefore one expects DM masses $\mathcal{O}(5)$ GeV to reproduce the DM relic abundance. This is well-motivated but model-dependent, and in the following we consider ADM-like scenarios with DM masses of up to a few hundreds GeV.

In Fig. 5.2 we show the detection rates for the *general* scenario, i.e., Eq. (5.6) (solid black), for equal number densities with a heavy mediator (dotted blue), and for the case of light mediators with $m_{A'} = 1$ MeV (dashed red). The only quantitative difference between the spectra of the equal number density case and the *general*

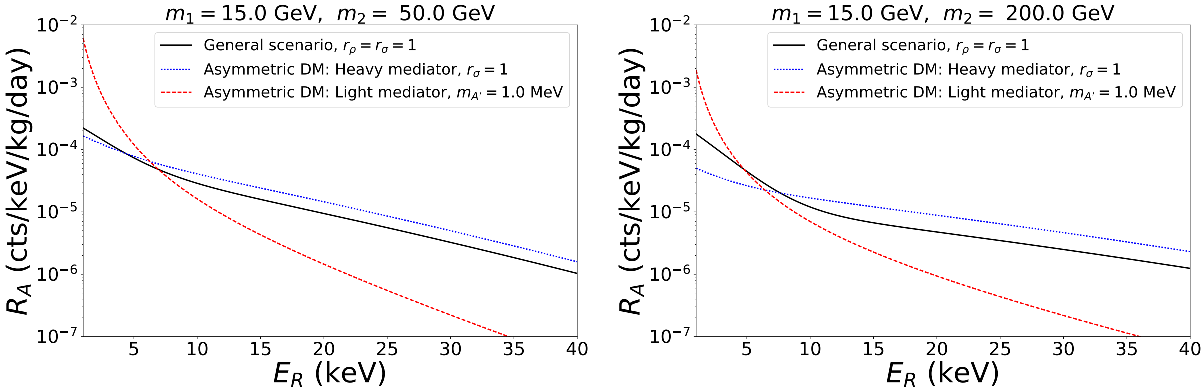

Fig. 5.2 Differential event rates in a xenon experiment for the *general* scenario (solid black), for equal number densities with a heavy mediator (dotted blue), and for the case of light mediators with $m_{A'} = 1$ MeV (dashed red). We fix $m_1 = 15$ GeV. *Left:* $m_2 = 50$ GeV. *Right:* $m_2 = 200$ GeV.

scenario (studied in detail in Ref. [195]) is the fact that now we are fixing $r_\rho = m_2/m_1$, which leads to a smoothened *kink* feature in the recoil spectrum. The result is that the resolving power of the 1DM versus 2DM hypothesis is expected to be worse for ADM-like models.

To quantify this, we plot in Fig. 5.3 the 'median significance' for such discrimination in the case of ADM with a heavy mediator, and compare it to our previous study, namely Fig. 7 of Ref. [195] for xenon and germanium type detectors[3]. For details and definitions of the analysis used to forecast the median sensitivity of an experiment to discriminating between 1DM and 2DM see App. 5.6.1. In Fig. 5.3 we show the results of the hypothesis testing in the planes $m_2 - m_1$ (top) and $\log_{10}(r_\sigma) - m_1$ (bottom). The left panel is for Xe and the right one for Ge. We see that the maximum median significance achieved for the heavy mediator model (max $Z \sim 5$ for Xe) relative to the *general* case (max $Z \sim 12.8$ for Xe) is reduced. We notice throughout this work that xenon-type experiments typically give a better median significance overall than germanium type experiments, with the exception of thermal freeze-out scenarios with light mediators (Sec. 5.4.3). Aside from the overall reduction in median sensitivity, as can be seen in the top panel of Fig. 5.3, the point of maximum Z is shifted to lower m_2 in the heavy mediator model. This is because at low m_2 the total rate gets larger at low recoil energies, producing more events and hence increasing Z. Furthermore, as can be seen in the lower panel of Fig. 5.3, there is an upper cut-off in the lobe at $r_\sigma \sim 3$. This is due to the enhancement in the r_R factor at large r_σ that drives the rate to look like a single heavy component.

---

[3] Note we do not include sodium as we did in our previous study since the median significance was always found to be heavily suppressed relative to the Xe and Ge cases.

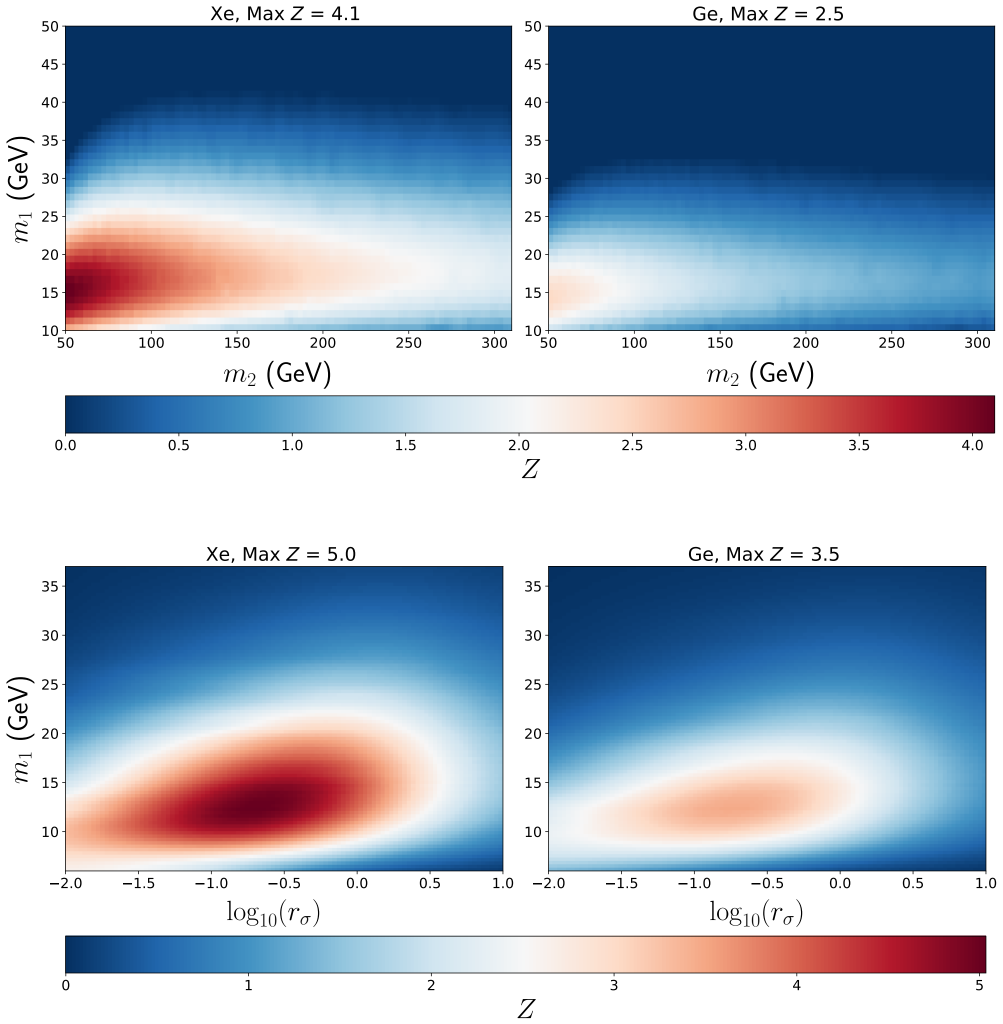

Fig. 5.3 Median significance Z with which an ADM scenario with heavy mediators can reject the 1DM hypothesis in favour of the 2DM hypothesis. *Top:* $m_2 - m_1$ plane, with fixed $r_\sigma = 1$. *Bottom:* $\log_{10}(r_\sigma) - m_1$ plane, with fixed $m_2 = 50$ GeV. The left panel is for Xe, and the right one for Ge.

Next we show in Fig. 5.4 how well the parameters can be estimated in the case of a heavy mediator by calculating the Asimov likelihood and generating the Profile Likelihood Ratio (PLR) in 2D regions of the parameter space. We use the analysis methods summarised in App. 5.6.2. The benchmarks used in this study to generate the Asimov data are provided in Tab. 5.1. These benchmark values belong to regions of parameter space which give a large discrimination between the 1DM and the 2DM hypotheses as ascertained by the results of the hypothesis testing. We show 2σ C.L regions for the first benchmark point given in Tab. 5.1 in the $m_1 - m_2$ plane (left panel), $m_1(\text{GeV}) - \log_{10}(r_\rho)$ plane (middle panel) and the $\log_{10}(r_\rho) - \log_{10}(\sigma_1^p)$ plane. The different colour contours correspond to a xenon only (black dashed), germanium only (orange dotted) and xenon + germanium combined (grey solid) experiment. We observe no degeneracies in the PLR with excellent parameter reconstruction.

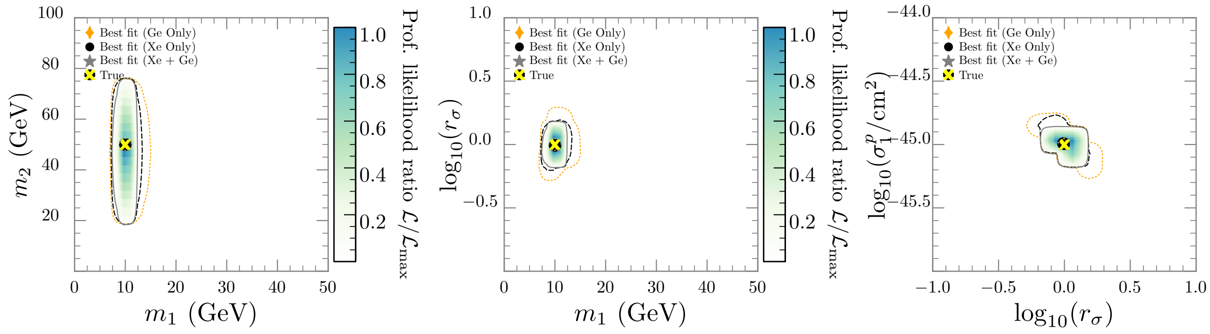

Fig. 5.4 PLR density for the ADM scenario with a heavy mediator. *Left:* $m_1 - m_2$ plane. *Middle:* $m_1 - \log_{10}(r_\sigma)$ plane. *Right:* $\log_{10}(r_\sigma) - \log_{10}(\sigma_1^p/\mathrm{cm}^2)$ plane. Contours represent 2σ C.L regions. Benchmark points for generating the Asimov data are given in Tab. 5.1. The different colour contours correspond to a xenon only (black dashed), germanium only (orange dotted) and combined xenon + germanium (grey solid) experiments.

5.3.2 Light mediators

We now consider the case that the two species are produced in some asymmetric scenario but are couple to a light vector mediator with mass $m_{A'}$. We consider an extra $U(1)$ gauge symmetry with dark coupling g_D, such that the gauge theory becomes $SU(3)_C \times SU(2)_L \times U(1)_Y \times U(1)_D$. As the dark symmetry is Abelian, a Stueckelberg mass for the dark photon is gauge invariant, but it can also be generated by a new scalar that takes a VEV. The fermionic DM component β ($\beta = 1, 2$) has charge Q_β under this new $U(1)_D$ symmetry. For definiteness we take $Q_2 = 1$. We consider the case where there is an induced kinetic mixing ϵ between the dark and the visible photons parameterised by a term in the Lagrangian $-\frac{\epsilon}{2} F_{\mu\nu} F'_{\mu\nu}$. For our purposes, it is sufficient to consider the interaction terms generated at low energies after diagonalising the gauge boson kinetic terms,

$$\mathcal{L}_{\rm int} \supset \epsilon\, e J^\mu_{\rm EM} {A'}_\mu + g_D\, J^\mu_{\rm DM} {A'}_\mu \ , \tag{5.7}$$

where e is the magnitude of the electric charge, $J^\mu_{\rm EM} \equiv \sum_f q_f \bar{f} \gamma^\mu f$ is the electromagnetic current of Standard Model fermion f (with electric charges q_f in units of e) and $J^\mu_{\rm DM} \equiv \sum_\beta Q_\beta \bar{\chi}_\beta \gamma^\mu \chi_\beta$ is the dark fermion current. These are the interaction terms that are relevant for tree-level DD. The scattering cross section of DM component β

reads

$$\bar{\sigma}^p_\beta(|\vec{q}|) = \sigma^p_\beta \times \frac{m^4_{A'}}{(|\vec{q}|^2 + m^2_{A'})^2} \,, \tag{5.8}$$

where $\vec{q}$ is the momentum transfer, whose absolute value can be expressed in terms of the recoil energy as $|\vec{q}| = \sqrt{2m_A E_R}$, and σ^p_β is the zero-momentum WIMP-proton cross-section of DM β, given by

$$\sigma^p_\beta = \frac{16\pi\, \epsilon_{\rm eff}\, \alpha_{\rm EM}\; \mu^2_{p_\beta}\, Q^2_\beta}{m^4_{A'}} \,, \tag{5.9}$$

where $\epsilon_{\rm eff} \equiv \epsilon^2 \alpha_{\rm D}$ and $\alpha_{\rm EM} = e^2/(4\pi)$ $[\alpha_D = g_D^2/(4\pi)]$ is the electromagnetic [dark] fine structure constant. The universal neutrality of the $U(1)_D$ charge implies that a plasma containing two species has charges of opposite sign with

$$n_1 Q_1 + n_2 Q_2 = 0 \,. \tag{5.10}$$

As we assume that the species have equal number density $n_1 = n_2$, this implies that $Q_2 = -Q_1 = 1$, and hence $r_\sigma = \mu^2_{p_2}/\mu^2_{p_1}$. With this in mind, the total DD rate is simplified to

$$R_A(E_R) = \frac{\rho_{\rm loc}\, \sigma^p_1\, Z^2}{2\,(m_1 + m_2)\, \mu^2_{p_1}}\, F^2_A(E_R) \left[\eta(v^{(1)}_{m,A}) + \eta(v^{(2)}_{m,A})\right] \times \frac{m^4_{A'}}{(2m_A E_R + m^2_{A'})^2} \,. \tag{5.11}$$

One should note that since kinetic mixing only produces interactions with the SM photons, the DM couples to the electric charge. Therefore, the rate is proportional to the number of protons Z, and not to A.

In Fig. 5.2 we plot the rate of Eq. (5.11) for $m_{A'} = 1$ MeV as a red dashed curve. The momentum-dependent suppression factor $1/(q^2 + m^2_{A'})$ in the scattering cross-section, Eq. (5.8), produces a steeper decrease with energy of the event rate. One should immediately notice that whilst there is a slight enhancement in the rate at low recoil energies, there is an absence of any distinct *kink* feature in the spectrum. We therefore expect the maximum median sensitivity Z in the case of an asymmetric scenario with a light mediator to be small except for large values of the effective mixing $\epsilon_{\rm eff}$ or very small mediator masses $m_{A'}$ (compared to $\vec{q}$), both of which give enhancements in $\sigma^p_1(|\vec{q}|)$.[4]

---

[4] Also notice that in the limit of large $m_{A'} \gg |\vec{q}|$ we recover the contact case, where the discrimination is larger than for light mediators.

In Fig. 5.5 we show the results of the hypothesis testing in the planes $m_2 - m_1$ (top), $\log_{10}(m_{A'}) - \log_{10}(\epsilon_{\rm eff})$ (middle) and $\log_{10}(m_{A'}) - m_1$ (bottom). The left panel is for Xe and the right one for Ge. We use 90% C.L constraints on the $U(1)_{\rm DM}$ coupling derived from PandaX [202] to put a conservative upper limit on the parameter combination $\epsilon_{\rm eff} \equiv \epsilon^2 \alpha_{\rm DM} \lesssim 10^{-22}$. These limits are shown as solid white lines in the middle and bottom panels. In the middle panel only the most conservative limit is shown for a DM mass of 10 GeV. Furthermore, a lower limit can be placed on the combination $\epsilon_{\rm eff}\, m_{A'}$ from requiring that thermally produced A' particles decay before Big Bang Nucleosynthesis (BBN), with a lifetime below a few seconds [203–205]. We use the 2σ C.L limits from Ref. [203] which are calculated at two benchmark values for the mediator/decoupling temperature ratio $T^{\rm cd}_{A'}/T^{\rm cd}$. These lower limits are overlaid in the middle panels for $T^{\rm cd}_{A'}/T^{\rm cd} = 1$ (dotted white) and $T^{\rm cd}_{A'}/T^{\rm cd} = 0.5$ (dashed white). We see from these results that, as expected, one needs go to larger $\epsilon_{\rm eff}$ and smaller $m_{A'}$ to increase the median sensitivity. However the PandaX limits severely restrict the forecasting potential, in the most conservative case allowing a median significance of $Z \sim 2\,(3)$ for Ge (Xe) for $m_{A'} \sim 10$ MeV. That is, in all cases the regions of highest Z are disfavoured by PandaX null results.

In Fig. 5.6 we show the results of the parameter estimation for the second benchmark point in Tab. 5.1 in the planes $m_1 - m_2$ (left), $m_1 - \log_{10}(m_{A'}/\text{GeV})$ (middle) and $\log_{10}(m_{A'}/\text{GeV}) - \log_{10}(\epsilon_{\rm eff})$ (right). We notice a large degeneracy in the $m_1 - m_2$ plane. The extended region in the mass of the lightest DM mass, m_1, is reduced in the combined Xe+Ge case, however a very large uncertainty remains in m_2 at the 2σ level.

5.4 Thermal freeze-out

5.4.1 Generic scenarios

Another very natural way to obtain the correct dark matter relic abundance is via thermal freeze-out. In this case, ignoring logarithmic corrections of the DM masses, the relic abundance implies a relation between the thermally averaged annihilation cross sections at freeze-out, that is,

$$\Omega_1 + \Omega_2 = \Omega_{\rm DM} \;\longrightarrow\; \langle\sigma_{\rm ann} v\rangle_1^{-1} + \langle\sigma_{\rm ann} v\rangle_2^{-1} = \langle\sigma_{\rm ann} v\rangle_{\rm th}^{-1}\,. \tag{5.12}$$

Therefore, the DM particles have similar energy densities if their annihilation cross sections are similar. We can further assume that the local densities of the DM species scale as the cosmological ones, see Refs. [138, 139], which for cold DM is a natural expectation [199],

$$\frac{\rho_\beta}{\rho_{\rm loc}} = \frac{\Omega_\beta h^2}{\Omega_{\rm DM} h^2} = \frac{\langle \sigma_{\rm ann} v \rangle_{\rm th}}{\langle \sigma_{\rm ann} v \rangle_\beta} \, , \tag{5.13}$$

where we take the canonical value $\langle \sigma_{\rm ann} v \rangle_{\rm th} = 2.2 \times 10^{-26}$ cm^3 s^{-1}. v is the DM relative velocity at freeze-out, $v \simeq \sqrt{12/x_f}$, with $x_f \equiv m_{\rm DM}/T_f$. In the following we assume that both DM particles have the same velocity at freeze-out, which is a very good approximation given the fact that x_f only has a logarithmic dependence on the DM mass.

The relationship between the scattering and the annihilation cross sections is model-dependent. We restrict ourselves to scenarios in which the relationship between the two is simple. An example is s-wave annihilations mediated by some vector mediator into first generation quarks, with SI interactions for scattering. In this case, the annihilation cross section at freeze-out for DM β can be written as

$$\langle \sigma_{\rm ann} v \rangle_\beta \simeq g_\beta^2 \, \frac{m_\beta^2}{(m_\beta^2 + m_{A'}^2)^2} \, v, \tag{5.14}$$

where $m_{A'}$ is the mass of the mediator and g_β is the effective coupling between quarks and DM particles β. Note that s-wave annihilation is severely constrained by CMB constraints for $m_\beta < \mathcal{O}(10)$ GeV [4, 206] and so we only consider heavy DM in the following. Similarly, the DD WIMP-proton cross-sections have the form

$$\sigma_\beta^p(|\vec{q}|) \simeq g_\beta^2 \frac{\mu_{\beta p}^2}{(|\vec{q}|^2 + m_{A'}^2)^2} \, . \tag{5.15}$$

Hence, neglecting order one factors, we can express the product $r_\sigma \, r_\rho$ in terms of the masses as

$$r_\rho \, r_\sigma \simeq \frac{(m_2^2 + m_{A'}^2)^2}{(m_1^2 + m_{A'}^2)^2} \, \frac{\mu_{p2}^2}{\mu_{p1}^2} \, \frac{m_1^2}{m_2^2} \, , \tag{5.16}$$

where we have also used Eq. (5.13). In the following two subsections we analyse the cases of heavy and light mediators, each of which yields a different phenomenology.

5.4.2 Heavy mediators

In the heavy mediator limit, with $m_{A'} \gg m_{1,2}$, we can simplify Eq. (5.16) to

$$r_\rho \, r_\sigma \simeq \frac{\mu_{p2}^2}{\mu_{p1}^2} \frac{m_1^2}{m_2^2} \, , \tag{5.17}$$

and the rate in Eq. (5.6) reduces to

$$R_A(E_R) = \frac{\rho_{\rm loc}\,\sigma_1^p}{2\,(1+r_\rho)\,\mu_{1p}^2\,m_1}\,A^2\,F_A^2(E_R)\,\left[\eta(v_{m,A}^{(1)}) + \frac{m_1^3}{m_2^3}\,\eta(v_{m,A}^{(2)})\right]\,. \tag{5.18}$$

Notice how in this case the contribution of DM2 is suppressed by m_1^3/m_2^3. One should therefore expect that the total rate is rapidly dominated by DM1 for $m_2 \gg m_1$. Hence, the discriminating power between 1DM and 2DM in this region of the parameter space should correspondingly be suppressed. Furthermore, the rate is enhanced for small $r_\rho \simeq g_1^2\,m_1^2/(g_2^2\,m_2^2)$ and hence we would expect the median significance to increase. To see this behaviour, we plot in Fig. 5.7 the rate in Eq. (5.18) as a blue dotted line for two different mass splittings. One should immediately notice the *kink* feature becoming more prominent for $m_1 = 8$ GeV and $m_2 = 40$ GeV (right plot).

In Fig. 5.8 we show the results of the hypothesis testing in the $m_2 - m_1$ (top) and $\log_{10}(r_\rho) - m_1$ (bottom) planes for the case of thermally produced DM species coupled to a heavy mediator. As expected we find that the median significance falls off for large m_2 due to the m_1^3/m_2^3 suppression factor. We also observe in the lower panel an increase and approximate degeneracy in the median significance for vanishingly small r_ρ (i.e., $g_1^2\,m_1^2 \ll g_2^2\,m_2^2$) and $m_1 \in [5, 20]$. The median significance drops for masses below $m_1 \sim 5$ due to the light component producing scatterings below threshold.

In Fig. 5.9 we show the results of the parameter estimation for the third benchmark point given in Tab. 5.1 in the $m_1 - m_2$, $\sigma_1^p - m_2$ and $\log_{10}(r_\rho) - \sigma_1^p$ planes. We observe interesting degeneracies in the PLR. Starting with the left panel, there appears to be an extended degeneracy in the m_2 direction for $m_2 \gtrsim 40$ GeV whilst reconstruction of the true m_1 value is good. This is due to the suppressed number of events for $m_2 > 40$ GeV rendering the rate indistinguishable from a single component. In the middle panel we see no ability in the average experiment to be able to reconstruct the true σ_1^p accurately with the degeneracy extending over the entire plane. This is because larger σ_1^p drives the overall normalisation of the rate higher, but it does not make the kink more pronounced. The right panel shows perhaps the most interesting degeneracy. We see that the benchmark is found with good precision in σ_1^p for $r_\rho \sim 1$, whereas above this value there is a degeneracy with σ_1^p. This can be easily understood from Eq. (5.18), where for $r_\rho > 1$ they enter in the normalisation of the rate as σ_1^p/r_ρ.

5.4.3 Light mediators

In the following we also consider the simplified model with the vector mediator introduced in Sec. 5.3.2. Up to order one factors, the t-channel $\chi_\beta + \chi_\beta \to A' + A'$

(secluded) annihilation cross-section into light mediators reads

$$\langle \sigma_{\rm ann} v \rangle_\beta \simeq Q_\beta^2 \frac{\pi \alpha_D^2}{m_\beta^2}\, v \,, \tag{5.19}$$

where we neglected the phase-space factor, as $m_{A'} \ll m_\beta$. Using Eq. (5.9) we can now relate the DD scattering cross-section to the annihilation one,

$$\sigma_\beta^p \simeq \frac{16\, \epsilon^2\, \mu_{p_\beta}^2\, \alpha_{\rm EM}\, \langle \sigma_{\rm ann} v \rangle_\beta\, m_\beta^2}{\alpha_{\rm D}\, m_{A'}^4\, v} \,. \tag{5.20}$$

Hence, we obtain

$$r_\rho\, r_\sigma \simeq \frac{m_2^2}{m_1^2} \frac{\mu_{p2}^2}{\mu_{p1}^2} \,, \tag{5.21}$$

where we assumed that both DM particles have similar velocities at freeze-out. The rate then becomes

$$R_A(E_R) = \frac{\rho_{\rm loc}\, \sigma_1^p}{2\,(1+r_\rho)\, \mu_{p1}^2\, m_1}\, Z^2\, F_A^2(E_R) \left[\eta(v_{m,A}^{(1)}) + \frac{m_2}{m_1}\, \eta(v_{m,A}^{(2)}) \right] \times \frac{m_{A'}^4}{(2 m_A E_R + m_{A'}^2)^2} \,. \tag{5.22}$$

Interestingly, notice how the DM2 term is now enhanced by m_2/m_1, as opposed to the case of heavy mediators in Eq. (5.18). The total rate, measured in events/(kg keV day), can we written as (see App. 5.7 for details)

$$R_A(E_R) = \frac{15\, \epsilon^2}{\alpha_{\rm D}}\, F_A^2(E_R) Z^2\, m_1 \left[\eta(v_{m,A}^{(1)}) + \frac{m_2}{m_1}\, \eta(v_{m,A}^{(2)}) \right] \times \frac{1}{(2 m_A E_R + m_{A'}^2)^2} \,, \tag{5.23}$$

where all the masses are to be evaluated in GeV. The dark fine structure constant $\alpha_{\rm D}$ can be expressed in terms of m_1 and r_ρ by making use of Eq. (5.12) and charge conservation from Eq. (5.10) as

$$\alpha_{\rm D} = \frac{5 \times 10^{-3}}{r_\rho} \sqrt{1 + r_\rho^2} \left(\frac{m_2}{100\,{\rm GeV}} \right) \,, \tag{5.24}$$

which can be plugged into Eq. (5.23). The rate in Eq. (5.22) is shown in Fig. 5.7 as a red dashed curve for two mass splittings, for a mediator mass of 1 MeV. As for the case of a heavy mediator in Fig. 5.2, there exists a much steeper decrease with recoil energy than for the heavy mediator cases, due to the $1/(|\vec{q}|^2 + m_{A'}^2)$ factor in the rate. This smoothens the *kink* in the spectrum, which is the crucial feature needed to provide a good discrimination between the 1DM and 2DM cases. Hence, one should expect that the average experiments capability to discriminate the one and two component cases will be limited unless there is a significant enhancement in the rate from exposure or cross-section.

For the hypothesis testing shown in Fig. 5.10, we first perform a scan in the $m_1 - m_2$ plane (top) and fix $r_\rho = 1$ and $m_{A'} = 1$ MeV. Instead of overlaying the PandaX upper limits as we did earlier in Fig. 5.5 we instead calculate Z at points in the parameter space that are not excluded. That is, for every m_2 (and $r_\rho = 1$) that gives a particular α_D as per Eq. (5.24), we set the value of the kinetic mixing parameter ϵ^2 to satisfy $\epsilon^2\,\alpha_{\rm D} = 10^{-22}$ which is the conservative upper limit. Immediately obvious is the fact that the Ge experiment provides larger median sensitivity than the Xe experiment. Upon inspection of the rates, this feature is due to the fact that at small mediator masses the overall normalisation of the rate goes as $1/(4m_A^2 E_R^2)$. We note that the maximum median significance occurs for Ge at $m_1 \sim 8$ GeV and $m_2 \sim 20$ GeV, which corresponds to a maximum allowed $\epsilon^2 \sim 7 \times 10^{-20}$. The median significance completely drops off however above $m_2 \sim 40$ GeV. This is because the second term in the parentheses in Eq. (5.23) starts to saturate the rate, which becomes 1DM like (i.e., dominated by the heavy component, DM2). Also enhancing this effect is the overall $1/m_2$ suppression in the rate stemming from the $1/\alpha_D$ factor in Eq. (5.23).

We also show in Fig. 5.10 the planes $\log_{10}(m_{A'}/\mathrm{GeV}) - \log_{10}(\epsilon^2)$ (middle) and $\log_{10}(r_\rho) - \log_{10}(\epsilon^2)$ (bottom), for fixed $m_1 = 8$ and $m_2 = 20$ GeV. In the general one-component scenario the PandaX limits on the scattering cross-section translate into $\epsilon^2\alpha_D < 10^{-22}$. On the other hand, for the model considered here this constraint implies the upper limit $\epsilon^2/\alpha_D \lesssim 10^{-13}(\mathrm{GeV}/m_1)^2(1 + r_\rho)$ for DM1 and similarly (divided by r_ρ) for DM2, where we have corrected for the 2DM local energy densities. All points that do no satisfy this are set to $Z = 0$. In the middle panel, we keep $r_\rho = 1$ and hence the upper limit on ϵ^2 remains at 7×10^{-20}, and hence above this value the median significance is set to zero. We observe in the middle panel that the maximum Z is achieved by making the mediator mass small which is again expected from the $1/(|\vec{q}|^2 + m_{A'}^2)$ enhancement in the rate as in the asymmetric case. Furthermore the median significance is maximised for $\epsilon^2 \sim 5 \times 10^{-20}$ which is slightly less than the maximum allowed by PandaX. In the bottom panel, we observe that the median significance is maximised and remains constant for $r_\rho > \mathcal{O}(1)$. This is because unlike other scenarios studied in this paper, the rate in Eq. (5.23) is proportional to the factor $r_\rho/\sqrt{1 + r_\rho^2}$, which for $r_\rho < 1$ suppresses the rate and therefore Z, while for

$r_\rho \gg 1$ saturates to 1. Hence, for large enough r_ρ, the rate (and therefore Z) falls off to a constant (since the DM masses are fixed). This is indeed what is observed.

In Fig. 5.11 we show the results of the parameter estimation for the fourth benchmark point given in Tab. 5.1. We find that in all displayed cases the germanium experiment provides a tighter 2σ C.L region than the xenon experiment. This is because as seen from the hypothesis testing, for this scenario the germanium type experiment provides better maximum median sensitivity. In each panel the combined experiment has a better overall precision as expected. The DM masses are well reconciled with the best fit points finding the true values. The middle plot however shows an extended region of degenerate PLR whilst at the same time the best fit points do not recover the true value. This is because above $m_{A'} > 10^{-2.5}$ GeV the kink becomes less prevalent in the rate, whilst as $m_{A'} \to 0$ the rate becomes independent of the mediator mass. In the final panel we observe an anti-correlation between ϵ^2 and r_ρ below $r_\rho \sim 1$, due to the fact that the rate scales as $\epsilon^2 r_\rho$. For $r_\rho > 1$ the rate becomes independent of r_ρ, hence, as a result there is an extended region where the latter cannot be extracted.

5.5 Conclusions

We have studied the implications that reproducing the relic abundance has on the DD event rates of multi-component DM. We considered two generic genesis scenarios: asymmetric DM and thermal freeze-out. In the asymmetric scenario we restrict the WIMPs to have equal number densities, while in the freeze-out scenario we formulate the analysis based on the assumption that the local energy densities of each component scale like the global relic abundances, so that we are able to relate the thermally averaged annihilation cross-section at freeze-out with the DD WIMP-proton cross-section. For each case we consider two types of mediators, light and heavy. We also analysed the implications on DD of scenarios where the DM components interact with each other, so that their velocity dispersions become mass-dependent. This effect caused a mild smoothing out of the *kink* feature in the two component spectrum.

For each scenario considered, we first, looked at the shape of the recoil rate spectrum to get an idea of the existence and prominence of any *kink* features which are smoking gun signatures of two-component DM. We then did a hypothesis test to determine regions of the model parameter space where the median experiment can significantly discriminate between the 1DM and 2DM hypothesis. Lastly, we extracted the DM parameters from mock data for a few benchmark model values.

As a general conclusion, we observe a decrease in the maximum median sensitivity relative to the *general* scenario studied in Ref. [195] across all models studied. As a result the maximum median significance to reject the 2DM hypothesis in favour of the 1DM one is suppressed relative to the latter.

In the asymmetric scenario with heavy mediators, we found that imposing equal number densities smoothens the *kink* feature in the rate relative to the *general* scenario. We also observed that the point that maximises the median sensitivity is at lower m_2 than the *general* case. We found that the median experiment is able to sufficiently reconstruct benchmarks in regions of good model discrimination without the presence of any degeneracies. The second model considered in the asymmetric scenario involved the addition of a light vector mediator. We observed that the current PandaX limits on the kinetic mixing parameter and dark $U(1)_\chi$ coupling exclude regions of the model parameter space that give the best hypothesis discrimination. We also observed that the limit on the mediator lifetime from BBN considerations also places a strong constraint on the allowed parameter space. We obtained extended uncertainties in the resolving power of m_1, but the true benchmark had the largest PLR.

For the case of freeze-out, we observed that the rate for the case of a heavy mediator has a deeper and more pronounced *kink* at low recoil energies relative to the *general* case, whereas the light mediator case still has a smoothened rate. With the heavy mediator, we find that the median sensitivity is largest for $r_\rho < 1$, whilst the m_1^3/m_2^3 suppression factor in the rate of the second component causes the median significance to be maximised for smaller m_2. In this scenario we find that parameter reconstruction of the heavy DM mass and the cross-section have large associated uncertainties. For the case of the light mediator we considered secluded annihilation to a light vector species that produces a thermally averaged cross-section that is independent of the kinetic mixing parameter ϵ and is only dependent on the dark coupling α_D. Regardless of parameter configuration the spectrum in this case is a smooth curve as opposed to the clear *kink* needed to successfully discriminate between 1DM and 2DM. We find that the maximum median sensitivity is suppressed for $r_\rho < 1$. Our analysis also shows that the DM masses can be recovered whilst the kinetic mixing parameter ϵ^2 experiences some interesting degeneracies with the mediator mass $m_{A'}$ and r_ρ.

To summarise, in this study we found that even when applying reasonable DM genesis model constraints to a general two-component DM scenario, therefore reducing the allowed parameter space, there are cases where the 1DM and the 2DM hypothesis can be significantly discriminated, but typically with smaller significance than for the most general case. We have also uncovered interesting degeneracies in the median experiments capability for reconstructing the model parameters in these scenarios, giving insight into the reconstruction of such models in future direct detection experiments.

Acknowledgements

This work is supported by the Australian Research Council through the Centre of Excellence for Particle Physics at the Terascale CE110001004. MW is supported by the Australian Research Council Future Fellowship FT140100244.

5.6 Analysis methods

The analysis methods used in this work are detailed in Ref. [195]. Here for completeness we briefly review the main aspects.

5.6.1 Hypothesis testing

For assessing the average capability of an experiment for discriminating 1DM (modelled by parameters $\theta_{H_{1\mathrm{DM}}}$) from 2DM (modelled by parameters $\theta_{H_{2\mathrm{DM}}}$) we formulate our analysis as a frequentist hypothesis test with the null-hypothesis being 1DM, and the alternative hypothesis being 2DM. We use a common test statistic constructed from the difference of χ^2:

$$\mathcal{T} = \min_{\theta_{H_{1\mathrm{DM}}}} \chi^2(\theta_{H_{1\mathrm{DM}}}) - \min_{\theta_{H_{2\mathrm{DM}}}} \chi^2(\theta_{H_{2\mathrm{DM}}}) \,. \tag{5.25}$$

Notice that the definition of $\mathcal{T}$ is such that the larger its value, the larger the preference for $H_{2\mathrm{DM}}$, and the smaller its value, the more $H_{1\mathrm{DM}}$ is preferred. The median significance Z quantifies an average experiments capability to discriminate a 1DM hypothesis from a 2DM one. It is defined as

$$Z(p) = \sqrt{2}\,\mathrm{erfc}^{-1}(\mathrm{p}) \;, \tag{5.26}$$

where p is a p-value given by

$$p = 1 - \mathrm{CDF}^{\chi^2}_{\mathrm{k\ d.o.f}}(\mathcal{T}_0^{2\mathrm{DM}}) \;, \tag{5.27}$$

and $\mathcal{T}_0^{2\mathrm{DM}}$ is the 'Asimov likelihood' defined by

$$\mathcal{T}_0^{2\mathrm{DM}} \equiv \mathcal{T}(x_i = \mu_i(\theta^{\mathrm{true}}_{H_{2\mathrm{DM}}})) = \min_{\theta_{H_{1\mathrm{DM}}}} \sum_i^n \left(\frac{\mu_i(\theta^{\mathrm{true}}_{H_{2\mathrm{DM}}}) - \mu_i(\theta_{H_{1\mathrm{DM}}})}{\sqrt{\mu_i(\theta^{\mathrm{true}}_{H_{2\mathrm{DM}}})}} \right)^2 \,. \tag{5.28}$$

The 'Asimov data' θ^{true} is generated for Xe and Ge type detectors.

5.6.2 Parameter estimation

For examples of parameter configurations that provide good discrimination (high Z) we conduct parameter estimates. For this we use the method of maximum likelihood which involves calculating the profile likelihood ratio (PLR)

$$\lambda(\theta_1, \theta_2) = \frac{\mathcal{L}(\mathbf{x}\,|\,\theta_1, \theta_2, \hat{\hat{\theta}}_3 ... \hat{\hat{\theta}}_n)}{\mathcal{L}(\mathbf{x}\,|\,\hat{\boldsymbol{\theta}})} \equiv \frac{\mathcal{L}(\mathbf{x}\,|\,\theta_1, \theta_2, \hat{\hat{\theta}}_3 ... \hat{\hat{\theta}}_n)}{\mathcal{L}_{\max}} \,. \tag{5.29}$$

In our analysis we call the point in the θ_1-θ_2 plane that maximises the profile likelihood ratio the 'best-fit' point. In the limit of large statistics, the distribution of $-2\ln\lambda(\theta_1, \theta_2)$ tends towards a χ^2 with $k = 2$ degrees of freedom as given by Wilk's theorem. As a result, this leads to a critical region that is defined by a cut on λ that we choose to represent contours of the standard 2σ (95.45%) frequentist confidence level (C.L). For this analysis we use Gaussian likelihoods where we again make use of the Asimov data $\boldsymbol{\theta}^{\text{true}}$:

$$\mathcal{L}(\mathbf{x} = \mu(\boldsymbol{\theta}^{\text{true}})\,|\,\boldsymbol{\theta}) = \prod_i^N \frac{1}{\sqrt{2\pi\mu_i(\boldsymbol{\theta}^{\text{true}})}} e^{-\frac{\left[\mu_i(\boldsymbol{\theta}^{\text{true}}) - \mu_i(\boldsymbol{\theta})\right]^2}{2\mu_i(\boldsymbol{\theta}^{\text{true}})}} \,. \tag{5.30}$$

Visualisation is done with the `Pippi` plotting package [180]. We show the best-fit point and normalised profile likelihood density $\mathcal{L}/\mathcal{L}_{\max}$ on the colour scale.

5.7 Expressions for freeze-out scenarios with light mediators

We can simplify the pre-factor in Eq. (5.22) by using Eq. 5.20,

$$\frac{\rho_{\text{loc}}\,\sigma_1^p}{2\,(1 + r_\rho)\,\mu_{1p}^2} = \frac{2.5 \times 10^{-38}\, m_1^2}{m_{A'}^4} \frac{\epsilon^2}{\alpha_{\text{D}}} \left(\frac{\rho_{\text{loc}}}{0.4\,\text{GeV cm}^{-3}}\right) \left(\frac{\langle\sigma_{\text{ann}} v\rangle_{\text{th}}}{2.2 \times 10^{-26}\,\text{cm}^3\ \text{s}^{-1}}\right) \text{GeV}^{-1}\,\text{cm}^{-1} \,, \tag{5.31}$$

where we used $v = 0.7c$ and the masses are measured in GeV. Then the total rate in Eq. (5.22), measured in events/(kg keV day), can easily be written as in Eq. (5.23). Furthermore, the dark fine structure constant α_{D} can be expressed in terms of m_1 and r_ρ as in Eq. (5.24). This can be checked by making use of Eq. (5.12), which using Eq. (5.19) reduces to

$$\frac{1}{\alpha_{\text{D}}^2\, v} \left(\frac{m_1^2}{Q_1^2} + \frac{m_2^2}{Q_2^2}\right) = \frac{1}{\langle\sigma_{\text{ann}} v\rangle_{\text{th}}} \quad \longrightarrow \quad \alpha_{\text{D}} = 5 \times 10^{-5} \sqrt{\frac{m_1^2}{Q_1^2} + \frac{m_2^2}{Q_2^2}}\,\text{GeV}^{-1} \,, \tag{5.32}$$

with the masses measured in GeV. Charge conservation from Eq. (5.10) implies that $Q_1 = -m_1 r_\rho / m_2$ for $Q_2 = 1$, so one obtains Eq. (5.24), which can be directly plugged into Eq. (5.23).

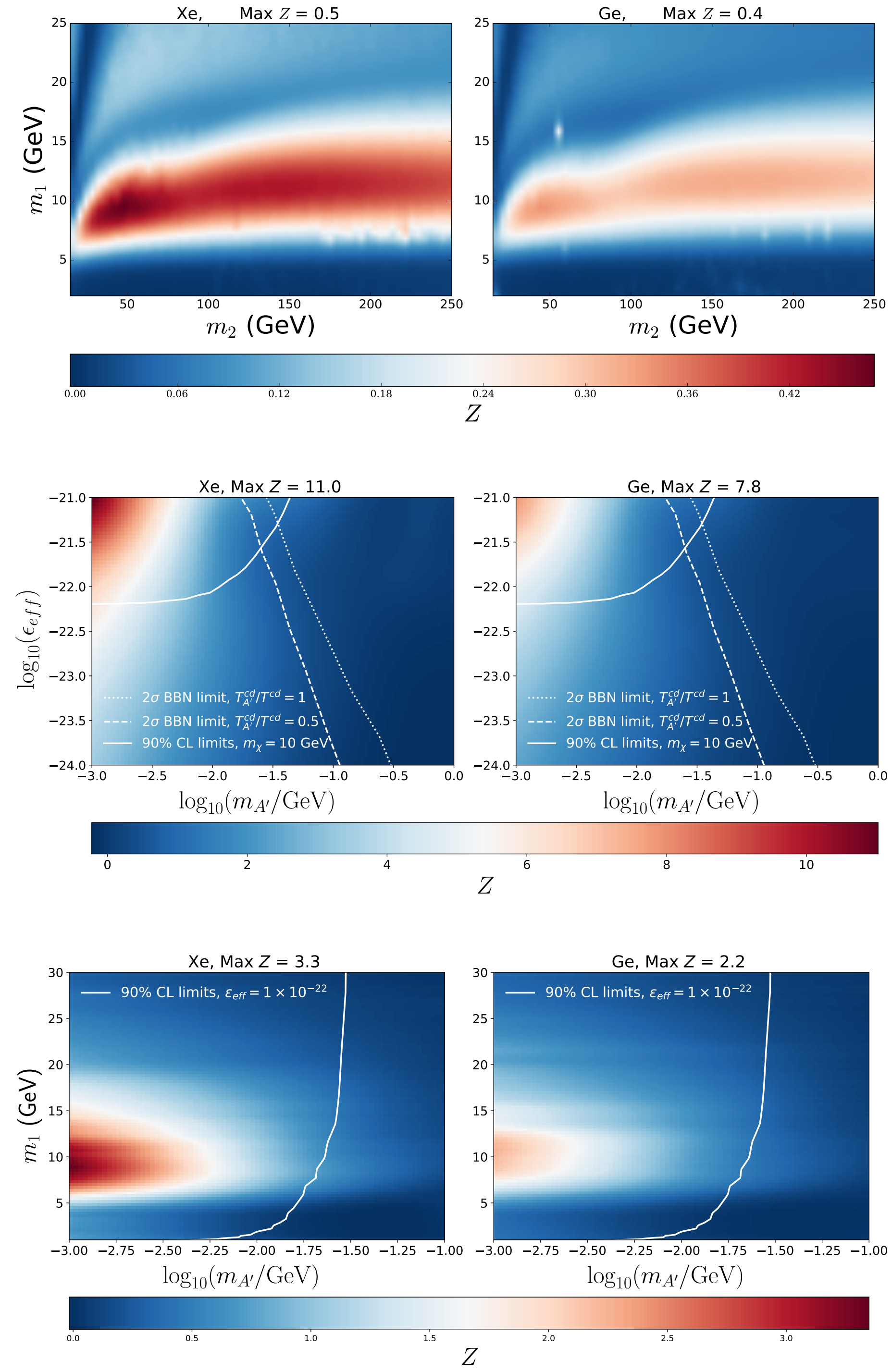

Fig. 5.5 Median significance Z with which and ADM model with a light mediator can reject the 1DM hypothesis in favour of the 2DM one. *Top:* $m_2 - m_1$ plane, with fixed $m_{A'} = 5$ MeV and $\epsilon_{\rm eff} = 1 \times 10^{-22}$. *Middle:* $\log_{10}(m_{A'}/\mathrm{GeV}) - \log_{10}(\epsilon_{\rm eff})$ plane, with fixed $m_2 = 50$ GeV and $m_1 = 10$ GeV. *Bottom:* $\log_{10}(m_{A'}/\mathrm{GeV}) - m_1$ plane, with fixed $m_2 = 50$ GeV and $\epsilon_{\rm eff} = 1 \times 10^{-22}$. The left panel is for Xe and the right one for Ge. In the last two panels the solid white line is the 90% CL upper limit on $\epsilon_{\rm eff}$ from the latest PandaX results [202], and in the middle panel the dashed and dotted-dashed lines are the 2σ *lower* bounds placed on the lifetime of the mediator from BBN [203] for two benchmark $T_{A'}^{\rm cd}/T^{\rm cd}$ ratios, 0.5 and 1.

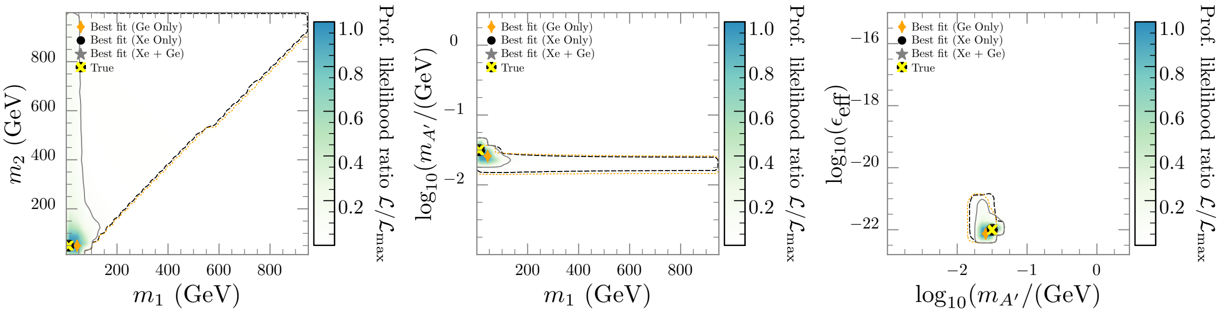

Fig. 5.6 Similar to Fig. 5.4 but for parameter estimation in the ADM scenario with a light mediator. *Left:* $m_1 - m_2$ plane. *Middle:* $m_1 - \log_{10}(m_{A'}/\text{GeV})$ plane. *Right:* $\log_{10}(m_{A'}/\text{GeV}) - \log_{10}(\epsilon_{\text{eff}})$ plane.

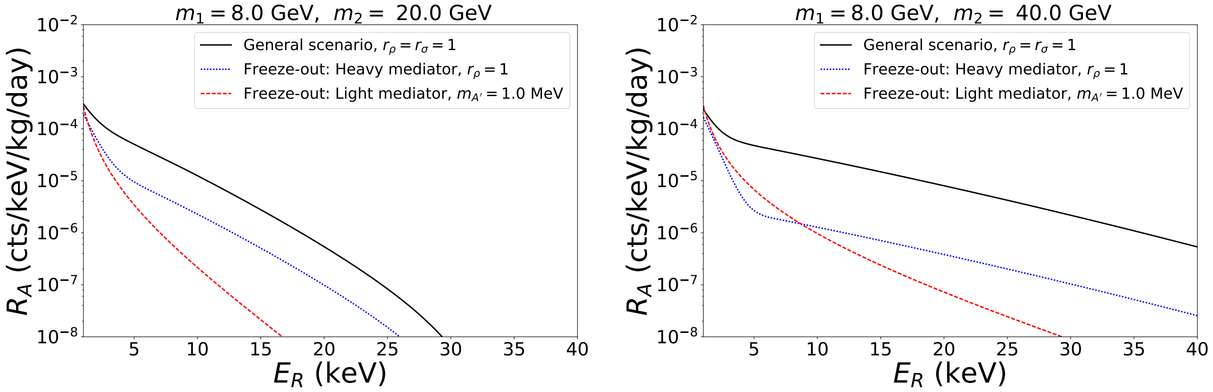

Fig. 5.7 Rates in a xenon experiment after imposing constraints from thermal freeze-out discussed in this section for the *general* model (solid black), with a heavy mediator (dotted blue) and a light mediator with mass $m_{A'} = 1$ MeV (dashed red). We use $m_1 = 8$ GeV. *Left:* $m_2 = 20$ GeV. *Right:* $m_2 = 40$ GeV.

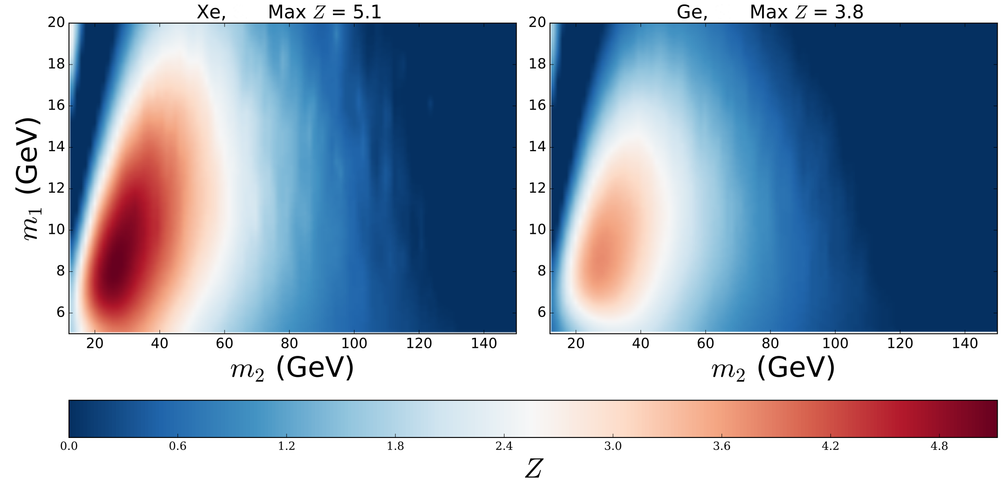

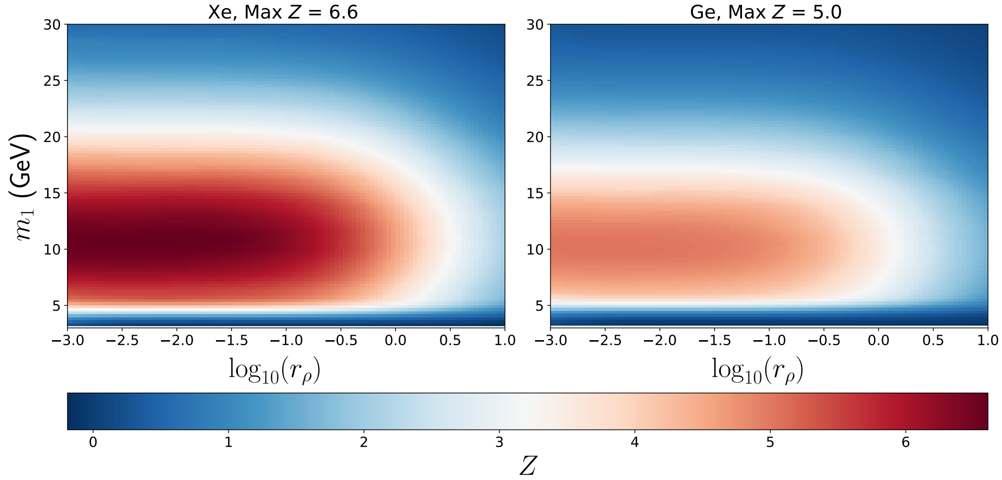

Fig. 5.8 Significance Z for thermal freeze-out with heavy mediators for scenarios where the local density scales as the global one. *Top:* $m_2 - m_1$ plane, with fixed $r_\rho = 1$. *Bottom:* $\log_{10}(r_\rho) - m_1$ plane, with fixed $m_2 = 30$. The left panels are for Xe, and the right ones for Ge.

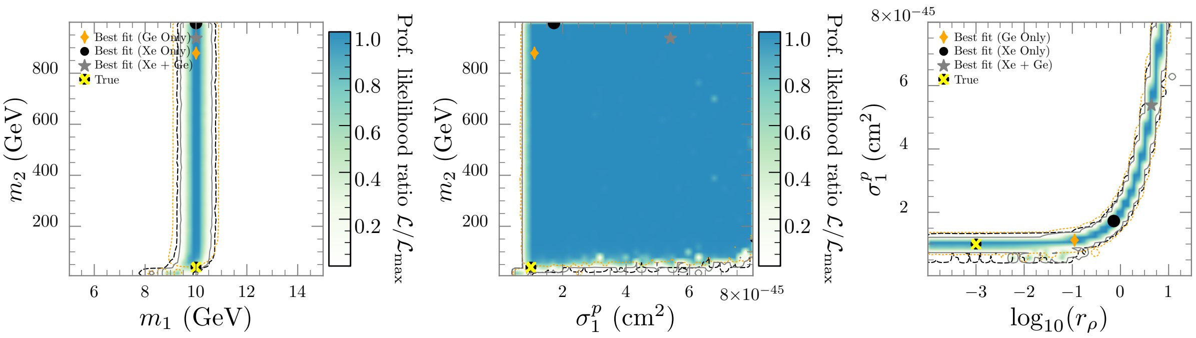

Fig. 5.9 Similar to Fig. 5.4 for parameter estimation for thermal freeze-out models with heavy mediators. *Left:* $m_1 - m_2$ plane. *Middle:* $\sigma_1^p - m_2$ plane. *Right:* $\log_{10}(r_\rho) - \sigma_1^p$ plane.

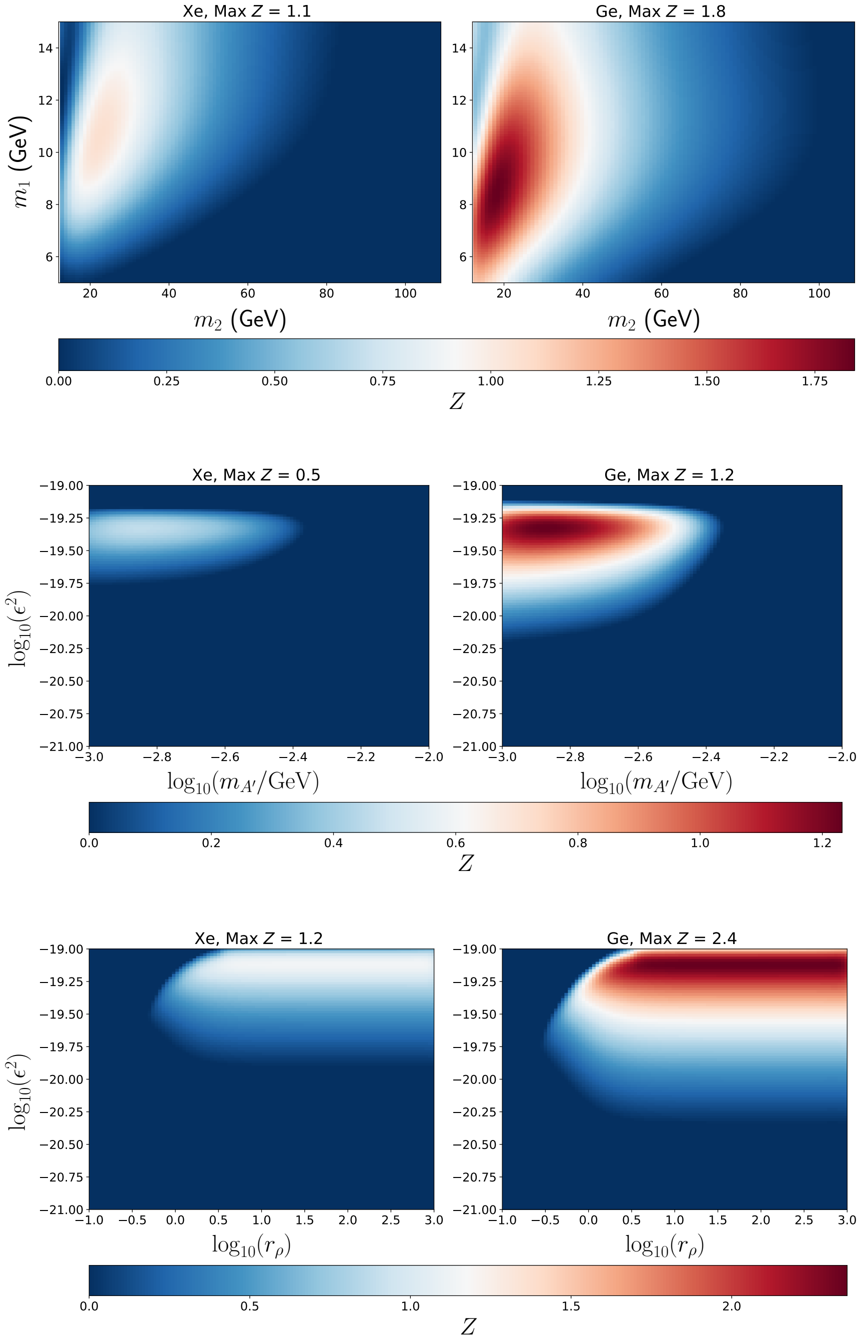

Fig. 5.10 Significance Z of thermal freeze-out models with light mediators. *Top:* $m_2 - m_1$ plane with fixed $r_\rho = 1$ and $m_{A'} = 1$ MeV. In the top panel, we dynamically set ϵ^2 to be the maximum allowed by PandaX for each given point in parameter space. The point of maximal Z in the $m_2 - m_1$ plane corresponds to $\epsilon^2 \sim 10^{-21}$. *Middle:* $\log_{10}(m_{A'}/\mathrm{GeV}) - \log_{10}(\epsilon^2)$ plane, with fixed and $r_\rho = 1$, $m_2 = 20$ GeV and $m_1 = 8$ GeV. *Bottom:* $\log_{10}(r_\rho) - \log_{10}(\epsilon^2)$, with fixed $m_{A'} = 1$ MeV. Here we set all points that violate the PandaX limit to $Z = 0$. The left panels are for Xe and the right ones are for Ge.

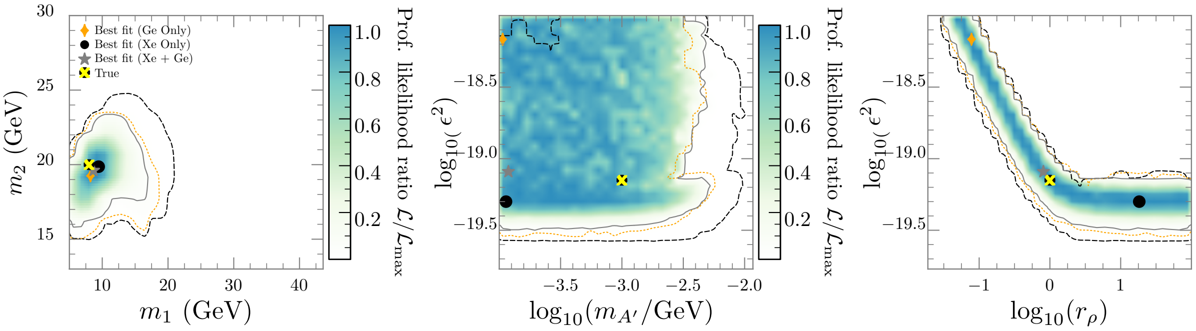

Fig. 5.11 Similar to Fig. 5.4 for parameter estimation for thermal freeze-out models with light mediators. *Left:* $m_1 - m_2$ plane. *Middle:* $\log_{10}(\epsilon^2) - \log_{10}(m_{A'})$ plane. *Right:* $\log_{10}(r_\rho) - \log_{10}(\epsilon^2)$ plane.

Chapter 6

Background and supplementary material for Publication three: The annually modulating dark matter signal

6.1 Motivation

For the next phase of the multi-component DM study, we turned to an investigation of the hypothesized annually modulating dark matter signal that should arise due to the relative motion of the Earth around the sun. Because the relative velocity of the detector with respect to the WIMPs depends on the time of year, the count rate will exhibit a sinusoidal dependence with time as graphically depicted in Fig. 6.1. For the simplest assumptions about the dark matter distribution in the halo, the flux is maximal in June and minimal in December. Annual modulation is a powerful signature for dark matter because most background signals are not expected to exhibit this kind of time dependence. This was a perfect test bed for a minimal two-component WIMP sector since two modulating signals that correspond to two distinct DM masses would yield a very distinct modulation signal arising from both components modulating out of phase.

6.2 Velocity distribution in Earth frame

The astrophysical distribution of DM velocities in the local vicinity of our solar system, $f(\mathbf{v}, t)$, is a hotly debated topic in astroparticle physics. This is because knowledge of this distribution is a major bottleneck for direct detection experiments

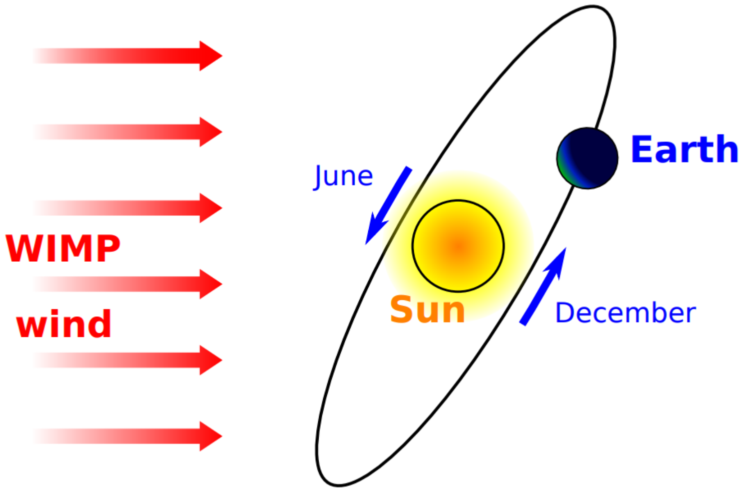

Fig. 6.1 A simplified view of the WIMP velocities as seen from the Sun and Earth. Due to the rotation of the Galactic Disk (containing the Sun) through the essentially non-rotating dark matter halo, the solar system experiences an effective "WIMP wind." From the perspective of the Earth, the wind changes throughout the year due to the Earth's orbital motion: the wind is at maximum speed around the beginning of June, when the Earth is moving fastest in the direction of the disk rotation, and at a minimum speed around the beginning of December, when the Earth is moving fastest in the direction opposite to the disk rotation. The Earth's orbit is inclined at $\sim 60^o$ relative to the plane of the Disk. Figure from [112].

in that it directly enters the observed scattering rate in a time dependent manner:

$$\text{DM-Nucleus scattering rate} \quad \sim \quad \text{Particle phsyics} \times \text{Velocity distribution} \; . \qquad (6.1)$$

This section contains a detailed overview of the time dependence of the annually modulating dark matter signal, which is rarely covered thoroughly in the literature. Specifically, we will cover the details arising from the Earth's orbit of the sun as well as notation conventions used in the literature. Consider the schematic in Fig. 6.2. In the rest frame of the Earth, we observe a 'wind' of DM as the sun orbits the galactic centre through the DM halo. In order to obtain the velocity distribution in the lab (Earth) frame we must transform the halo rest frame accordingly. This is obtained by means of a Galilean boost (assuming the dark matter is a WIMP and thus cold). Define (as introduced in section 3.2.3)

$$f(\mathbf{v}, t) \equiv \tilde{f}(\mathbf{v} + \mathbf{v}_{\text{obs}}(t)) \; , \qquad (6.2)$$

where $\mathbf{v}_{\mathrm{obs}}$ is the velocity of the Earth in the dark matter halo rest frame. $\mathbf{v}_{\mathrm{obs}}$ can be decomposed as follows:

$$\mathbf{v}_{\mathrm{obs}}(t) = \mathbf{v}_{\odot} + \mathbf{V}_{\oplus}(t) \tag{6.3}$$

where $\mathbf{v}_{\odot}$ is the suns motion relative to the halo rest frame and $\mathbf{V}_{\oplus}(t)$ is Earth's velocity relative to the sun. In the remainder of this section we will discuss in detail and derive the contributions to $\mathbf{v}_{\mathrm{obs}}(t)$.

Suns velocity through the DM halo: $\mathbf{v}_{\odot}$

The Sun's velocity through the galactic standard of rest, and therefore the DM halo, is

$$\mathbf{v}_{\odot} = \mathbf{v}_{\mathrm{LSR}} + \mathbf{v}_{\odot,\mathrm{pec}} \ , \tag{6.4}$$

where $\mathbf{v}_{\mathrm{LSR}}$ is the motion of the Local Standard of Rest and $\mathbf{v}_{\odot,\mathrm{pec}}$ km/s is the Sun's peculiar velocity relative to the local standard of rest. Both the local standard of rest and peculiar velocities are standard vectors with component values given in galactic coordinates and are adapted from Ref. [207]:

$$\mathbf{v}_{\mathrm{LSR}} = [8.50, 13.38, 6.49] \ \ \mathrm{km/s} \ , \tag{6.5}$$

$$\mathbf{v}_{\odot,\mathrm{pec}} = [0.0, 235, 0] \ \ \mathrm{km/s} \ . \tag{6.6}$$

Earth's trajectory relative to the sun: $\mathbf{V}_{\oplus}(t)$

The following analysis follows from the methods and parameter values of Ref. [208]. The Earth follows a counterclockwise orbit around the Sun, constrained to the ellipse shown in Fig. 6.2, with $a \approx 1.4960 \times 10^8$km – the length of the semi-major axis – labelling the perihelion. The Sun is located at one of the focal points, which is a distance $f = ae$ from the centre of the ellipse, with $e \approx 0.016722$ the eccentricity of the orbit. The eccentric anomaly is labelled E, and it is found geometrically using the procedure shown in Fig. 6.2; it is the angle between the perihelion, the centre of the ellipse, and a point on a fictitious circle of radius a. If t_p denotes the time of perihelion, then the angle E evolves with time through the well-known relation

$$g(t) = E - e \sin E, \quad g(t) = \omega\left(t - t_p\right) \ . \tag{6.7}$$

where $g(t)$ is commonly referred to as the mean anomaly and the time t is measured in years. The angle between the perihelion, the Sun and the Earth, denoted ν on

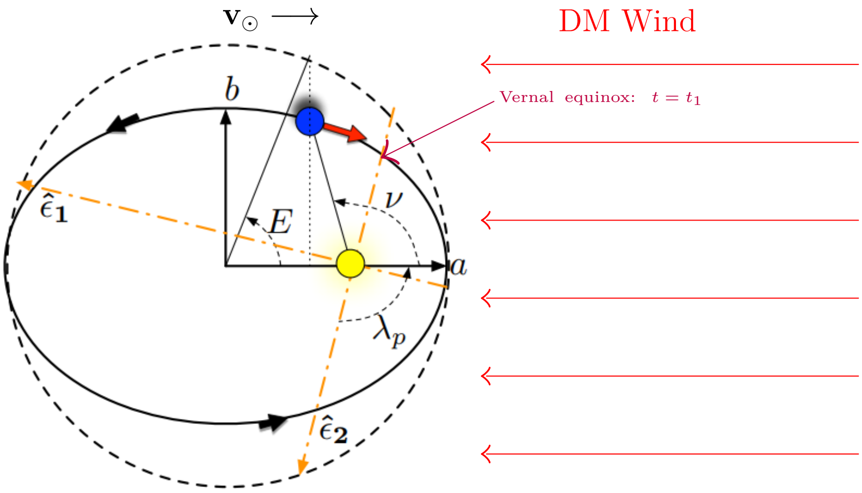

Fig. 6.2 The Earth (blue) orbits the Sun (yellow) counterclockwise along the solid-black ellipse. The perihelion of the orbit is denoted by a, which is also the length of the semi-major axis. The Sun is located a distance $f = ae$ from the center of the ellipse, where e is the eccentricity. The eccentric anomaly E is the angle between a fictitious point on the dashed-black circle of radius a, the center of the ellipse (circle), and the perihelion. The true anomaly ν is the angle between the perihelion, Sun, and Earth. At the vernal equinox, the vector $\hat{\boldsymbol{\epsilon}}_2$ points from the Earth to the Sun. Note that the Earth has just passed the vernal equinox in this diagram. The ecliptic longitude of the perihelion λ_p is the angle between the autumnal equinox, the Sun, and the perihelion. The projection of the Earth's rotational axis to the ecliptic plane (red arrow) points in the $-\hat{\boldsymbol{\epsilon}}_1$ direction. The obliquity of the Earth's rotational axis $\epsilon \sim 23.4^o$ is the angle between the Earth's rotational axis and $\hat{\epsilon}_3$ ($\hat{\epsilon}_3 = \hat{\epsilon}_1 \times \hat{\epsilon}_2$). The time of vernal equinox $t = t_1$ is defined when the Earth aligns onto the equatorial vector $\hat{\epsilon_2}$. The diagram is not to scale

Fig. 6.2 is called the true anomaly. It can be shown that up to second order in the eccentricity

$$\nu \approx g(t) + 2e \sin g(t) + \frac{5}{4} e^2 \sin 2g(t) \ . \tag{6.8}$$

The distance from the Earth to the sun is given by

$$r(t) = \frac{a\,(1 - e^2)}{1 + e \cos \nu} \ . \tag{6.9}$$

In Galactic coordinates defined in Sec. 3.2.3, the basis vectors that define the eclipse of the Earths orbit are given by [208]

$$\hat{\epsilon}_1 \approx [0.9940, 0.1095, 0.003116] \tag{6.10}$$

$$\hat{\epsilon}_2 \approx [-0.05173, 0.4945, -0.8677] \ . \tag{6.11}$$

The trajectory vector of the Earth throughout the year is then given by

$$\mathbf{r}(t) = r(t)\left[-\sin\lambda(t)\hat{\epsilon}_1 + \cos\lambda(t)\hat{\epsilon}_2\right] \tag{6.12}$$

where $\lambda(t) = \lambda_p + \nu(t)$ is the ecliptic longitude of the Earth measured counterclockwise with respect to the $\hat{\epsilon}_2$ axis; $\lambda_p \sim 102^o$ is the ecliptic longitude of the perihelion as shown in Fig. 6.2.

The vector of interest $\mathbf{V}_\oplus(t)$ is then calculated promptly ignoring $\mathcal{O}(e)$ terms in the eccentricity:

$$\mathbf{V}_\oplus(t) = \dot{\mathbf{r}}(t) \approx V_\oplus\left(\hat{\epsilon}_1 \cos\omega\,(t - t_1) + \hat{\epsilon}_2 \sin\omega\,(t - t_1)\right)\ , \tag{6.13}$$

where $\omega = 2\pi/\text{year}$ is the orbital frequency, $V_\oplus = 29.79$ km/s is the mean speed of the Earth, and t_1 is the time of vernal equinox.

6.2.1 Defining the phase of the angular modulation

Equation 6.13 is quoted often in the literature, however the time t_1 is not very intuitive, especially in the context of DM direct detection. What is often done is to transform t_1 into a more phenomenologically useful quantity, namely:

$$t_0 = \text{ the time of year at which } |\mathbf{v}_{\text{obs}}| \text{ is maximised.} \tag{6.14}$$

This is done via the transformations

$$\cos\omega\,(t_0 - t_1) = \frac{b_1}{\sqrt{b_1^2 + b_2^2}}, \quad \sin\omega\,(t_0 - t_1) = \frac{b_2}{\sqrt{b_1^2 + b_2^2}}\ , \tag{6.15}$$

where $b = \sqrt{b_1^2 + b_2^2}$ for $b_i \equiv \hat{\varepsilon}_i \cdot \hat{\mathbf{v}}_\odot$ [114]. The parameter t_0 is often referred to the *phase* of the annual modulation in the literature. From [113] we will adopt $t_0 = 0.41$, which corresponds to about June 2nd.

6.2.2 Kinematic cut-off

There exists a kinematic cut off in the recoil spectrum $R(E,t)$ for when

$$v_{\text{esc}} + v_{\text{obs}}(t) < v_{\text{min}}\ . \tag{6.16}$$

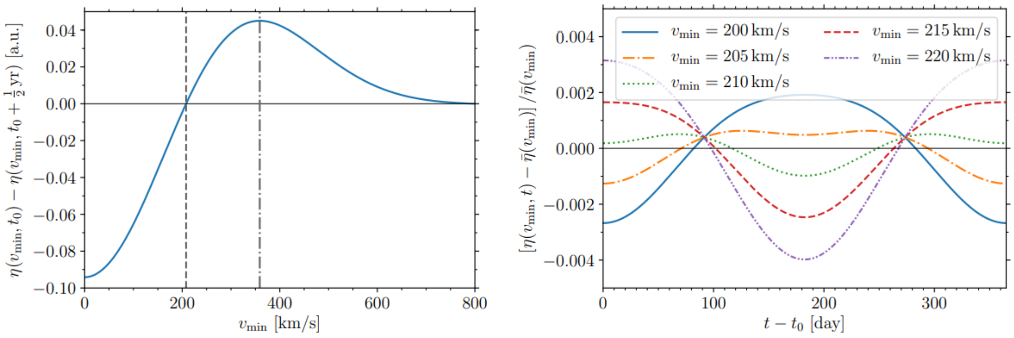

Fig. 6.3 Figure from Ref. [209]. Left: Amplitude of the modulation (in arbitrary units) as a function of v_{min}. The vertical grey dashed and dash dotted lines indicated the values of v_{min} for which the phase flip occurs $v_{\text{min}} \sim 210$ km/s and for which the modulation amplitude becomes maximal $v_{\text{min}} \sim 360$ km/s. Right: Time dependence of the modulation signal parameterized as the relative difference of the mean inverse speed η defined in Eq. 3.45 from its average value as a function of time over a year for different values of v_{min} indicated in the legend.

This originates from the constraint that requires no DM to have a velocity greater than that of v_{esc}. The energy threshold will be

$$\frac{2\mu^2\left(|v_{\text{esc}}| + |v_{\text{obs}}(t)|\right)^2}{m_N} < E_{\text{Cut-off}} \tag{6.17}$$

Any recoil energy that does not satisfy this inequality is kinematically forbidden.

6.3 The modulating Dark Matter signal

The time-dependence introduced in section 6.2 will manifest in the total scattering rate as a constant (non-modulating) piece plus a time dependent (modulating) piece:

$$\mathcal{R}\left(E_R, t\right) = \bar{R}\left(E_R\right) + \mathcal{M}\left(E_R, t\right) \tag{6.18}$$

where

$$\mathcal{M}\left(E_R, t\right) = \mathcal{M}\left(E_R\right)\cos\left[2\pi\left(t - t_0\right)\right] \; . \tag{6.19}$$

$\mathcal{M}\left(E_R\right)$ is called the “modulation amplitude”. All of the time dependence in the modulating rate is wrapped up in the mean inverse speed $\eta(v_{\text{min}}, t)$. Hence, one can visualize the modulation properties using η as a proxy. Without any assumed perturbations, the rate will modulate sinusoidally and so the modulation amplitude is simply derived by taking the difference between when the signal is maximized and minimized, i.e, when the Earth is travelling directly into/with the DM wind. As defined in section 6.2.1, this occurs at $t_0 = 0.41$ and $t_0 + 0.5$ yrs. Figure 6.3 shows

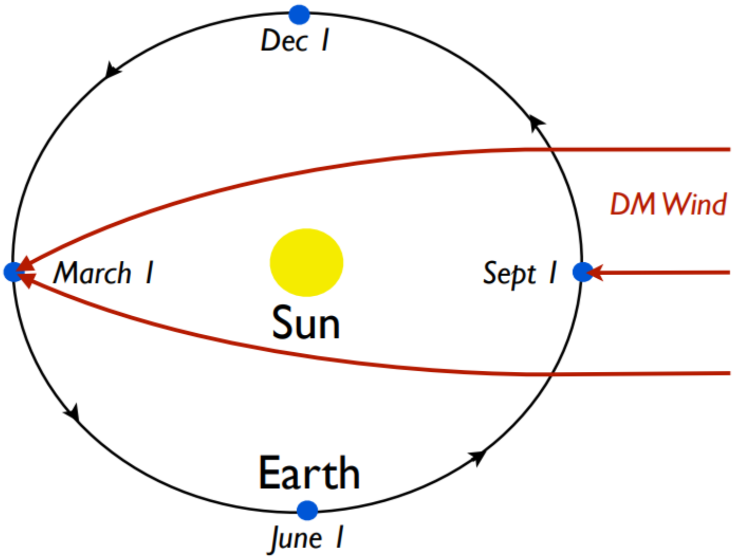

Fig. 6.4 An illustration of the how the phase space density of DM changes due to the gravitational focusing of unbound DM particles in the DM wind. The phase-space density of DM at Earth is greater around March 1 than around September 1 due to this effect.

the modulation amplitude as a function of v_{min} as well as a few examples of the time dependence of the modulation for varying v_{min}. At approximately $v_{\text{min}} \sim 210$ km/s the modulation amplitude flips sign. This phenomena was coined the *phase flip* (see Ref. [210] and references therein), though this should not be confused with the phase of the modulation t_0 introduced in Eqn. 6.14, which is the time of year that the rate is maximized *or* minimized. Fig. 6.3 right shows how the phase flip (or more accurately, π phase shift) manifests in the modulating signal as an explicit function of v_{vmin}.

6.4 Gravitational focusing

Gravitational focusing (GF) is a correction to the time dependence of the local DM density, which manifests in the diret detection rate via the velocity profile due to the gravitational influence of the sun on the local DM wind [147]. A basic sketch of the phenomenon can be seen in Fig. 6.4. We use the various parameterizations taken from Ref. [211].

$$\rho f(\mathbf{v}, t) = \rho_\infty \tilde{f}\left(\mathbf{v}_\odot + \mathbf{v}_\infty\left[\mathbf{v}_\mathbf{s}\right]\right) \ , \tag{6.20}$$

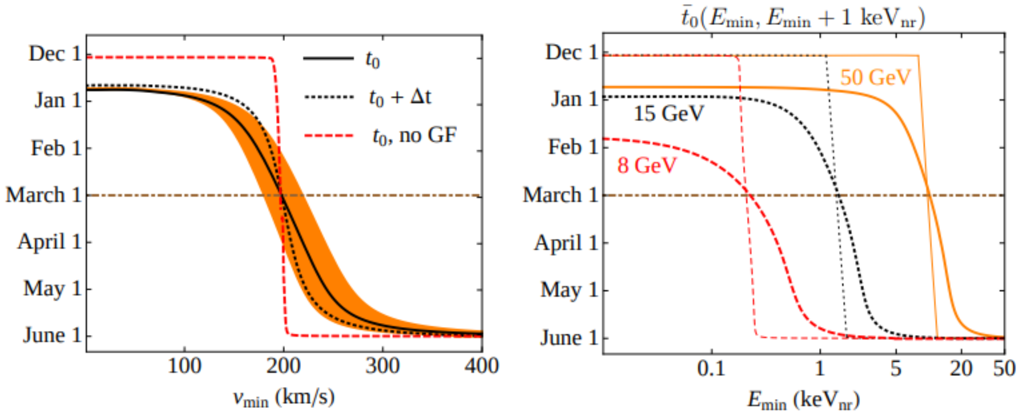

Fig. 6.5 (left) The time t_0 when the differential rate is maximized changes as a function of $v_{\min}$. Without GF, this time is around June 1 for $v_{\min}$ and 200 km/s and ∼half a year earlier for smaller vmin. With GF, t_0 is still approximately June 1 at high vmin, but as vmin decreases, GF becomes more significant, and t_0 ultimately asymptotes to a value $\sim$ 21 days later than that expected with no GF. The dot-dashed brown line marks March 1, which is the time when GF is maximal. The orange region roughly accounts for the astrophysical error in t_0 by varying v_0 from 180 to 260 km/s. (right) The time $\bar{t}_0$ that maximizes the binned rate as a function of the minimal bin energy E_{min} for DM masses 8, 15, and 50 GeV (thick lines). The thin lines show the corresponding phases when GF is neglected. We assume 1 keVee energy bins at a germanium detector; note that the shapes of these curves are highly sensitive to the bin size and target nucleus. Figure from Ref. [211].

where $\mathbf{v_s} \equiv \mathbf{v} + \mathbf{V}_\oplus$. The GF corrections enter in the following:

$$\mathbf{v}_\infty\left[\mathbf{v_s}\right] = \frac{v_\infty^2 \mathbf{v_s} + v_\infty \left(GM_\odot/r_s\right)\mathbf{\hat{r}_s} - v_\infty \mathbf{v_s}\left(\mathbf{v_s}\cdot\mathbf{\hat{r}_s}\right)}{v_\infty^2 + \left(GM_\odot/r_s\right) - v_\infty\left(\mathbf{v_s}\cdot\mathbf{\hat{r}_s}\right)}\ , \tag{6.21}$$

where $v_\infty^2 = v^2 - 2GM_\odot/r_s$ comes from requiring energy conservation and $\mathbf{\hat{r}_s}$ is the time-dependent unit vector that points from the Sun to the Earth, the magnitude of which is the distance between the sun and the earth r_s. The full vector is given by Eqn. 6.12. Figure 6.5 demonstrates the effects of GF on the phase of the modulated differential rate.

A secondary result of the work presented in publication 3 is that gravitational focusing has a non-trivial effect on the modulating signal, especially for heavier DM masses. While we indeed derive and display this result in the main results of publication 3 in chapter 7, we do not emphasize that GF is a correction that necessarily must be taken into account always, since it will always be present irrespective of the DM model being investigated.

6.5 The DAMA/LIBRA experiment as a test bed for two-component dark matter

At the time that we undertook this study, the only experiment with a significant amount of detector exposure that was also actively looking for a modulating signal was the the DAMA/LIBRA apparatus located at the Gran Sasso laboratory in Italy [212, 213]. There is one long-standing exception to the null results from direct detection experiments: the DAMA/LIBRA collaboration has been reporting an excess in their DM search for more than a decade, claiming a statistical significance of more than 9σ, compatible with a ~ 10 GeV or ~ 70 GeV WIMP [214–217]. Unlike the majority of WIMP direct detection experiments, which seek to measure the total rate $\mathcal{R}\left(E_R, t\right)$ shown in Eq. 6.18[1], by accounting for and minimizing all background sources, the DAMA/LIBRA detector simply collects all events and aims to observe the modulation $\mathcal{M}\left(E_R, t\right)$. Although the rate of the modulated signal $\mathcal{M}\left(E_R, t\right)$ is much smaller than the total scattering rate, this approach is advantageous because it offers powerful background rejection: most backgrounds are not expected to be modulated, and if any backgrounds would be modulated their period should differ from 1 year and/or their phase should be different from that of the DM signal for which the maximum for most recoil energies is expected around June 2nd. There is strong statistical tension between the DAMA/LIBRA claim and the majority of other direct searches. No other experiment has produced anything other than a null result. Most people in the field have an opinion on this tension and it's origin (i.e dark matter, standard model background or otherwise). A full review of the DAMA/LIBRA tension, and potential standard model reconciliations are beyond the scope of this work, but refer to Refs. [214, 218, 219] and references therein for a thorough overview. To summarize, in light of this tension, many attempts have been made to reconcile the DAMA/LIBRA claim with the null results using other types of interactions, e.g. all allowed operators in the non-relativistic effective field theory for WIMP-nucleus scattering or by using halo-independent methods. In addition, numerous proposals to explain the signal observed by DAMA/LIBRA by modulated backgrounds have been brought forward, all of which have been refuted by the DAMA/LIBRA collaboration.

Recently, the DAMA/LIBRA collaboration has released first results from the upgraded DAMA/LIBRA phase2 experiment [220] whereby they almost double the total exposure of the DAMA/LIBRA experiment as well as allow for a lower recoil

---

[1] Measuring the total rate requires extremely good rejection of background events as well as knowledge of the remaining backgrounds.

energy E_R threshold of 1 keV electron equivalent (keVee) compared to the 2 keVee threshold of DAMA/LIBRA-phase1. As soon as the first results were made public, it was immediately observed that the previously held DM interpretations were no longer statistically valid with the lowest energy bin in the recoil energy spectrum. Indeed we confirmed this ourselves and show the result in section 6.6.1. Ref. [221] considered three possible types of DM interactions with the DAMA detector: canonical spin-independent (SI), SI isospin-violating (IV), and spin-dependent (SD) interactions, all within the standard halo model. They found that in all cases the DAMA/LIBRA modulation results appear to be in severe tension with the null results from other direct detection searches, explicitly demonstrating that it was this new lowest energy bin centred at 1.5 keVee that was responsible. Several months later, and after the publication of the work shown in chapter 7, the DAMA/LIBRA collaboration itself released an in depth corollary to the inconsistency to salvage a DM interpretation [222]. They found that fine-tuning the DM sector to include a slew of new interaction types including inelastic and isospin-violating, as well as detector effects and nuisance parameters like the channelling of low energy ions along planes of the NaI(Tl) DAMA crystals and quenching factors provided tenuous fits to the new phase-2 data.

6.5.1 Energy resolution and quenching factors of the DAMA/LIBRA apparatus

In this section we will go over some of the DAMA/LIBRA-specific details of the rate calculations first introduced in section 3.2, which were left out of the manuscript of publication 3. Recall from Eqn. 3.50 that the differential response function $\phi(E_R, E_{\rm ee})$ is folded in with the differential recoil rate in order to determine the number of expected events to be observed in a detector. Since in publication 3 we were more accurately simulating a real detector, we adopt the energy resolution function for the DAMA/LIBRA detector that was employed by Ref. [55]

$$\phi\left(E_R, E_{\rm ee}\right) = \frac{1}{2\pi\sigma^2\left(Q, E_R\right)} e^{-\frac{\left(E_{\rm ee}-QE_R\right)^2}{2\sigma^2\left(QE_R\right)}} , \tag{6.22}$$

where the target-dependent quenching factors $E_{\rm ee} = Q\,E_R$ (we use $Q_{\rm Na} = 0.3$, $Q_{\rm I} = 0.09$ for Sodium and Iodide nuclei respectively). The uncertainty in the Gaussian in Eqn. 6.22 is given by

$$\sigma\left(QE_R\right) = \alpha\sqrt{QE_R} + \beta QE_R \tag{6.23}$$

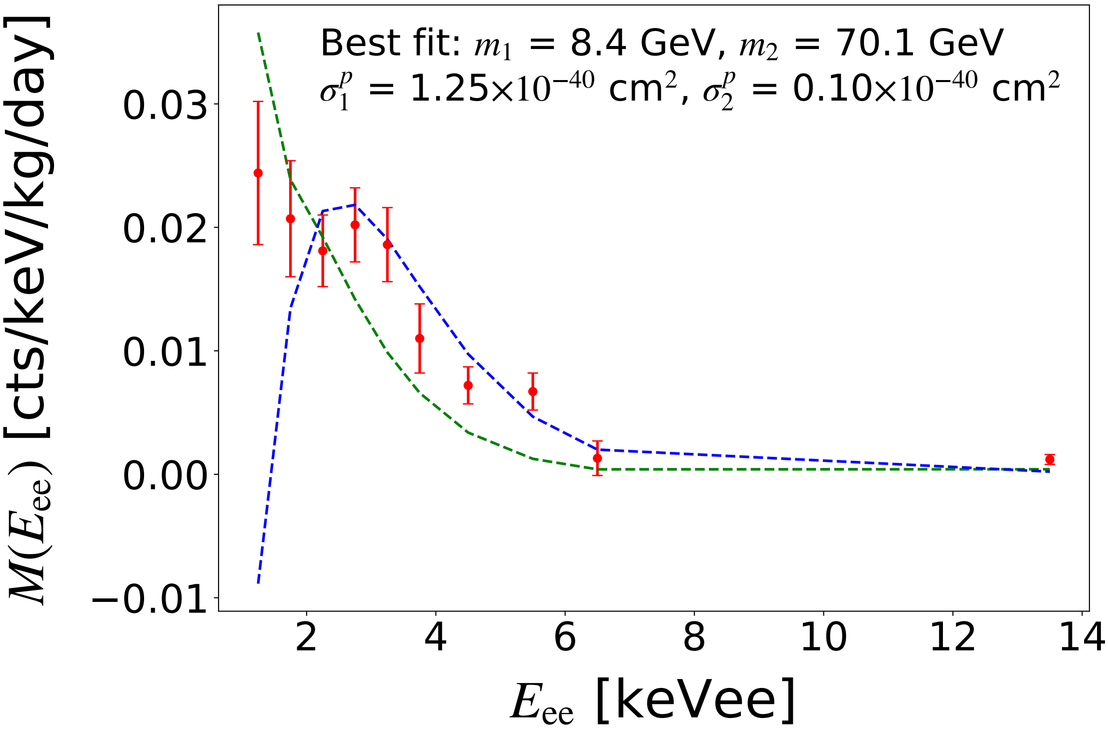

Fig. 6.6 Best fit light and heavy DM solutions to the DAMA/LIBRA phase-2 data after re-binning in accordance with ref. [221]. Modulation amplitude (in units of [counts/day/kg/keVee]) is shown as a function of ionization energy E_{ee} for the best heavy (blue) and light (green) DM interpretations. DM masses, interaction cross-sections and p-values can be found in table 7.1.

where MT is the detector mass×exposure time. This parameter is often refered to as just the exposure. The parameters $\alpha = (0.448 \pm 0.035)\sqrt{\text{keVee}}$ and $\beta = (9.1 \pm 5.1) \times 10^{-3}$.

6.6 Supplementary results for publication 3

In this section we briefly reveal some plots that were deemed complementary to the final manuscript of publication 3. The context for the next subsections is better understood in conjunction with the published manuscript presented in chapter 7.

6.6.1 One component best fits to the DAMA/LIBRA Phase-2 recoil energy spectrum

The first thing we did after being made aware of the DAMA/LIBRA phase-2 self inconsistency discussed in section 6.5 was reproduce the best fit single-species WIMP interpretations with a standard SI interaction. Figure 6.6 shows the best fit light

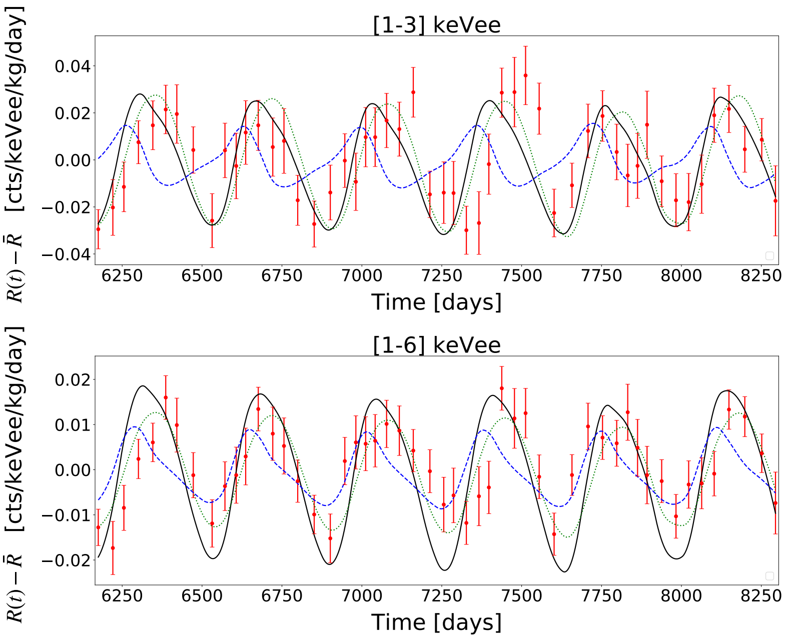

Fig. 6.7 Best fit two component DM signal to the DAMA/LIBRA phase-2 time dependant data in *upper*: the [1-3] keVee energy bin and *lower*: [1-6] keVee energy bin. Shown are the light (green line) and heavy (blue line) WIMP components as well as the combined modulation signal (black). Fit parameters (DM mass, cross sections and relative densities) are taken from table 7.2.

and heavy DM solutions after including all standard effects in addition to corrections from gravitational focusing. The parameters and statistical exclusion strengths of these fits can be found in table 7.1.

6.6.2 Time dependent fits 1-3, 1-6 keVee bins

The fits shown in Fig. 6.6 to the recoil energy spectrum can be realized in time space and presented on a plot of the modulation residual, defined as the modulation at a time t minus the average observed rate. The DAMA/LIBRA collaboration only present the residual (that is, not the *total* number of events they observed) averaged over energy bins [1-3],[1-6] and [2-6] keVee. In a proper analysis, one would fit the full time-dependent signal in every energy bin the detector is sensitive to. However, as described in our manuscript in the next chapter, this cannot be done due to lack of data made publicly available. For publication 3 we undertook the best possible statistical examination of the data we could, but what we did not publish are what our best fit two-component DM spectrum looks like as a time-dependent modulating signal in the [1-3] keVee and [1-6] keVee energy bins. These fits are shown in Fig. 6.7. The reason for the choice of these energy bins is to explicitly show the lower energy threshold ($E_{\mathrm{min}} = 1$ keVee), where we expect non sinusoidal GF effects to be most prominent, and hence most demonstrative.

Chapter 7

Publication three: Time-dependent rate of multicomponent dark matter: Reproducing the DAMA/LIBRA phase-2 results

Statement of Authorship

Title of Paper	Time-dependent rate of multicomponent dark matter: Reproducing the DAMA/LIBRA phase-2 results
Publication Status	Published
Publication Details	J. Herrero-Garcia, A. Scaffidi, M. White, and A. G. Williams. Time-dependent rate of multicomponent dark matter: Reproducing the DAMA/LIBRA phase-2 results. Phys. Rev., D98(12):123007, 2018.

Principal Author

Name of Principal Author (Candidate)	Andre Scaffidi		
Contribution to the Paper	Writing of manuscript Numerical results Theoretical results		
Overall percentage (%)	80%		
Certification:	This paper reports on original research I conducted during the period of my Higher Degree by Research candidature and is not subject to any obligations or contractual agreements with a third party that would constrain its inclusion in this thesis. I am the primary author of this paper.		
Signature		Date	

Co-Author Contributions

By signing the Statement of Authorship, each author certifies that:

i. the candidate's stated contribution to the publication is accurate (as detailed above);

ii. permission is granted for the candidate in include the publication in the thesis; and

iii. the sum of all co-author contributions is equal to 100% less the candidate's stated contribution.

Name of Co-Author	Juan Herrero-Garcia		
Contribution to the Paper	Writing of manuscript Numerical results Theoretical results		
Signature		Date	17/02/2020

Name of Co-Author	Anthony G. Willimas
Contribution to the Paper	Writing of manuscript Theoretical results

Signature		Date	31/01/2020

Name of Co-Author	Martin White		
Contribution to the Paper	Writing of manuscript Numerical results Theoretical results		
Signature		Date	21/1/20

Abstract

The current paradigm for dark matter direct detection is to assume that the dark sector is solely composed of a single particle species. In this short paper, we make the observation that dark matter comprising both a light and a heavy component that modulate out of phase leads to interesting phenomenology in annual modulation experiments. For an illustrative example, we use the recently released DAMA/LIBRA phase-2 results with a lower energy threshold. Immediately after, it was argued that a one-component spin- independent dark matter explanation of the observed annual modulation is strongly disfavored or excluded unless isospin-violating couplings are invoked. We show that a simple two-component extension can reproduce the observed spectrum without the need to invoke fine-tuned couplings. Using the publicly available DAMA/LIBRA data, we perform a fit of the DAMA/LIBRA energy spectrum of the annual modulation amplitude to a scenario with two dark matter components. We also take into account how gravitational focusing affects the phases of the light and a heavy components differently, which leads to nontrivial effects in the total time-dependent rate. Our results show that there exists a unique solution in agreement with the data in the simplest case of isospin-conserving couplings with equal cross sections. The distinctive features found in this work are crucial for a dark matter interpretation of any observed annual modulation.

7.1 Introduction

Dark matter (DM) is one of natures greatest enigmas. Until now evidence for its existence stems from its gravitational interactions. However, it is by no means guaranteed that just a single state or particle (1DM) constitutes the whole dark sector, which may have a multi-component nature similarly to the visible sector. Multi-component DM in direct detection has only been studied in a few works which have then only focused on time-averaged (not modulated) event rates [127–133, 195]. A generic prediction of two-component DM (2DM) is the presence of kinks in the differential event rates in mono-target experiments due to the different DM components [195]. In the following study, we observe another interesting prediction of

2DM in annual modulation experiments. Namely, that a light and heavy component will modulate out of phase, producing non-trivial modulation ampli- tudes that significantly affect the interpretation of the results. To study this effect, we adopt a purely phenomenological approach to try to reproduce the modulated signal observed by the DAMA/LIBRA collaboration [56, 223] (denoted by DAMA in the following). We do so without going into further details regarding the model building, which would affect the interactions anda the abundances of the DM components. This is in fact studied for averaged rates in Ref. [224]. In this work we also include gravitational focusing (GF) [147, 148, 200], which has a non-trivial effect on the 2DM time dependence of the direct detection rates, and therefore on the modulation amplitude and phase. Although in our work we use the DAMA data, the physics discussed and the results obtained in the following apply to generic time-dependent signals of multi-component scenarios.

Very recently, the DAMA collaboration released the long-waited phase-2 results with a lower energy threshold, with two new energy bins below 2 keVee [85, 225]. As first pointed out in version 3 of Ref. [226], and studied in Ref. [209] (see also Ref. [227]), the consistency of the DM interpretation of DAMA's signal is now under question both for the light and the heavy DM mass solutions mentioned above for vanilla isospin-conserving spin-independent (SI) interactions, even before considering its compatibility with other null-result experiments. This is because below 2 keVee, the direct detection rates for the two standard DM solutions behave very differently with decreasing recoil energy: the light DM gives rise to scatterings off iodine, increasing its rate significantly, while for the heavy DM (that scatters predominately off iodine) the modulation amplitude decreases, eventually giving rise to a phase flip. This was already pointed out in Ref. [228]. We confirm in this work that for SI interactions the energy spectrum for the one-component DM scenario (1DM) is disfavoured. Indeed we find that the heavy solution is excluded at an even higher significance level when GF effects are accounted for.

The current significance for the modulation in the complete DAMA data set is $12.9\,\sigma$. The DAMA collaboration, as well as several independent studies, have not found that modulated backgrounds like those of neutrons, muons, solar neutrinos or radon can be responsible for the signal [229–234]. Until the very latest phase-2 results, under reasonable particle physics and astrophysical assumptions, the signal was consistent in both amplitude and phase with that expected from Weakly Interacting Massive Particles (WIMPs). Assuming the Standard Halo Model (SHM) and elastic scattering, the best-fit masses (and cross sections) are well-known: a light DM with mass ~ 10 GeV scattering mainly on sodium (light mass solution), or a heavy DM with mass ~ 70 GeV scattering mainly on iodine (heavy mass solution) [164, 183, 235–240]. We show that the modulation observed by DAMA at low energies can be reproduced in a natural way by a combination of two DM particles (2DM), without the need to invoke fine-tuned isospin-violating couplings[1].

The main issue with a DM interpretation of the DAMA modulation is that there is currently no accepted explanation that reconciles DAMA's signal with the absence of a positive signal in all other experiments [150, 183, 242–244], even independently of the DM velocity distribution [135, 145, 146, 245–248]. This has motivated a large experimental effort to try to reproduce the DAMA experiment with NaI crystals in order to independently either confirm or reject its results [160, 249–252]. The SABRE experiment [250] plans to have a northern and southern hemisphere pair of NaI detectors to search for a seasonal correlation or anti-correlation of any DAMA-like modulation signal [253]. Interestingly, the COSINUS experiment [251] aims to also measure the constant rate by developing a cryogenic detector. A null result in the latter experiment may rule out a DM explanation of DAMA model-independently [226].

This letter is structured as follows. In Sec. 7.2 we introduce the relevant notation to describe the DM time-dependent signal in direct detection experiments. In Sec. 7.3 we fit the binned amplitude of the DAMA modulation. We do this by generating pseudo-mock data from a modulating 2DM signal, including GF, and extracting the modulation amplitude by fitting a sinusoid to the resulting time-dependent signal. This allows us to draw conclusions regarding the effect of GF and the non-sinusoidal component. In this section we also conduct the analysis for a single light/heavy DM to compare with results from other studies. We give our conclusions and final remarks in Sec. 7.4.

7.2 The dark matter direct detection signal

In this section, we present the relevant expressions for the direct detection of 2DM, with individual DM masses $m_{1,2}$ (we take $m_1 < m_2$), SI cross-sections with protons $\sigma^p_{1,2}$, and local energy densities $\rho_{1,2}$. We use $\rho_1 + \rho_2 = \rho_{\rm loc}$, where $\rho_{\rm loc}$ is the local DM mass density. We take the astrophysical values of Ref. [195], and use the notation $r_\rho \equiv \rho_2/\rho_1$ and $r_\sigma \equiv \sigma^p_2/\sigma^p_1$.

---

[1] We note that there have been studies that show that other effective operators can relieve the DAMA self-tension [227]. Also the same authors claim that compatibility with other null results can be achieved in a proton-philic spin-dependent inelastic scenario when the DM velocity distribution departs from Maxwellian [241].

For 2DM with SI interactions, we can parameterise the differential event rate produced on a target nucleus with mass number A as [195]:

$$\begin{aligned}\mathcal{R}_A(E_R,t) = {} & \frac{x_A\,\rho_{\rm loc}\,\sigma_1^p}{2\,(1+r_\rho)\,\mu_{p1}^2}\,A^2F_A^2(E_R) \\ & \times\left[\frac{\eta(v_{m,A}^{(1)},t)}{m_1}+\frac{r_\rho r_\sigma\mu_{p1}^2}{\mu_{p2}^2}\frac{\eta(v_{m,A}^{(2)},t)}{m_2}\right],\end{aligned} \tag{7.1}$$

where here we define the halo integral as

$$\eta(v_{m,A}^{(\alpha)},t) = \int_{v>v_{m,A}^{(\alpha)}} d^3v\,\frac{f_{\rm det}^{(\alpha)}(\vec{v},t)}{v}\,. \tag{7.2}$$

From kinematics, the DM particle α ($\alpha = 1,2$) is required to have a velocity larger than $v_{m,A}^{(\alpha)} = \sqrt{m_A E_R/(2\mu_{\alpha A}^2)}$ to produce a recoil of energy E_R. m_A is the mass of the nucleus, x_A its mass faction in the detector, $\mu_{\alpha A}$ is the reduced DM-nucleus mass and $F_A(E_R)$ is its nuclear form factor, for which we use the Helm parametrisation [141, 142]. In Eq. (7.2) $f_{\rm det}^{(\alpha)}(\vec{v},t)$ describes the distribution of DM particle velocities in the detector rest frame. In the following we use the SHM, i.e., a Maxwellian velocity distribution, with equal velocity dispersions for both DM components (see Ref. [224] for a study regarding this assumption). As before, the total rate is given by the sum of the contributions on each target nucleus, i.e., $\mathcal{R}(E_R,t) = \sum_A \mathcal{R}_A(E_R,t)$. The rate for 1DM is obtained from Eq. (7.1) in the limit $r_\rho = 0$.

In this work we deal with the time-dependent signal caused by the motion of the Earth around the Sun [110, 111]. The total differential event rate can be decomposed as (see for instance Refs. [112, 145, 146, 164])

$$\mathcal{R}_A^{(\alpha)}(E_R,t) \equiv \bar{R}_A^{(\alpha)}(E_R) + \mathcal{M}_A^{(\alpha)}(E_R,t)\,, \tag{7.3}$$

where $\bar{R}_A^{(\alpha)}$ is the time-averaged rate and $\mathcal{M}_A^{(\alpha)}(E_R,t)$ the time-dependent signal. In the following we assume that all the time-dependence stems from the velocity of the Earth $v_e(t)$, which is a reasonable assumption for the time scales of direct detection experiments. For isotropic and sufficiently smooth DM haloes, to leading order on $v_e(t)$,[2] the time-dependent signal consists of the annual modulation,

$$\mathcal{M}_A^{(\alpha)}(E_R,t) = \mathcal{M}_A^{(\alpha)}(E_R)\cos[2\pi(t-t_0(v_{m,A}^{(\alpha)})]\,, \tag{7.4}$$

---

[2] A nonsinusoidal modulation is expected when higher-order harmonics, which are, however, suppressed by extra powers of v_e , are considered [147, 148, 229].

where $t_0(v_{m,A}^{(\alpha)})$ is the phase of the modulation and

$$\mathcal{M}_A^{(\alpha)}(E_R) = \frac{1}{2}\left[\mathcal{M}_A^{(\alpha)}(E_R, t_{\rm J}) - \mathcal{M}_A^{(\alpha)}(E_R, t_{\rm J} + 0.5)\right] , \tag{7.5}$$

is the amplitude. $t_{\rm J}$ $(t_{\rm J} + 0.5)$ measured in years corresponds to June (December) 1st, which for minimum velocities $v_{m,A}^{(\alpha)}$ above $\sim 200\,\rm kms^{-1}$ is the time of the year when the velocity of the WIMP flow in the Earth's frame is maximum (minimum). For $v_{m,A}^{(\alpha)} < 200\,\rm kms^{-1}$, the situation is the opposite: $t_{\rm J}\,(t_{\rm J} + 0.5)$ $t_{\rm J}$ $(t_{\rm J} + 0.5)$ corresponds to minimum (maximum) WIMP flow, such that $\mathcal{M}_A^{(\alpha)}(E_R)$ becomes negative. In other words, for small enough $v_{m,A}^{(\alpha)}$, the phase of the modulation flips by 6 months. As we show below, this is precisely what happens for heavy DM components scattering off iodine in DAMA at the lowest energies. The total rates are given by the sum over nuclei and DM components, $\bar{R}(E_R) = \sum_{\alpha,A} \bar{R}_A^{(\alpha)}(E_R)$ and $\mathcal{M}(E_R, t) = \sum_{\alpha,A} \mathcal{M}_A^{(\alpha)}(E_R, t)$.

7.2.1 Gravitational focusing and the non-sinusoidal signal

GF of DM particles by the Sun affects the phase of the modulation t_0, which, for an observed E_R, is sensitive to the DM mass via the dependence on $v_{m,A}^{(\alpha)}$ [147, 148, 200]. The effect is significant for $v_{m,A}^{(\alpha)} \lesssim 200\,\rm km\,s^{-1}$, in which case the phase is changed from the vanilla case of December 1st towards a later value. In the case of DAMA the effect on the phase is important for heavy DM masses, for which it can change by tens of days. For light DM particles, the effect is negligible and the phase remains at June 1st. In 2DM the most interesting feature is that the sum of the time-dependent signals of the individual components, with their phases $t_0^{(1,2)}$ being different due to GF ($t_0^{(2)} > t_0^{(1)}$ as $m_2 > m_1$), leads to a non-sinusoidal time-dependent signal only suppressed by the (small) phase difference of the 2DM components $\Delta t_0 \equiv t_0^{(2)} - t_0^{(1)} > 0$.

We can see this by expanding the combined signal in Δt_0 (see also Ref. [112]). For a given nuclei and recoil energy, Δt_0 depends on the mass splitting of both DM components. We find that the combined $\mathcal{M}(E_R, t)$ is given to leading order in Δt_0 by

$$\begin{aligned}\mathcal{M}(t) &= \mathcal{M}^{(1)}\cos[2\pi(t - t_0^{(1)})] + \mathcal{M}^{(2)}\cos[2\pi(t - t_0^{(1)} - \Delta t_0)] \\ &= (\mathcal{M}^{(1)} + \mathcal{M}^{(2)})\,\cos[2\pi(t - t_0^{(1)})] \\ &+ \mathcal{M}^{(2)}\left(\frac{\Delta t_0}{t - t_0^{(1)}}\right)\sin[2\pi(t - t_0^{(1)})] ,\end{aligned} \tag{7.6}$$

where the expansion is valid for $t \gg t_0^{(2)} > t_0^{(1)}$. For $t \sim t_0^{(1,2)}$ higher order terms become important. As can be observed, the sine term is proportional to Δt_0. Therefore, for non-negligible Δt_0, the total time-dependent signal is non-sinusoidal. For the DAMA observation, how good this approximation is depends on the DM masses, which we study in the following by fitting the DAMA-phase 2 time-dependent signal to the numerically computed one using Eq. (7.1) with GF effects implemented.

7.3 The DAMA energy spectrum of the modulation amplitude

We perform our analysis on the whole energy spectrum of the DAMA annual modulation amplitude, which combines results from DAMA/NaI and DAMA/LIBRA phases 1 and 2. The total exposure is 2.46 kg·y. The events are measured in electron equivalent energy (keVee), which is related to the true recoil energy E_R through the target-dependent quenching factors $E_{\rm ee} = Q_A\, E_R$ (we use $Q_{\rm Na} = 0.3$, $Q_{\rm I} = 0.09$). We employ the differential response function of Ref. [55], treating the parameters $\alpha_{\rm LE} = (0.448 \pm 0.035)\,\sqrt{\rm keVee}$ and $\beta_{\rm LE} = (9.1 \pm 5.1) \times 10^{-3}$ as nuisance parameters. The results made public by the DAMA collaboration are presented in slide 22 of Ref. [85]. We use the data of Tab. I of Ref. [209], which gives the observed binned annual modulation amplitude M_i in $N = 10$ bins in the energy range [1, 20] keVee in order to increase the signal to noise ratio in our fit.

We undertake our analysis as follows:

1. We first generate pseudo-mock data from a modulating DM signal with gravitational focusing corrections implemented and 2.46 ton y of exposure in the time intervals used by DAMA. The term ‘pseudo-mock’ here refers to the fact that we use the ‘Asimov data’, which in the large statistics limit corresponds to the expected Poisson mean in each time bin. This is done to ensure smooth likelihood functions in our statistical analyses. We only generate signal events, since the DAMA collaboration releases no information about the observed constant backgrounds.

2. As DAMA does, we then fit the function $R_A(t) = S_0 + S_m \cos[2\pi(t - t_0)/T]$ to the pseudo-mock data set in each energy bin. Since the DAMA experiment does not veto backgrounds, we fit a sinusoidal component plus a constant offset

1DM	m (GeV)	σ_1^p ($\times 10^{-40}\,\mathrm{cm}^2$)	$\chi^2_{\mathrm{min}}/\mathrm{dof}$	p-value	$\mathcal{Z}$
Light	8.42	1.25	48.4/8	8.15×10^{-8}	5.40
Heavy	70.1	0.10	56.8/8	1.94×10^{-9}	6.00

Table 7.1 Results of 1DM fit to the DAMA energy spectrum after accounting for GF corrections. The different fits are for both the light and the heavy DM mass solutions. The dashes refer to the parameters that are fixed to 1.

to extract the best fit modulation amplitude S_m. We take a constant phase of $t_0 = 152.5$ days and a period $T = 1\,\mathrm{yr}$.[3]

3. We take the estimated amplitude for each energy bin and compare these to the DAMA data using a maximum likelihood analysis in order to extract the goodness of fit and best-fit values of the 1DM and 2DM model parameters.

The reason for this roundabout approach is that the DAMA collaboration does not release time-dependent data in 0.5 keVee bins,[4] and so we proceed as closely as possible to the method used by the collaboration to extract the modulation amplitude. This would not be necessary if we did not consider GF, but GF non-trivially changes the phase of the modulation away from June 1st as well as the shape of the time-dependent signal.

We use the open source software `Minuit` [254] to compute the best-fit points, which we give in Tabs. 7.1 and 7.2. For completeness, we also compute the corresponding p-values for the fits, as well as the corresponding number of equivalent two-sided Gaussian standard deviations $\mathcal{Z}$. We deem a ‘good fit’ to be one that gives a p-value $p > 0.05$ which corresponds to $\mathcal{Z} < 1.96$. For 2DM, we also employ the `MultiNest` implementation of the nested sampling algorithm [255–257], with 5000 live points and a tolerance of 0.5. We then determine the distribution of the profile likelihood ratio (PLR) $\mathcal{L}/\mathcal{L}_{\mathrm{max}}$ throughout the parameter space from the obtained samples.

2DM	m_1	m_2	σ_1^p	r_ρ	$\chi^2_{\mathrm{min}}/\mathrm{dof}$	p-value	$\mathcal{Z}$
$r_\sigma = 1$	22.0	80.3	0.14	3.35	11.8/6	0.07	1.84

Table 7.2 Same as Tab. 7.1 for 2DM fit to the DAMA energy spectrum.

---

[3] The DAMA collaboration also presents results assuming variable phases and additional non-sinusoidal components. Energy spectra for these fits however are presented in larger integrated energy bins of 1 keVee width. Since any interesting behaviour in the spectrum occurs in the lowest $[1-1.5]$ keVee energy bin we do not use these other data sets.

[4] The only time-dependent information released by the DAMA collaboration are residuals in large integrated energy bins [1-3], [2-6] and [1-6] keVee. However, in the latter the energy information of the (most interesting) lowest energy bins is washed out.

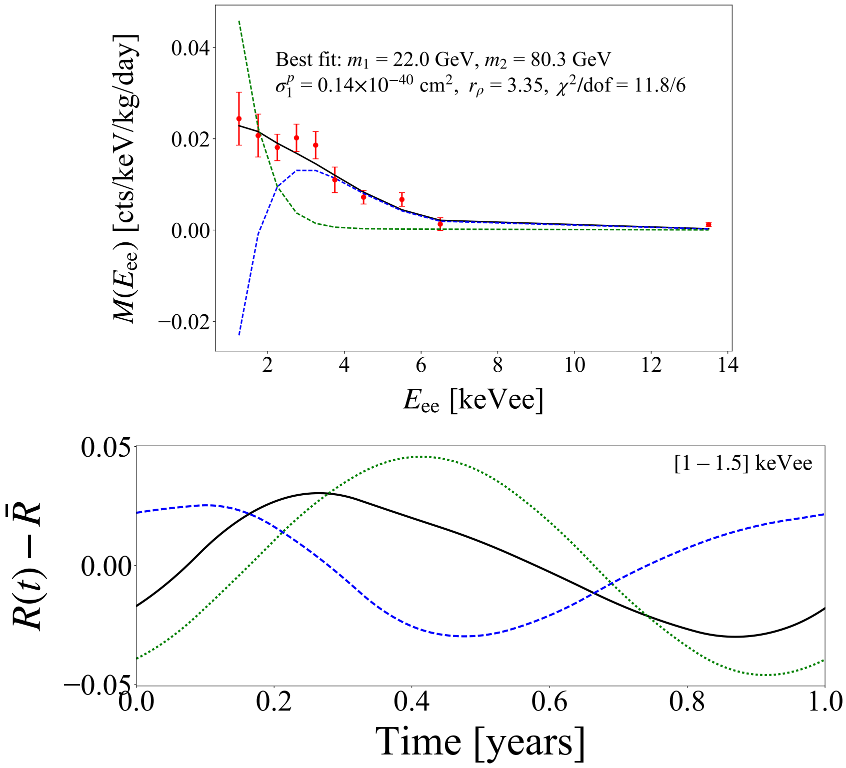

Fig. 7.1 Two-component fit to the DAMA/LIBRA phase-2 data. We also show the contribution from DM1 (DM2) in *dotted green* (*dashed blue*) and the combined (*solid black*). *Upper panel:* Best-fit spectra of the DAMA energy spectrum for the 2DM model. The experimental best-fit modulation amplitudes to the combined DAMA phases 1 and 2 rebinned [209] are shown with *red points*. Below the phase flip, which occurs at ~ 2 keVee, the contributions of the two components partially neutralise each other in the combined modulation. *Lower panel:* Time-dependent residuals in the lowest energy bin, [1-1.5] keVee. Notice the anti-modulation of DM2, and the non-sinusoidality of DM2 and the combined signal.

7.3.1 One-component dark matter fit

In Tab. 7.1 we show results of 1DM fits for the light and the heavy DM mass solutions, which correspond to scatterings mainly in Na and I, respectively. We also check the exclusion significances for the 1DM case neglecting gravitational focusing effects to check consistency with previous studies. Since GF does not effect the sinusoidality of the DAMA signal for DM masses below ~ 30 GeV, we find that the light solution is excluded at 5.4σ, which is roughly the same significance as observed in previous studies. Interestingly, however, we see that including GF corrections non-trivially increases the exclusion significance of the heavy solution from $\sim 3\sigma$ to 6σ.

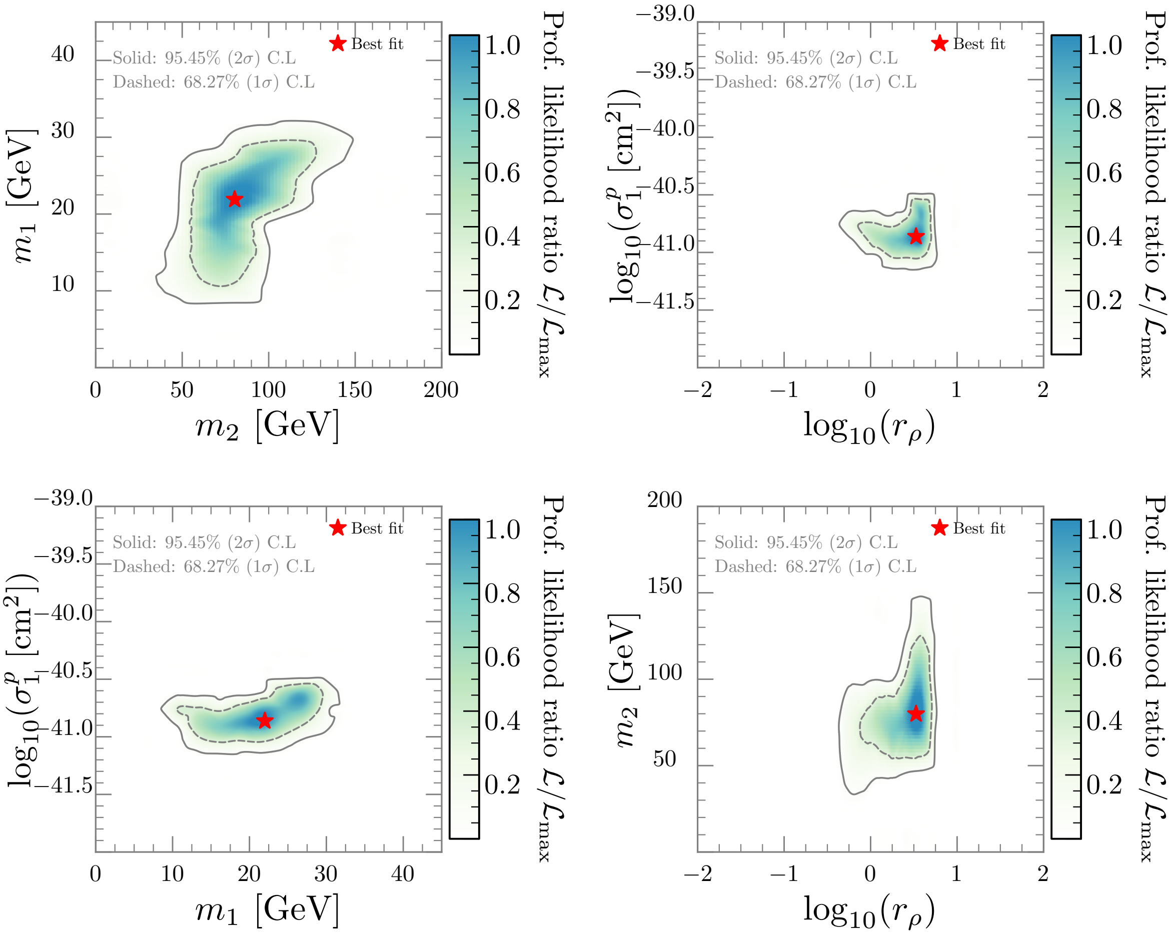

Fig. 7.2 Profile likelihood ratio (PLR) density overlaid with 1 and 2σ C.L. contours for the 2DM fit to the DAMA energy spectrum of the modulation amplitude as calculated in Sec. 7.3.2. We indicate the best fit points with a red star (see Tab. 7.2.)

7.3.2 Two-component dark matter fit

We show in Tab. 7.2 the result of the fit for two DM particles (2DM). We fix $r_\sigma = 1$, leaving r_ρ free.[5] One can observe that the 2DM model provides a good fit with an exclusion significance of only 1.84σ. In Fig. 7.1 (upper panel) we show the binned modulation amplitude (solid black) for the best-fit points of the 2DM solution. This corresponds to scattering of both DM components *dominantly* off iodine. The fact that the lighter component scatters dominantly off iodine with a negligible contribution from sodium is due to two factors: first, the smaller quenching factor in iodine compensates its larger mass, translating into smaller $v_{\mathrm{m,I}}^{(1)}(E_R)$ and thus into larger $\eta(v_{\mathrm{m,I}}^{(1)})$; second is the A^2 enhancement factor for iodine due to coherent

---

[5] The energy density and the cross section enter identically in the rate. Therefore, apart from the overall normalisation, one can fix r_σ and consider r_ρ as a free parameter.

SI scatterings. Below 2 keVee DM2 becomes negative (i.e., a phase flip) and DM1 dominates the total rate. Therefore there is a partial cancellation in the combined modulation between the individual DM contributions. This is illustrated in Fig. 7.1 (lower panel), where we plot the time-dependent residual for 2DM in the lowest recoil energy bin [1-1.5] keVee.[6]

In Fig. 7.2 we present the frequentist 1 and 2σ C.L. contours using `pippi` [180]. We show the planes m_1–m_2 (*top left*), $\log_{10}(r_\rho)$–$\log_{10}(\sigma_1^p)$ (*top right*), $\log_{10}(r_\rho)$–m_2 (*bottom left*) and $\log_{10}(r_\rho)$-m_2 (*bottom right*). The regions are very well-defined around the best-fit values. The 2σ range of m_1 is quite narrow, [8, 30] GeV, while that of m_2 is larger, [30, 150] GeV, i.e., there is more freedom in the heavy component since for heavier DM the dependence on the mass via $\eta(v_{m,A}^{(\alpha)})$ is milder. For large mass values, m_1 and m_2 show a mild positive correlation, such that both individual terms in the square bracket of Eq. (7.1) become similar in size. Moreover, one can observe how the largest m_2 region corresponds to large r_ρ (*bottom right* panel), which is easily understood looking at the second term in the square bracket of Eq. (7.1). Also, the region of large σ_1^p corresponds to large r_ρ, see *top left* panel, as expected from the overall normalisation of the rate.

7.4 Conclusions

In this letter, we have studied how a simple 2DM can lead to interesting signals in annual modulation experiments. Furthermore, we showed that implementing corrections due to GF leads to non-sinusoidal and non-trivial phase effects in the evaluation of the 2DM time-dependent rate. As an illustrative example, we studied whether a 2DM model comprising both a light and heavy component can revive the vanilla DM interpretation of the low threshold DAMA data. We performed a fit of 2DM to the publicly available DAMA data using the energy spectrum of the amplitude of the modulation. For the first time, we also fully incorporate gravitational focusing effects into such an analysis. Firstly, we fit 1DM to the energy spectrum data and find that the heavy solution is even more excluded than shown in previous studies after GF effects are considered. On the contrary, we find that 2DM provides very good agreement to the energy spectrum data.

We show our solution in Fig. 7.1, where scatterings are predominantly off iodine, with a crossing between the spectrum of the two individual DM components at

---

[6] For completeness, we have also conducted a similar analysis without including GF. In this case, we obtain *two* solutions. One which corresponds to a similar one as with GF, and another one at $m_1 \sim 8$ GeV and $m_2 \sim 170$ with $r_\rho \sim 0.07$. That is, the second solution prefers a suppressed heavy component, i.e., a 1DM scenario.

roughly 2 keVee. The crossing occurs due to a phase flip in the heavier component at low recoil energy. The results of the 2DM fits are summarised in Tab. 7.2 and Figs. 7.1 and 7.2, which involve reasonable values of the relative energy densities and the cross section. The key feature found in the analysis is that, at the lowest energies, the modulation of the heavy DM particle becomes negative, so that in the combined modulation the individual DM contributions partially cancel each other.

Therefore two-component DM looks like a natural solution to the first part of the DAMA puzzle: the compatibility of the spectrum with that expected from DM under standard astrophysical and particle physics assumptions. The second part of the DAMA puzzle, that is, the compatibility of DAMA data with other null results is not solved.

We would like to conclude by saying that it would be very helpful if the DAMA collaboration made public the temporal data in smaller energy bins, which would allow the use of all information. In particular it would show whether or not there is a non-sinusoidal behaviour in the current data in the [1,1.5] keVee bin, as present in the case of 2DM (see lower panel of Fig. 7.1).

In any case, even if the DAMA signal turns out not to be related to DM, the distinctive features of the time-dependent signal of multi-component DM found in this work, like the non-sinusoidal behaviour and the possibility of having a partial cancellation at low energies, are generic predictions that should be searched for in case an annual modulation signal is observed in next generation experiments.

Acknowledgements: JHG would like to thank Thomas Schwetz for useful discussions. This work is supported by the Australian Research Council through the Centre of Excellence for Particle Physics at the Terascale CE110001004. MW is supported by the Australian Research Council Future Fellowship FT140100244. MW wishes to thank Lucien Boland and Sean Crosby for their administration of, and ongoing assistance with, the MPI-enabled computing cluster on which this work was performed.

Chapter 8

Background and supplementary material for Publication four

8.1 Motivation

The last publication presented in this thesis will attack the DM problem from a different angle. Motivated by the null results of direct, indirect and collider searches over the years, theorists have turned to model building in order to develop DM candidates that can evade experimental constraints. “Pseudo-Nambu-Goldstone dark mater” (pNG DM) extends the standard model with the introduction of a new complex scalar field which yields a DM candidate that can evade direct detection bounds. In publication 4 shown in chapter 8.4 we for the first time combine all known experimental constraints and theoretical limits on the pNG model. The statistical procedure that one follows to do this is often referred to as a *global fit*.

The publication presented in chapter 8.4 is very pedagogical in nature with a detailed set of appendices, leaving little to discuss here in the supplementary overview. There are however a couple of points that are glossed over in the main text. Firstly, the discussion of the constraints obtained from the Fermi-LAT gamma-ray observations in section 9.3.6 leaves a lot to assumed knowledge. Therefore a brief overview of the observables and nomenclature utilized in gamma-ray searches from DM-DM annihilation is discussed here in this chapter. In addition, supplementary context is given for sections of the main text that deal with Higgs invisible width constraints and electroweak precision observables.

8.2 Indirect detection and the Fermi-LAT gamma ray observations

The indirect detection of dark matter involves using Earth bound observatories (either space or ground based) to measure an observable flux ϕ [particles/cm^2/s] of particle descendants arising from the self annihilation of DM. The flux is a function of the particle physics of the DM (mass and cross-section), as well as the astrophysical density distribution $\rho(\mathbf{r})$. One usually uses the term *prompt emission* to refer to the production of final state particles from the annihilation process itself. An example of NON-prompt annihilation products would be the secondary photons produced when the charged products of the DM annihilation process interact with the interstellar medium as they propagate to Earth. Such secondary processes are not considered in this work but have been considered in various other indirect studies [36, 258].

By convention astrophysics and particle physics are usually separated into distinct pieces, as we will see in section 8.2.2:

$$\text{Total particle flux} = [\text{Particle physics term}] \times [\text{Astrophysics term}]\ . \tag{8.1}$$

The particle physics piece depends explicitly on the number spectrum $\frac{dN}{dE}$ of annihilation products and the DM-DM scattering cross-section. As we will see in this section the scattering cross-section that parameterizes the DM self-annihilation is averaged over the DM velocity distribution. The notation for this new cross-section parameter is $\langle\sigma v\rangle$ and it is called the *velocity averaged cross section* (or thermally averaged cross-section).

8.2.1 Velocity averaged Cross-Section

First introduced in section 3.3.1, the *thermally averaged cross-section* $\langle\sigma v\rangle$ is the primary parameter that quantifies the DM-DM annihilation process. That is,

$$\langle\sigma v\rangle \propto |\mathcal{M}|^2_{\text{DM-DM}\to\text{X}}\ . \tag{8.2}$$

The velocity averaged cross-section includes an integral over the initial state momenta weighted by the Maxwell-Boltzmann distribution. To get the relevant behaviour we can simply expand $\langle\sigma v\rangle$ in powers of the relative velocity squared v^2 and insert the moments of the MB distribution. Usually, only the first and second terms in the expansion are required

$$\text{Taylor expansion} \quad \Rightarrow \sigma v = a + bv^2 + ... \tag{8.3}$$

On taking the expectation value, the second term becomes $6b/x_f$ since $\langle v^2 \rangle = 6/x_f$, where $x_f \equiv m_\chi/T$, T being the temperature of WIMP freeze out (see appendix 3.3.1). Hence, the velocity averaged cross-section will be expanded as

$$\langle \sigma v \rangle = a + 6\frac{b}{x_f} + ... \tag{8.4}$$

This realisation was made by Jungman and Kamionkowaki [259].

8.2.2 Differential Flux

The physical observable that quantifies a measurement of a population of prompt photons originating from DM annihilation is called the *differential flux* or differential flux density in some astrophysical contexts. The differential flux is usually denoted $d\phi/dE$ and has units [GeV^{-1} cm^{-2} s^{-1}]. It is defined as the number of radiant-energy particles incident on a surface during a given period of time divided by the product of the area of that surface, the characteristic energy of the incident particles, and the given period of time. From dimensional analysis, the differential element of flux originating from the infinitesimal volume element dV is

$$d\phi = \frac{1}{4\pi|\mathbf{r}|^2}\frac{dN}{dt}. \tag{8.5}$$

The rate of DM-DM annihilation within this volume element is defined by

$$\Gamma(t) \equiv \frac{\langle \sigma v \rangle}{m_\chi}\rho(\mathbf{r}) \tag{8.6}$$

where $\langle \sigma v \rangle$ is the velocity averaged annihilation cross-section discussed in section 8.2.1, $\rho(\mathbf{r})$ is the DM density and the location of the volume element $\mathbf{r}$. This alone does not tell us about how many γ producing collisions are taking place however. The number of two body collisions within dV happening in time element dt is given by

$$\Gamma(t) \times \frac{1}{2} \cdot \frac{dV\rho(\mathbf{r})}{m_\chi}. \tag{8.7}$$

Note the factor of two here is because there are always assumed to be *two* DM particles in one annihilation event. This quantity is what enters the expression for

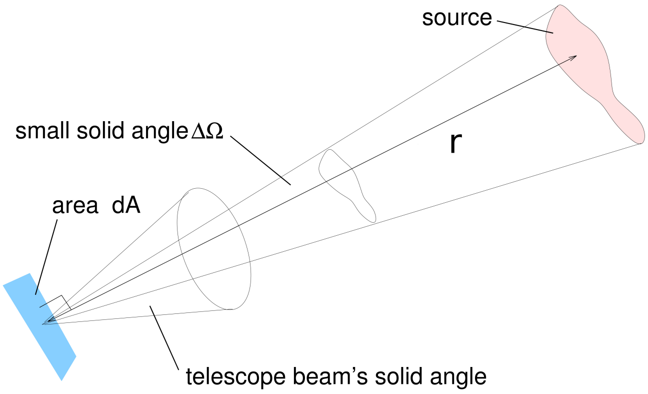

Fig. 8.1 Diagrammatic representation of the differential flux through a surface dA originating from some source at a distance $\mathbf{r}$. As shown in the text, one must integrate over the volume of sky parameterized by the telescope beam's solid angle to obtain the differential flux.

the flux element as $1/dt$. Hence:

$$d\phi = \frac{1}{8\pi|\mathbf{r}|^2}\frac{\langle\sigma v\rangle}{m_\chi^2}\,\rho^2(\mathbf{r})\,dN\,dV \tag{8.8}$$

$$= \frac{1}{8\pi|\mathbf{r}|^2}\frac{\langle\sigma v\rangle}{m_\chi^2}\,\rho^2(\mathbf{r})\,\frac{dN}{dE}dE\,|\mathbf{r}|^2\,dr\;d\Omega\;, \tag{8.9}$$

where we have explicitly written the volume element dV in polar coordinates and the photon spectrum per DM annihilation $\frac{dN}{dE}$ has been separated out intentionally to later distinguish the particle physics from the astrophysics. The differential flux originating from some infinitesimal volume element of the DM halo dV is then

$$\frac{d\phi}{dE} = \frac{1}{8\pi}\frac{\langle\sigma v\rangle}{m_\chi^2}\,\rho^2(\mathbf{r})\,\frac{dN}{dE}\,dr d\Omega\;. \tag{8.10}$$

Given that any detector has a finite angular resolution Ω, one must integrate over this volume of the sky to derive the total differential flux. This is diagrammatically represented in figure 8.1. Writing this explicitly, we obtain

$$\frac{d\phi}{dE} = \left(\frac{1}{8\pi}\frac{\langle\sigma v\rangle}{m_\chi^2}\frac{dN}{dE}\right)\int\limits_{\Omega}\;\int\limits_{l.o.s}\rho^2(\mathbf{r})\,dr\;d\Omega\;, \tag{8.11}$$

where the integration is over the detector resolution and the line of sight ($l.o.s$). This expression is often parametrised into particle physics and astrophysics components.

Namely the J factor defined as

$$J \equiv \int\limits_{\Delta\Omega} \int\limits_{l.o.s} \rho^2(\mathbf{r})\, dr\, d\Omega \tag{8.12}$$

and

$$\frac{d\Phi_{\rm pp}}{dE} \equiv \frac{1}{8\pi} \frac{\langle \sigma v \rangle}{m_\chi^2} \frac{dN}{dE} \;. \tag{8.13}$$

Hence

$$\Rightarrow \frac{d\phi}{dE} = \frac{d\Phi_{\rm pp}}{dE} \times J \tag{8.14}$$

Note that throughout this derivation only one annihilation channel for $\chi\chi \to \gamma\gamma$ with branching ratio $(BR) = 1$ was assumed. To account for the possibility of any DM model, the model dependent spectrum needs to be adjusted accordingly

$$\frac{dN}{dE} \to \sum_i \mathrm{BR}_i \cdot \frac{dN}{dE}_i \tag{8.15}$$

where the spectrum of each possible decay mode is weighted by the appropriate branching ratio. Hence we can write the total differential flux

$$\frac{d\phi}{dE} = \left(\frac{1}{8\pi} \frac{\langle \sigma v \rangle}{m_\chi^2} \left[\sum_i \mathrm{BR}_i \cdot \frac{dN}{dE}_i \right] \right) \int\limits_{\Delta\Omega} \int\limits_{l.o.s} \rho^2(\mathbf{r})\, dr\, d\Omega \;. \tag{8.16}$$

Differential flux in galactic coordinates

One further point is that one may define the length of the radial vector $\mathbf{r}$ in terms of galactic coordinates. Galactic coordinates are defined as shown in figure 8.2. In such a coordinate system, we have

$$|\mathbf{r}| = \sqrt{R_\odot - 2sR_\odot \cos(b)\cos(l) + s^2} \;, \tag{8.17}$$

where s is the distance from the earth to the source of flux, in this case, a star. Hence the solid angle differential is

$$d\Omega = db\, dl \cos(b) \;. \tag{8.18}$$

This makes the integral in 8.16 explicitly a function of galactic longitude b and latitude l.

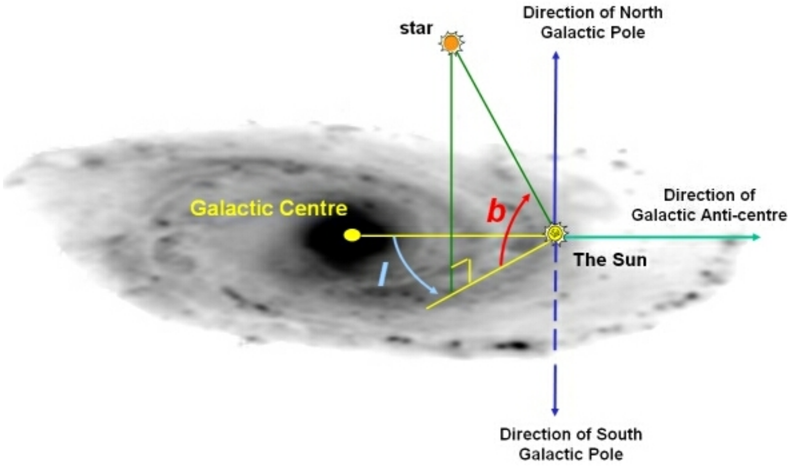

Fig. 8.2 Definition of galactic coordinates. Image from [260].

8.2.3 The Fermi dwarfs

The Fermi dwarfs are some of the most DM rich objects known to astrophysics. Given their relatively close proximity they make excellent targets for indirect detection. The Fermi Large Area Telescope (LAT) has surveyed 45 stellar systems, 28 of which are kinematically confirmed dark-matter-dominated dwarf spheroidal galaxies, with 17 recently discovered systems having photometric characteristics consistent with the population of known dSphs [261]. These compact dwarf spherodials (dSphs) have been probed for a significant excess of γ-rays in the energy range 20 MeV to 500 GeV stemming from DM annihilation. At present, no such significant excess has been detected, although four of the recently added objects have shown a slight ($\sim 2\sigma$) excess above background estimates.

The Fermi collaboration use estimates of the J factors of the dwarf galaxies determined through dynamical modelling of their stellar density and velocity dispersion profiles provided by Martinez et al. [262]. The measured J factor estimates are denoted $J_{\rm meas}$ and are shown in column 6 of table 8.1. In their latest release, Fermi-LAT report on 6 years of data implementing their latest data set called the `Pass 8` event-level analysis which, along with increased exposure time provides a range of systematic experimental improvements [263]. In addition to the improvements from Pass 8, Fermi employ the updated third LAT source catalog (3FGL), based on four years of `pass 7` reprocessed data, to model point-like background sources. For demonstrative illustration, Fig. 8.3 shows a variety of dwarfs overlayed on top of a γ-ray map of the Milky Way[1].

---

[1] These were the dwarfs used in the first `Pass8` analysis by Ackermann et al. [263].

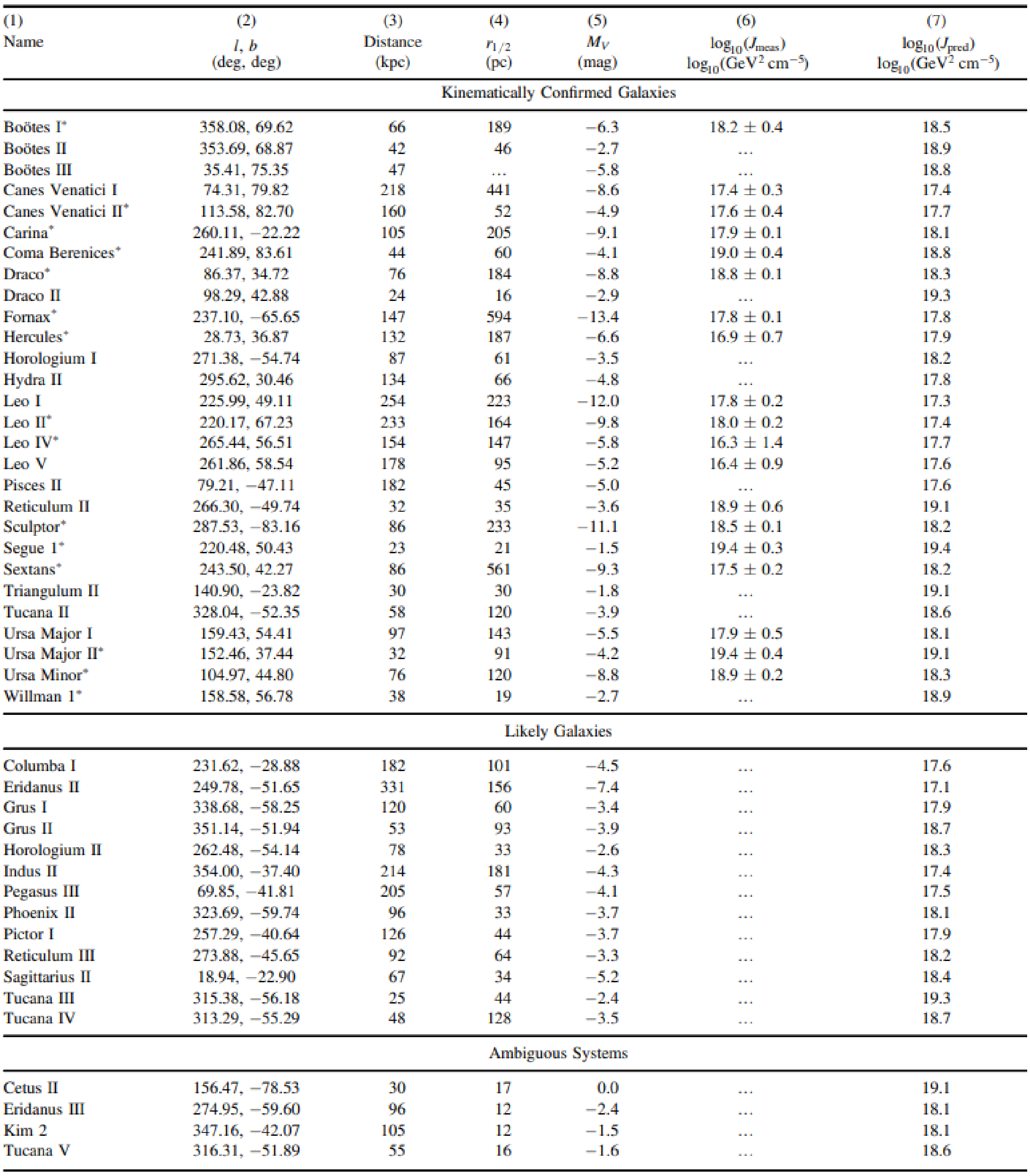

(1) Name	(2) l, b (deg, deg)	(3) Distance (kpc)	(4) $r_{1/2}$ (pc)	(5) M_V (mag)	(6) $\log_{10}(J_{\rm meas})$ $\log_{10}(\rm GeV^2\ cm^{-5})$	(7) $\log_{10}(J_{\rm pred})$ $\log_{10}(\rm GeV^2\ cm^{-5})$
			Kinematically Confirmed Galaxies			
Boötes I*	358.08, 69.62	66	189	−6.3	18.2 ± 0.4	18.5
Boötes II	353.69, 68.87	42	46	−2.7	…	18.9
Boötes III	35.41, 75.35	47	…	−5.8	…	18.8
Canes Venatici I	74.31, 79.82	218	441	−8.6	17.4 ± 0.3	17.4
Canes Venatici II*	113.58, 82.70	160	52	−4.9	17.6 ± 0.4	17.7
Carina*	260.11, −22.22	105	205	−9.1	17.9 ± 0.1	18.1
Coma Berenices*	241.89, 83.61	44	60	−4.1	19.0 ± 0.4	18.8
Draco*	86.37, 34.72	76	184	−8.8	18.8 ± 0.1	18.3
Draco II	98.29, 42.88	24	16	−2.9	…	19.3
Fornax*	237.10, −65.65	147	594	−13.4	17.8 ± 0.1	17.8
Hercules*	28.73, 36.87	132	187	−6.6	16.9 ± 0.7	17.9
Horologium I	271.38, −54.74	87	61	−3.5	…	18.2
Hydra II	295.62, 30.46	134	66	−4.8	…	17.8
Leo I	225.99, 49.11	254	223	−12.0	17.8 ± 0.2	17.3
Leo II*	220.17, 67.23	233	164	−9.8	18.0 ± 0.2	17.4
Leo IV*	265.44, 56.51	154	147	−5.8	16.3 ± 1.4	17.7
Leo V	261.86, 58.54	178	95	−5.2	16.4 ± 0.9	17.6
Pisces II	79.21, −47.11	182	45	−5.0	…	17.6
Reticulum II	266.30, −49.74	32	35	−3.6	18.9 ± 0.6	19.1
Sculptor*	287.53, −83.16	86	233	−11.1	18.5 ± 0.1	18.2
Segue 1*	220.48, 50.43	23	21	−1.5	19.4 ± 0.3	19.4
Sextans*	243.50, 42.27	86	561	−9.3	17.5 ± 0.2	18.2
Triangulum II	140.90, −23.82	30	30	−1.8	…	19.1
Tucana II	328.04, −52.35	58	120	−3.9	…	18.6
Ursa Major I	159.43, 54.41	97	143	−5.5	17.9 ± 0.5	18.1
Ursa Major II*	152.46, 37.44	32	91	−4.2	19.4 ± 0.4	19.1
Ursa Minor*	104.97, 44.80	76	120	−8.8	18.9 ± 0.2	18.3
Willman 1*	158.58, 56.78	38	19	−2.7	…	18.9
			Likely Galaxies			
Columba I	231.62, −28.88	182	101	−4.5	…	17.6
Eridanus II	249.78, −51.65	331	156	−7.4	…	17.1
Grus I	338.68, −58.25	120	60	−3.4	…	17.9
Grus II	351.14, −51.94	53	93	−3.9	…	18.7
Horologium II	262.48, −54.14	78	33	−2.6	…	18.3
Indus II	354.00, −37.40	214	181	−4.3	…	17.4
Pegasus III	69.85, −41.81	205	57	−4.1	…	17.5
Phoenix II	323.69, −59.74	96	33	−3.7	…	18.1
Pictor I	257.29, −40.64	126	44	−3.7	…	17.9
Reticulum III	273.88, −45.65	92	64	−3.3	…	18.2
Sagittarius II	18.94, −22.90	67	34	−5.2	…	18.4
Tucana III	315.38, −56.18	25	44	−2.4	…	19.3
Tucana IV	313.29, −55.29	48	128	−3.5	…	18.7
			Ambiguous Systems			
Cetus II	156.47, −78.53	30	17	0.0	…	19.1
Eridanus III	274.95, −59.60	96	12	−2.4	…	18.1
Kim 2	347.16, −42.07	105	12	−1.5	…	18.1
Tucana V	316.31, −51.89	55	16	−1.6	…	18.6

Table 8.1 Table from Ref. [261]. Milky Way satellite systems consistent with being dSphs. Horizontal lines divide systems that have been kinematically determined to be DM dominated (top), systems with photometry consistent with being dSphs (middle), and systems with small physical sizes populating an ambiguous region of the size–luminosity plane between dSphs and globular clusters (bottom). Columns represent (1) name of stellar system, (2) Galactic coordinates, (3) heliocentric distance, (4) azimuthally averaged half-light radius, (5) absolute visual magnitude, (6) measured J-factor derived from stellar kinematics. (7) predicted J-factor. Targets used in the first analysis to derive combined limits from Ackermann et al. [263] are marked with asterisks.

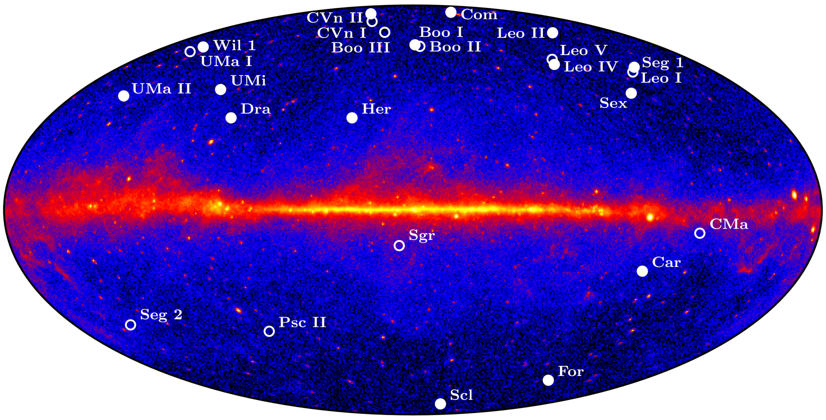

Fig. 8.3 Figure from [264]. Known dwarf spheroidal satellite galaxies of the Milky Way overlaid on a Hammer-Aitoff projection of a 4-year LAT counts map ($E > 1$ GeV) of the galactic plane. The 15 dwarf galaxies included in the Fermi-LAT Pass 8 combined likelihood analysis are shown as filled circles, while additional dwarf galaxies are shown as open circles.

Fermi-LAT likelihood

Something not detailed in publication 4 are the details surrounding the inclusion of the J-factor as a nuisance parameter in the Fermi-LAT likelihood. As such it is briefly discussed here. The primary quantity used in the Fermi analysis is the total energy flux

$$s_{k,i}(m_\chi, \langle\sigma v\rangle, J) = \int_{E_{\mathrm{i,min}}}^{E_{\mathrm{i,max}}} E\, \frac{d\phi_k}{dE}\, dE\,. \tag{8.19}$$

The likelihood function for a particular dwarf k and energy bin i is therefore a function of this expected signal, while the J factors enter as nuisance parameters:

$$\mathcal{L}_{k,i}(s_{k,i}) = \mathcal{L}_{k,i}(m_\chi, \langle\sigma v\rangle, J_k)\,. \tag{8.20}$$

Fermi use a standard binned Poisson likelihood consistend with other LAT analyses [264]:

$$\mathcal{L}_{k,i}(m_\chi, \langle\sigma v\rangle, J_k) = \frac{\lambda_k^{n_k} e^{-\lambda_k}}{n_k!}\,, \tag{8.21}$$

where n_k is the number of photon data from the dwarf k and $\lambda_k = \lambda_k(m, \langle\sigma v\rangle)$ is some function that depends on the model input parameters m_χ and $\langle\sigma v\rangle$. While Fermi do not release the functional form of the λ_k, they do release the tabulated versions of Eqn.(8.21) on their official data release page [265]. These tabulations give

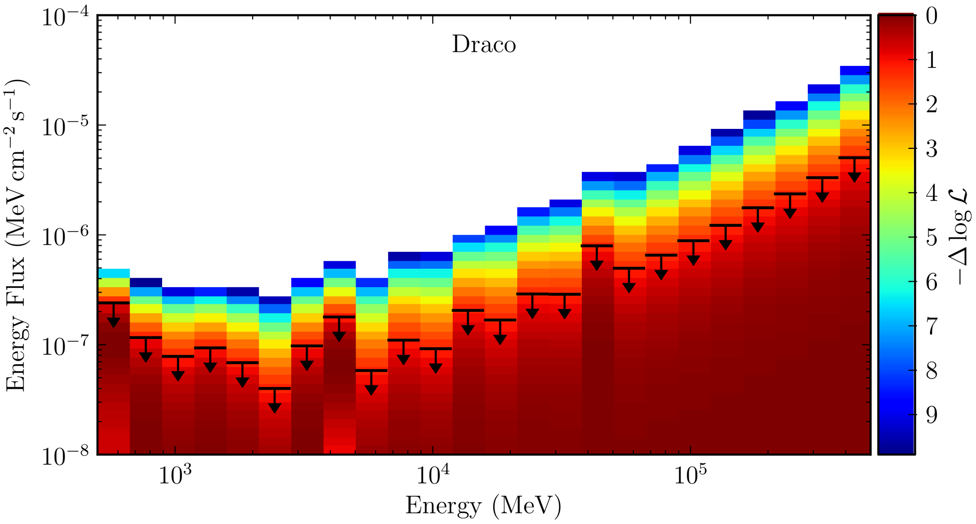

Fig. 8.4 Figure from [264]. Histogram of the bin-by-bin LAT likelihood function given in Eqn. (8.21) used to test for a gamma- ray source at the position of the Draco dwarf spheroidal galaxy. Within each bin, the color scale denotes the variation of the logarithm of the likelihood with respect to the best fit value of the source flux (truncated at $-\Delta \log \mathcal{L} > 10$). Upper limits on the integrated energy flux are set at 95% CL within each bin using the delta-log-likelihood technique and are largely independent of the source spectrum.

three columns: E_γ, $s_{k,i}(E_\gamma)$ [MeV cm^{-2} s^{-1}] and $-\Delta \log \mathcal{L}(s_{k,i})$, where

$$-\Delta \log \mathcal{L}(s_{k,i}) = [\log \mathcal{L}(s_{k,i}) - \log(s^0_{k,i})] \,, \tag{8.22}$$

and $s^0_{i,k}$ is the configuration that maximises the likelihood 8.21 for a particular i and k. Hence, if one is to make use of these likelihoods, one needs to interpolate the correct value of the likelihood for a given model dependent $s_{k,i}$. To make this clear:

$$\text{Generate}: \quad s_{k,i}(m_\chi, \langle \sigma v \rangle) \longrightarrow \text{Interpolate:} \; -\Delta \log \mathcal{L}(s_{k,i}) \,. \tag{8.23}$$

Hence, we can extract a log likelihood corresponding to a given energy flux (and hence particle physics number spectrum dN/dE). Figure 8.4 shows the log likelihood distribution as a function of energy flux for the Draco dwarf galaxy taken from [264] for a C.L of 95%.

The J-factor is incorporated as a nuisance parameter in the maximum likelihood. The uncertainty is emulated by assuming log-Gaussian spread with standard deviation σ_k in the probability distribution for each J-factor peaked at the numerical values of J^k_{obs} shown in table 8.1. Furthermore, the Fermi functional form of this uncertainty is emulated with a "log normal" distribution $N(J_k)$ given by

$$N(J_k) = \frac{1}{\ln(10) J^k_{\text{obs}} \sqrt{2\pi}\sigma_k} \times e^{\frac{-\left(\log_{10}(J_k) - \log_{10}(J^k_{\text{obs}})\right)^2}{2\sigma_k}} . \tag{8.24}$$

This typical normalization is done when we have theoretical parameters with observational constraints. Here the J_k are such parameters. The likelihood for a particular dwarf k is given by multiplying the log normal distribution with the combination of the likelihoods over each energy bin. The total likelihood for a given dwarf k accounts for instrument performance, the observed counts, exposure, and background fluxes and is given by

$$\mathcal{L}_k(m, \langle\sigma v\rangle, J_k) = \frac{1}{\ln(10) J^k_{\text{obs}} \sqrt{2\pi}\sigma_k} \, e^{\frac{-\left(\log_{10}(J_k) - \log_{10}(J^k_{\text{obs}})\right)^2}{2\sigma_k}} \times \prod_i \mathcal{L}_{k,i}(m, \langle\sigma v\rangle, J_k) \, . \tag{8.25}$$

Combining the dwarf Likelihoods we get the total combined-likelihood function

$$\mathcal{L}(m, \langle\sigma v\rangle, \bar{J}) \equiv \prod_k \mathcal{L}_k \, , \tag{8.26}$$

where $\bar{J}$ represents the set of J factors $\{J_k\}$.

8.3 Higgs portal at colliders

This section contains a brief primer on Higgs portal DM and the invisible Higgs decay width which was used as one of the constraints in the global fit in publication 4. Section 9.3.3 contains the exact expressions and the detail that are relevant for the study. One of the experimental constraints we consider in chapter 8.4 is the collider

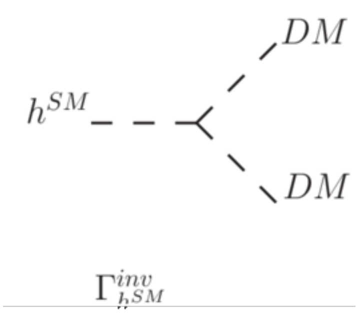

Fig. 8.5 Standard model Higgs invisible decay channel ($h \rightarrow \chi\chi$).

bounds on the Higgs boson's invisible decay width (Fig. 8.5). Higgs portal models are constructed by adding only DM and no other new particles to the Standard Model. Only the latest generations of collider experiments have achieved the energies and luminosities required to check for these types of DM model. Direct collider searches for the invisibly decaying Higgs boson ($hh \to \chi\chi$) are augmented by measurements of other Higgs properties, which can be very sensitive to couplings to new particles. The Higgs boson is light in comparison to the LHC energy and can be produced on-shell, so collider searches may still constrain these models through precision studies of the visible decays of the Higgs bosons, even if the invisible particles are much heavier and invisible decays of the mediator are absent.

8.4 Electroweak precision observables

Adding an extra scalar field to the SM as is the case with the pNG model, induces corrections to the gauge boson self-energy diagrams. This effect on the electroweak precision observables (EWPO) can be parameterized by the oblique parameters S, T and U [266]. Section 9.6.2, which appears as an appendix in the published version of the paper, details the explicit forms of the oblique parameters. The $\gamma\gamma$ and γZ self-energies ($\Pi_{\gamma\gamma}$ and $\Pi_{\gamma Z}$ respectively) are not modified as the new scalar is electrically neutral. Thus, only the W and Z boson self-energies are subject to corrections.

Chapter 9

Publication four: Global fit of pseudo-Nambu-Goldstone Dark Matter

Statement of Authorship

Title of Paper	Global fit of pseudo-Nambu-Goldstone Dark Matter	
Publication Status	☒ Published	☐ Accepted for Publication
	☐ Submitted for Publication	☐ Unpublished and Unsubmitted work written in manuscript style
Publication Details	JHEP04 (2020) 015, JHEP 04 (2020) 015 • e-Print: 1912.04008 DOI: 10.1007/JHEP04(2020)015	

Principal Author

Name of Principal Author (Candidate)	Andre		
Contribution to the Paper	I aided with the literature review on the topic, and wrote the FeynRules and FeynArts model files for the direct detection componenet of the work. I also contributed to the development of the likelihood terms that would enter into the global fit. With Ankit Beniwal, I ran multiple numerical scans of the model on Adelaide University super-computing resources and generated the frequentist and Bayesian scan results. I also made important contributions toward writing up the draft.		
Overall percentage (%)	60%		
Certification:	This paper reports on original research I conducted during the period of my Higher Degree by Research candidature and is not subject to any obligations or contractual agreements with a third party that would constrain its inclusion in this thesis. I am the primary author of this paper.		
Signature		Date	

Co-Author Contributions

By signing the Statement of Authorship, each author certifies that:

i. the candidate's stated contribution to the publication is accurate (as detailed above);

ii. permission is granted for the candidate in include the publication in the thesis; and

iii. the sum of all co-author contributions is equal to 100% less the candidate's stated contribution.

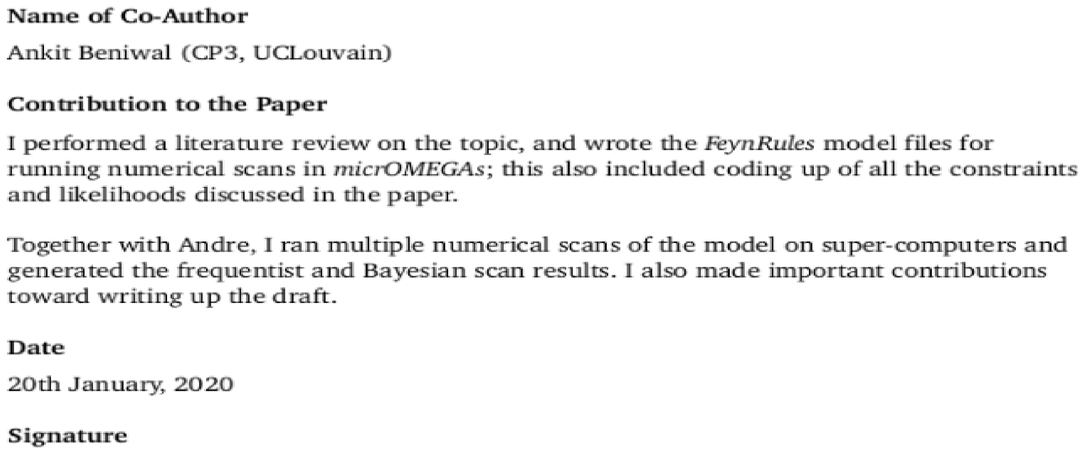

Name of Co-Author

Ankit Beniwal (CP3, UCLouvain)

Contribution to the Paper

I performed a literature review on the topic, and wrote the *FeynRules* model files for running numerical scans in *micrOMEGAs*; this also included coding up of all the constraints and likelihoods discussed in the paper.

Together with Andre, I ran multiple numerical scans of the model on super-computers and generated the frequentist and Bayesian scan results. I also made important contributions toward writing up the draft.

Date

20th January, 2020

Signature

Name of Co-Author

Jan Heisig (CP3, UCLouvain)

Contribution to the Paper

- Numerical results (computation of Fermi-LAT limits, cross-checks, interpretation)
- Writing manuscript

Date

20th January, 2020

Signature

Name of Co-Author

Chiara Arina

Contribution to the Paper

I contributed in the writing of the paper, in the discussion of the results and in their cross-checking.

Date

20th January, 2020

Signature

Name of Co-Author

Celine Degrande (CP3/UCLouvain)

Contribution to the Paper

Discussion of the results and their validity.
Writing a small part of the paper.
Checking the FeynRules model file.

Date

23th January, 2020

Signature

Abstract

We perform a global fit within the pseudo-Nambu-Goldstone dark matter (DM) model emerging from an additional complex scalar singlet with a softly broken global $U(1)$ symmetry. Leading to a momentum-suppressed DM-nucleon cross section at tree level, the model provides a natural explanation for the null results from direct detection experiments. Our global fit combines constraints from perturbative unitarity, DM relic abundance, Higgs invisible decay, electroweak precision observables and latest Higgs searches at colliders. The results are presented in both frequentist and Bayesian statistical frameworks. Furthermore, post-processing our samples, we include the likelihood from gamma-ray observations of *Fermi*-LAT dwarf spheroidal galaxies and compute the one-loop DM-nucleon cross section. We find two favoured regions characterised by their dominant annihilation channel: the Higgs funnel and annihilation into Higgs pairs. Both are compatible with current *Fermi*-LAT observations, and furthermore, can fit the slight excess observed in four dwarfs in a mass range between about 30–300 GeV. While the former region is hard to probe experimentally, the latter can partly be tested by current observations of cosmic-ray antiprotons as well as future gamma-ray observations.

9.1 Introduction

The true particle nature of dark matter (DM) continues to remain a mystery despite a plethora of astrophysical/cosmological evidence to support its existence [267]. Although the well-known Weakly Interacting Massive Particle (WIMP) offers a viable solution, most common models are strongly constrained by direct detection experiments [242, 243, 268]. This has forced us to either seek alternate particle DM candidates (e.g., axions [269–272], sterile neutrinos [273, 274]) or explore new ways of saving the canonical ‘WIMP paradigm.

A natural way of achieving the latter is to suppress the DM-nucleon interaction at tree level. For instance, in certain particle DM models, some parameter combinations can lead to blind spots in direct detection experiments or even a suppression of the DM-nucleon coupling [275–278]. Alternatively, the DM-nucleon couplings could vanish due to symmetries [279, 280]. More commonly, however, particle DM models with a pseudoscalar mediator [185, 191, 281–284] leads to a momentum-suppressed DM-nucleon cross section. Thus, this class of models can naturally evade the strong limits from direct detection experiments.

A popular example in this regards is the pseudo-Nambu-Goldstone (pNG) DM. It is realised by adding a complex scalar singlet with a softly broken global $U(1)$ symmetry [285–287] to the Standard Model (SM) particle content. Due to the soft symmetry breaking, the resulting Goldstone becomes massive, i.e., a pNG boson. An additional CP symmetry ensures the stability of the pNG boson, which serves as a viable DM candidate. The Goldstone nature of the DM particle implies that the pNG DM-nucleon cross section is momentum-suppressed at tree-level.[1] Thus, a pNG DM model offers a natural way of evading the strong direct detection limits. A leading-order contribution to the pNG DM-nucleon cross section in the zero-momentum limit appears at the one-loop level [289, 290]. For typical DM velocities in our galaxy, $v_\chi \sim 10^{-3}$, it can easily dominate over the tree-level contribution. The one-loop cross section can vary by several orders of magnitude in the allowed model parameter space. It has been shown that for parameter points which satisfy the relic density constraint, the one-loop cross section is typically below $\sim 10^{-50}$ cm^2 [289] and thus beyond the expected reach of future direct detection experiments, e.g., LUX-ZEPLIN (LZ) [291] and DARWIN [157].

More recently, the pNG DM model was confronted against the constraints from perturbative unitarity, DM relic density, Higgs invisible decay, XENON1T, *Fermi*-LAT dwarf spheroidal (dSph) galaxies [292] and LHC searches at $\sqrt{s} = 13$ TeV [287, 293–295]. Projected limits from DARWIN were also imposed in ref. [290], although they were only slightly stronger than the perturbative unitarity constraint. The *Fermi*-LAT limits in ref. [294] were computed in an approximate way by considering annihilation into $b\bar{b}$, (on-shell) W^+W^-, ZZ and hh, where the latter three channels were included by applying a re-scaling factor on the $b\bar{b}$ limit from refs. [296, 297]. In addition, the model has also been used as a testbed for fitting the galactic centre gamma-ray and cosmic-ray antiproton excess [298].

The pNG DM model has also been studied in light of electroweak baryogenesis. In ref. [299], the authors found that the phase transition in this model is of second-order, and thus a sizable gravitational wave signal is not possible. However, the situation definitely improves if the model is extended to possess a $\mathbb{Z}_3$ symmetry. In this case,

---

[1] In fact, this suppression persists in the general case of N scalars which are symmetric under a global $U(1) \otimes S_N$ symmetry [288].

both a strong first-order phase transition and a sizable gravitational wave signal is possible [300].

In this paper, we perform a global fit of the pNG DM model. Our likelihood include constraints from perturbative unitarity, DM relic abundance, Higgs invisible decay width, electroweak precision observables, and latest Higgs searches at colliders. Our results are presented in both frequentist and Bayesian statistical frameworks. We also post-process our samples by computing the gamma-ray flux and the resulting likelihood from *Fermi*-LAT observations of dwarf Spheroidal galaxies (dSphs). We consider a set of 41 and 45 dSphs, excluding and including, respectively, those that show slight excesses compatible with DM annihilation. We take into account all relevant annihilation channels including annihilation into HH and hH as well as those proceeding via off-shell vector bosons. In addition, we compute the one-loop pNG DM-nucleon cross section for our samples and compare the resulting values against the current limits from XENON1T (2018), and projected future limits from LZ and DARWIN. Our FeynRules [301], UFO [302], CalcHEP [303] and FeynArts [304] model files are publicly available at the FeynRules database.[2]

The remainder of the paper is organised as follows. In section 9.2, we introduce the pNG DM model. In section 9.3, we describe the various observables and likelihoods used in our global fit and in the post-processing. Our numerical scan details, global fit results, including *Fermi*-LAT and direct detection constraints, are presented in section 9.4. We conclude in section 9.5. Appendices 9.6.1 and 9.6.2 summarise analytic expressions used in this paper.

9.2 Pseudo-Nambu-Goldstone Dark Matter

We extend the SM Lagrangian by adding a new complex scalar field S that couples to the SM particles via a *Higgs portal* term, $\Phi^\dagger\Phi$ (Φ is the SM Higgs doublet). The model Lagrangian is given by [285]

$$\mathcal{L} = \mathcal{L}_{\text{SM}} + \mathcal{L}_S + \mathcal{L}_{\text{soft}}, \tag{9.1}$$

where $\mathcal{L}_{\text{SM}}$ is the SM Lagrangian,

$$\mathcal{L}_S = (\partial_\mu S)^*(\partial^\mu S) + \frac{\mu_S^2}{2}|S|^2 - \lambda_{\Phi S}\,\Phi^\dagger\Phi|S|^2 - \frac{\lambda_S}{2}|S|^4, \tag{9.2}$$

$$\mathcal{L}_{\text{soft}} = \frac{\mu_S'^2}{4}(S^2 + S^{*2}). \tag{9.3}$$

---

[2] https://feynrules.irmp.ucl.ac.be/wiki/pNG

Notice that eq. (9.2) is invariant under a dark $U(1)$ global symmetry:

$$S \to e^{i\alpha} S, \tag{9.4}$$

where α is a real, space-time independent parameter. However, the $\mu_S'^2$ term in eq. (9.3) softly breaks this symmetry. Thus, the model contains a *massive* Goldstone boson, i.e., a pNG boson. After this symmetry breaking, we are left with a residual $\mathbb{Z}_2$ symmetry, $S \to -S$, of the dark $U(1)$ group, which forbids a linear term in S in the above Lagrangians.

The parameter $\mu_S'^2$ can be made real and positive by the phase redefinition of S. Thus, eq. (9.1) is invariant under a dark CP symmetry:

$$S \to S^*. \tag{9.5}$$

This symmetry is unbroken by the S vacuum expectation value (VEV) as for positive $\mu_S'^2$, the VEV is real. Thus, the total symmetry of the model Lagrangian is $\mathbb{Z}_2 \otimes CP$.

With an extra scalar, the scalar potential becomes

$$V = V_{\text{SM}} + V_S + V_{\text{soft}}, \tag{9.6}$$

where V_S and V_{soft} can be read directly from eqs. (9.2) and (9.3) respectively. Meanwhile, the SM part of the potential reads

$$V_{\text{SM}} = -\frac{\mu_\Phi^2}{2}\Phi^\dagger\Phi + \frac{\lambda_\Phi}{2}(\Phi^\dagger\Phi)^2. \tag{9.7}$$

After electroweak symmetry breaking, the model spectrum can be analysed by decomposing Φ and S in the unitary gauge as

$$\Phi = \frac{1}{\sqrt{2}}\begin{pmatrix} 0 \\ v_h + \phi \end{pmatrix}, \quad S = \frac{v_s + s + i\chi}{\sqrt{2}}, \tag{9.8}$$

where v_h is the SM Higgs VEV. Under the dark CP symmetry in eq. (9.5), $\chi \to -\chi$. This guarantees the stability of χ and makes it a viable DM candidate; the physical χ mass is $m_\chi^2 = \mu_S'^2$.

After imposing the stationary point conditions at $(\phi,\, s) = (0,\, 0)$, we get

$$\mu_\Phi^2 = \lambda_\Phi v_h^2 + \lambda_{\Phi S} v_s^2, \tag{9.9}$$

$$\mu_S^2 = \lambda_S v_s^2 + \lambda_{\Phi S} v_h^2 - \mu_S'^2. \tag{9.10}$$

Given that the S VEV is non-zero in general, the $\lambda_{\Phi S}$ term in eq. (9.2) leads to a mixing between the CP-even interaction eigenstates (ϕ, s). Thus, the squared mass matrix $\mathcal{M}^2$ is non-diagonal, namely

$$\mathcal{M}^2 = \begin{pmatrix} \lambda_\Phi v_h^2 & \lambda_{\Phi S} v_h v_s \\ \lambda_{\Phi S} v_h v_s & \lambda_S v_s^2 \end{pmatrix}. \tag{9.11}$$

As $\mathcal{M}^2$ is real and symmetric, it can be diagonalised by a unitary transformation:

$$\mathcal{O}^T \mathcal{M}^2 \mathcal{O} = \begin{pmatrix} m_h^2 & 0 \\ 0 & m_H^2 \end{pmatrix}, \tag{9.12}$$

where

$$\mathcal{O} = \begin{pmatrix} \cos\theta & \sin\theta \\ -\sin\theta & \cos\theta \end{pmatrix}. \tag{9.13}$$

Here θ is a mixing angle that satisfies the following relation:

$$\tan 2\theta = \frac{2\lambda_{\Phi S} v_h v_s}{\lambda_S v_s^2 - \lambda_\Phi v_h^2}. \tag{9.14}$$

The eigenvalues of $\mathcal{M}^2$ correspond to the masses of the CP-even mass eigenstates (h, H),

$$m_{h,\,H}^2 = \frac{1}{2}\left[\lambda_\Phi v_h^2 + \lambda_S v_s^2 \mp \left(\frac{\lambda_S v_s^2 - \lambda_\Phi v_h^2}{\cos 2\theta}\right)\right]. \tag{9.15}$$

Given the discovery of a SM-like Higgs at the LHC [305, 306], we identify h as a SM-like Higgs boson with

$$m_h = 125~\text{GeV}, \quad v_h = 246~\text{GeV}. \tag{9.16}$$

Thus, the pNG DM model contains 4 free parameters:

$$\{m_\chi,\, v_s,\, \theta,\, m_H\}. \tag{9.17}$$

The remaining parameters in eqs. (9.2) and (9.3) can be expressed as

$$\lambda_\Phi = \frac{1}{v_h^2}\left(m_h^2 \cos^2\theta + m_H^2 \sin^2\theta\right), \qquad \mu_S'^2 = m_\chi^2, \tag{9.18}$$

$$\lambda_S = \frac{1}{v_s^2}\left(m_h^2 \sin^2\theta + m_H^2 \cos^2\theta\right), \qquad \mu_\Phi^2 = \lambda_\Phi v_h^2 + \lambda_{\Phi S} v_s^2, \tag{9.19}$$

$$\lambda_{\Phi S} = \frac{1}{v_h v_s}\left(m_H^2 - m_h^2\right)\sin\theta\cos\theta, \qquad \mu_S^2 = \lambda_S v_s^2 + \lambda_{\Phi S} v_h^2 - \mu_S'^2. \tag{9.20}$$

9.3 Observables and constraints

In this section, we describe the set of constraints included in our global fit and post-processing of final samples.

9.3.1 Theoretical bounds

We require the model parameters to satisfy the following two theoretical bounds.

1. *Bounded tree-level potential*: The tree-level potential in eq. (9.6) must be bounded from below. This translates into the following lower bounds:

$$\lambda_\Phi > 0, \quad \lambda_S > 0, \quad \lambda_{\Phi S} > -\sqrt{\lambda_\Phi \lambda_S}. \tag{9.21}$$

2. *Perturbative unitarity*: We require the perturbative unitarity of scattering amplitudes [307]. Using the $HH \to HH$ scattering process, we impose the following upper bound on the S quartic coupling [308]:

$$\lambda_S < 8\pi/3. \tag{9.22}$$

   Although this bound can vary with the exact scattering process of interest, we choose this form to maintain comparability with previous studies in literature [285, 287, 290, 298].

Parameter points that do not fulfill these requirements are discarded from our scan. This is formally achieved by assigning a very small likelihood to such points.

9.3.2 Thermal relic abundance

The pNG boson χ is the DM candidate. Similar to the extended scalar singlet model [309], χ can annihilate into $f\overline{f}$ (where f = quarks/leptons), W^+W^-, ZZ, hh, hH and HH final states via an s-channel h/H exchange. In addition, χ annihilation into hh, hH and HH final states is also possible via t- and u-channels via χ exchange.

In our numerical scans, we require χ to make up *all* of the observed DM relic abundance.[3] This is achieved using a Gaussian likelihood function for the DM relic density that is centered at the *Planck* (2018) measured value [310]:

$$\Omega_{\rm DM} h^2 = 0.120 \pm 0.001. \tag{9.23}$$

---

[3] In general, χ can account for a subdominant component of the observed DM relic abundance, i.e., $f_{\rm rel} \equiv \Omega_\chi/\Omega_{\rm DM} < 1$. However, this choice (generally) leads to a larger allowed parameter space than the $f_{\rm rel} = 1$ case [309]. We adopt the latter choice in our study.

We also include a 5% theoretical uncertainty and combine it in quadrature with the *Planck* measured uncertainty. This is done to reflect any uncertainties arising from the relic density calculation in micrOMEGAs v5.0.8 [311].

With two neutral scalar mediators, the χ annihilation cross section is resonantly enhanced when $m_\chi \sim m_{h,\,H}/2$. To obtain the correct DM abundance, the χ annihilation cross section must be sufficiently suppressed. This is achieved for small values of v_h/v_s (or large v_s); an expression for the DM-scalar coupling can be found in Appendix 9.6.1. Away from these resonances, large values of v_h/v_s (or small v_s) generally saturates the χ relic density to the observed value.

9.3.3 Higgs invisible decay width

When $m_\chi \lesssim m_{h,\,H}/2$, the two scalars $\{h,\ H\}$ are kinematically allowed to decay into a pair of DM particles, i.e., $h,\ H \to \chi\chi$. This contributes to the following invisible decay widths [287]:

$$\Gamma_{\text{inv}}(h \to \chi\chi) = \frac{1}{32\pi}\frac{m_h^3 \sin^2\theta}{v_s^2}\sqrt{1-\frac{4m_\chi^2}{m_h^2}}, \tag{9.24}$$

$$\Gamma_{\text{inv}}(H \to \chi\chi) = \frac{1}{32\pi}\frac{m_H^3 \cos^2\theta}{v_s^2}\sqrt{1-\frac{4m_\chi^2}{m_H^2}}. \tag{9.25}$$

Recently, both the ATLAS [312] and CMS [313] experiments released new upper limits on the Higgs invisible branching ratio $\mathcal{BR}(h \to \chi\chi)$ for a SM-like Higgs from a combination of Run 1 and 2 analyses. Here we adopt the conservative upper limit from the ATLAS experiment [312], namely

$$\mathcal{BR}(h \to \chi\chi) \equiv \frac{\Gamma_{\text{inv}}(h \to \chi\chi)}{\Gamma_h^{\text{tot}}(m_h)} \leq 0.26, \tag{9.26}$$

where $\Gamma_h^{\text{tot}}(m_h)$ is the total decay width of h into SM and non-SM final states.

In the following, we apply the limit in eq. (9.26) only on the scalar h whose mass is fixed at 125 GeV. This experimental limit is derived from Higgs production in association with a weak gauge boson or through vector boson fusion (VBF), and assuming a SM-like Higgs except for the fact that it can decay to a pair of invisible particles, e.g., DM. The experimental signatures are large missing energy with either a weak boson or a pair of jets. Thus, the invariant mass of the invisible particles is not measured, and the second scalar can contribute as well to these processes. However, this contribution is small when the mixing angle is small as the production of the second (first) scalar is suppressed by a factor $\sin^2\theta$ ($\cos^2\theta$) compared to the SM production rate. The production rate also varies with the mass of the scalar but this effect is small for a light scalar ($m_H \sim 100\,\text{GeV}$) in the most constraining channel, i.e., VBF, as the cuts on the invariant mass of the two jets ($m_{jj} > 1\,\text{TeV}$) are already requiring a very large partonic center-of-mass energy. As the second scalar mass increases, its production rate is further reduced. To sum up, our approximation is only valid for small mixing angles and for $m_H \neq m_h$. However, as we show in the results section, the mixing angle is allowed to be large and even maximal when the two scalars are degenerate, i.e., when $m_H \sim m_h = 125\,\text{GeV}$. In this case, both scalars contribute to the process and interfere quite strongly. The amplitude can be written as

$$\mathcal{A} \propto \frac{\cos\theta\sin\theta}{v_s}\left(\frac{m_h^2}{p^2 - m_h^2 + i m_h \Gamma_h^{\text{tot}}} - \frac{m_H^2}{p^2 - m_H^2 + i m_H \Gamma_H^{\text{tot}}}\right), \tag{9.27}$$

where Γ_h^{tot} (Γ_H^{tot}) are the total decay width of scalars $h\,(H)$. The amplitude for the production of the scalar is multiplied by a factor $\cos\theta$ ($\sin\theta$) compared to the SM due to the modification of the couplings between the gauge bosons and h (H). The remaining factors, besides the propagators, are due to the couplings with the DM particle χ (see Appendix 9.6.1). The missing pre-factor in eq. (9.27) depends only on pure SM couplings and its exact expression depends on the process considered. The two terms in the brackets can cancel exactly for $\theta = \pi/4$ if the two masses are identical, as in that case, the two widths are also identical. Thus, these points are unconstrained experimentally but many of them would be excluded by applying blindly the constraints on the invisible decay width, which is the dominant channel for low values of m_χ and v_s. However, the correct re-interpretation of the invisible width constraint goes beyond the scope of this paper and thus is left as a future work.

The upper limit in eq. (9.26) constrains the $m_\chi \lesssim m_h/2$ region where $\Gamma_{\text{inv}}(h \to \chi\chi)$ can be sizeable. In our numerical scans, we use a one-sided Gaussian likelihood function that is centered at the above measured value for $\mathcal{BR}(h \to \chi\chi)$. Similar to the relic density likelihood, we add a 5% theoretical uncertainty from our calculation of $\mathcal{BR}(h \to \chi\chi)$ and combine it in quadrature with the (expected) branching ratio uncertainty of 0.07 [312].

9.3.4 Electroweak precision observables

The extra scalar S contributes to the gauge boson self-energy diagrams. Its effect on the electroweak precision observables (EWPO) can be parametrised by the oblique parameters S, T and U [266, 314]. As S is electrically neutral, only the W and Z boson self-energies are modified.

Given that only the real component of S acquires a non-zero VEV, the pNG DM χ (imaginary component of S) does not contribute to the W/Z self-energies. Thus, the oblique parameters in our model have the same functional dependency as in the extended scalar singlet model [309], namely,

$$\Delta\mathcal{O} \equiv \mathcal{O} - \mathcal{O}_{\rm SM} = (1-\cos^2\theta)\Big[\mathcal{O}_{\rm SM}(m_H) - \mathcal{O}_{\rm SM}(m_h)\Big], \tag{9.28}$$

where $\mathcal{O} \in (S,\, T,\, U)$; for the analytical expressions, see Appendix 9.6.2. From eq. (9.28), it is clear that for large m_H, $\theta \sim 0$ is required, whereas large mixing angles θ are allowed for $m_H \simeq m_h$ (see e.g., ref. [315]).

Using the SM reference as $m_h^{\rm ref} = 125\,\text{GeV}$ and $m_t^{\rm ref} = 172.5\,\text{GeV}$, a recent global electroweak fit obtains [316]

$$\Delta S = 0.04 \pm 0.11, \quad \Delta T = 0.09 \pm 0.14, \quad \Delta U = -0.02 \pm 0.11, \tag{9.29}$$

and the following correlation matrix:

$$\rho_{ij} = \begin{pmatrix} 1 & 0.92 & -0.68 \\ 0.92 & 1 & -0.87 \\ -0.68 & -0.87 & 1 \end{pmatrix}. \tag{9.30}$$

In our numerical scans, we use the following EWPO likelihood function [317]:

$$\ln\mathcal{L}_{\rm EWPO} = -\frac{1}{2}\sum_{i,j}(\Delta\mathcal{O}_i - \overline{\Delta\mathcal{O}_i})\left(\Sigma^2\right)^{-1}_{ij}(\Delta\mathcal{O}_j - \overline{\Delta\mathcal{O}_j}), \tag{9.31}$$

where $\overline{\Delta\mathcal{O}_i}$ are the central values for the shifts in eq. (9.29), $\Sigma^2_{ij} \equiv \sigma_i\rho_{ij}\sigma_j$ is the covariance matrix, ρ_{ij} is the correlation matrix in eq. (9.30) and σ_i are the associated errors in eq. (9.29).

9.3.5 Higgs searches at colliders

In the narrow-width approximation, the signal strength μ_h for a SM-like Higgs h [287] is

$$\mu_h \equiv \sigma(pp\to h)\cdot\mathcal{BR}(h\to\text{SM}). \tag{9.32}$$

The inclusion of H in our model leads to a universal suppression of couplings between h and SM particles. Thus, the h production cross section is

$$\sigma(pp\to h) = \cos^2\theta\;\sigma^{\rm SM}_{pp\to h}(m_h), \tag{9.33}$$

where $\sigma^{\rm SM}_{pp\to h}(m_h)$ is the h production cross section in the SM. Similarly, the branching ratio of h into SM particles is

$$\mathcal{BR}(h \to {\rm SM}) \equiv \frac{\Gamma(h\to {\rm SM})}{\Gamma_h^{\rm tot}} = \frac{\cos^2\theta\;\Gamma_h^{\rm SM}(m_h)}{\cos^2\theta\;\Gamma_h^{\rm SM}(m_h) + \Gamma(h\to\chi\chi) + \Gamma(h\to HH)}, \tag{9.34}$$

where $\Gamma_h^{\rm SM}(m_h)$ is the total decay width of a SM-like Higgs h with mass m_h into SM final states. The last two terms in the denominator corresponds to the new decay modes of h, namely $h\to\chi\chi$ and $h\to HH$.

Thus, the signal strength μ_h in eq. (9.32) becomes

$$\mu_h = \frac{\cos^4\theta\;\mu_h^{\rm SM}}{\cos^2\theta\;\Gamma_h^{\rm SM}(m_h) + \Gamma(h\to\chi\chi) + \Gamma(h\to HH)}, \tag{9.35}$$

where $\mu_h^{\rm SM} \equiv \sigma^{\rm SM}_{pp\to h}(m_h)\cdot\Gamma_h^{\rm SM}(m_h)$ is the h signal strength in the SM. From the above expression, it is clear that $\mu_h \neq \mu_h^{\rm SM}$ when the mixing angle $\theta\neq 0$, or when h decay into non-SM final states is kinematically allowed.

To constrain the scalar masses and mixings in the pNG DM model, we adopt the following two approaches and construct a likelihood function for each one.

- For $m_H \lesssim 120\,$GeV, we compute a LEP χ^2 using the HiggsBounds v5.3.2beta [318, 319] package. Using the two scalar masses, their total decay widths, effective Higgs-SM couplings, and branching ratios of h/H into SM and non-SM particles as input parameters, we determine the most-sensitive LEP analysis that is relevant for each parameter point in our numerical scan. This is used to compute a LEP chi-square $\chi^2_{\rm LEP}$, and consequently a LEP likelihood function:

$$\ln\mathcal{L}_{\rm LEP} = -\frac{1}{2}\chi^2_{\rm LEP}. \tag{9.36}$$

- For $m_H \gtrsim 120\,$GeV, we rely on the observed Higgs signal strength and mass measurements performed for a SM-like Higgs at the LHC. This is achieved using the HiggsSignals v2.2.3beta [320] package. In practice, we compute three contributions to the χ^2 that are based on *i*) combined run 1 results ($\chi^2_{\rm R1}$); *ii*) results from 13 TeV LHC analyses ($\chi^2_{13\,\rm TeV}$); and *iii*) results in the form of Simplified Template Cross Sections (STXS) ($\chi^2_{\rm STXS}$). The final HiggsSignals likelihood that we use in our numerical scans is

$$\ln\mathcal{L}_{\rm HS} = -\frac{1}{2}\left(\chi^2_{\rm R1} + \chi^2_{13\,\rm TeV} + \chi^2_{\rm STXS}\right). \tag{9.37}$$

Each of the individual chi-squares are computed using the *peak-centered* method with Gaussian probability density function and zero theoretical mass uncertainty for the two scalar masses. For more details, see ref. [320].

9.3.6 *Fermi*-LAT gamma-ray observations

Gamma-ray observations of dSphs by *Fermi*-LAT provide robust limits on the DM annihilation flux. To constrain our model, we use the publicly available energy-binned likelihood profiles[4] from *Fermi*-LAT [292], as implemented in MadDM v3.0 [321]. We consider the set of all 45 observed dSphs and use the measured J-factors based on spectroscopic observations [292] as adopted from ref. [322]. When measurements are not available, we use the values predicted from the distance scaling relationship with a nominal uncertainty of 0.6 dex [292]. We profile over the J-factor of each dwarf galaxy according to its uncertainty and obtain a total likelihood function as described in ref. [263].

The corresponding gamma-ray energy spectra are computed using MadDM, while showering and hadronisation is achieved using Pythia v8.0 [323]. We include all annihilation channels that contribute at least 1% to the total DM annihilation rate today. In particular, besides the usual $2 \to 2$ processes in MadDM, we also include $2 \to 3$ annihilation processes, $\chi\chi \to VV^*$, where V^* is an off-shell weak gauge boson. In addition, we include $2 \to 3$, $2 \to 4$, $2 \to 5$ and $2 \to 6$ processes such as $\chi\chi \to Hh$, HH where H decays further into pairs of SM particles, including VV^*. The decay of all on-shell SM particles is performed within Pythia.

In four (Reticulum II, Tucana III, Tucana IV and Indus II) of the 45 dSphs, slight excesses have been found with a local significance of roughly 2σ each [292, 324, 325]. Consequently, a combination of the likelihoods from all dwarfs favors a certain range of DM masses and annihilation cross sections that provide a flux compatible with the excess. However, as the DM origin of these excesses is not yet established, we show our results in section 9.4 with and without including the respective four dwarfs. The latter choice imposes an upper bound on the DM annihilation cross section only.

9.3.7 Direct detection at one-loop level

The elastic spin-independent (SI) pNG DM-nucleon cross section is momentum-suppressed at tree-level (see Appendix 9.6.1) and given by [289]

$$\sigma_{\chi N}^{\text{tree-level}} \approx \frac{4\sin^2\theta\cos^2\theta\, f_N^2}{3\pi}\frac{m_N^2\mu_{\chi N}^6}{m_\chi^2 v_h^2 v_s^2}\frac{(m_h^2 - m_H^2)^2}{m_h^4 m_H^4}v_\chi^4, \tag{9.38}$$

---

[4] https://www-glast.stanford.edu/pub_data/1203/

where $\mu_{\chi N} \equiv m_\chi m_N/(m_\chi + m_N)$ is the DM-nucleon reduced mass, $f_N = 0.3$ is the effective Higgs-nucleon coupling [326–328], $m_N = 939\,\text{MeV}$ is the averaged nucleon mass and v_χ is the DM velocity in the laboratory frame. In the vicinity of the Earth, $v_\chi \sim 10^{-3}$. Thus, the nuclear recoil rate is suppressed by a factor of $v_\chi^4 \sim 10^{-13}$. For a typical choice of model parameters, the tree-level cross section in eq. (9.38) is too small to be experimentally observed at current or future planned experiments [289].

A leading order contribution to the DM-nucleon cross section appears at one-loop level. It can be approximated by [285, 289]

$$\sigma_{\chi N}^{\text{1-loop}}\Big|_{\text{Approx}} \approx \begin{cases} \dfrac{\sin^2\theta}{64\pi^5}\dfrac{m_N^4 f_N^2}{m_h^4 v_h^2}\dfrac{m_H^4 m_\chi^2}{v_s^6}, & m_\chi \leq m_H, \\ \dfrac{\sin^2\theta}{64\pi^5}\dfrac{m_N^4 f_N^2}{m_h^4 v_h^2}\dfrac{m_H^8}{m_\chi^2 v_s^6}, & m_\chi > m_H. \end{cases} \tag{9.39}$$

In the limit of $m_\chi^2 \equiv \mu_S'^2 \to 0$, the DM particle χ becomes a true Goldstone boson of the spontaneously broken global $U(1)$ symmetry. Thus, the direct detection amplitude should vanish. This behavior is observed in eq. (9.39).

In ref. [289], the authors point out that the approximate one-loop cross section in eq. (9.39) can under/overestimate the actual cross section by several orders of magnitude depending on the model parameters. Thus, we use the full one-loop cross section from ref. [289] in our study:

$$\sigma_{\chi N}^{\text{1-loop}} = \frac{\mu_{\chi N}^2}{\pi}\frac{f_N^2 m_N^2}{v_h^2 m_\chi^2}\mathcal{F}^2, \tag{9.40}$$

where the one-loop function $\mathcal{F}$ is

$$\begin{aligned} \mathcal{F} = -\frac{\sin 2\theta\,(m_h^2 - m_H^2)m_\chi^2}{128\pi^2\, v_h v_s^3\, m_h^2 m_H^2} \Big[& \mathcal{A}_1 C_2(0, m_\chi^2, m_\chi^2, m_h^2, m_H^2, m_\chi^2) \\ & + \mathcal{A}_2 D_3(0, 0, m_\chi^2, m_\chi^2, 0, m_\chi^2, m_h^2, m_h^2, m_H^2, m_\chi^2) \\ & + \mathcal{A}_3 D_3(0, 0, m_\chi^2, m_\chi^2, 0, m_\chi^2, m_h^2, m_H^2, m_H^2, m_\chi^2)\Big]. \end{aligned} \tag{9.41}$$

Here the C and D terms are Passarino-Veltman functions [329–331] as computed using LoopTools v2.14 [331, 332].[5] The coefficients $\mathcal{A}_i$ are defined as

$$\begin{aligned} \mathcal{A}_1 &\equiv 4(m_h^2\sin^2\theta + m_H^2\cos^2\theta)(2m_h^2 v_h\sin^2\theta + 2m_H^2 v_h\cos^2\theta - m_h^2 v_s\sin 2\theta + m_H^2 v_s\sin 2\theta), \\ \mathcal{A}_2 &\equiv -2m_h^4\sin\theta\left[(m_h^2 + 5m_H^2)v_s\cos\theta - (m_h^2 - m_H^2)(v_s\cos 3\theta + 4v_h\sin^3\theta)\right], \\ \mathcal{A}_3 &\equiv 2m_H^4\cos\theta\left[(5m_h^2 + m_H^2)v_s\sin\theta - (m_h^2 - m_H^2)(v_s\sin 3\theta + 4v_h\cos^3\theta)\right]. \end{aligned} \tag{9.42}$$

---

[5] http://www.feynarts.de/looptools/

Note that $\mathcal{F}$ is proportional to m_χ^2, and the fact that both the C_2 and D_3 functions behave as constants in the limit of $m_\chi \to 0$ [285, 289], the direct detection amplitude indeed vanishes in this limit.

By means of our global fit, we are able to check the conclusions of ref. [289] more generally. We post-process our final samples, compute the approximate and actual one-loop cross sections using eqs. (9.39) and (9.40) respectively, and present results in the $\{m_\chi, \sigma_{\chi N}^{\text{1-loop}}\}$-plane. This allows us to confront the allowed parameter space of the model against the current limits from XENON1T [268], and projected sensitivities from LZ [291] and DARWIN [157]. These results are presented in section 9.4.

The authors of ref. [290] have also computed the full one-loop DM-nucleon scattering cross section. Their results are consistent with ref. [289] in most parts of the parameter space. However, large deviations appear at small DM masses. We have verified that for the parameter space that we consider, these deviations do not impact our conclusions. In regions where these differences can be sizeable, the overall cross section lies well below the experimental limits that we show in section 9.4.

9.4 Results

In this section, we discuss the statistical treatment of the various constraints included in our global fit and show the corresponding results.

9.4.1 Statistical analysis

To find the allowed regions in the model parameter space, we use MultiNest v3.10.0 [255] with $50,000$ live points[6] and a stopping tolerance of 0.01. MultiNest is based on an implementation of the Importance Nested Sampling algorithm. It is primarily a Bayesian inference tool designed to compute the Bayesian evidence $\mathcal{Z}$ (defined below). As a by-product, it draws posterior samples from a distribution that may contain a high multiplicity of nodes and/or degeneracies. Furthermore, MultiNest is capable of sampling the profile likelihood ratio (defined below) for the purpose of frequentist analysis.

---

[6] For our frequentist analysis, we combine results from multiple MultiNest scans with 10k, 12k, 25k and 50k live points, see footnote 10 for more details. For our Bayesian analysis, we instead rely on a single MultiNest scan with 50k live points.

Parameters	**Ranges**	**Priors**
m_χ (GeV)	$[10,\ 10^3]$	log
v_s (GeV)	$[10,\ 10^6]$	log
θ (rad)	$[0,\ \pi/2]$	flat
m_H (GeV)	$[10,\ 10^3]$	log

Table 9.1 Ranges and priors for the free model parameters.

A key ingredient for both a frequentist and Bayesian analysis is the likelihood (or log-likelihood) function. In our numerical scans, the total log-likelihood function is

$$\ln \mathcal{L}_{\text{total}}(\boldsymbol{\theta}) = \ln \mathcal{L}_{\Omega_\chi h^2}(\boldsymbol{\theta}) + \ln \mathcal{L}_{\Gamma_{h\to\chi\chi}}(\boldsymbol{\theta}) + \ln \mathcal{L}_{\text{EWPO}}(\boldsymbol{\theta}) + \ln \mathcal{L}_{\text{LEP}}(\boldsymbol{\theta}) + \ln \mathcal{L}_{\text{HS}}(\boldsymbol{\theta}), \tag{9.43}$$

where $\boldsymbol{\theta} \equiv (m_\chi,\ v_s,\ \theta,\ m_H)$ are the free model parameters. Each of the individual likelihood functions are described in section 9.3.

The range and prior types for our free model parameters are summarised in table 9.1. For the mixing angle θ, we find that our results are symmetric under $\theta \to -\theta$. In addition, the case $\theta = \pi$ is analogous to $\theta = 0$, thus we only restrict $\theta \in [0, \pi/2]$. To cover the region close to the two resonances, $m_\chi \simeq m_{h,H}/2$, where the annihilation cross section is enhanced, we scan up to very large values for the second scalar VEV, i.e., $v_s \in [10,\ 10^6]$ GeV. The upper boundary corresponds to very small couplings λ_S and $\lambda_{\Phi S}$, see eqs. (9.19) and (9.20) respectively.

Profile likelihoods

In a frequentist analysis, the statistical precision of a parameter estimate is represented by a confidence interval that encapsulates the frequentist 'coverage probability'. Such an interval is dependent on the data $\boldsymbol{x}$, and thus changes upon each re-iteration of the experiment. As proper frequentist coverage is usually not possible for complicated likelihoods and parameter spaces, approximate methods are often used [333]. One such method is the well-known *profile construction* [334], which depends on the profile likelihood ratio (PLR):

$$\Lambda(\theta_i,\ \theta_j) \equiv \frac{\mathcal{L}_{\text{total}}(\theta_i,\ \theta_j,\ \hat{\hat{\boldsymbol{\nu}}}(\theta_i,\ \theta_j))}{\mathcal{L}_{\text{total}}(\hat{\boldsymbol{\theta}})}. \tag{9.44}$$

Here $\hat{\hat{\boldsymbol{\nu}}}(\theta_i,\ \theta_j)$ are the parameter values $\{\theta_k | \, k \neq i,\ j\}$ that maximise $\mathcal{L}_{\text{total}}(\boldsymbol{\theta})$ for a fixed $(\theta_i,\ \theta_j)$, whereas $\hat{\boldsymbol{\theta}}$ is the maximum likelihood estimate for $\boldsymbol{\theta}$, i.e., a 'best-fit' point that maximises $\mathcal{L}_{\text{total}}(\boldsymbol{\theta})$ [335, 336]. To construct confidence intervals, we

	Global fit	**Post-processing with *Fermi*-LAT**	
		41 dSphs	**45 dSphs**
Parameters			
m_χ (GeV)	62.573	121.632	62.598
v_h/v_s	0.0187	3.46	8.93×10^{-3}
θ (rad)	1.53	1.54	1.49
m_H (GeV)	125.30	125.30	125.30
Observables			
$\Omega_\chi h^2$	0.119	0.119	0.120
Dominant channel (FO)	$\chi\chi \to b\bar{b}$ (76%)	$\chi\chi \to hh$ (100%)	$\chi\chi \to b\bar{b}$ (76%)
Dominant channel (today)	$\chi\chi \to b\bar{b}$ (77%)	$\chi\chi \to WW$ (70%)	$\chi\chi \to b\bar{b}$ (77%)
$\langle\sigma v\rangle_0\,(\mathrm{cm^3\,s^{-1}})$	8.6×10^{-27}	4.4×10^{-31}	1.1×10^{-26}
$\sigma_{\chi N}^{\text{1-loop}}\,(\mathrm{cm^2})$	6.3×10^{-68}	3.1×10^{-54}	3.3×10^{-69}
$\ln \mathcal{L}_{\text{total}}^{\text{BF}}(\boldsymbol{\theta})$	-91.568	-91.569	-87.620

Table 9.2 A summary of the best-fit (BF) points, key DM observables (the DM relic abundance, the dominant annihilation channel during freeze-out (FO) and today, the DM annihilation cross section today and the one-loop DM-nucleon cross section) and total log-likelihood $\ln \mathcal{L}_{\text{total}}^{\text{BF}}(\boldsymbol{\theta})$ from our global fit (*column 1*), and after post-processing our samples with *Fermi*-LAT likelihood with 41 (*column 2*) and 45 (*column 3*) dwarf spheroidal (dSph) galaxies.

maximise Λ in the relevant parameter planes of interest while profiling over the other parameters and construct iso-likelihood contours at fixed confidence level (CL), e.g., 68.3% for 1σ and 95.4% for 2σ CL.

In figure 9.1, we show our PLR plots in six 2D planes spanned by all combinations of four model parameters. These are generated using `pippi v2.0` [180]. In each plane, model parameters that are not shown are profiled over. The 1σ (2σ) CL contours are marked by solid (dashed) lines. The best-fit point is shown as a red star; it is also summarised in column 1 of table 9.2.[7]

A central constraint is imposed by the relic density selecting a thin slice in parameter space that provides a thermally averaged cross section $\langle\sigma v\rangle_{\text{FO}} \sim 3 \times 10^{-26}\,\mathrm{cm^3\ s^{-1}}$. We find two phenomenologically distinct regions characterised by the type of annihilation channels relevant during freeze-out:

---

[7] From our plots, it is evident that the exact position of the best-fit point is not significant, as the PLR $\mathcal{L}/\mathcal{L}_{\text{max}}$ is mostly flat and close to 1 in a large portion of the 1σ CL region.

1. Dominant annihilation via s-channel Higgs exchange (h and/or H) into SM fermions and vector bosons. Within this region, we encounter resonant and non-resonant annihilation. In the former case (also known as the *Higgs funnel*), the thermally averaged cross section has a sizeable contribution from the center-of-mass energy $\sqrt{s} = m_{h/H}$ providing a significant resonant enhancement. According to the thermal momentum distribution, it is supported by DM mass in the range between somewhat below $m_{h/H}/2$ and $m_{h/H}/2$. The point of maximal resonant enhancement is close to the upper boundary of this range. The H- and h-resonance is visible as the (lower) diagonal stripe around $m_\chi \sim m_H/2$ and the horizontal band around $m_\chi \sim m_h/2$, respectively, in the (m_H, m_χ)-plane in figure 9.1. Due to the small coupling involved (i.e., small v_h/v_s, see Appendix 9.6.1), the resonant regions are not subject to strong constraints from other observables.[8]

   Non-resonant annihilation via Higgs exchange only leads to allowed points in the range $m_\chi > m_h/2$ and $m_\chi < m_H$. For points in the region $m_\chi \gtrsim m_H$, annihilation into Higgs pairs is dominant (see the next bullet point). Points below the resonance are (mostly) excluded by the perturbativity condition (see discussion further below) as the required coupling towards small DM masses quickly becomes too large. This can be understood from eq. (9.27), representing the amplitude of the respective annihilation process. For small center-of-mass energies compared to $m_h/2$ and $m_H/2$, a partial cancellation takes place and the amplitude is suppressed by s. This is in contrast to the singlet scalar Higgs portal model [338–340] where this suppression is not present and the region below the resonance can satisfy the relic density constraint for perturbative couplings. The features at low m_χ are made more apparent by zooming into a small DM mass window around the Higgs mass resonance region, $m_\chi \sim m_h/2$, as shown in figure 9.2.

2. Annihilation into Higgs pairs ($\chi\chi \to HH$, hH, hh) can be the dominant channel for $m_\chi > m_{h/H}$, and according to the thermal momentum distribution during freeze-out, for DM masses slightly below the Higgs threshold $m_\chi \lesssim m_{h/H}$. In our scan $\theta \sim 0$ is preferred except for $m_H \simeq m_h$ (see discussion further below). As the annihilation cross section into HH (hh) is proportional to $\cos^4\theta$ ($\sin^4\theta$), we find that $\chi\chi \to HH$ dominates over $\chi\chi \to hh$ except for the

---

[8] As pointed out in ref. [337], the assumption of local thermal equilibrium during freeze-out can break down near the resonances. This has the effect of changing the coupling value by a factor of order $\mathcal{O}(1)$. However, this part of the parameter space has small v_h/v_s and is well beyond the sensitivity of current and future experiments. Thus, we employ the standard calculation of the DM relic density within micrOMEGAs assuming local thermal equilibrium during freeze-out.

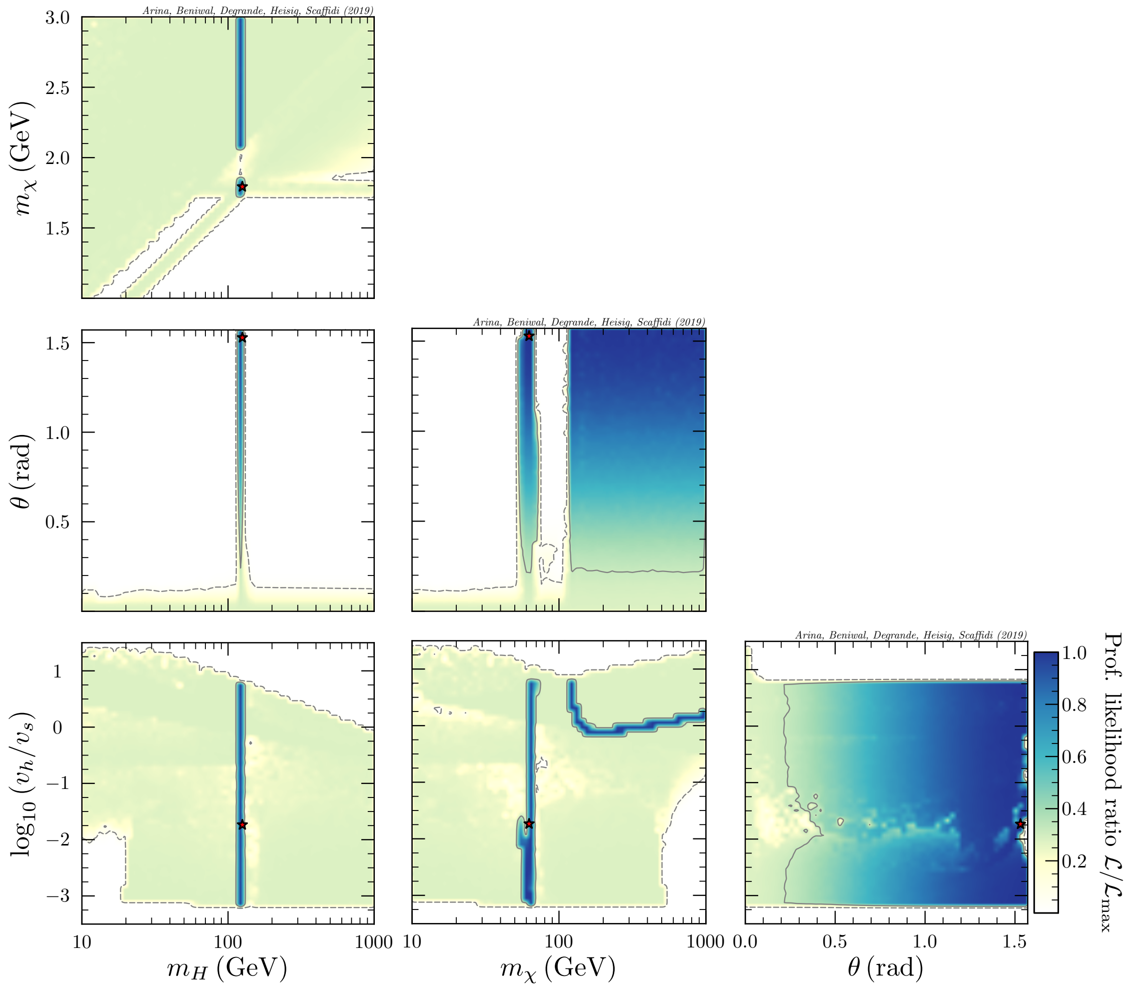

Fig. 9.1 2D profile likelihood ratio (PLR) plots in the planes of pNG DM model parameters. The 1σ (2σ) CL regions are marked by solid (dashed) lines. The best-fit point is marked by a red star; it is also summarised in column 1 of table 9.2.

region $m_H \simeq m_h$ where both are present. Consequently, annihilation into HH and hh leads to allowed points in the area above the diagonal band $m_\chi \sim m_H$ in the (m_H, m_χ)-plane in figure 9.1. Annihilation into hH is only relevant for $m_H \simeq m_h$ and $\theta \simeq \pi/4$ as well as in a small region where $m_\chi > m_h$ and $m_\chi \lesssim m_H$.

Mixing between h and H is highly constraint by several observations. First, to obtain a good agreement with the global electroweak fit results for the oblique parameters S, T and U, according to eq. (9.28), either a small mixing angle θ or $m_H \simeq m_h$ is required. Secondly, Higgs searches at LEP exclude most of the model parameter space for $m_H \lesssim 120\,\text{GeV}$ and sizeable θ. For larger m_H, the measured signal strength at the LHC impose strong constraints on the parameter space. In summary, a SM-like Higgs h is compatible with $\theta \lesssim 0.1$ rad for all values of m_H,

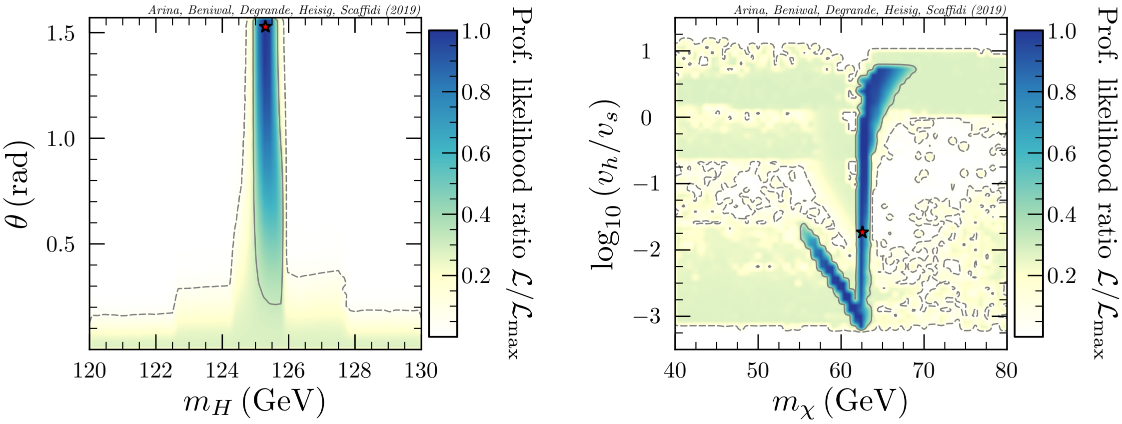

Fig. 9.2 2D PLR plots from our global fit in the (m_H, θ)- and (m_χ, v_h/v_s)-planes after zooming into the region $m_H \sim m_h$ and the resonance region, $m_\chi \sim m_h/2$, respectively.

except for $m_H \simeq m_h$ where arbitrary values of θ are allowed, see the (m_H, θ)-plane of figure 9.1. A similar behaviour was found in ref. [315]. On top of this, the observed signal strengths for a SM-like Higgs at the LHC exhibits a slight preference (around 1σ) for $m_H \simeq m_h$ and sizeable θ over the SM only prediction with $m_h = 125\,\text{GeV}$. However, the presence of a second Higgs improves the fit only due to the freedom in m_H. In fact, keeping m_h as a free parameter as well is expected to improve the fit and broaden the 1σ CL region beyond $m_H \simeq m_h$.[9]

As mentioned above, constraints from perturbative unitarity are relevant in and exclude parts of the parameter space where the measured relic density could only be matched with extremely large couplings. In the limit of small mixing, the perturbative unitarity limit in eq. (9.22) translates to

$$\lambda_S v_h^2 \overset{\theta\to 0}{\approx} \frac{m_H^2}{v_s^2} v_h^2 < \frac{8\pi}{3} v_h^2 \implies \frac{v_h}{v_s} < \sqrt{\frac{8\pi}{3}} \frac{v_h}{m_H} \simeq \frac{713\,\text{GeV}}{m_H}. \tag{9.45}$$

This limit is evident in the (m_H, v_h/v_s)-plane for $m_H \gtrsim 10\,\text{GeV}$, i.e., parameter points that lie outside the boundary of the 2σ CL implies $v_h/v_s > 713\,\text{GeV}/m_H$. Due to the strong constraints from perturbative unitarity towards small masses, limits from the invisible Higgs decay are less relevant than e.g., in the singlet scalar Higgs portal model. We found that dropping the likelihood from invisible Higgs decay does not significantly change the results shown in figure 9.1.

In figure 9.3, we show the PLR plots for key DM observables such as the pNG DM relic density, and its annihilation cross section into SM and non-SM particles today,

---

[9] The observed signal strengths are sensitive to the exact value of the SM-like Higgs mass, m_h. In a global fit, one could include m_h as a nuisance parameter and associate a corresponding Gaussian likelihood function that can be profiled (marginalised) over in a frequentist (Bayesian) analysis.

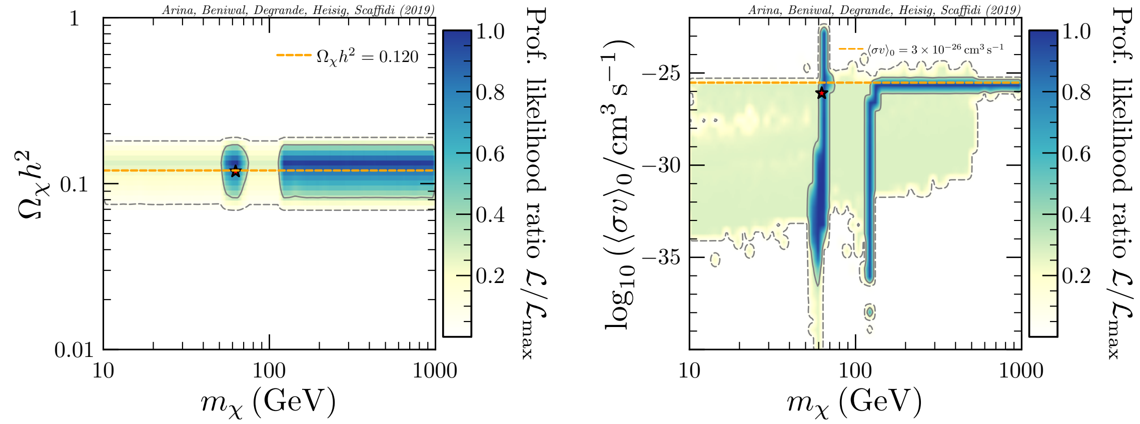

Fig. 9.3 2D PLR plots for key DM observables: the pNG DM relic abundance, $\Omega_\chi h^2$ (*left panel*) and DM annihilation cross section today, $\langle\sigma v\rangle_0$ (*right panel*). The solid (dashed) contours and red star have the same meaning as in figure 9.1. In the left panel, the orange dashed line shows the relic density measured by *Planck*; in the right panel, it shows the canonical freeze-out cross section, $\langle\sigma v\rangle_0 = 3 \times 10^{-26}\,\mathrm{cm^3\,s^{-1}}$.

$\langle\sigma v\rangle_0$. The 1σ CL region shows up as two disconnected islands. The small island at $m_\chi \simeq m_h/2 = 62.5\,\mathrm{GeV}$ corresponds to the h resonance, where $\chi\chi \to b\bar{b}$ channel is most dominant. The second island appears for $m_\chi \gtrsim 125\,\mathrm{GeV}$. As m_H is profiled over, and given that $m_H \simeq m_h$ is favoured, this island corresponds to the region where $\chi\chi \to hh,\, HH$ is dominant during freeze-out and sets the pNG DM relic abundance to the observed value today. Note that, although $\langle\sigma v\rangle_{\mathrm{FO}} \sim 3 \times 10^{-26}\,\mathrm{cm^3\,s^{-1}}$ as required by the relic density constraint, the annihilation cross section today, $\langle\sigma v\rangle_0$ varies over many order of magnitude. This is due to the large velocity dependence of the annihilation cross section in the vicinity of a resonance and a threshold. Resonant annihilation can lead to both $\langle\sigma v\rangle_0$ smaller or larger than $\langle\sigma v\rangle_{\mathrm{FO}}$ depending on whether the DM mass is smaller or slightly larger than the point of maximal enhancement during freeze-out. For the 1σ CL region, this behaviour can be seen in the right panel of figure 9.3. For annihilation into Higgs pairs, in contrast, $\langle\sigma v\rangle_0$ can only be suppressed compared to $\langle\sigma v\rangle_{\mathrm{FO}}$ due to the smaller phase space around threshold today. Again, this behaviour can be seen for the 1σ CL region above 125 GeV in the right panel of figure 9.3.

The best-fit point lies in the h-resonance region exhibiting large mixing and relatively small v_h/v_s. The best-fit for the second Higgs mass is $m_H = 125.3\,\mathrm{GeV}$ resulting from LHC signal strength measurements. The corresponding values are summarised in table 9.2. Note, however, that the PLR is relatively flat within the 1σ CL region. Furthermore, as stated above, the 1σ preference for $m_H \simeq 125.3\,\mathrm{GeV}$ to some extend is a result of our choice $m_h = 125\,\mathrm{GeV}$. This is in slight tension with the the LHC Higgs signal strength and could be alleviated by treating the Higgs mass as a nuisance parameter in the fit. We therefore consider the entire 2σ CL region to be consistent with observation on a compatible level.

Marginalised posteriors

In Bayesian statistics, we rely on the Bayes' theorem:

$$\mathcal{P}(\boldsymbol{\theta}|\boldsymbol{x}) = \frac{\mathcal{L}(\boldsymbol{x}\,|\boldsymbol{\theta})\,\pi(\boldsymbol{\theta})}{\int d\boldsymbol{\theta}\,\mathcal{L}(\boldsymbol{x}\,|\boldsymbol{\theta})\,\pi(\boldsymbol{\theta})}, \tag{9.46}$$

where $\boldsymbol{\theta}$ are the free parameters of our model, $\boldsymbol{x}$ is the observed data, $\mathcal{P}(\boldsymbol{\theta}|\boldsymbol{x})$ is the posterior pdf, $\mathcal{L}(\boldsymbol{x}\,|\boldsymbol{\theta})$ is the likelihood function and $\pi(\boldsymbol{\theta})$ is the prior pdf. The denominator involves an integral over the free model parameters and is known as the Bayesian evidence $\mathcal{Z}$.

In our case of a multi-dimensional model, we are interested in 2D marginalised posterior (MP) distributions. These are constructed in the following way [341]

$$\mathcal{P}(\theta_i,\,\theta_j|\boldsymbol{x}) = \int_{l\neq i,\,j} d\theta_1, \ldots, d\theta_l\,\mathcal{P}(\boldsymbol{\theta}|\boldsymbol{x}), \tag{9.47}$$

where we integrate over the irrelevant parameters $\{\theta_l|\,l \neq i,\,j\}$. The MP distribution above is used to define a Bayesian *credible region* (CR) ω in such a way that there is a probability α of containing the true values of model parameters:

$$\int_\omega d\theta_i\,d\theta_j\,\mathcal{P}(\theta_i,\,\theta_j|\boldsymbol{x}) = \alpha. \tag{9.48}$$

In figure 9.4, we show the MP distributions in various 2D planes of the model parameter space. Similar to the PLR plots in figure 9.1, these are also generated using pippi v2.0 [180]. The 1σ (2σ) credible intervals are marked by solid (dashed) lines. The posterior mean is shown as a black circle. In each panel, model parameters that are not shown are integrated/marginalised over. Consequently, regions with a smaller "volume of support" [342] are less favoured as they require an extra degree of tuning of model parameters to satisfy all of the included constraints.

In comparison to the PLR plots in figure 9.1, the allowed regions in the MP plots are more constrained, especially where a large degree of tuning is required from marginalising over the model parameters. Again, we see a vertical stripe in the $(m_H,\,m_\chi)$-plane. On the other hand, the second resonance region, $m_\chi \simeq m_{h,\,H}/2$, is less-favoured as it falls outside the 2σ credible interval due to an extra need for tuning over v_h/v_s. In addition, regions where $m_\chi > m_H$ also appears to be fine-tuned, especially after marginalising over v_h/v_s.

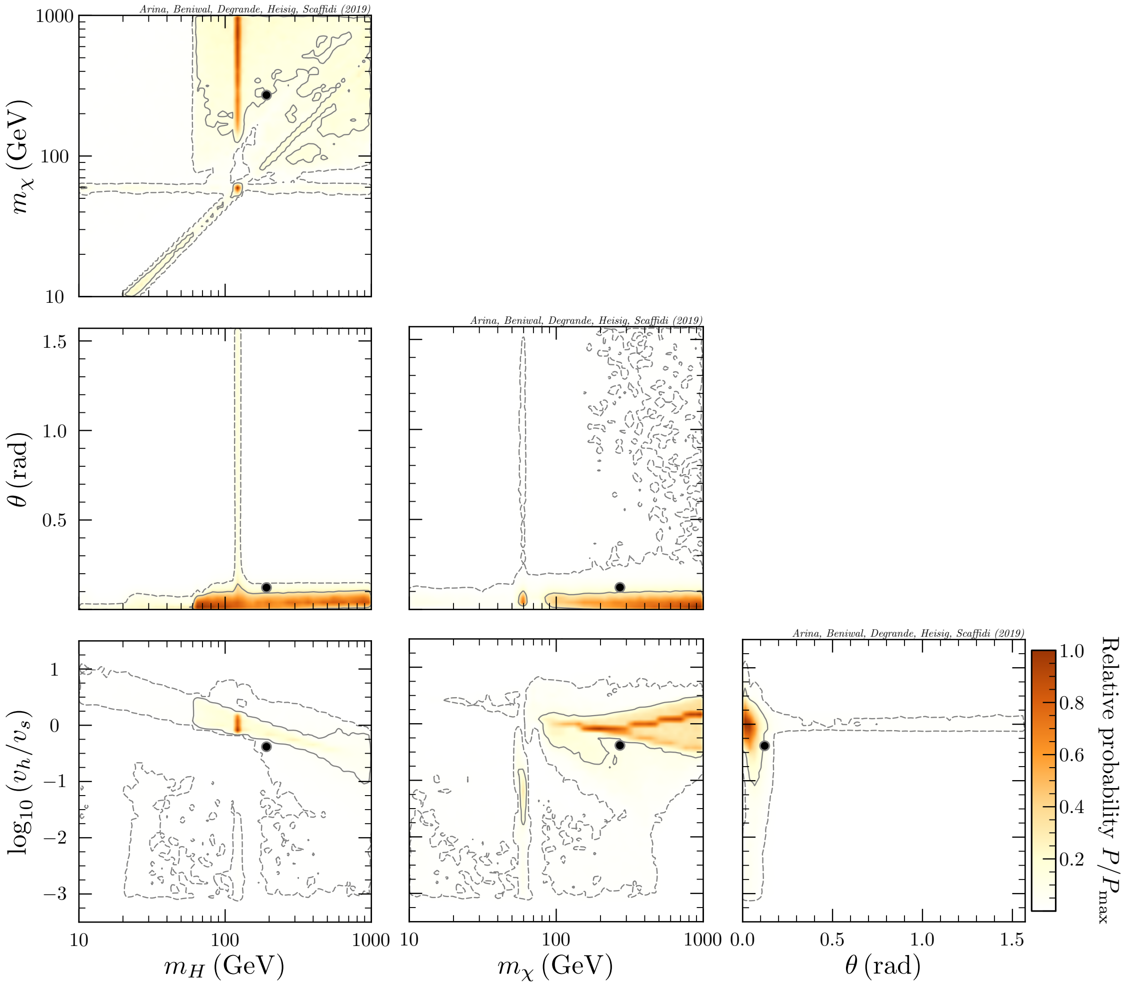

Fig. 9.4 2D marginalised posterior (MP) distributions in planes of the pNG DM model parameters. The 1σ (2σ) credible intervals are marked by solid (dashed) lines. The posterior mean is shown as a black circle.

In the (m_H, θ)- and (m_χ, θ)-planes, large values of θ fall inside the 2σ credible interval. On the other hand, regions with $\theta \lesssim 0.1$ rad have a larger volume of support, as is evident from a large posterior density. In the (m_χ, v_h/v_s)-plane for $m_\chi \gtrsim 100\,$GeV, the 1σ credible interval is larger than the 1σ CL region seen in the PLR plots. On the other hand, $m_\chi \lesssim m_h/2$ region requires a large degree of fine-tunning in v_s and m_H to satisfy the relic density constraint, and thus is less favoured. Lastly, in the (θ, v_h/v_s)-plane, the posterior mass is large for $\theta \lesssim 0.1$ rad. However, large values of θ are still allowed as they fall within the 2σ credible interval.

In figure 9.5, we show the MP distributions for key DM observables. In contrast to the right panel of figure 9.3, we do not see at least 4 orders of magnitude smaller DM annihilation cross sections than the freeze-out value; the region with velocity

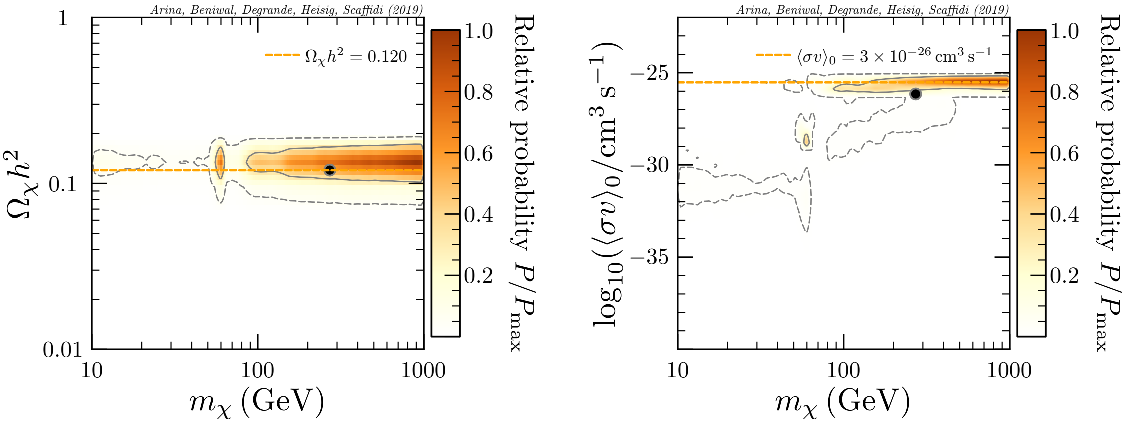

Fig. 9.5 2D MP distributions for key DM observables such as the pNG DM relic density (*left panel*) and its annihilation rate today (*right panel*). The meaning between the solid (dashed) lines and black circle is same as in figure 9.4.

suppressed annihilation cross section is somehow fine-tuned and less favoured after marginalising over m_H & v_h/v_s.

9.4.2 Post-processing of samples

In addition to the constraints included in our global fit, we consider indirect and direct detection constraints, see sections 9.3.6 and 4.3, respectively. For the computation of corresponding observables, we post-process our final samples. This greatly reduces the computational time, in particular, for indirect detection constraints. The *Fermi*-LAT likelihood is computationally intensive due to the generation of the annihilation spectra for $2 \to 2$ up to $2 \to 6$ processes (see section 9.3.6). We nevertheless expect a sufficient coverage within the resulting $(1-2)\sigma$ CL contours after combining various scans.[10] Accordingly, for the post-processed samples, we provide a frequentist interpretation only. While indirect detection constraints from *Fermi*-LAT observations of dSphs have a significant effect on the PLR, current direct detection experiments are not yet sensitive to our model, as we will show below. We thus refrain from including a likelihood for the latter, and restrict ourselves to comparing the model prediction to the reach of current and future experiments for this case.

Indirect detection

As explained in section 9.3.6, we consider two cases regarding the set of dSphs included. We take into account the likelihoods from all 45 dSphs considered in

---

[10] As stated in footnote 6, we combine results from several MultiNest scans. This is done with various specific priors to guarantee sufficient coverage in the resonant regions as well as in regions preferred by *Fermi*-LAT when considering 45 dSphs. The resulting samples contain more than 3 million samples.

ref. [292] as well as excluding the four dSphs that show an excess, correspondingly including 41 dSphs. The latter choice only imposes an upper limit on the annihilation cross section and is described first.

In figures 9.6 and 9.7, we show the PLR plots in the planes of pNG DM model parameters as well as the DM relic abundance and annihilation cross section today, respectively, after accounting for the likelihoods of 41 dSphs. The implications on the parameter space compared to our global fit results (see figure 9.1) are moderate. However, for $m_\chi \lesssim 100\,\text{GeV}$, the *Fermi*-LAT limits exclude a large portion of the parameter space where the pNG DM annihilation today proceeds via $\chi\chi \to HH$ channel, i.e., where $m_\chi > m_H$. The constraint becomes stronger for smaller DM masses as lighter DM requires a larger DM number density to match the same energy density. This enhances the annihilation rate. The tendency is partly softened by the fact that for a given m_H, the spectrum becomes more peaked for larger m_χ, which tends to strengthen the constraints.

Taking into account the *Fermi*-LAT likelihood, the new best-fit point has moved to the region of dominant annihilation into Higgs pairs during freeze-out ($\chi\chi \to hh$ in this case), see column 2 in table 9.2. However, m_χ is slightly smaller than m_h such that $\chi\chi \to hh$ is kinematically forbidden today. Thus, $\langle \sigma v \rangle_0$ is largely suppressed as now it proceeds via (a highly off-shell) Higgs propagator (dominantly into WW^* final states). Consequently, the best-fit point effectively evades any constraint from indirect detection.

Note that other indirect detection searches can impose further constraints on the parameter space. Here we would like to comment on current constraints from cosmic-ray (CR) antiproton fluxes as measured by AMS-02 [346]. While the corresponding analyses are typically plagued by large CR propagation uncertainties, recent progress has been made by fitting propagation and DM parameters at the same time [344]. This analysis provides very strong bounds on the DM annihilation cross section for DM masses above 200 GeV. While performing a respective, dedicated analysis for the considered model is beyond the scope of this work, we can, nevertheless, interpret the results of ref. [344] in parts of our model parameter space. The analysis provides limits for annihilation into a pair of Higgses with $m_h = 125\,\text{GeV}$. In our model, $m_H \sim m_h$ in the entire 1σ CL region. Moreover, for $m_\chi > 200\,\text{GeV}$ (where the analysis becomes constraining), the dominant annihilation channels are $\chi\chi \to hh$, hH and HH. Hence, for the 1σ CL region, the result from ref. [344] can be directly applied without approximation (except for neglecting the small difference between m_H and m_h, which is however, not expected to have a noticeable effect on the gamma-ray energy spectrum). We show the corresponding 95% CL limit as solid blue

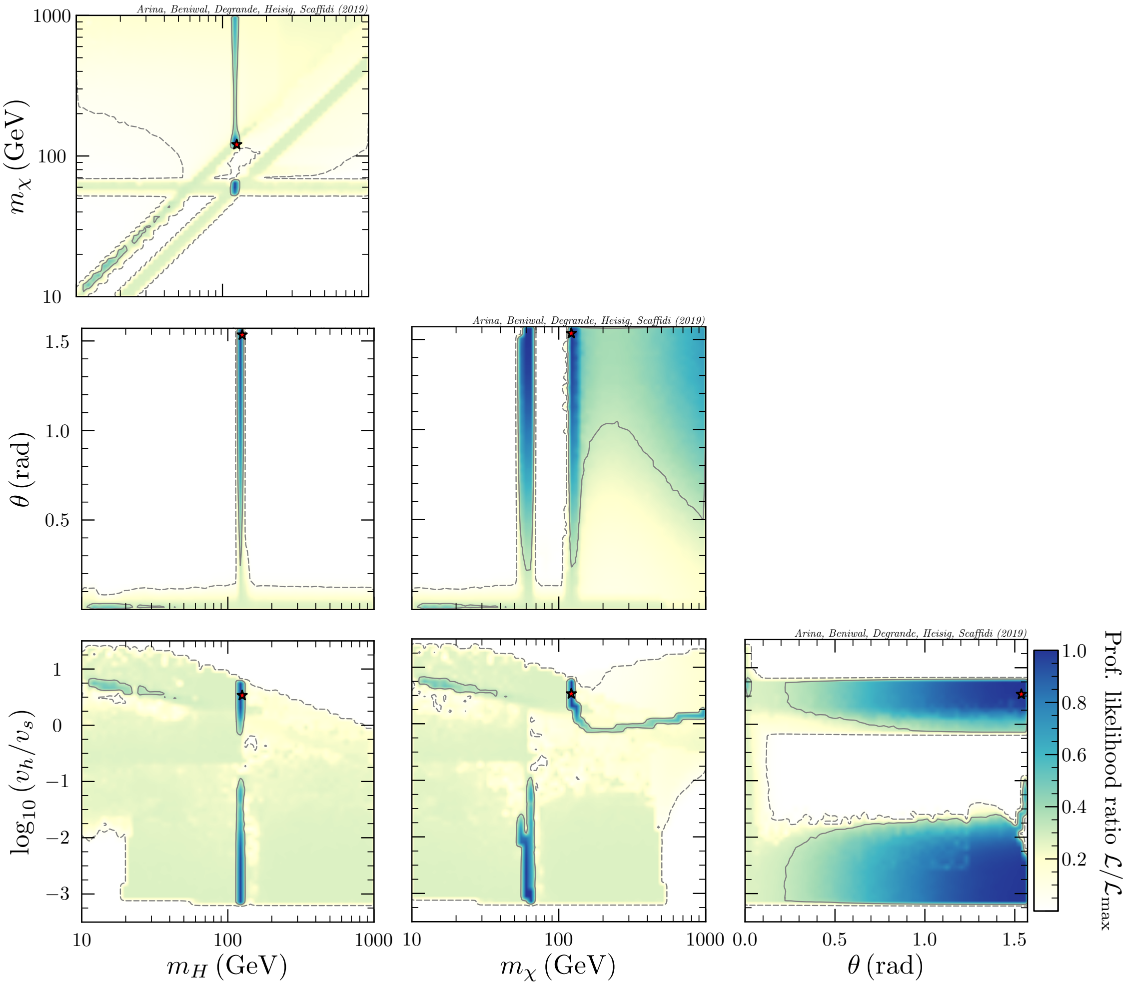

Fig. 9.6 2D PLR plots for the pNG DM model parameters after post-processing our MultiNest samples with *Fermi*-LAT likelihood from 41 dSphs. The best-fit point is shown as a red star and summarised in column 2 of table 9.2.

curve in the right panel of figure 9.7. For the 2σ CL region, in general, $m_H \neq m_h$. Nevertheless, the dashed blue curve is expected to provide an order of magnitude estimate of the sensitivity of CR antiproton searches.

With future experiments, the pNG DM parameter space can be tested with gamma-ray observation with improved sensitivity. A large part of the region of dominant annihilation into Higgs pairs is expected to be probed in the near future by a combination of new dSphs discovered by the Large Synoptic Survey Telescope (LSST) [347] with *Fermi*-LAT observations. First, the inclusion of more satellite galaxies will augment the *Fermi*-LAT data [343, 348]. Secondly, the LSST novel spectroscopic observations will provide precise measurements of J-factors, decreasing the associated astrophysical uncertainties. These improvements are expected to provide sensitivity to the thermal cross-section for DM masses up to around 600 GeV.

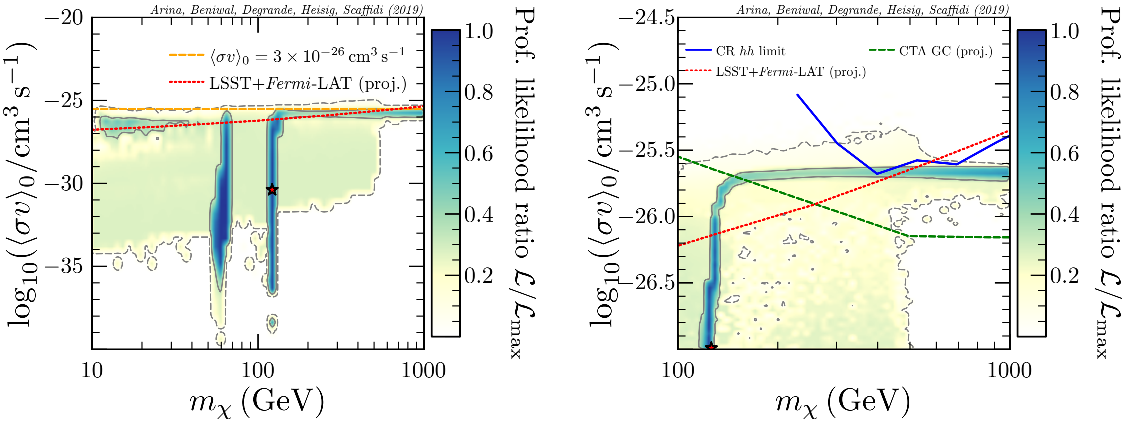

Fig. 9.7 *Left panel*: 2D PLR plots for the pNG DM annihilation cross section today after post-processing our samples with *Fermi*-LAT likelihood for 41 dSphs. Projected limits from LSST+*Fermi*-LAT dSphs [343] are shown as red dotted curve. *Right panel*: Same as the left panel, except for $m_\chi \in [100, 1000]$ GeV. The blue solid curve shows the current cosmic-ray (CR) antiproton limit for the $\chi\chi \to hh$ channel [344]. Projected limits from CTA Galactic Centre (GC) [345] (green dashed), and LSST+*Fermi*-LAT dSphs [343] (red dotted) for the $b\bar{b}$ channel are also shown.

For illustration, we show the corresponding projected limit for annihilation into $b\bar{b}$ (assuming 18 years of observation) as the red dashed curve in figure 9.7. Furthermore, in the right panel of figure 9.7 only, we display the recent projection for Galactic centre gamma-ray observations with the Cherenkov Telescope Array (CTA) [345], assuming 500 hours of exposure (no systematics), again using DM annihilation into $b\bar{b}$ as a benchmark channel, which is expected to provide a reasonable order of magnitude estimate for the sensitivity for our model. It can probe cross sections down to $5 \times 10^{-27}\,\mathrm{cm^3\ s^{-1}}$ for masses above 500 GeV, i.e., a large portion of the allowed pNG DM parameter space characterised by dominant annihilation into Higgs pairs.

In figures 9.8 and 9.9, we show the respective results after accounting for the *Fermi*-LAT likelihood from all 45 dSphs, i.e., including Reticulum II, Tucana III, Tucana IV and Indus II, which exhibit slight excesses with a local significance of around 2σ each [292, 324, 325]. Interestingly, the excess can be fitted by an annihilation cross section in the ballpark of the thermal one, $\langle\sigma v\rangle_0 \sim 3 \times 10^{-26}\,\mathrm{cm^3\ s^{-1}}$, i.e., in regions where the annihilation cross section today is similar to the one typically required during freeze-out. This places additional constraints on the parameter space and excludes parts of the resonant region where the cross section is highly velocity dependent, and hence $\langle\sigma v\rangle_0$ deviates strongly from $\langle\sigma v\rangle_{\mathrm{FO}}$. More concretely, for DM masses below the point of maximal resonant enhancement, $\langle\sigma v\rangle_0 < \langle\sigma v\rangle_{\mathrm{FO}}$ and the flux today tends to be too low to fit the signal. In contrast, for DM masses above that point, the flux tends to be too high. Finally, in between, $\langle\sigma v\rangle_0 \sim \langle\sigma v\rangle_{\mathrm{FO}}$. This is approximately the point of maximal resonant enhancement of the thermally averaged cross section during freeze-out which allows for the smallest possible couplings in the scan. If the annihilation proceeds via an on-shell Higgs (h or H), the respective cross section is proportional to

$$\sigma \propto \frac{\cos^2\theta\sin^2\theta}{v_s^2\,\Gamma^{\mathrm{tot}}_{h/H}}\,. \tag{9.49}$$

Here $\Gamma^{\mathrm{tot}}_{h/H}$ is the total Higgs decay width, which is dominated by the partial width into SM particles if the DM mass is very close to $m_{h/H}/2$, such that the corresponding phase space is suppressed. In this case, $\Gamma^{\mathrm{tot}}_{h/H}$ is proportional to $\cos^2\theta$ ($\sin^2\theta$) for h (H), thereby cancelling the respective factors in the numerator of eq. (9.49). Consequently, the cross section for resonant annihilation via h or H is approximately proportional to $(\sin\theta/v_s)^2$ and $(\cos\theta/v_s)^2$, respectively. The two regions can be recognised in the lower part of the (θ, v_h/v_s)-plane as the two overlapping thin bands with decreasing ($\propto \sin^{-1}\theta$) and increasing ($\propto \cos^{-1}\theta$) slope. The best-fit point falls in the second band where the pNG DM annihilation proceeds dominantly via a resonant H (see column 3 in table 9.2).

The second region fitting the signal is characterized by annihilation into a pair of Higgses, where (unless very close to or below threshold) no strong velocity dependence of the annihilation cross section is present, and thus $\langle\sigma v\rangle_0 \sim \langle\sigma v\rangle_{\mathrm{FO}}$ naturally. This region extends from the respective threshold up to around 200 (300) GeV within 1σ (2σ) CL region away from the best-fit point. Accordingly, the allowed region spans roughly an order of magnitude in the pNG DM mass, i.e., around 30–300 GeV.

Note that in ref. [298], the pNG DM model has been considered as an explanation of the gamma-ray galactic centre excess [98, 349–356] and the CR antiproton excess [357–361]. While a discussion of the robustness of a DM explanation of these excesses as well as an explicit interpretation is beyond the scope of this work, we briefly comment on this possibility. In particular, we distinguish two cases.

1. For pNG DM annihilation via a resonant h or H exchange in the s-channel, the composition of final states is the same as for the (singlet scalar) Higgs portal model, unless $m_\chi > m_{h,H}$. For this case, explicit fits to the gamma-ray galactic centre excess [362] and the CR antiproton excess [359] have been performed. The latter analysis also provides a joint fit of both observations and the above-mentioned excess in the *Fermi*-LAT dSphs. It reveals that all three observations, if arsing from DM annihilation, are compatible and point to

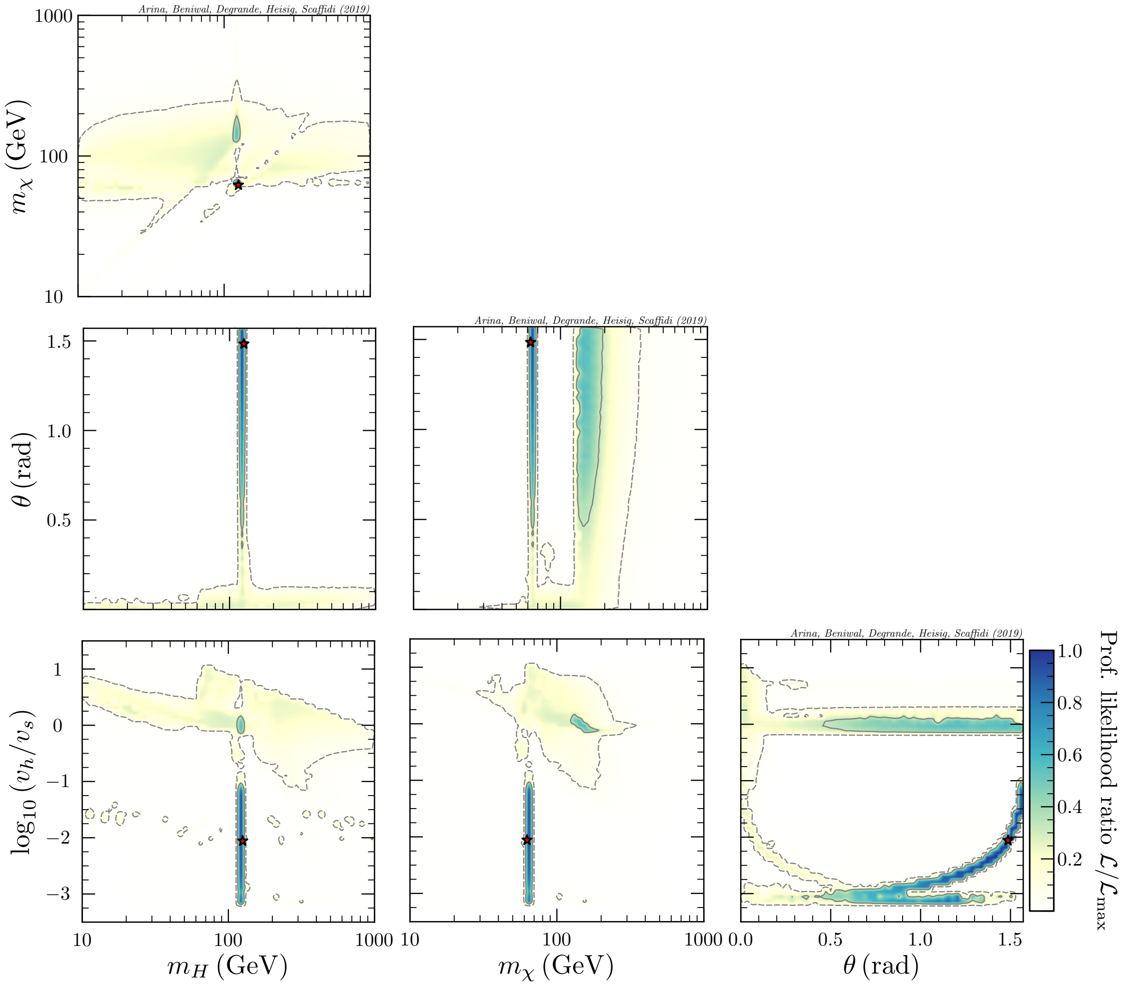

Fig. 9.8 2D PLR plots for the pNG DM model parameters after post-processing our samples with *Fermi*-LAT likelihood from 45 dSphs.

a DM mass of around (50–60) GeV and a velocity averaged annihilation cross section today of around $(1-2)\times10^{-26}\,\mathrm{cm}^3\,\mathrm{s}^{-1}$.

2. The other case concerns dominant annihilation into h or H. Due to their subsequent decays into lighter SM particles, their gamma-ray spectra are typically softer. For instance, just above its threshold, the photon spectrum for $\chi\chi \to HH \to b\bar{b}b\bar{b}$ has the same shape as the one for $\chi\chi \to b\bar{b}$ but is shifted by a factor of 2 towards smaller energies. This is also reflected in the fact that the three observations can be fitted by DM annihilation into a SM-like Higgs for masses around the threshold [359], i.e., roughly a factor of two larger than the DM mass providing the best fit for $\chi\chi \to b\bar{b}$.

In conclusion, the regions that fit the gamma-ray galactic centre excess and the CR antiproton excess are very similar to those preferred by the 45 dSphs (see figures 9.8

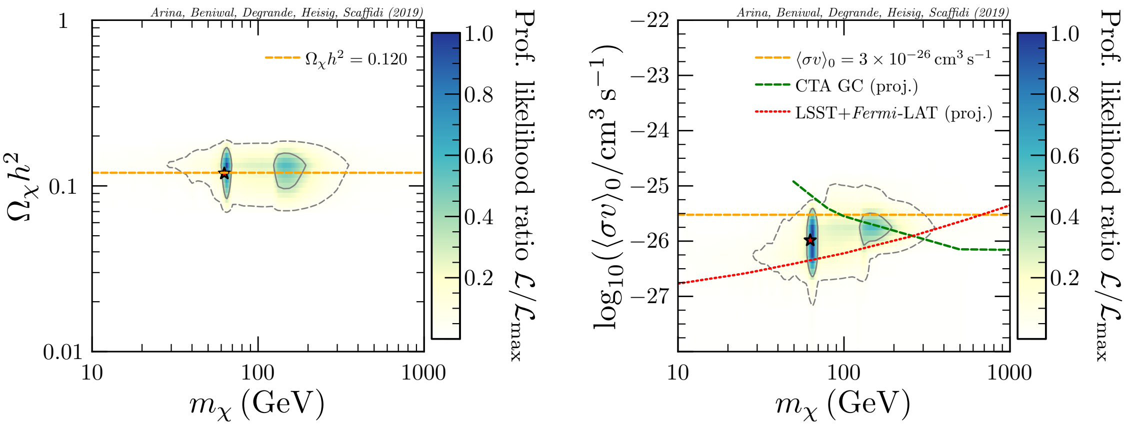

Fig. 9.9 2D PLR plots for the pNG DM relic abundance and its annihilation cross section today after post-processing our samples with *Fermi*-LAT likelihood from 45 dSphs. In the right panel, projected limits from CTA GC searches [345] and LSST+*Fermi*-LAT dSphs [343] are also shown.

and 9.9). We expect all three observations to be well fitted by a significant subset of the parameter points fitting the 45 dSphs.

Similar to the case of 41 dSphs (see figure 9.7), we also display the projected limits (for the $b\bar{b}$ channel) for future gamma-ray observations of dSphs from LSST+*Fermi*-LAT and for CTA in the right panel of figure 9.9. It is evident that LSST+*Fermi*-LAT will be able to test almost the entire 2σ CL region preferred by the 45 dSphs.

Direct detection

In figure 9.10, we show the PLR plots for the pNG DM-nucleon cross section at one-loop level after post-processing our MultiNest samples. These cross sections are based on the approximate expressions (*left panel*) and full computations (*right panel*), i.e., eqs. (9.39) and (9.40), respectively. The solid red curve shows the current sensitivity of XENON1T [268], whereas the dashed orange and dotted magenta curves show the projected sensitivities of LZ [291] and DARWIN [157], respectively.

The approximate cross section overestimates the full one-loop predition up to several orders of magnitude. For instance, parts of the 1σ CL region in the left panel are already excluded by XENON1T, while they are currently allowed when considering the full one-loop computation. In fact, we find that the entire 2σ CL region is not challenged by the current limits from XENON1T. Even the projected LZ and DARWIN experiments will probe only a small portion of the 2σ CL region. The best-fit point lies completely out of reach of these experiments. In particular, the resonance region, $m_\chi \simeq m_h/2$, predicts a DM-nucleon cross section that is smaller than $\sim 10^{-50}\,\mathrm{cm}^2$ and lies well below the proposed neutrino floor [363]. It is still

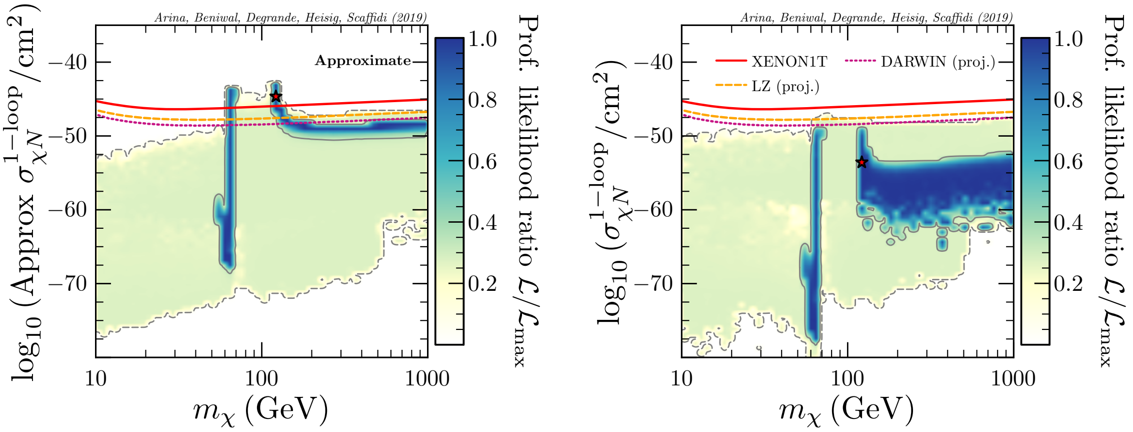

Fig. 9.10 2D PLR plots for the pNG DM-nucleon cross section at one-loop level using approximate expression (*left panel*) and full computation (*right panel*). The red solid curve shows the current exclusion limit of XENON1T [268], whereas the orange dashed and magenta dotted curves show the projected sensitivities of LUX-ZEPLIN (LZ) [291] and DARWIN [157], respectively.

interesting to see that upcoming generation of direct detection experiments are starting to probe models of DM with momentum-suppressed tree-level cross-section.

9.5 Conclusions

We performed a global fit of the pNG DM model by combining constraints from the DM relic abundance, perturbative unitarity, Higgs invisible decay, electroweak precision observables and Higgs searches at colliders. We presented our results in both frequentist and Bayesian statistical frameworks. In addition, we post-processed our samples by imposing indirect detection constraints from *Fermi*-LAT dwarf spheroidal galaxies within the former framework. Furthermore, we computed the one-loop pNG DM-nucleon cross sections, and compared the resulting values against the current limit from XENON1T (2018), and projected future limits from LUX-ZEPLIN (LZ) and DARWIN.

In the frequentist analysis, we found two main regions with similar profile likelihood ratio that are compatible with all observations: the Higgs funnel region where DM annihilates resonantly via one of the two Higgs bosons, $m_\chi \sim m_{h,H}/2$, and the region of dominant annihilation into Higgs pairs, $m_\chi \gtrsim m_{h,H}$. In contrast, the region of non-resonant annihilation into SM fermions and gauge bosons is highly constrained and mostly falls outside the 2σ CL region, in particular, for DM masses below the resonant region where the annihilation cross section is suppressed and requires non-perturbative couplings to match the measured relic density.

Electroweak precision observables, LEP searches and observed Higgs signal strengths at the LHC impose strong constraints on the mixing angle θ between the two Higgs bosons in our model. They require $\theta \lesssim 0.1$ rad except for the mass degenerate case $m_h \sim m_H$, where large mixing angles are allowed as well. In fact, the observed Higgs signal strength exhibit a slight preference (around 1σ) for the latter choice. However, this preference arises from the fact that the LHC signal strengths are better fitted with a slightly heavier Higgs of around 125.3 GeV while the SM Higgs mass is fixed at 125 GeV in our scan. Hence, the fit prefers the second Higgs to have a mass of 125.3 GeV and non-suppressed couplings to the SM particles. We expect this preference to be alleviated if the SM Higgs mass is included as a nuisance parameter in the fit.

Our Bayesian results led to an even stronger constraint after marginalisation over the free model parameters. In particular, regions with a smaller volume of support fell outside the 2σ credible interval. For instance, this concerns regions where the annihilation cross section today is much larger or smaller than the canonical freeze-out cross section $\langle\sigma v\rangle_{\mathrm{FO}} \sim 3 \times 10^{-26}\,\mathrm{cm}^3\,\mathrm{s}^{-1}$, arising very close to the resonant condition $m_\chi \sim m_{h,H}/2$ or the threshold $m_\chi \sim m_{h,H}$. Similarly, our Bayesian results do not imply a preference for large mixing angles θ induced by Higgs signal strength observations, as it requires m_H to be very close to 125.3 GeV, again, providing a small volume of support.

We computed the pNG DM-nucleon cross section at one-loop level for all of our samples after utilising the results of ref. [289]. We found that none of the points in our scan are challenged by current direct detection limits from XENON1T (2018). Future based experiments (e.g., LUX-ZEPLIN, DARWIN) will only probe a small portion of the 2σ CL region.

We took into account the *Fermi*-LAT likelihood by considering two different sets of dSphs. On the one hand, we considered those imposing an upper limit on the annihilation cross section only (41 dSph). The effect on the parameter space is mild and the DM mass is not constrained towards large values within the consider range. On the other hand, we considered all 45 dSphs analysed by *Fermi*-LAT, including the four dwarfs that show slight excesses at the level of 2σ each. These excesses can be well fitted within our model. They favour a DM masses in range $30\,\mathrm{GeV} \lesssim m_\chi \lesssim 300\,\mathrm{GeV}$ at the 2σ CL. We also expect a large part of this region to provide a good fit to the gamma-ray Galactic centre excess and the cosmic-ray antiproton excess seen in the AMS-02 data, if interpreted as a signal of DM annihilation.

Other indirect detection searches can further constrain our model. For instance, limits from AMS-02 antiprotons already exclude parts of the 1σ CL region in the 41-dSph fit with a DM mass around 400 GeV. Future gamma-ray observations by *Fermi*-LAT of newly discovered dSphs by LSST and CTA observations of the Galactic centre are expected to improve on the sensitivity and probe a significant portion of the allowed parameter space for DM masses above m_h in the 41 dSPhs fit. They are also expected to probe almost the entire 2σ CL region preferred by the current *Fermi*-LAT observations of all 45 dSphs.

9.6 Appendices

9.6.1 Dark matter-nucleon coupling

The dimensionful coupling between the mass eigenstates (h, H) and pNG DM χ arises from eq. (9.2), namely

$$\mathcal{L}_S \supset -\left(\lambda_{\Phi S}\,\Phi^\dagger\Phi|S|^2 + \frac{\lambda_S}{2}|S|^4\right). \tag{9.50}$$

After EWSB, this term expands to (keeping only terms proportional to $\phi\chi^2$ and $s\chi^2$)

$$\begin{aligned}\lambda_{\Phi S}\,\Phi^\dagger\Phi|S|^2 &= \frac{\lambda_{\Phi S}}{4}(v_h+\phi)^2\left[(v_s+s)^2+\chi^2\right] \supset \frac{\lambda_{\Phi S}}{4}(2v_h\phi)\chi^2 = \frac{\lambda_{\Phi S}v_h}{2}\phi\chi^2,\\ \frac{\lambda_S}{2}|S|^4 &= \frac{\lambda_S}{8}\left[(v_s+s)^2+\chi^2\right]^2 \supset \frac{\lambda_S}{8}\left[2(v_s+s)^2\chi^2\right] \supset \frac{\lambda_S}{8}(4v_s s)\chi^2 = \frac{\lambda_S v_s}{2}s\chi^2.\end{aligned}$$

Thus, eq. (9.50) can be expressed as

$$\mathcal{L}_S \supset -\frac{1}{2}\chi^2\left(\lambda_{\Phi S}v_h\,\phi + \lambda_S v_s\,s\right). \tag{9.51}$$

Using the following relation for the interaction eigenstates:

$$\begin{pmatrix}\phi\\ s\end{pmatrix} = \begin{pmatrix}\cos\theta & \sin\theta\\ -\sin\theta & \cos\theta\end{pmatrix}\begin{pmatrix}h\\ H\end{pmatrix}, \tag{9.52}$$

we can rewrite eq. (9.51) as

$$\mathcal{L}_S \supset -\frac{1}{2}\chi^2(\kappa_{\chi\chi h}\,h + \kappa_{\chi\chi H}\,H), \tag{9.53}$$

where the *dimensionful* couplings $\{\kappa_{\chi\chi h},\, \kappa_{\chi\chi H}\}$ are [285]

$$\begin{aligned}\kappa_{\chi\chi h} = (\lambda_{\Phi S} v_h \cos\theta - \lambda_S v_s \sin\theta) &= \frac{1}{v_s}\Big[(m_H^2 - m_h^2)\sin\theta\cos^2\theta - \sin\theta(m_h^2\sin^2\theta + m_H^2\cos^2\theta)\Big] \\ &= -\frac{m_h^2}{v_s}\sin\theta, \qquad (9.54)\\ \kappa_{\chi\chi H} = (\lambda_{\Phi S} v_h \sin\theta + \lambda_S v_s \cos\theta) &= \frac{1}{v_s}\Big[(m_H^2 - m_h^2)\sin^2\theta\cos\theta + \cos\theta(m_h^2\sin^2\theta + m_H^2\cos^2\theta)\Big] \\ &= +\frac{m_H^2}{v_s}\cos\theta. \qquad (9.55)\end{aligned}$$

On the other hand, the Yukawa interaction term in the SM Lagrangian reads

$$\mathcal{L}_{\text{Yukawa}} \supset -\phi\sum_f \frac{m_f}{v_h}\bar{f}f = -\sum_f \kappa_{hf\bar{f}}\, h\bar{f}f + \kappa_{Hf\bar{f}}\, H\bar{f}f, \tag{9.56}$$

where

$$\kappa_{hf\bar{f}} = \frac{m_f}{v_h}\cos\theta, \quad \kappa_{Hf\bar{f}} = \frac{m_f}{v_h}\sin\theta, \tag{9.57}$$

are the *dimensionless* couplings between h/H and SM quarks/leptons. Finally, the pNG DM-nucleon interaction Lagrangian can be written as

$$\mathcal{L}_{\chi f} \supset -\frac{1}{2}\chi^2(\kappa_{\chi\chi h}\, h + \kappa_{\chi\chi H}\, H) - \sum_f \kappa_{hf\bar{f}}\, h\bar{f}f + \kappa_{Hf\bar{f}}\, H\bar{f}f. \tag{9.58}$$

For a $\chi f \to \chi f$ scattering process via an h/H exchange in t-channel, the tree-level direct detection (DD) scattering amplitude is proportional to

$$\mathcal{A}_{\text{DD}}(q^2) \propto \frac{\kappa_{\chi\chi h}\kappa_{hf\bar{f}}}{q^2 - m_h^2} + \frac{\kappa_{\chi\chi H}\kappa_{Hf\bar{f}}}{q^2 - m_H^2} \propto \sin\theta\cos\theta\left(\frac{m_H^2}{q^2 - m_H^2} - \frac{m_h^2}{q^2 - m_h^2}\right),$$

where $q \equiv \sqrt{2ME}$ is the momentum transfer and $M = 939\,\text{MeV}$ is the (average) nucleon mass. In the limit of $q^2 \ll m_{h,H}^2$, the above expression becomes

$$\mathcal{A}_{\text{DD}}(q^2) \propto \sin\theta\cos\theta\left(\frac{1}{1 - q^2/m_h^2} - \frac{1}{1 - q^2/m_H^2}\right). \tag{9.59}$$

For $x \ll 1$, the Taylor expansion for $(1-x)^{-1} = 1 + x + \mathcal{O}(x^2)$. Thus, the above expression expands to

$$\mathcal{A}_{\text{DD}}(q^2) \propto q^2\sin\theta\cos\theta\left(\frac{1}{m_h^2} - \frac{1}{m_H^2}\right). \tag{9.60}$$

As $q \sim \mathcal{O}(\text{MeV})$, the pNG DM-nucleon cross section is momentum-suppressed at tree-level.

9.6.2 The S, T and U parameters

In our model, the oblique parameters are shifted from their SM values by [309, 364]

$$\begin{aligned}\Delta T = \frac{3}{16\pi s_W^2}\Bigg[&\cos^2\theta\left\{f_T\left(\frac{m_h^2}{m_W^2}\right) - \frac{1}{c_W^2}f_T\left(\frac{m_h^2}{m_Z^2}\right)\right\} + \sin^2\theta\left\{f_T\left(\frac{m_H^2}{m_W^2}\right)\right.\\ &\left.-\frac{1}{c_W^2}f_T\left(\frac{m_H^2}{m_Z^2}\right)\right\} - \left\{f_T\left(\frac{m_h^2}{m_W^2}\right) - \frac{1}{c_W^2}f_T\left(\frac{m_h^2}{m_Z^2}\right)\right\}\Bigg], \end{aligned} \tag{9.61}$$

$$\Delta S = \frac{1}{2\pi}\left[\cos^2\theta f_S\left(\frac{m_h^2}{m_Z^2}\right) + \sin^2\theta f_S\left(\frac{m_H^2}{m_Z^2}\right) - f_S\left(\frac{m_h^2}{m_Z^2}\right)\right], \tag{9.62}$$

$$\Delta U = \frac{1}{2\pi}\left[\cos^2\theta f_S\left(\frac{m_h^2}{m_W^2}\right) + \sin^2\theta f_S\left(\frac{m_H^2}{m_W^2}\right) - f_S\left(\frac{m_h^2}{m_W^2}\right)\right] - \Delta S, \tag{9.63}$$

where $\Delta\mathcal{O} \equiv \mathcal{O} - \mathcal{O}_{\rm SM}$ for $\mathcal{O} \in (S,T,U)$, $m_W\,(m_Z)$ is the $W\,(Z)$ boson mass, $c_W^2 = m_W^2/m_Z^2$ and $s_W^2 = 1 - c_W^2$. The loop functions $f_T(x)$ and $f_S(x)$ are given by

$$f_T(x) = \frac{x\log x}{x-1}, \tag{9.64}$$

$$f_S(x) = \begin{cases} \dfrac{1}{12}\Bigg[-2x^2 + 9x + \left((x-3)\left(x^2-4x+12\right) + \dfrac{1-x}{x}\right)f_T(x) \\ \quad +2\sqrt{(4-x)x}\left(x^2-4x+12\right)\tan^{-1}\left(\sqrt{\dfrac{4-x}{x}}\right)\Bigg], \quad 0 < x < 4, \\ \dfrac{1}{12}\Bigg[-2x^2 + 9x + \left((x-3)\left(x^2-4x+12\right) + \dfrac{1-x}{x}\right)f_T(x) \\ \quad +\sqrt{(x-4)x}\left(x^2-4x+12\right)\log\left(\dfrac{x-\sqrt{(x-4)x}}{x+\sqrt{(x-4)x}}\right)\Bigg], \quad x \geq 4. \end{cases} \tag{9.65}$$

Chapter 10

Conclusions

The particle nature of DM is still unknown. With the current experimental prospectus in full swing and the generically-interacting single DM species interpretation having been extensively studied, alternative models must be considered. Whilst there exists a multitude of different DM models, modifications to the WIMP sector are still of great interest, with a multi-component dark sector becoming more and more prevalent from a model building perspective. The newest direct searches are currently and will continue to push the generic WIMP picture toward the neutrino floor. If this happens and no WIMP like particle(s) are detected, one needs to then consider models that evade these constraints or experimental alternatives.

After a brief review of particle dark matter, this thesis presented four publications that constitute the main body of work of my PhD. The first body of work detailed the introduction of a multi-component WIMP sector and the extent to which future direct detection experiments in the presence of a signal could discriminate between the two new particles. We found that the most statistically powerful discrimination between the 1DM and 2DM hypothesis was driven by the mass splitting of the two DM particles, however there are significant phenomenological changes when different parameters of the DM are varied. Specifically, the velocity dispersions, local density ratios and interaction cross sections for both SI and SD couplings. This study was then naturally extended by considering constraints introduced by the DM particles' cosmological history. Namely, whether the DM genesis involved canonical freeze-out or some asymmetric scenario. We also considered a simplified model where the DM-DM coupling is mediated by some light mediator. We found that even when applying reasonable DM genesis model constraints to a general two-component DM scenario, therefore reducing the allowed parameter space, there are cases where the 1DM and the 2DM hypothesis can be significantly discriminated.

The next section of work detailed a two-component dark sector and the phenomenological ramifications for annual modulation signals. Motivated by the recent claim that the single WIMP interpretation of the DAMA/LIBRA phase-1 analysis was self inconsistent with the new results from the phase-2 data, it was found that a two component dark sector would produce an anti-modulating signal that could provide an extremely good fit to the DAMA/LIBRA phase-2 data. Something to stress however is that what was important about this study was not the DAMA/LIBRA interpretation per se, but rather that a two-component signal would manifest in an interesting way, giving non-sinusoidal modulation and partial cancellations, especially when including the correction due to gravitational focusing - something that is not often done in similar analyses.

The last part of this thesis presented the most complete and robust constraints on the pseudo-Nambu-Goldstone Dark Matter model via means of a global fit. Motivated by a tree-level aversion of modern direct detection constraints, the pNG DM model has a rich phenomenology that manifests in a variety of detection channels; Indirect, collider, and one-loop direct detection was considered, as well as electroweak precision observables and theoretical constraints.

The work in this thesis lays a nice foundation for future studies. The seminal work on multi-component dark matter could potentially be applied to future sensitivity studies with the SABRE dark matter experiment, currently being finalized in Stawell (Australia) and Gran Sasso (Italy). In addition, the techniques utilized for publication 4 can be extended to other dark matter models.

References

[1] F. Zwicky. On the Masses of Nebulae and of Clusters of Nebulae. *Astrophys.J.*, 86:217–246, 1937.

[2] Gianfranco Bertone, Dan Hooper, and Joseph Silk. Particle dark matter: Evidence, candidates and constraints. *Phys. Rept.*, 405:279–390, 2005.

[3] R. Adam et al. Planck 2015 results. I. Overview of products and scientific results. 2015.

[4] P. A. R. Ade et al. Planck 2015 results. XIII. Cosmological parameters. *Astron. Astrophys.*, 594:A13, 2016.

[5] E. Komatsu et al. Seven-Year Wilkinson Microwave Anisotropy Probe (WMAP) Observations: Cosmological Interpretation. *Astrophys.J.Suppl.*, 192:18, 2011.

[6] M. Tanabashi et al. Review of Particle Physics. *Phys. Rev. D*, 98(3):030001, 2018.

[7] Lars Bergstrom. Nonbaryonic dark matter: Observational evidence and detection methods. *Rept.Prog.Phys.*, 63:793, 2000.

[8] J. Beringer et al. Review of Particle Physics (RPP). *Phys.Rev.*, D86:010001, 2012.

[9] Mark W. Goodman and Edward Witten. Detectability of Certain Dark Matter Candidates. *Phys. Rev.*, D31:3059, 1985.

[10] Gianfranco Bertone, Dan Hooper, and Joseph Silk. Particle dark matter: Evidence, candidates and constraints. *Physics Reports*, 405(5):279–390, 2005.

[11] Juerg Beringer, JF Arguin, RM Barnett, K Copic, O Dahl, DE Groom, CJ Lin, J Lys, H Murayama, CG Wohl, et al. Review of particle physics. *Physical Review D*, 86(1), 2012.

[12] KG Begeman, AH Broeils, and RH Sanders. Extended rotation curves of spiral galaxies: Dark haloes and modified dynamics. *Monthly Notices of the Royal Astronomical Society*, 249(3):523–537, 1991.

[13] John Dubinski and RG Carlberg. The structure of cold dark matter halos. *The Astrophysical Journal*, 378:496–503, 1991.

[14] Yoshiaki Sofue and Vera Rubin. Rotation curves of spiral galaxies. *Annual Review of Astronomy and Astrophysics*, 39(1):137–174, 2001.

[15] Fabio Iocco, Miguel Pato, and Gianfranco Bertone. Evidence for dark matter in the inner milky way. *Nature Physics*, 2015.

[16] J. Anthony Tyson, Greg P. Kochanski, and Ian P. Dell'Antonio. Detailed mass map of CL0024+1654 from strong lensing. *Astrophys. J.*, 498:L107, 1998.

[17] Richard Massey et al. Dark matter maps reveal cosmic scaffolding. *Nature*, 445:286, 2007.

[18] Douglas Clowe, Marusa Bradac, Anthony H. Gonzalez, Maxim Markevitch, Scott W. Randall, Christine Jones, and Dennis Zaritsky. A direct empirical proof of the existence of dark matter. *Astrophys. J.*, 648:L109–L113, 2006.

[19] Arno A Penzias and Robert Woodrow Wilson. A measurement of excess antenna temperature at 4080 mc/s. *The Astrophysical Journal*, 142:419–421, 1965.

[20] PAR Ade, N Aghanim, C Armitage-Caplan, M Arnaud, M Ashdown, F Atrio-Barandela, J Aumont, C Baccigalupi, AJ Banday, RB Barreiro, et al. Planck 2013 results. xvi. cosmological parameters. *arXiv preprint arXiv:1303.5076*, 2013.

[21] Willem De Sitter. On the curvature of space. In *Proc. Kon. Ned. Akad. Wet*, volume 20, pages 229–243, 1917.

[22] Planck Collaboration, PAR Ade, N Aghanim, MIR Alves, C Armitage-Caplan, M Arnaud, M Ashdown, F Atrio-Barandela, J Aumont, H Aussel, et al. Planck 2013 results. i. overview of products and scientific results. 2013.

[23] Volker Springel, Simon DM White, Adrian Jenkins, Carlos S Frenk, Naoki Yoshida, Liang Gao, Julio Navarro, Robert Thacker, Darren Croton, John Helly, et al. Simulating the joint evolution of quasars, galaxies and their large-scale distribution. *arXiv preprint astro-ph/0504097*, 2005.

[24] Sebastiano Cantalupo, Fabrizio Arrigoni-Battaia, J Xavier Prochaska, Joseph F Hennawi, and Piero Madau. A cosmic web filament revealed in lyman-[agr] emission around a luminous high-redshift quasar. *Nature*, 2014.

[25] Matthew Colless, Gavin Dalton, Steve Maddox, Will Sutherland, Peder Norberg, Shaun Cole, Joss Bland-Hawthorn, Terry Bridges, Russell Cannon, Chris Collins, et al. The 2df galaxy redshift survey: spectra and redshifts. *Monthly Notices of the Royal Astronomical Society*, 328(4):1039–1063, 2001.

[26] Alexander Kusenko and Leslie J. Rosenberg. Working Group Report: Non-WIMP Dark Matter. In *Community Summer Study 2013: Snowmass on the Mississippi (CSS2013) Minneapolis, MN, USA, July 29-August 6, 2013*, 2013.

[27] Samuel D. McDermott, Hai-Bo Yu, and Kathryn M. Zurek. Turning off the Lights: How Dark is Dark Matter? *Phys. Rev.*, D83:063509, 2011.

[28] Santiago De Lope Amigo, William Man-Yin Cheung, Zhiqi Huang, and Siew-Phang Ng. Cosmological Constraints on Decaying Dark Matter. *JCAP*, 0906:005, 2009.

[29] Annika H. G. Peter and Andrew J. Benson. Dark-matter decays and Milky Way satellite galaxies. *Phys. Rev.*, D82:123521, 2010.

[30] Annika H. G. Peter, Christopher E. Moody, Andrew J. Benson, and Marc Kamionkowski. Constraints on Decaying Dark Matter. *PoS*, IDM2010:084, 2011.

[31] Katherine Freese, Brian Fields, and David Graff. Limits on stellar objects as the dark matter of our halo: nonbaryonic dark matter seems to be required. *Nucl. Phys. Proc. Suppl.*, 80:0305, 2000.

[32] Brian D. Fields, Katherine Freese, and David S. Graff. Chemical abundance constraints on white dwarfs as halo dark matter. *Astrophys. J.*, 534:265–276, 2000.

[33] C. Alcock et al. The MACHO project: Microlensing results from 5.7 years of LMC observations. *Astrophys. J.*, 542:281–307, 2000.

[34] Wayne Hu and Naoshi Sugiyama. Small-scale cosmological perturbations: an analytic approach. *The Astrophysical Journal*, 471(2):542, 1996.

[35] Lars Bergström. Non-baryonic dark matter: observational evidence and detection methods. *Reports on Progress in Physics*, 63(5):793, 2000.

[36] Jan Conrad. Indirect Detection of WIMP Dark Matter: a compact review. In *Interplay between Particle and Astroparticle physics London, United Kingdom, August 18-22, 2014*, 2014.

[37] Jonathan L Feng and Jason Kumar. Wimpless dark matter. *arXiv preprint arXiv:0909.2877*, 2009.

[38] Jonathan L Feng and Jason Kumar. Dark-matter particles without weak-scale masses or weak interactions. *Physical review letters*, 101(23):231301, 2008.

[39] James E. Gunn and III Gott, J. Richard. On the Infall of Matter into Clusters of Galaxies and Some Effects on Their Evolution. *Astrophys.J.*, 176:1–19, 1972.

[40] Marc Schumann. Direct detection of wimp dark matter: concepts and status. *Journal of Physics G: Nuclear and Particle Physics*, 46(10):103003, Aug 2019.

[41] Katherine Freese, Mariangela Lisanti, and Christopher Savage. Annual modulation of dark matter: a review. *arXiv preprint arXiv:1209.3339*, 2012.

[42] J. Amare, S. Borjabad, S. Cebrian, C. Cuesta, D. Fortuno, et al. Low energy events in NaI(Tl) scintillators. ANAIS status and prospects. *PoS*, IDM2010:020, 2011.

[43] A. Marchionni et al. ArDM: a ton-scale LAr detector for direct Dark Matter searches. *J.Phys.Conf.Ser.*, 308:012006, 2011.

[44] Henry T. Wong and Shin-Ted Lin. Dark matter searches with germanium detectors with sub-keV sensitivities. *PoS*, ICHEP2010:439, 2010.

[45] D.S. Akerib et al. Exclusion limits on the WIMP-nucleon cross section from the first run of the Cryogenic Dark Matter Search in the Soudan Underground Laboratory. *Phys.Rev.*, D72:052009, 2005.

[46] Z. Ahmed et al. Dark Matter Search Results from the CDMS II Experiment. *Science*, 327:1619–1621, 2010.

[47] Z. Ahmed et al. Results from a Low-Energy Analysis of the CDMS II Germanium Data. *Phys.Rev.Lett.*, 106:131302, 2011.

[48] Z. Ahmed et al. Search for annual modulation in low-energy CDMS-II data. 2012.

[49] C.E. Aalseth et al. CoGeNT: A Search for Low-Mass Dark Matter using p-type Point Contact Germanium Detectors. *Physical Review D 88,*, 012002, 2013.

[50] C.E. Aalseth et al. Results from a Search for Light-Mass Dark Matter with a P-type Point Contact Germanium Detector. *Phys.Rev.Lett.*, 106:131301, 2011.

[51] C.E. Aalseth et al. Search for an Annual Modulation in a P-type Point Contact Germanium Dark Matter Detector. *Phys.Rev.Lett.*, 107:141301, 2011.

[52] E. Behnke et al. First Dark Matter Search Results from a 4-kg CF_3I Bubble Chamber Operated in a Deep Underground Site. *Phys.Rev.*, D86:052001, 2012.

[53] G. Angloher, M. Bauer, I. Bavykina, A. Bento, C. Bucci, et al. Results from 730 kg days of the CRESST-II Dark Matter Search. *Eur.Phys.J.*, C72:1971, 2012.

[54] R. Bernabei, Pierluigi Belli, F. Cappella, R. Cerulli, F. Montecchia, et al. Dark matter search. *Riv.Nuovo Cim.*, 26N1:1–73, 2003.

[55] R. Bernabei et al. The DAMA/LIBRA apparatus. *Nucl. Instrum. Meth.*, A592:297–315, 2008.

[56] R. Bernabei et al. New results from DAMA/LIBRA. *Eur. Phys. J.*, C67:39–49, 2010.

[57] Marek Kos. Dark matter detection with the DEAP/CLEAN detectors. *PoS*, ICHEP2010:455, 2010.

[58] J. Cherwinka, R. Co, D.F. Cowen, D. Grant, F. Halzen, et al. A Search for the Dark Matter Annual Modulation in South Pole Ice. *Astropart.Phys.*, 35:749–754, 2012.

[59] G.J. Alner, H. Araujo, A. Bewick, S. Burgos, M.J. Carson, et al. The DRIFT-II dark matter detector: Design and commissioning. *Nucl.Instrum.Meth.*, A555:173–183, 2005.

[60] E. Daw, J.R. Fox, J.L. Gauvreau, C. Ghag, L.J. Harmon, et al. Spin-Dependent Limits from the DRIFT-IId Directional Dark Matter Detector. *Astropart.Phys.*, 35:397–401, 2012.

[61] V. Sanglard et al. Final results of the EDELWEISS-I dark matter search with cryogenic heat-and-ionization Ge detectors. *Phys.Rev.*, D71:122002, 2005.

[62] E. Armengaud et al. Final results of the EDELWEISS-II WIMP search using a 4-kg array of cryogenic germanium detectors with interleaved electrodes. *Phys.Lett.*, B702:329–335, 2011.

[63] E. Armengaud et al. A search for low-mass WIMPs with EDELWEISS-II heat-and-ionization detectors. *Phys.Rev.*, D86:051701, 2012.

[64] H. Kraus, E. Armengaud, C. Augier, M. Bauer, N. Bechtold, et al. EURECA. *PoS*, IDM2010:109, 2011.

[65] C. Hall, D. Akerib, X. Bai, S. Bedikian, A. Bernstein, et al. A search for weakly interacting dark matter with the LUX experiment. *PoS*, ICHEP2010:431, 2010.

[66] G.J. Alner et al. Limits on WIMP cross-sections from the NAIAD experiment at the Boulby Underground Laboratory. *Phys.Lett.*, B616:17–24, 2005.

[67] H. Gong, K.L. Giboni, X. Ji, A. Tan, and L. Zhao. The Cryogenic System for the Panda-X Dark Matter Search Experiment. *JINST*, 8:P01002, 2013.

[68] M. Barnabe-Heider et al. Response of superheated droplet detectors of the picasso dark matter search experiment. *Nucl.Instrum.Meth.*, A555:184–204, 2005.

[69] S. Archambault et al. Constraints on Low-Mass WIMP Interactions on ^{19}F from PICASSO. *Phys.Lett.*, B711:153–161, 2012.

[70] N. Coron, J. Gironnet, P. de Marcillac, M. Martinez, T. Redon, et al. 2010 update on the ROSEBUD project. *PoS*, IDM2010:054, 2011.

[71] M. Felizardo, T.A. Girard, T. Morlat, A.C. Fernandes, A.R. Ramos, et al. Final Analysis and Results of the Phase II SIMPLE Dark Matter Search. *Phys.Rev.Lett.*, 108:201302, 2012.

[72] S.T. Lin et al. New limits on spin-independent and spin-dependent couplings of low-mass WIMP dark matter with a germanium detector at a threshold of 220 eV. *Phys.Rev.*, D79:061101, 2009.

[73] R. Acciarri, M. Antonello, B. Baibussinov, P. Benetti, F. Calaprice, et al. The WArP experiment. *J.Phys.Conf.Ser.*, 308:012005, 2011.

[74] E. Aprile et al. Design and Performance of the XENON10 Dark Matter Experiment. *Astropart.Phys.*, 34:679–698, 2011.

[75] J. Angle et al. First Results from the XENON10 Dark Matter Experiment at the Gran Sasso National Laboratory. *Phys.Rev.Lett.*, 100:021303, 2008.

[76] J. Angle et al. A search for light dark matter in XENON10 data. *Phys.Rev.Lett.*, 107:051301, 2011.

[77] E. Aprile et al. The XENON100 Dark Matter Experiment. *Astropart.Phys.*, 35:573–590, 2012.

[78] E. Aprile et al. Dark Matter Results from 225 Live Days of XENON100 Data. *Phys.Rev.Lett.*, 109:181301, 2012.

[79] Elena Aprile. The XENON1T Dark Matter Search Experiment. 2012.

[80] S. Moriyama. Status of XMASS experiment. *PoS*, IDM2010:057, 2011.

[81] D. Yu. Akimov, G.J. Alner, H.M. Araujo, A. Bewick, C. Bungau, et al. The ZEPLIN-III dark matter detector: instrument design, manufacture and commissioning. *Astropart.Phys.*, 27:46–60, 2007.

[82] D. Yu. Akimov, H.M. Araujo, E.J. Barnes, V.A. Belov, A. Bewick, et al. WIMP-nucleon cross-section results from the second science run of ZEPLIN-III. *Phys.Lett.*, B709:14–20, 2012.

[83] S.E. Vahsen, H. Feng, M. Garcia-Sciveres, I. Jaegle, J. Kadyk, Y. Nguyen, M. Rosen, S. Ross, T. Thorpe, and J. Yamaoka. The directional dark matter detector (d3). *EAS Publications Series*, 53:43–50, 2012.

[84] Andrzej K Drukier, Katherine Freese, and David N Spergel. Detecting cold dark-matter candidates. *Physical Review D*, 33(12):3495, 1986.

[85] DAMA/LIBRA Collaboration R. Bernabei. https://agenda.infn.it/conferencedisplay.py?confid=15474. *LNGS Scientific Committee Meeting*, March 2018.

[86] L. Accardo et al. High Statistics Measurement of the Positron Fraction in Primary Cosmic Rays of 0.5-500 GeV with the Alpha Magnetic Spectrometer on the International Space Station. *Phys.Rev.Lett.*, 113:121101, 2014.

[87] Aous A. Abdo et al. Measurement of the Cosmic Ray e+ plus e- spectrum from 20 GeV to 1 TeV with the Fermi Large Area Telescope. *Phys.Rev.Lett.*, 102:181101, 2009.

[88] Oscar Adriani et al. An anomalous positron abundance in cosmic rays with energies 1.5-100 GeV. *Nature*, 458:607–609, 2009.

[89] O. Adriani et al. Cosmic-Ray Positron Energy Spectrum Measured by PAMELA. *Phys.Rev.Lett.*, 111:081102, 2013.

[90] S.W. Barwick et al. Measurements of the cosmic ray positron fraction from 1-GeV to 50-GeV. *Astrophys.J.*, 482:L191–L194, 1997.

[91] M.A. DuVernois, S.W. Barwick, J.J. Beatty, A. Bhattacharyya, C.R. Bower, et al. Cosmic ray electrons and positrons from 1-GeV to 100-GeV: Measurements with HEAT and their interpretation. *Astrophys.J.*, 559:296–303, 2001.

[92] J.J. Beatty, A. Bhattacharyya, C. Bower, S. Coutu, M.A. DuVernois, et al. New measurement of the cosmic-ray positron fraction from 5 to 15-GeV. *Phys.Rev.Lett.*, 93:241102, 2004.

[93] Kavali Institute for Astrophysics and Cosmology. Indirect dark matter detection. *arXiv preprint arXiv:1604.00744*, 2016.

[94] Daniel Whiteson. Disentangling instrumental features of the 130 gev fermi line. *Journal of Cosmology and Astroparticle Physics*, 2012(11):008, 2012.

[95] Bumseok Kyae and Jong-Chul Park. 130 gev fermi gamma-ray line from dark matter decay. *Physics Letters B*, 718(4):1425–1429, 2013.

[96] Andrew W Strong, Igor V Moskalenko, and Olaf Reimer. Diffuse continuum gamma rays from the galaxy. *The Astrophysical Journal*, 537(2):763, 2000.

[97] AA Abdo, M Ackermann, Marco Ajello, L Baldini, J Ballet, G Barbiellini, D Bastieri, K Bechtol, R Bellazzini, B Berenji, et al. Constraints on cosmological dark matter annihilation from the fermi-lat isotropic diffuse gamma-ray measurement. *Journal of Cosmology and Astroparticle Physics*, 2010(04):014, 2010.

[98] Tansu Daylan, Douglas P. Finkbeiner, Dan Hooper, Tim Linden, Stephen K. N. Portillo, Nicholas L. Rodd, and Tracy R. Slatyer. The characterization of the gamma-ray signal from the central Milky Way: A case for annihilating dark matter. *Phys. Dark Univ.*, 12:1–23, 2016.

[99] HESS Collaboration, A Abramowski, F Acero, F Aharonian, AG Akhperjanian, G Anton, S Balenderan, A Balzer, A Barnacka, Y Becherini, et al. Search for photon line-like signatures from dark matter annihilations with hess. *arXiv preprint arXiv:1301.1173*, 2013.

[100] W. de Boer, C. Sander, V. Zhukov, A. V. Gladyshev, and D. I. Kazakov. Egret excess of diffuse galactic gamma rays as tracer of dark matter. *Astron. Astrophys.*, 444:51, 2005.

[101] J. Albert et al. Observation of gamma-rays from the galactic center with the magic telescope. *Astrophys. J.*, 638:L101–L104, 2006.

[102] Antonio Boveia and Caterina Doglioni. Dark matter searches at colliders. *Annual Review of Nuclear and Particle Science*, 68(1):429–459, Oct 2018.

[103] Stefano Giagu. Wimp dark matter searches with the atlas detector at the lhc. *Frontiers in Physics*, 7:75, 2019.

[104] Nadir Daci and. Dark matter searches in CMS. *Journal of Physics: Conference Series*, 623:012029, jun 2015.

[105] Taeil Hur, Hye-Sung Lee, and Salah Nasri. Supersymmetric u1 model with multiple dark matters. *Physical Review D*, 77(1), Jan 2008.

[106] Kathryn M. Zurek. Multicomponent dark matter. *Physical Review D*, 79(11), Jun 2009.

[107] Nikhil Anand, A. Liam Fitzpatrick, and W. C. Haxton. Weakly interacting massive particle-nucleus elastic scattering response. *Physical Review C*, 89(6), Jun 2014.

[108] A. Liam Fitzpatrick, Wick Haxton, Emanuel Katz, Nicholas Lubbers, and Yiming Xu. The effective field theory of dark matter direct detection. *Journal of Cosmology and Astroparticle Physics*, 2013(02):004–004, Feb 2013.

[109] A Liam Fitzpatrick, Wick Haxton, Emanuel Katz, Nicholas Lubbers, and Yiming Xu. The effective field theory of dark matter direct detection. *Journal of Cosmology and Astroparticle Physics*, 2013(02):004, 2013.

[110] A. K. Drukier, Katherine Freese, and D. N. Spergel. Detecting Cold Dark Matter Candidates. *Phys. Rev.*, D33:3495–3508, 1986.

[111] Katherine Freese, Joshua A. Frieman, and Andrew Gould. Signal Modulation in Cold Dark Matter Detection. *Phys. Rev.*, D37:3388–3405, 1988.

[112] Katherine Freese, Mariangela Lisanti, and Christopher Savage. Colloquium: Annual modulation of dark matter. *Rev. Mod. Phys.*, 85:1561–1581, 2013.

[113] Matthew J. Lewis and Katherine Freese. The Phase of the annual modulation: Constraining the WIMP mass. *Phys.Rev.*, D70:043501, 2004.

[114] Christopher Savage, Katherine Freese, and Paolo Gondolo. Annual Modulation of Dark Matter in the Presence of Streams. *Phys. Rev.*, D74:043531, 2006.

[115] Christopher McCabe. The Astrophysical Uncertainties Of Dark Matter Direct Detection Experiments. *Phys.Rev.*, D82:023530, 2010.

[116] J I Read. The local dark matter density. *Journal of Physics G: Nuclear and Particle Physics*, 41(6):063101, may 2014.

[117] S Sivertsson, H Silverwood, J I Read, G Bertone, and P Steger. The localdark matter density from SDSS-SEGUE G-dwarfs. *Monthly Notices of the Royal Astronomical Society*, 478(2):1677–1693, 04 2018.

[118] Scott Dodelson. *Modern cosmology.* Academic press, 2003.

[119] Dan Hooper. TASI 2008 Lectures on Dark Matter. pages 709–764, 2009.

[120] Iason Baldes, Marco Cirelli, Paolo Panci, Kalliopi Petraki, Filippo Sala, and Marco Taoso. Asymmetric dark matter: residual annihilations and self-interactions. *SciPost Phys.*, 4:041, 2018.

[121] Pavel Fileviez Perez and Mark B. Wise. Baryon Asymmetry and Dark Matter Through the Vector-Like Portal. *JHEP*, 05:094, 2013.

[122] Kari Enqvist and Anupam Mazumdar. Cosmological consequences of MSSM flat directions. *Phys. Rept.*, 380:99–234, 2003.

[123] Antonio Riotto and Mark Trodden. Recent progress in baryogenesis. *Ann. Rev. Nucl. Part. Sci.*, 49:35–75, 1999.

[124] Glennys R. Farrar and Gabrijela Zaharijas. Dark matter and the baryon asymmetry. *Phys. Rev. Lett.*, 96:041302, 2006.

[125] Lawrence J. Hall, John March-Russell, and Stephen M. West. A Unified Theory of Matter Genesis: Asymmetric Freeze-In. 2010.

[126] Andrew G. Cohen and David B. Kaplan. Thermodynamic generation of the baryon asymmetry. *Physics Letters B*, 199(2):251–258, Dec 1987.

[127] Adisorn Adulpravitchai, Brian Batell, and Josef Pradler. Non-Abelian Discrete Dark Matter. *Phys. Lett.*, B700:207–216, 2011.

[128] Brian Batell, Maxim Pospelov, and Adam Ritz. Direct Detection of Multi-component Secluded WIMPs. *Phys. Rev.*, D79:115019, 2009.

[129] Keith R. Dienes, Jason Kumar, and Brooks Thomas. Direct Detection of Dynamical Dark Matter. *Phys. Rev.*, D86:055016, 2012.

[130] Stefano Profumo, Kris Sigurdson, and Lorenzo Ubaldi. Can we discover multi-component WIMP dark matter? *JCAP*, 0912:016, 2009.

[131] Subhaditya Bhattacharya, Purusottam Ghosh, Tarak Nath Maity, and Tirtha Sankar Ray. Mitigating Direct Detection Bounds in Non-minimal Higgs Portal Scalar Dark Matter Models. *JHEP*, 10:088, 2017.

[132] Subhaditya Bhattacharya, Poulose Poulose, and Purusottam Ghosh. Multipartite Interacting Scalar Dark Matter in the light of updated LUX data. *JCAP*, 1704(04):043, 2017.

[133] Diego Chialva, P. S. Bhupal Dev, and Anupam Mazumdar. Multiple dark matter scenarios from ubiquitous stringy throats. *Phys. Rev.*, D87(6):063522, 2013.

[134] Mattias Blennow, Stefan Clementz, and Juan Herrero-Garcia. Pinning down inelastic dark matter in the Sun and in direct detection. *JCAP*, 1604(04):004, 2016.

[135] Nassim Bozorgnia, Juan Herrero-Garcia, Thomas Schwetz, and Jure Zupan. Halo-independent methods for inelastic dark matter scattering. *JCAP*, 1307:049, 2013.

[136] David Tucker-Smith and Neal Weiner. The Status of inelastic dark matter. *Phys. Rev.*, D72:063509, 2005.

[137] Gian Francesco Giudice, Ben Gripaios, and Rakhi Mahbubani. Counting dark matter particles in LHC events. *Phys. Rev.*, D85:075019, 2012.

[138] Gianfranco Bertone, David G. Cerdeno, Mattia Fornasa, Roberto Ruiz de Austri, and Roberto Trotta. Identification of Dark Matter particles with LHC and direct detection data. *Phys. Rev.*, D82:055008, 2010.

[139] Mattias Blennow, Juan Herrero-Garcia, Thomas Schwetz, and Stefan Vogl. Halo-independent tests of dark matter direct detection signals: local DM density, LHC, and thermal freeze-out. *JCAP*, 1508(08):039, 2015.

[140] Kalliopi Petraki and Raymond R. Volkas. Review of asymmetric dark matter. *Int. J. Mod. Phys.*, A28:1330028, 2013.

[141] Richard H. Helm. Inelastic and elastic scattering of 187-mev electrons from selected even-even nuclei. *Phys. Rev.*, 104:1466–1475, Dec 1956.

[142] J.D. Lewin and P.F. Smith. Review of mathematics, numerical factors, and corrections for dark matter experiments based on elastic nuclear recoil. *Astroparticle Physics*, 6(1):87 – 112, 1996.

[143] P. Klos, J. Menéndez, D. Gazit, and A. Schwenk. Large-scale nuclear structure calculations for spin-dependent WIMP scattering with chiral effective field theory currents. *Phys. Rev.*, D88(8):083516, 2013. [Erratum: Phys. Rev.D89,no.2,029901(2014)].

[144] Graciela Gelmini and Paolo Gondolo. WIMP annual modulation with opposite phase in Late-Infall halo models. *Phys. Rev.*, D64:023504, 2001.

[145] Juan Herrero-Garcia, Thomas Schwetz, and Jure Zupan. Astrophysics independent bounds on the annual modulation of dark matter signals. *Phys. Rev. Lett.*, 109:141301, 2012.

[146] Juan Herrero-Garcia, Thomas Schwetz, and Jure Zupan. On the annual modulation signal in dark matter direct detection. *JCAP*, 1203:005, 2012.

[147] Samuel K. Lee, Mariangela Lisanti, Annika H. G. Peter, and Benjamin R. Safdi. Effect of Gravitational Focusing on Annual Modulation in Dark-Matter Direct-Detection Experiments. *Phys. Rev. Lett.*, 112(1):011301, 2014.

[148] Nassim Bozorgnia and Thomas Schwetz. Is the effect of the Sun's gravitational potential on dark matter particles observable? *JCAP*, 1408:013, 2014.

[149] Eugenio Del Nobile, Graciela B. Gelmini, and Samuel J. Witte. Gravitational Focusing and Substructure Effects on the Rate Modulation in Direct Dark Matter Searches. *JCAP*, 1508(08):041, 2015.

[150] E. Aprile et al. First Dark Matter Search Results from the XENON1T Experiment. 2017.

[151] C. Amole et al. Improved dark matter search results from PICO-2L Run 2. *Phys. Rev.*, D93(6):061101, 2016.

[152] C. Amole et al. Dark Matter Search Results from the PICO-60 C_3F_8 Bubble Chamber. *Phys. Rev. Lett.*, 118(25):251301, 2017.

[153] Nasim Fatemighomi. DEAP-3600 dark matter experiment. In *35th International Symposium on Physics in Collision (PIC 2015) Coventry, United Kingdom, September 15-19, 2015*, 2016.

[154] J. Calvo et al. Commissioning of the ArDM experiment at the Canfranc underground laboratory: first steps towards a tonne-scale liquid argon time projection chamber for Dark Matter searches. *JCAP*, 1703(03):003, 2017.

[155] E. Aprile et al. Conceptual design and simulation of a water Cherenkov muon veto for the XENON1T experiment. *JINST*, 9:P11006, 2014.

[156] D. S. Akerib et al. LUX-ZEPLIN (LZ) Conceptual Design Report. 2015.

[157] J. Aalbers et al. DARWIN: towards the ultimate dark matter detector. *JCAP*, 1611:017, 2016.

[158] Teresa Marrodán Undagoitia and Ludwig Rauch. Dark matter direct-detection experiments. *J. Phys.*, G43(1):013001, 2016.

[159] Jianglai Liu, Xun Chen, and Xiangdong Ji. Current status of direct dark matter detection experiments. *Nature Phys.*, 13(3):212–216, 2017.

[160] K. Fushimi et al. Dark matter search project PICO-LON. *J. Phys. Conf. Ser.*, 718(4):042022, 2016.

[161] R. Agnese et al. Projected Sensitivity of the SuperCDMS SNOLAB experiment. *Phys. Rev.*, D95(8):082002, 2017.

[162] Brian Feldstein and Felix Kahlhoefer. Quantifying (dis)agreement between direct detection experiments in a halo-independent way. *JCAP*, 1412(12):052, 2014.

[163] Bradley J. Kavanagh and Anne M. Green. Improved determination of the WIMP mass from direct detection data. *Phys. Rev.*, D86:065027, 2012.

[164] J. Herrero-Garcia. Halo-independent tests of dark matter annual modulation signals. *JCAP*, 1509(09):012, 2015.

[165] Mattias Blennow, Pilar Coloma, Patrick Huber, and Thomas Schwetz. Quantifying the sensitivity of oscillation experiments to the neutrino mass ordering. *JHEP*, 03:028, 2014.

[166] Emilio Ciuffoli. Statistical Methods for the Neutrino Mass Hierarchy. In *Prospects in Neutrino Physics (NuPhys2016) London, London, United Kingdom, December 12-14, 2016*, 2017.

[167] Emilio Ciuffoli, Jarah Evslin, and Xinmin Zhang. Sensitivity to the neutrino mass hierarchy. *arXiv preprint arXiv:1305.5150*, 2013.

[168] Karl Pearson F.R.S. X. on the criterion that a given system of deviations from the probable in the case of a correlated system of variables is such that it can be reasonably supposed to have arisen from random sampling. *Philosophical Magazine*, 50(302):157–175, 1900.

[169] Samuel S Wilks. The large-sample distribution of the likelihood ratio for testing composite hypotheses. *The Annals of Mathematical Statistics*, 9(1):60–62, 1938.

[170] Glen Cowan, Kyle Cranmer, Eilam Gross, and Ofer Vitells. Asymptotic formulae for likelihood-based tests of new physics. *The European Physical Journal C*, 71(2):1554, 2011.

[171] Jonathan L. Feng, Jason Kumar, Danny Marfatia, and David Sanford. Isospin-Violating Dark Matter. *Phys. Lett.*, B703:124–127, 2011.

[172] Carlos E. Yaguna. Isospin-violating dark matter in the light of recent data. *Phys. Rev.*, D95(5):055015, 2017.

[173] Miguel Pato, Laura Baudis, Gianfranco Bertone, Roberto Ruiz de Austri, Louis E. Strigari, and Roberto Trotta. Complementarity of Dark Matter Direct Detection Targets. *Phys. Rev.*, D83:083505, 2011.

[174] Annika H. G. Peter, Vera Gluscevic, Anne M. Green, Bradley J. Kavanagh, and Samuel K. Lee. WIMP physics with ensembles of direct-detection experiments. *Phys. Dark Univ.*, 5-6:45–74, 2014.

[175] F Feroz, MP Hobson, and M Bridges. Multinest: an efficient and robust bayesian inference tool for cosmology and particle physics. *Monthly Notices of the Royal Astronomical Society*, 398(4):1601–1614, 2009.

[176] Bradley J. Kavanagh, Mattia Fornasa, and Anne M. Green. Probing WIMP particle physics and astrophysics with direct detection and neutrino telescope data. *Phys. Rev.*, D91(10):103533, 2015.

[177] Mattias Blennow, Juan Herrero-Garcia, and Thomas Schwetz. A halo-independent lower bound on the dark matter capture rate in the Sun from a direct detection signal. *JCAP*, 1505(05):036, 2015.

[178] Francesc Ferrer, Alejandro Ibarra, and Sebastian Wild. A novel approach to derive halo-independent limits on dark matter properties. *JCAP*, 1509(09):052, 2015.

[179] Alejandro Ibarra and Andreas Rappelt. Optimized velocity distributions for direct dark matter detection. 2017.

[180] Pat Scott. Pippi - painless parsing, post-processing and plotting of posterior and likelihood samples. *Eur. Phys. J. Plus*, 127:138, 2012.

[181] David Tucker-Smith and Neal Weiner. Inelastic dark matter. *Phys. Rev.*, D64:043502, 2001.

[182] Peter W. Graham, Roni Harnik, Surjeet Rajendran, and Prashant Saraswat. Exothermic Dark Matter. *Phys. Rev.*, D82:063512, 2010.

[183] Thomas Schwetz and Jure Zupan. Dark Matter attempts for CoGeNT and DAMA. *JCAP*, 1108:008, 2011.

[184] Mads T. Frandsen and Ian M. Shoemaker. Up-shot of inelastic down-scattering at CDMS-Si. *Phys. Rev.*, D89(5):051701, 2014.

[185] Marco Cirelli, Eugenio Del Nobile, and Paolo Panci. Tools for model-independent bounds in direct dark matter searches. *JCAP*, 1310:019, 2013.

[186] Zuowei Liu, Yushan Su, Yue-Lin Sming Tsai, Bingrong Yu, and Qiang Yuan. A combined analysis of PandaX, LUX, and XENON1T experiments within the framework of dark matter effective theory. 2017.

[187] Bogdan A. Dobrescu and Irina Mocioiu. Spin-dependent macroscopic forces from new particle exchange. *JHEP*, 11:005, 2006.

[188] A. Liam Fitzpatrick, Wick Haxton, Emanuel Katz, Nicholas Lubbers, and Yiming Xu. Model Independent Direct Detection Analyses. 2012.

[189] Nikhil Anand, A. Liam Fitzpatrick, and W. C. Haxton. Weakly interacting massive particle-nucleus elastic scattering response. *Phys. Rev.*, C89(6):065501, 2014.

[190] Moira I. Gresham and Kathryn M. Zurek. Effect of nuclear response functions in dark matter direct detection. *Phys. Rev.*, D89(12):123521, 2014.

[191] A. Liam Fitzpatrick, Wick Haxton, Emanuel Katz, Nicholas Lubbers, and Yiming Xu. The Effective Field Theory of Dark Matter Direct Detection. *JCAP*, 1302:004, 2013.

[192] Fady Bishara, Joachim Brod, Benjamin Grinstein, and Jure Zupan. Chiral Effective Theory of Dark Matter Direct Detection. *JCAP*, 1702(02):009, 2017.

[193] David E. Kaplan, Markus A. Luty, and Kathryn M. Zurek. Asymmetric Dark Matter. *Phys. Rev.*, D79:115016, 2009.

[194] Kathryn M. Zurek. Asymmetric Dark Matter: Theories, Signatures, and Constraints. *Phys. Rept.*, 537:91–121, 2014.

[195] Juan Herrero-Garcia, Andre Scaffidi, Martin White, and Anthony G. Williams. On the direct detection of multi-component dark matter: sensitivity studies and parameter estimation. *JCAP*, 1711(11):021, 2017.

[196] Aqeel Ahmed, Mateusz Duch, Bohdan Grzadkowski, and Michal Iglicki. Multi-Component Dark Matter: the vector and fermion case. 2017.

[197] Juan Herrero-Garcia, Andre Scaffidi, Martin White, and Anthony G. Williams. Reproducing the DAMA/LIBRA phase-2 results with two dark matter components. 2018.

[198] Edward W. Kolb and Michael S. Turner. The Early Universe. *Front. Phys.*, 69:1–547, 1990.

[199] Donnino Anderhalden, Juerg Diemand, Gianfranco Bertone, Andrea V. Maccio, and Aurel Schneider. The Galactic Halo in Mixed Dark Matter Cosmologies. *JCAP*, 1210:047, 2012.

[200] Moqbil S. Alenazi and Paolo Gondolo. Phase-space distribution of unbound dark matter near the Sun. *Phys. Rev.*, D74:083518, 2006.

[201] R. Foot. Hidden sector dark matter explains the DAMA, CoGeNT, CRESST-II and CDMS/Si experiments. *Phys. Rev.*, D88(2):025032, 2013.

[202] Xiangxiang Ren et al. Particle Physics Constraints on Self-Interacting Dark Matter from PandaX-II Experiment. 2018.

[203] Marco Hufnagel, Kai Schmidt-Hoberg, and Sebastian Wild. BBN constraints on MeV-scale dark sectors. Part II. Electromagnetic decays. 2018.

[204] Tongyan Lin, Hai-Bo Yu, and Kathryn M. Zurek. On Symmetric and Asymmetric Light Dark Matter. *Phys. Rev.*, D85:063503, 2012.

[205] Manoj Kaplinghat, Sean Tulin, and Hai-Bo Yu. Direct Detection Portals for Self-interacting Dark Matter. *Phys. Rev.*, D89(3):035009, 2014.

[206] Asher Berlin, Nikita Blinov, Gordan Krnjaic, Philip Schuster, and Natalia Toro. Dark Matter, Millicharges, Axion and Scalar Particles, Gauge Bosons, and Other New Physics with LDMX. 2018.

[207] Lina Necib, Mariangela Lisanti, and Vasily Belokurov. Inferred evidence for dark matter kinematic substructure with sdss–gaia. *The Astrophysical Journal*, 874(1):3, Mar 2019.

[208] Samuel K. Lee, Mariangela Lisanti, and Benjamin R. Safdi. Dark-Matter Harmonics Beyond Annual Modulation. *JCAP*, 1311:033, 2013.

[209] Sebastian Baum, Katherine Freese, and Chris Kelso. Dark Matter implications of DAMA/LIBRA-phase2 results. 2018.

[210] Matthew J. Lewis and Katherine Freese. Phase of the annual modulation as a tool for determining the mass of the weakly interacting massive particle. *Physical Review D*, 70(4), Aug 2004.

[211] Samuel K. Lee, Mariangela Lisanti, and Benjamin R. Safdi. Dark-matter harmonics beyond annual modulation. *Journal of Cosmology and Astroparticle Physics*, 2013(11):033, 2013.

[212] R. Bernabei, P. Belli, F. Cappella, R. Cerulli, C. J. Dai, A. d' Angelo, H. L. He, A. Incicchitti, H. H. Kuang, J. M. Ma, and et al. First results from dama/libra and the combined results with dama/nai. *The European Physical Journal C*, 56(3):333–355, Aug 2008.

[213] R. Bernabei, P. Belli, A. Di Marco, F. Montecchia, A. d' Angelo, A. Incicchitti, F. Cappella, V. Caracciolo, R. Cerulli, C.J. Dai, and et al. Dama/libra results and perspectives. *EPJ Web of Conferences*, 136:05001, 2017.

[214] C Savage, G Gelmini, P Gondolo, and K Freese. Compatibility of dama/libra dark matter detection with other searches. *Journal of Cosmology and Astroparticle Physics*, 2009(04):010–010, Apr 2009.

[215] Malcolm Fairbairn and Thomas Schwetz. Spin-independent elastic wimp scattering and the dama annual modulation signal. *Journal of Cosmology and Astroparticle Physics*, 2009(01):037–037, Jan 2009.

[216] Spencer Chang, Aaron Pierce, and Neal Weiner. Using the energy spectrum measured by dama/libra to probe light dark matter. *Phys. Rev. D*, 79:115011, Jun 2009.

[217] Frank J Petriello and Kathryn M Zurek. Dama and wimp dark matter. *Journal of High Energy Physics*, 2008(09):047–047, Sep 2008.

[218] R. Bernabei, P. Belli, F. Cappella, V. Caracciolo, R. Cerulli, C.J. Dai, A. d' Angelo, A. Di Marco, H.L. He, and et al. Improved model-dependent corollary analyses after the first six annual cycles of dama/libra-phase2. *Nuclear Physics and Atomic Energy*, 20(4):317–348, Dec 2019.

[219] Dario Buttazzo, Paolo Panci, Nicola Rossi, and Alessandro Strumia. Annual modulations from secular variations: relaxing dama?, 2020.

[220] R. Bernabei, P. Belli, A. Bussolotti, F. Cappella, V. Caracciolo, R. Cerulli, C.J. Dai, A. d' Angelo, A. Di Marco, and et al. First model independent results from dama/libra-phase2. *Nuclear Physics and Atomic Energy*, 19(4):307–325, Dec 2018.

[221] Sebastian Baum, Katherine Freese, and Chris Kelso. Dark matter implications of dama/libra-phase2 results. *Physics Letters B*, 789:262–269, Feb 2019.

[222] R. Bernabei et al. Improved model-dependent corollary analyses after the first six annual cycles of DAMA/LIBRA-phase2. 2019.

[223] R. Bernabei et al. Final model independent result of DAMA/LIBRA-phase1. *Eur. Phys. J.*, C73:2648, 2013.

[224] Juan Herrero-Garcia, Andre Scaffidi, Martin White, and Anthony G. Williams. On the direct detection of multi-component dark matter: implications of the relic abundance. *JCAP*, 1901(01):008, 2019.

[225] R. Bernabei et al. First model independent results from DAMA/LIBRA-phase2. 2018.

[226] Felix Kahlhoefer, Florian Reindl, Karoline Schäffner, Kai Schmidt-Hoberg, and Sebastian Wild. Model-independent comparison of annual modulation and total rate with direct detection experiments. 2018.

[227] Sunghyun Kang, Stefano Scopel, Gaurav Tomar, and Jong-Hyun Yoon. DAMA/LIBRA-phase2 in WIMP effective models. 2018.

[228] Chris Kelso, Pearl Sandick, and Christopher Savage. Lowering the Threshold in the DAMA Dark Matter Search. *JCAP*, 1309:022, 2013.

[229] Spencer Chang, Josef Pradler, and Itay Yavin. Statistical Tests of Noise and Harmony in Dark Matter Modulation Signals. *Phys. Rev.*, D85:063505, 2012.

[230] Enrique Fernandez-Martinez and Rakhi Mahbubani. The Gran Sasso muon puzzle. *JCAP*, 1207:029, 2012.

[231] Joel Klinger and Vitaly A. Kudryavtsev. Can muon-induced backgrounds explain the DAMA data? *J. Phys. Conf. Ser.*, 718(4):042033, 2016.

[232] P. Belli et al. Search for double beta decay in ^{106}Cd in the DAMA/CRYS setup. *AIP Conf. Proc.*, 1894(1):020005, 2017.

[233] Rita Bernabei and Fabio Cappella. Investigation of rare nuclear decays with the DAMA set-ups. *Int. J. Mod. Phys.*, A33(09):1843005, 2018.

[234] D. N. McKinsey. Is DAMA Bathing in a Sea of Radioactive Argon? 2018.

[235] A. Bottino, F. Donato, N. Fornengo, and S. Scopel. Light neutralinos and WIMP direct searches. *Phys. Rev.*, D69:037302, 2004.

[236] A. Bottino, F. Donato, N. Fornengo, and S. Scopel. Lower bound on the neutralino mass from new data on CMB and implications for relic neutralinos. *Phys. Rev.*, D68:043506, 2003.

[237] Paolo Gondolo and Graciela Gelmini. Compatibility of DAMA dark matter detection with other searches. *Phys. Rev.*, D71:123520, 2005.

[238] Malcolm Fairbairn and Thomas Schwetz. Spin-independent elastic WIMP scattering and the DAMA annual modulation signal. *JCAP*, 0901:037, 2009.

[239] Joachim Kopp, Thomas Schwetz, and Jure Zupan. Global interpretation of direct Dark Matter searches after CDMS-II results. *JCAP*, 1002:014, 2010.

[240] Eugenio Del Nobile, Graciela B. Gelmini, Andreea Georgescu, and Ji-Haeng Huh. Reevaluation of spin-dependent WIMP-proton interactions as an explanation of the DAMA data. *JCAP*, 1508(08):046, 2015.

[241] Sunghyun Kang, Stefano Scopel, Gaurav Tomar, and Jong-Hyun Yoon. Protonphilic spin-dependent inelastic Dark Matter (pSIDM) as a viable explanation of DAMA/LIBRA-phase2. 2018.

[242] D. S. Akerib et al. Results from a search for dark matter in the complete LUX exposure. *Phys. Rev. Lett.*, 118(2):021303, 2017.

[243] Xiangyi Cui et al. Dark Matter Results From 54-Ton-Day Exposure of PandaX-II Experiment. *Phys. Rev. Lett.*, 119(18):181302, 2017.

[244] Christopher Savage, Graciela Gelmini, Paolo Gondolo, and Katherine Freese. XENON10/100 dark matter constraints in comparison with CoGeNT and DAMA: examining the Leff dependence. *Phys. Rev.*, D83:055002, 2011.

[245] Christopher McCabe. DAMA and CoGeNT without astrophysical uncertainties. *Phys. Rev.*, D84:043525, 2011.

[246] Mads T. Frandsen, Felix Kahlhoefer, John March-Russell, Christopher McCabe, Matthew McCullough, and Kai Schmidt-Hoberg. On the DAMA and CoGeNT Modulations. *Phys. Rev.*, D84:041301, 2011.

[247] Mads T. Frandsen, Felix Kahlhoefer, Christopher McCabe, Subir Sarkar, and Kai Schmidt-Hoberg. Resolving astrophysical uncertainties in dark matter direct detection. *JCAP*, 1201:024, 2012.

[248] Graciela B. Gelmini, Ji-Haeng Huh, and Samuel J. Witte. Assessing Compatibility of Direct Detection Data: Halo-Independent Global Likelihood Analyses. *JCAP*, 1610(10):029, 2016.

[249] J. Amaré et al. From ANAIS-25 towards ANAIS-250. *Phys. Procedia*, 61:157–162, 2015.

[250] Emily Shields, Jingke Xu, and Frank Calaprice. SABRE: A New NaI(T1) Dark Matter Direct Detection Experiment. *Phys. Procedia*, 61:169–178, 2015.

[251] G. Angloher et al. The COSINUS project - perspectives of a NaI scintillating calorimeter for dark matter search. *Eur. Phys. J.*, C76(8):441, 2016.

[252] W. G. Thompson. Current status and projected sensitivity of COSINE-100. In *15th International Conference on Topics in Astroparticle and Underground Physics (TAUP 2017) Sudbury, Ontario, Canada, July 24-28, 2017*, 2017.

[253] Francis Froborg. SABRE: WIMP modulation detection in the northern and southern hemisphere. *J. Phys. Conf. Ser.*, 718(4):042021, 2016.

[254] F. James. MINUIT Function Minimization and Error Analysis: Reference Manual Version 94.1. 1994.

[255] F. Feroz, M. P. Hobson, and M. Bridges. MultiNest: an efficient and robust Bayesian inference tool for cosmology and particle physics. *Mon. Not. Roy. Astron. Soc.*, 398:1601–1614, 2009.

[256] Farhan Feroz and M. P. Hobson. Multimodal nested sampling: an efficient and robust alternative to MCMC methods for astronomical data analysis. *Mon. Not. Roy. Astron. Soc.*, 384:449, 2008.

[257] F. Feroz, M. P. Hobson, E. Cameron, and A. N. Pettitt. Importance Nested Sampling and the MultiNest Algorithm. 2013.

[258] Thomas Lacroix, Celine Boehm, and Joseph Silk. Fitting the Fermi-LAT GeV excess: On the importance of including the propagation of electrons from dark matter. *Phys.Rev.*, D90(4):043508, 2014.

[259] Gerard Jungman, Marc Kamionkowski, and Kim Griest. Supersymmetric dark matter. *Phys.Rept.*, 267:195–373, 1996.

[260] http://astronomy.swin.edu.au/cms/cpg15x/albums/userpics/galacticcoords.2.jpg.

[261] A. Albert, B. Anderson, K. Bechtol, A. Drlica-Wagner, M. Meyer, M. Sánchez-Conde, L. Strigari, M. Wood, T. M. C. Abbott, F. B. Abdalla, A. Benoit-Lévy, G. M. Bernstein, R. A. Bernstein, E. Bertin, D. Brooks, D. L. Burke, A. Carnero Rosell, M. Carrasco Kind, J. Carretero, M. Crocce, C. E. Cunha, C. B. D'Andrea, L. N. da Costa, S. Desai, H. T. Diehl, J. P. Dietrich, P. Doel, T. F. Eifler, A. E. Evrard, A. Fausti Neto, D. A. Finley, B. Flaugher, P. Fosalba, J. Frieman, D. W. Gerdes, D. A. Goldstein, D. Gruen, R. A. Gruendl, K. Honscheid, D. J. James, S. Kent, K. Kuehn, N. Kuropatkin, O. Lahav, T. S. Li, M. A. G. Maia, M. March, J. L. Marshall, P. Martini, C. J. Miller, R. Miquel, E. Neilsen, B. Nord, R. Ogando, A. A. Plazas, K. Reil, A. K. Romer, E. S. Rykoff, E. Sanchez, B. Santiago, M. Schubnell, I. Sevilla-Noarbe, R. C. Smith, M. Soares-Santos, F. Sobreira, E. Suchyta, M. E. C. Swanson, G. Tarle, V. Vikram, A. R. Walker, and R. H. Wechsler and. SEARCHING FOR DARK MATTER ANNIHILATION IN RECENTLY DISCOVERED MILKY WAY SATELLITES WITHFERMI-LAT. *The Astrophysical Journal*, 834(2):110, jan 2017.

[262] Gregory D Martinez. A robust determination of milky way satellite properties using hierarchical mass modelling. *Monthly Notices of the Royal Astronomical Society*, 451(3):2524–2535, 2015.

[263] M. Ackermann et al. Searching for Dark Matter Annihilation from Milky Way Dwarf Spheroidal Galaxies with Six Years of Fermi Large Area Telescope Data. *Phys. Rev. Lett.*, 115(23):231301, 2015.

[264] M. Ackermann et al. Dark matter constraints from observations of 25 Milky Way satellite galaxies with the Fermi Large Area Telescope. *Phys.Rev.*, D89:042001, 2014.

[265] Fermi-LAT collaboration. Figures and data files associated with the fermi lat paper"searching for dark matter annihilation from milky way dwarf spheroidal galaxies with six years of fermi-lat data".

[266] Michael E. Peskin and Tatsu Takeuchi. Estimation of oblique electroweak corrections. *Phys. Rev. D*, 46:381–409, 1992.

[267] J. Silk et al. *Particle Dark Matter: Observations, Models and Searches.* Cambridge Univ. Press, Cambridge, 2010.

[268] E. Aprile et al. Dark Matter Search Results from a One Ton-Year Exposure of XENON1T. *Phys. Rev. Lett.*, 121(11):111302, 2018.

[269] R. D. Peccei and Helen R. Quinn. CP Conservation in the Presence of Instantons. *Phys. Rev. Lett.*, 38:1440–1443, 1977. [,328(1977)].

[270] R. D. Peccei and Helen R. Quinn. Constraints Imposed by CP Conservation in the Presence of Instantons. *Phys. Rev. D*, 16:1791–1797, 1977.

[271] Steven Weinberg. A New Light Boson? *Phys. Rev. Lett.*, 40:223–226, 1978.

[272] Frank Wilczek. Problem of Strong P and T Invariance in the Presence of Instantons. *Phys. Rev. Lett.*, 40:279–282, 1978.

[273] Scott Dodelson and Lawrence M. Widrow. Sterile-neutrinos as dark matter. *Phys. Rev. Lett.*, 72:17–20, 1994.

[274] Xiang-Dong Shi and George M. Fuller. A New dark matter candidate: Non-thermal sterile neutrinos. *Phys. Rev. Lett.*, 82:2832–2835, 1999.

[275] Tao Han, Felix Kling, Shufang Su, and Yongcheng Wu. Unblinding the dark matter blind spots. *JHEP*, 02:057, 2017.

[276] Arghya Choudhury, Kamila Kowalska, Leszek Roszkowski, Enrico Maria Sessolo, and Andrew J. Williams. Blind Spots for Direct Detection with Simplified DM Models and the LHC. *Universe*, 3(2):41, 2017.

[277] Tao Han, Hongkai Liu, Satyanarayan Mukhopadhyay, and Xing Wang. Dark Matter Blind Spots at One-Loop. *JHEP*, 03:080, 2019.

[278] Wolfgang Altmannshofer, Brian Maddock, and Stefano Profumo. Doubly Blind Spots in Scalar Dark Matter Models. *Phys. Rev. D*, 100(5):055033, 2019.

[279] Qian-Fei Xiang, Xiao-Jun Bi, Peng-Fei Yin, and Zhao-Huan Yu. Exploring Fermionic Dark Matter via Higgs Boson Precision Measurements at the Circular Electron Positron Collider. *Phys. Rev. D*, 97(5):055004, 2018.

[280] Jin-Wei Wang, Xiao-Jun Bi, Qian-Fei Xiang, Peng-Fei Yin, and Zhao-Huan Yu. Exploring triplet-quadruplet fermionic dark matter at the LHC and future colliders. *Phys. Rev. D*, 97(3):035021, 2018.

[281] JiJi Fan, Matthew Reece, and Lian-Tao Wang. Non-relativistic effective theory of dark matter direct detection. *JCAP*, 1011:042, 2010.

[282] Celine Boehm, Matthew J. Dolan, Christopher McCabe, Michael Spannowsky, and Chris J. Wallace. Extended gamma-ray emission from Coy Dark Matter. *JCAP*, 1405:009, 2014.

[283] Martin Bauer, Ulrich Haisch, and Felix Kahlhoefer. Simplified dark matter models with two Higgs doublets: I. Pseudoscalar mediators. *JHEP*, 05:138, 2017.

[284] Patrick Tunney, Jose Miguel No, and Malcolm Fairbairn. Probing the pseudoscalar portal to dark matter via $\bar{b}bZ(\to \ell\ell)+ \not{E}_T$: From the LHC to the Galactic Center excess. *Phys. Rev. D*, 96(9):095020, 2017.

[285] Christian Gross, Oleg Lebedev, and Takashi Toma. Cancellation Mechanism for Dark-Matter Nucleon Interaction. *Phys. Rev. Lett.*, 119(19):191801, 2017.

[286] Reuven Balkin, Maximilian Ruhdorfer, Ennio Salvioni, and Andreas Weiler. Dark matter shifts away from direct detection. *JCAP*, 1811(11):050, 2018.

[287] Katri Huitu, Niko Koivunen, Oleg Lebedev, Subhadeep Mondal, and Takashi Toma. Probing pseudo-Goldstone dark matter at the LHC. *Phys. Rev. D*, 100(1):015009, 2019.

[288] Dimitrios Karamitros. Pseudo Nambu-Goldstone Dark Matter: Examples of Vanishing Direct Detection Cross Section. *Phys. Rev. D*, 99(9):095036, 2019.

[289] Duarte Azevedo, Mateusz Duch, Bohdan Grzadkowski, Da Huang, Michal Iglicki, and Rui Santos. One-loop contribution to dark-matter-nucleon scattering in the pseudo-scalar dark matter model. *JHEP*, 01:138, 2019.

[290] Koji Ishiwata and Takashi Toma. Probing pseudo Nambu-Goldstone boson dark matter at loop level. *JHEP*, 12:089, 2018.

[291] D. S. Akerib et al. Projected WIMP Sensitivity of the LUX-ZEPLIN (LZ) Dark Matter Experiment. 2018.

[292] A. Albert et al. Searching for Dark Matter Annihilation in Recently Discovered Milky Way Satellites with Fermi-LAT. *Astrophys. J.*, 834(2):110, 2017.

[293] Duarte Azevedo, Mateusz Duch, Bohdan Grzadkowski, Da Huang, Michal Iglicki, and Rui Santos. Testing scalar versus vector dark matter. *Phys. Rev. D*, 99(1):015017, 2019.

[294] Tommi Alanne, Matti Heikinheimo, Venus Keus, Niko Koivunen, and Kimmo Tuominen. Direct and indirect probes of Goldstone dark matter. *Phys. Rev. D*, 99(7):075028, 2019.

[295] Xue-Min Jiang, Chengfeng Cai, Zhao-Huan Yu, Yu-Pan Zeng, and Hong-Hao Zhang. Pseudo-Nambu-Goldstone Dark Matter and Two Higgs Doublets. *Phys. Rev. D*, 100(7):075011, 2019.

[296] Steven J. Clark, Bhaskar Dutta, and Louis E. Strigari. Dark Matter Annihilation into Four-Body Final States and Implications for the AMS Antiproton Excess. *Phys. Rev. D*, 97(2):023003, 2018.

[297] Kimberly Boddy, Jason Kumar, Danny Marfatia, and Pearl Sandick. Model-independent constraints on dark matter annihilation in dwarf spheroidal galaxies. *Phys. Rev. D*, 97(9):095031, 2018.

[298] James M. Cline and Takashi Toma. Pseudo-Goldstone dark matter confronts cosmic ray and collider anomalies. *Phys. Rev. D*, 100(3):035023, 2019.

[299] Kristjan Kannike and Martti Raidal. Phase Transitions and Gravitational Wave Tests of Pseudo-Goldstone Dark Matter in the Softly Broken U(1) Scalar Singlet Model. *Phys. Rev. D*, 99(11):115010, 2019.

[300] Kristjan Kannike, Kaius Loos, and Martti Raidal. Gravitational wave signals of pseudo-Goldstone dark matter in the $\mathbb{Z}_3$ complex singlet model. *Phys. Rev. D*, 101(3):035001, 2020.

[301] Adam Alloul, Neil D. Christensen, Céline Degrande, Claude Duhr, and Benjamin Fuks. FeynRules 2.0 - A complete toolbox for tree-level phenomenology. *Comput. Phys. Commun.*, 185:2250–2300, 2014.

[302] Celine Degrande, Claude Duhr, Benjamin Fuks, David Grellscheid, Olivier Mattelaer, and Thomas Reiter. UFO - The Universal FeynRules Output. *Comput. Phys. Commun.*, 183:1201–1214, 2012.

[303] Alexander Belyaev, Neil D. Christensen, and Alexander Pukhov. CalcHEP 3.4 for collider physics within and beyond the Standard Model. *Comput. Phys. Commun.*, 184:1729–1769, 2013.

[304] Thomas Hahn. Generating Feynman diagrams and amplitudes with FeynArts 3. *Comput. Phys. Commun.*, 140:418–431, 2001.

[305] Georges Aad et al. Observation of a new particle in the search for the Standard Model Higgs boson with the ATLAS detector at the LHC. *Phys. Lett. B*, 716:1–29, 2012.

[306] Serguei Chatrchyan et al. Observation of a new boson at a mass of 125 GeV with the CMS experiment at the LHC. *Phys. Lett. B*, 716:30–61, 2012.

[307] Benjamin W. Lee, C. Quigg, and H. B. Thacker. Weak interactions at very high energies: The role of the higgs-boson mass. *Phys. Rev. D*, 16:1519–1531, Sep 1977.

[308] Chien-Yi Chen, S. Dawson, and I. M. Lewis. Exploring resonant di-Higgs boson production in the Higgs singlet model. *Phys. Rev. D*, 91(3):035015, 2015.

[309] Ankit Beniwal, Marek Lewicki, Martin White, and Anthony G. Williams. Gravitational waves and electroweak baryogenesis in a global study of the extended scalar singlet model. *JHEP*, 02:183, 2019.

[310] N. Aghanim et al. Planck 2018 results. VI. Cosmological parameters. 2018.

[311] Genevieve Belanger, Fawzi Boudjema, Andreas Goudelis, Alexander Pukhov, and Bryan Zaldivar. micrOMEGAs5.0 : Freeze-in. *Comput. Phys. Commun.*, 231:173–186, 2018.

[312] Morad Aaboud et al. Combination of searches for invisible Higgs boson decays with the ATLAS experiment. *Phys. Rev. Lett.*, 122(23):231801, 2019.

[313] Albert M Sirunyan et al. Search for invisible decays of a Higgs boson produced through vector boson fusion in proton-proton collisions at $\sqrt{s} = 13$ TeV. *Phys. Lett. B*, 793:520–551, 2019.

[314] Michael E. Peskin and Tatsu Takeuchi. A New constraint on a strongly interacting Higgs sector. *Phys. Rev. Lett.*, 65:964–967, 1990.

[315] Tania Robens and Tim Stefaniak. Status of the Higgs Singlet Extension of the Standard Model after LHC Run 1. *Eur. Phys. J. C*, 75:104, 2015.

[316] Johannes Haller, Andreas Hoecker, Roman Kogler, Klaus Manig, Thomas Peiffer, and J?rg Stelzer. Update of the global electroweak fit and constraints on two-Higgs-doublet models. *Eur. Phys. J. C*, 78(8):675, 2018.

[317] Stefano Profumo, Michael J. Ramsey-Musolf, Carroll L. Wainwright, and Peter Winslow. Singlet-catalyzed electroweak phase transitions and precision Higgs boson studies. *Phys. Rev. D*, 91(3):035018, 2015.

[318] Philip Bechtle, Daniel Dercks, Sven Heinemeyer, Tim Stefaniak, and Georg Weiglein. HiggsBounds − 5: Testing Higgs sectors in the LHC 13 TeV era. *in preparation.*

[319] Philip Bechtle, Oliver Brein, Sven Heinemeyer, Oscar Stal, Tim Stefaniak, Georg Weiglein, and Karina E. Williams. HiggsBounds – 4: Improved Tests of Extended Higgs Sectors against Exclusion Bounds from LEP, the Tevatron and the LHC. *Eur. Phys. J. C*, 74(3):2693, 2014.

[320] Philip Bechtle, Sven Heinemeyer, Oscar Stal, Tim Stefaniak, and Georg Weiglein. *HiggsSignals*: Confronting arbitrary Higgs sectors with measurements at the Tevatron and the LHC. *Eur. Phys. J. C*, 74(2):2711, 2014.

[321] Federico Ambrogi, Chiara Arina, Mihailo Backović, Jan Heisig, Fabio Maltoni, Luca Mantani, Olivier Mattelaer, and Gopolang Mohlabeng. MadDM v.3.0: a Comprehensive Tool for Dark Matter Studies. *Phys. Dark Univ.*, 24:100249, 2019.

[322] Alex Geringer-Sameth, Savvas M. Koushiappas, and Matthew Walker. Dwarf galaxy annihilation and decay emission profiles for dark matter experiments. *Astrophys. J.*, 801(2):74, 2015.

[323] Torbjörn Sjostrand, Stefan Ask, Jesper R. Christiansen, Richard Corke, Nishita Desai, Philip Ilten, Stephen Mrenna, Stefan Prestel, Christine O. Rasmussen, and Peter Z. Skands. An Introduction to PYTHIA 8.2. *Comput. Phys. Commun.*, 191:159–177, 2015.

[324] Alex Geringer-Sameth, Matthew G. Walker, Savvas M. Koushiappas, Sergey E. Koposov, Vasily Belokurov, Gabriel Torrealba, and N. Wyn Evans. Indication of Gamma-ray Emission from the Newly Discovered Dwarf Galaxy Reticulum II. *Phys. Rev. Lett.*, 115(8):081101, 2015.

[325] Shang Li, Yun-Feng Liang, Kai-Kai Duan, Zhao-Qiang Shen, Xiaoyuan Huang, Xiang Li, Yi-Zhong Fan, Neng-Hui Liao, Lei Feng, and Jin Chang. Search for gamma-ray emission from eight dwarf spheroidal galaxy candidates discovered in Year Two of Dark Energy Survey with Fermi-LAT data. *Phys. Rev. D*, 93(4):043518, 2016.

[326] J. M. Alarcon, J. Martin Camalich, and J. A. Oller. The chiral representation of the πN scattering amplitude and the pion-nucleon sigma term. *Phys. Rev. D*, 85:051503, 2012.

[327] James M. Cline, Kimmo Kainulainen, Pat Scott, and Christoph Weniger. Update on scalar singlet dark matter. *Phys. Rev. D*, 88:055025, 2013. [Erratum: Phys. Rev.D92,no.3,039906(2015)].

[328] Xiu-Lei Ren, Xi-Zhe Ling, and Li-Sheng Geng. Pion-nucleon sigma term revisited in covariant baryon chiral perturbation theory. *Phys. Lett. B*, 783:7–12, 2018.

[329] G. Passarino and M. J. G. Veltman. One Loop Corrections for e^+e^- Annihilation Into $\mu^+\mu^-$ in the Weinberg Model. *Nucl. Phys. B*, 160:151–207, 1979.

[330] Ansgar Denner. Techniques for calculation of electroweak radiative corrections at the one loop level and results for W physics at LEP-200. *Fortsch. Phys.*, 41:307–420, 1993.

[331] T. Hahn and M. Perez-Victoria. Automatized one loop calculations in four-dimensions and D-dimensions. *Comput. Phys. Commun.*, 118:153–165, 1999.

[332] G. J. van Oldenborgh and J. A. M. Vermaseren. New Algorithms for One Loop Integrals. *Z. Phys. C*, 46:425–438, 1990.

[333] Yashar Akrami, Christopher Savage, Pat Scott, Jan Conrad, and Joakim Edsjo. Statistical coverage for supersymmetric parameter estimation: a case study with direct detection of dark matter. *JCAP*, 1107:002, 2011.

[334] K. Cranmer. Statistical Challenges for Searches for New Physics at the LHC. In Louis Lyons and Müge Karagöz Ünel, editors, *Statistical Problems in Particle Physics, Astrophysics and Cosmology*, page 112, Jan 2006.

[335] Glen Cowan, Kyle Cranmer, Eilam Gross, and Ofer Vitells. Asymptotic formulae for likelihood-based tests of new physics. *Eur. Phys. J. C*, 71:1554, 2011. [Erratum: Eur. Phys. J.C73,2501(2013)].

[336] Gregory D. Martinez, James McKay, Ben Farmer, Pat Scott, Elinore Roebber, Antje Putze, and Jan Conrad. Comparison of statistical sampling methods with ScannerBit, the GAMBIT scanning module. *Eur. Phys. J. C*, 77(11):761, 2017.

[337] Tobias Binder, Torsten Bringmann, Michael Gustafsson, and Andrzej Hryczuk. Early kinetic decoupling of dark matter: when the standard way of calculating the thermal relic density fails. *Phys. Rev. D*, 96(11):115010, 2017.

[338] Vanda Silveira and A. Zee. Scalar Phantoms. *Phys. Lett. B*, 161:136, 1985.

[339] John McDonald. Gauge singlet scalars as cold dark matter. *Phys. Rev. D*, 50:3637–3649, 1994.

[340] C. P. Burgess, Maxim Pospelov, and Tonnis ter Veldhuis. The Minimal model of nonbaryonic dark matter: A Singlet scalar. *Nucl. Phys. B*, 619:709–728, 2001.

[341] Roberto Trotta. Bayes in the sky: Bayesian inference and model selection in cosmology. *Contemp. Phys.*, 49:71–104, 2008.

[342] Peter Athron et al. Global analyses of Higgs portal singlet dark matter models using GAMBIT. *Eur. Phys. J. C*, 79(1):38, 2019.

[343] Alex Drlica-Wagner et al. Probing the Fundamental Nature of Dark Matter with the Large Synoptic Survey Telescope. 2019.

[344] Alessandro Cuoco, Jan Heisig, Michael Korsmeier, and Michael Krämer. Constraining heavy dark matter with cosmic-ray antiprotons. *JCAP*, 1804(04):004, 2018.

[345] Torsten Bringmann, Christopher Eckner, Anastasia Sokolenko, Lili Yang, and Gabrijela Zaharias. Probing the sensitivity of the Cherenkov Telescope Array to Dark Matter in the Galactic Center. TeV Particle Astrophysics 2018, 2018.

[346] M. Aguilar et al. Antiproton Flux, Antiproton-to-Proton Flux Ratio, and Properties of Elementary Particle Fluxes in Primary Cosmic Rays Measured with the Alpha Magnetic Spectrometer on the International Space Station. *Phys. Rev. Lett.*, 117(9):091103, 2016.

[347] Hu Zhan and J. Anthony Tyson. Cosmology with the Large Synoptic Survey Telescope: an Overview. *Rept. Prog. Phys.*, 81(6):066901, 2018.

[348] Shin'ichiro Ando et al. Discovery prospects of dwarf spheroidal galaxies for indirect dark matter searches. *JCAP*, 1910(10):040, 2019.

[349] Lisa Goodenough and Dan Hooper. Possible Evidence For Dark Matter Annihilation In The Inner Milky Way From The Fermi Gamma Ray Space Telescope. 2009.

[350] Dan Hooper and Tim Linden. On The Origin Of The Gamma Rays From The Galactic Center. *Phys. Rev. D*, 84:123005, 2011.

[351] Kevork N. Abazajian and Manoj Kaplinghat. Detection of a Gamma-Ray Source in the Galactic Center Consistent with Extended Emission from Dark Matter Annihilation and Concentrated Astrophysical Emission. *Phys. Rev. D*, 86:083511, 2012. [Erratum: Phys. Rev.D87,129902(2013)].

[352] Dan Hooper and Tracy R. Slatyer. Two Emission Mechanisms in the Fermi Bubbles: A Possible Signal of Annihilating Dark Matter. *Phys. Dark Univ.*, 2:118–138, 2013.

[353] Chris Gordon and Oscar Macias. Dark Matter and Pulsar Model Constraints from Galactic Center Fermi-LAT Gamma Ray Observations. *Phys. Rev. D*, 88(8):083521, 2013. [Erratum: Phys. Rev.D89,no.4,049901(2014)].

[354] Kevork N. Abazajian, Nicolas Canac, Shunsaku Horiuchi, and Manoj Kaplinghat. Astrophysical and Dark Matter Interpretations of Extended Gamma-Ray Emission from the Galactic Center. *Phys. Rev. D*, 90(2):023526, 2014.

[355] Francesca Calore, Ilias Cholis, and Christoph Weniger. Background model systematics for the Fermi GeV excess. *JCAP*, 1503:038, 2015.

[356] M. Ajello et al. Fermi-LAT Observations of High-Energy γ-Ray Emission Toward the Galactic Center. *Astrophys. J.*, 819(1):44, 2016.

[357] Alessandro Cuoco, Michael Krämer, and Michael Korsmeier. Novel Dark Matter Constraints from Antiprotons in Light of AMS-02. *Phys. Rev. Lett.*, 118(19):191102, 2017.

[358] Ming-Yang Cui, Qiang Yuan, Yue-Lin Sming Tsai, and Yi-Zhong Fan. Possible dark matter annihilation signal in the AMS-02 antiproton data. *Phys. Rev. Lett.*, 118(19):191101, 2017.

[359] Alessandro Cuoco, Jan Heisig, Michael Korsmeier, and Michael Krämer. Probing dark matter annihilation in the Galaxy with antiprotons and gamma rays. *JCAP*, 1710(10):053, 2017.

[360] Alessandro Cuoco, Jan Heisig, Lukas Klamt, Michael Korsmeier, and Michael Krämer. Scrutinizing the evidence for dark matter in cosmic-ray antiprotons. *Phys. Rev. D*, 99(10):103014, 2019.

[361] Ilias Cholis, Tim Linden, and Dan Hooper. A Robust Excess in the Cosmic-Ray Antiproton Spectrum: Implications for Annihilating Dark Matter. *Phys. Rev. D*, 99(10):103026, 2019.

[362] Alessandro Cuoco, Benedikt Eiteneuer, Jan Heisig, and Michael Krämer. A global fit of the γ-ray galactic center excess within the scalar singlet Higgs portal model. *JCAP*, 1606(06):050, 2016.

[363] C. Boehm, D. G. Cerdeño, P. A. N. Machado, A. Olivares-Del Campo, E. Perdomo, and E. Reid. How high is the neutrino floor? *JCAP*, 1901(01):043, 2019.

[364] W. Grimus, L. Lavoura, O. M. Ogreid, and P. Osland. The Oblique parameters in multi-Higgs-doublet models. *Nucl. Phys. B*, 801:81–96, 2008.